

# Measurement of the Neutron Radius of $^{208}\text{Pb}$ Through Parity Violation in Electron Scattering

Kiadtsak Saenboonruang  
Lampang, Thailand

B.S., University of Virginia, 2008

A Dissertation presented to the Graduate Faculty of  
the University of Virginia in Candidacy for the Degree of  
Doctor of Philosophy

Department of Physics

University of Virginia  
May, 2013



Dr. Nilanga K. Liyanage (Advisor)



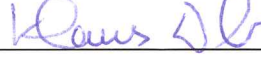
Dr. Kent D. Paschke



Dr. Simonetta Liuti



Dr. Scott M. Ransom



Dr. Klaus Dehmelt

---

# Measurement of the Neutron Radius of $^{208}\text{Pb}$ Through Parity-Violation in Electron Scattering

by

Kiadtsak Saenboonruang

## ABSTRACT

In contrast to the nuclear charge densities, which have been accurately measured with electron scattering, the knowledge of neutron densities still lack precision. Previous model-dependent hadron experiments suggest the difference between the neutron radius,  $R_n$ , of a heavy nucleus and the proton radius,  $R_p$ , to be in the order of several percent. To accurately obtain the difference,  $R_n - R_p$ , which is essentially a neutron skin, the Jefferson Lab Lead ( $^{208}\text{Pb}$ ) Radius Experiment (PREX) measured the parity-violating electroweak asymmetry in the elastic scattering of polarized electrons from  $^{208}\text{Pb}$  at an energy of 1.06 GeV and a scattering angle of  $5^\circ$ . Since  $Z^0$  boson couples mainly to neutrons, this asymmetry provides a clean measurement of  $R_n$  with respect to  $R_p$ .

PREX was conducted at the Jefferson lab experimental Hall A, from March to June 2010. The experiment collected a final data sample of  $2 \times 10^7$  helicity-window quadruplets. The measured parity-violating electroweak asymmetry  $A_{PV} = 0.656 \pm 0.060$  (stat)  $\pm 0.014$  (syst) ppm corresponds to a difference between the radii of the neutron and proton distributions,  $R_n - R_p = 0.33_{-0.18}^{+0.16}$  fm and provides the first electroweak observation of the neutron skin as expected in a heavy, neutron-rich nucleus.

The value of the neutron radius of  $^{208}\text{Pb}$  has important implications for models of nuclear structure and their application in atomic physics and astrophysics such as atomic parity non-conservation (PNC) and neutron stars.

In memory of my father  
Wan Saenboonruang  
1938-2011

## Acknowledgements

First of all, I would like to thank my dedicated and hard-working advisor, Professor Nilanga Liyanage, for introducing me to the world of nuclear physics. I joined Prof. Nilanga's research group during my 4<sup>th</sup> year as an undergraduate and later decided to continue doing researches under his supervision during my graduate study. Prof. Nilanga not only taught me priceless knowledge academically but also shaped me to be responsible and enthusiastic about the work. The experiences from working with Prof. Nilanga ensured me that I have chosen the right field of study and the right path for my career.

I would like to thank spokespersons of PREX, Professor Krishna Kumar, Professor Paul Souder, Dr. Robert Michaels, and Dr. G.M. Urciuoli for their great motivation and eager to pursue a new and advanced parity violating electron scattering experiment to measure the neutron radius of  $^{208}\text{Pb}$ , for all of their hard work, and for allowing me to participate in the experiment as a graduate thesis student. I also would like to thank Professor C.J. Horowitz, a great nuclear theorist, for all of the theoretical work in PREX.

I would like to thank Professor Kent Paschke for all the helps and suggestions during my data analysis. I also would like to thank Professor Gordon Cates and Professor Stefan Baeßler for being my graduate committee and for giving valuable comments during the research evaluation meeting.

I would like to thank Dr. Seamus Riodan for helping me on programming issues and for suggesting me on data analysis. Whenever I had a question, Seamus would give me useful answers, which helped me finish my work quickly. Moreover, Seamus worked so hard both during and after the experiment to ensure that PREX headed in the right direction. Seamus also helped me settle down quickly when I moved to Newport News.

I would like to thank fellow graduate students: Dr. Megan Friend, Chun-Min Jen,

Jon Wexler, Dr. Zafar Ahmed, and Dr. Rupesh Silwal, for making times spending together in Hall A enjoyable, and for collaborating and working tirelessly both during and after the experiment. Without their hard-worked contributions, the PREX would never be able to publish its notable results.

I would like to thank the members of Hall A collaboration and JLAB staffs for their efforts to put together the experimental setup, for collaboration during the experiment, and for taking shifts during the experiment.

I would like to thank Dr. Kondo Gnanvo for helping and for teaching me all the technical details about the Gas Electron Multiplier (GEM) chambers. Without Kondo, I would never learn as much knowledge of GEM and the data acquisition system as much as working with him. There are always interesting and useful ideas from Kondo, which helped our detector group improving at much faster pace. I also would like to thank Dr. Vladimir Nelyubin for working closely with me during the GEM construction processes and for all the useful suggestions.

I would like to thank former and recent members of Prof. Nilang's research group: Dr. Mitra Shabestari, Chao Gu, Jie Liu, and Xinzhan Bai, for being parts of this great group and for helping me working on all of the projects.

I would like to thank all the teachers and instructors for guiding and teaching me all the useful knowledge. They all took parts to shape me to be not only a good student but also a good member of the communities. Their efforts to teach me all the priceless knowledge have brought me this far. I truly appreciate everything from them.

I would like to thank my parents, Wan and Boonrian Seanboonruang, for always supporting and for all their love they have given me. They always supported me for whatever path I chose. They always encourage and cheer me up whenever I face any hardship. I also would like to thank my sister, Thitinan Saenboonruang, for taking care of me and for always getting a smile out of me even when I do not feel like to.

I would like to thank all of my friends for all the friendship and supports they have given me. Ten years away from homeland and family would be much worse if I do not have all the good friends.

Last but not least, I would like to thank Pintila Pam Wangviwat for being everything to me. Pam shares not only happiness but also sadness I have. Whenever I felt like giving up, Pam would always cheer me up and encourage me to keep fighting. Pam could magically put a smile on my face even without saying a word.

# Contents

<b>1</b>	<b>Introduction</b>	<b>1</b>
1.1	Motivation for the Neutron Radius Measurement . . . . .	3
1.2	Knowledge of Neutron Density and Radius . . . . .	4
1.2.1	Neutron Density and Neutron Radius Theory . . . . .	4
1.2.2	Neutron Density and Neutron Radius Measurement . . . . .	5
1.3	Implications of Neutron Radius Measurement . . . . .	6
1.3.1	Neutron Stars . . . . .	6
1.3.2	Atomic Parity Non-Conservation (PNC) Experiments . . . . .	8
<b>2</b>	<b>Theoretical Aspects</b>	<b>10</b>
2.1	Underlying Concepts for PREX . . . . .	10
2.1.1	Elastic Electron Scattering . . . . .	10
2.1.2	Helicity and Chirality . . . . .	12
2.1.3	Parity . . . . .	15
2.2	Weak Interaction . . . . .	16
2.2.1	Weak Neutral Current . . . . .	18
2.2.2	Electroweak Interaction . . . . .	19
2.3	Parity-Violating Elastic Electron Scattering . . . . .	21
2.3.1	Potential Scattering . . . . .	21
2.3.2	Parity Violation . . . . .	23

2.3.3	Electron-Nucleon Scattering . . . . .	25
2.3.4	Electron Scattering off $^{208}\text{Pb}$ . . . . .	29
2.4	Coulomb Distortions . . . . .	32
<b>3</b>	<b>The Experiment</b>	<b>33</b>
3.1	Choice of Target and Kinematics for PREX . . . . .	33
3.2	Thomas Jefferson National Accelerator Facility (Jefferson Lab) . . . . .	36
3.3	The Accelerator . . . . .	36
3.4	The Polarized Electron Source . . . . .	39
3.4.1	The Fiber-based Laser System . . . . .	39
3.4.2	Intensity Attenuator System . . . . .	41
3.4.3	GaAs Photocathode . . . . .	41
3.4.4	Helicity Pockels Cell . . . . .	43
3.4.5	Insertable Half-wave Plate . . . . .	44
3.4.6	Rotatable Half-wave Plate . . . . .	44
3.4.7	Spin Precession and Double Wien Filters . . . . .	45
3.4.8	Electron Guns and the Injector . . . . .	46
3.5	Hall A Overview . . . . .	47
3.6	Hall A Beamline . . . . .	47
3.6.1	Beam Energy Measurement . . . . .	48
3.6.2	Beam Current Measurement . . . . .	51
3.6.3	Beam Polarization Measurement . . . . .	53
3.6.4	Beam Position Measurement . . . . .	59
3.6.5	Raster . . . . .	61
3.6.6	Beam Modulation . . . . .	62
3.7	Targets . . . . .	63
3.7.1	Target Configurations . . . . .	63
3.7.2	Lead/Diamond Target . . . . .	65

3.7.3	Other Targets . . . . .	67
3.8	Luminosity Monitor . . . . .	68
3.9	Septum Magnet . . . . .	69
3.10	Collimator . . . . .	70
3.11	High Resolution Spectrometers (HRS) . . . . .	72
3.11.1	Magnets . . . . .	72
3.11.2	HRS Detectors . . . . .	74
3.12	Data Acquisition System (DAQ) . . . . .	78
3.13	Contributions of Author to the Experiment . . . . .	80
3.13.1	Contributions to Hardware Installations . . . . .	81
3.13.2	Contributions to Data Analysis . . . . .	81
3.14	The Summary of Experimental Procedures . . . . .	81
<b>4</b>	<b>Data Analysis</b>	<b>83</b>
4.1	High Resolution Spectrometer (HRS) Calibrations . . . . .	83
4.1.1	Spatial and Angular Calibration . . . . .	86
4.1.2	Momentum Calibration . . . . .	91
4.2	$Q^2$ Measurement . . . . .	93
4.2.1	$Q^2$ Components . . . . .	93
4.2.2	Average $Q^2$ Analysis . . . . .	100
4.2.3	Other Systematic Errors on the $Q^2$ Measurement . . . . .	105
4.3	Background Analysis . . . . .	109
4.3.1	Contamination due to Excited States of $^{208}\text{Pb}$ . . . . .	109
4.3.2	$^{12}\text{C}$ Contamination . . . . .	113
4.3.3	Rescattering in the HRS . . . . .	121
4.3.4	Summary of Corrections and Uncertainties from Background .	123
4.4	Asymmetry Analysis . . . . .	124
4.4.1	Blinded Analysis . . . . .	125

4.4.2	Raw Asymmetry ( $A_{raw}$ ) . . . . .	125
4.4.3	Beam Intensity Asymmetry ( $A_I$ ) . . . . .	127
4.4.4	False Beam Asymmetry from Beam Fluctuations ( $A_{Fb}$ ) . . . .	128
4.4.5	False Beam Asymmetry from Transverse Beam Polarization ( $A_{FT}$ ) . . . . .	131
4.4.6	Helicity-Correlated Beam Asymmetry and Position Differences	133
4.4.7	Normalizations and Corrections to $A_{PV}$ . . . . .	135
4.4.8	Corrected Asymmetry ( $A_{corr}$ ) . . . . .	138
4.4.9	Calculation of $A_{PV}$ . . . . .	139
4.4.10	Finite Acceptance Effects and Energy Loss Correction for $Q^2$ .	140
4.5	Calculation of Weak Charge Radius and Neutron Radius . . . . .	142
4.5.1	Weak Charge Radius . . . . .	143
4.5.2	Neutron Radius . . . . .	150
<b>5</b>	<b>Results and Conclusions</b>	<b>155</b>
5.1	Parity-Violating Asymmetry ( $A_{PV}$ ) . . . . .	155
5.2	Weak Charge Radius, Neutron Radius, and Neutron Skin . . . . .	156
5.2.1	Weak Charge Radius . . . . .	156
5.2.2	Neutron Radius and Neutron Skin . . . . .	157
5.3	Technical Accomplishments and Issues Faced in PREX . . . . .	158
5.3.1	Septum Magnet . . . . .	158
5.3.2	Double Wien Filter . . . . .	160
5.3.3	Transverse Asymmetry Systematic . . . . .	160
5.3.4	Statistical Noise . . . . .	161
5.3.5	Main Target . . . . .	161
5.3.6	Radiation Damages . . . . .	164
5.4	Possible Improved Strategies for Future Experiments . . . . .	164
5.4.1	Target Modifications . . . . .	164

5.4.2	Radiation Load and Septum Modifications . . . . .	165
5.5	Proposed Future PREX-Like Experiments . . . . .	166
5.5.1	PREX-II (E12-11-101) . . . . .	166
5.5.2	CREX (E12-12-004) . . . . .	168
5.6	Conclusions . . . . .	171
<b>A</b>	<b>Hall A Coordinate Systems</b>	<b>173</b>
A.1	Hall Coordinate System (HCS) . . . . .	173
A.2	Target Coordinate System (TCS) . . . . .	174
A.3	Detector Coordinate System (DCS) . . . . .	174
A.4	Transport Coordinate System (TRCS) . . . . .	175
A.5	Focal Plane Coordinate System (FCS) . . . . .	177
<b>B</b>	<b>Optics Calibration Procedures</b>	<b>179</b>
B.1	Spatial and Angular Calibration . . . . .	179
B.2	Momentum Calibration . . . . .	181
<b>C</b>	<b>HRS Optics Tensors Elements for PREX</b>	<b>184</b>
C.1	LHRS Optics Tensors Elements Used for PREX . . . . .	185
C.2	RHRS Optics Tensors Elements Used for PREX . . . . .	187
	<b>Bibliography</b>	<b>189</b>

# List of Tables

1.1	The table shows the comparison of strong interaction and electromagnetic interaction. . . . .	1
2.1	The table shows the comparison of strong, electromagnetic, and weak interactions for types of particles involved and lifetimes of decays. . .	18
2.2	Electromagnetic and neutral weak charges of the electron and light quarks. . . . .	20
3.1	PREX beam requirements . . . . .	39
3.2	Lead foils' mass and dimensions measurement . . . . .	66
3.3	Diamond foils' mass and dimensions measurement . . . . .	67
3.4	Characteristics of targets in water cell target ladder. The last column gives the average thickness of the target foil (average over the area of the foil) . . . . .	67
3.5	Characteristics of targets in standard solid target ladder. The last column gives the average thickness of the target foil (average over the area of the foil) . . . . .	68
3.6	Main design characteristics of the Hall A high resolution spectrometers; the resolution values are for the FWHM [6] . . . . .	73
3.7	ADC specifications for PREX . . . . .	79

4.1	Angle errors obtained after angular calibration . . . . .	89
4.2	$E_f^{ground} - E_f^{first}$ for carbon target on right HRS . . . . .	92
4.3	$E_{beam} - E' - E_{loss}$ for various nuclei in PREX at the central scattering angle of 5° . . . . .	96
4.4	Average $E_{loss}$ for two types of target materials used for measuring spectrometer central angle. . . . .	96
4.5	$E'_0 - E'_H$ for watercell target on left HRS . . . . .	97
4.6	$E'_0 - E'_H$ for watercell target on right HRS . . . . .	97
4.7	Spectrometer angles for PREX . . . . .	99
4.8	Errors from all angle measurements . . . . .	100
4.9	Errors of scattering angles . . . . .	100
4.10	$Q^2$ values for left HRS. The uncertainty of each $Q^2$ value is $\pm 0.00009$ GeV <sup>2</sup> . . . . .	102
4.11	$Q^2$ values for right HRS. The uncertainty of each $Q^2$ value is $\pm 0.00009$ GeV <sup>2</sup> . . . . .	102
4.12	average $Q^2$ values for left and right HRSs, which is calculated by a simple average over all the $Q^2$ runs. . . . .	103
4.13	Summary of $Q^2$ and useful information for PREX . . . . .	108
4.14	Summary of errors in $Q^2$ for PREX . . . . .	108
4.15	Energy differences between the ground state and some excited states of <sup>208</sup> Pb . . . . .	110
4.16	Pedestal values for each quartz detector that were applied for “ADC cut” . . . . .	110
4.17	The acceptance values for some excited states of <sup>208</sup> Pb . . . . .	112
4.18	The cross section ratios of the first excited state and the ground state of <sup>208</sup> Pb . . . . .	112
4.19	Explanations of terms in Eq. 4.25 - Eq. 4.27 . . . . .	114

---

4.20	Changes in the target thickness of Pb/D target 1 . . . . .	117
4.21	Changes in the target thickness of Pb/D target 2 . . . . .	117
4.22	Changes in the target thickness of Pb/D target 3 . . . . .	117
4.23	Average $Q^2$ from $^{12}\text{C}$ and $^{208}\text{Pb}$ and its corresponding $\frac{\sigma_C}{\sigma_{Pb}}$ . . . . .	121
4.24	Table shows the values of $^{12}\text{C}$ background fraction, $f$ , and asymmetry of this background, $A_C$ . . . . .	121
4.25	Main sources of background in PREX and their corresponding corrections and errors to the final parity-violating asymmetry. . . . .	123
4.26	The table shows the helicity-correlated (HC) position differences averaged over the experiment. . . . .	134
4.27	The table shows the non-linearities in PREX and their associated correction and systematic uncertainties. . . . .	137
4.28	The table shows the corrections and their systematic errors in $A_{PV}$ from various sources. . . . .	137
4.29	Values of $A_{corr}$ and the statistical error, for each helicity reversal state and for the grand average. The $\chi^2$ per degree of freedom for each average is also shown. . . . .	138
4.30	The table shows the values for quantities used to calculate a parity-violating asymmetry ( $A_{PV}$ ) . . . . .	140
4.31	Least squares fits of Wood Saxon parameters to theoretical mean field model weak charge densities. . . . .	145
4.32	Least squares fits of Helm parameters to theoretical mean field model weak charge densities. . . . .	149
5.1	The table shows the corrections and their systematic errors in $A_{PV}$ from various sources. . . . .	156
5.2	The table shows the calculations of $R_n$ and $R_n - R_p$ from the two methods. . . . .	157

5.3	The table shows the important parameters for the approved PREX-II experiment. . . . .	168
5.4	The table shows the important details in the CREX proposal. . . . .	171
C.1	Tensor elements for LHR.S. . . . .	186
C.2	Tensor elements for RHR.S. . . . .	188

# List of Figures

1.1	The plot shows the stability of various isotopes of different nuclei. The black dots illustrate stable nuclei. . . . .	2
1.2	The difference between neutron radii and proton radii for several nuclei of different mass number $A$ . The filled symbols are for the relativistic mean field NL1 interaction while the open symbols are for the nonrelativistic zero range Skyrme skiii interaction. A possible 1% measurement in $^{208}\text{Pb}$ is indicated by the error bar which has been arbitrarily placed at $R_n-R_p=0$ . . . . .	5
1.3	Cross sectional of neutron star. Densities are in terms of $\rho_0$ , the saturation nuclear matter density, which happens when nucleus begin to touch. . . . .	7
2.1	The figure shows the schematic of elastic electron scattering off a nucleus. The scattering angle depends on the impact parameters and the strength of the potential from the nucleus and the incident electrons. BSE stands for “back scattered electrons”. . . . .	11
2.2	The figure illustrates the definitions of the helicity of a particle. A right-handed particle is a particle with the direction of the spin the same as the direction of its motion. A left-handed particle is a particle with the direction of the spin opposite the direction of its motion. . .	13

2.3	The figure illustrates how the parity transformation changes the handedness of a particle. Under the parity transformation, the momentum changes its direction, while spin remains the same, and thus changes the handedness of a particle. . . . .	15
2.4	Beta emission is preferentially in the direction opposite to the nuclear spin, indicating the violation of parity conservation. . . . .	17
3.1	Figures of Merit (FOM) for PREX to determine choices of kinematics. This figure shows the FOM from optimizing the $^{208}\text{Pb}$ target . . . . .	35
3.2	Thomas Jefferson National Accelerator (JLAB) . . . . .	37
3.3	Schematic overview of the CEBAF accelerator and a new experimental hall (Hall D) . . . . .	37
3.4	Schematic of beam entering the Hall A . . . . .	38
3.5	Schematic overview of the polarized electron source and the accelerator	40
3.6	Schematic of the fiber-based laser system . . . . .	40
3.7	Various types of GaAs photocathode. PREX used the superlattice photocathode due to its higher polarization. . . . .	41
3.8	Details of superlattice photocathode used in PREX . . . . .	42
3.9	A diagram of the bandgap and energy levels for superlattice GaAs. The arrow indicates the allowed transitions for left-helicity photons .	43
3.10	Helicity Pockels Cell converts linearly polarized electron beam to circularly polarized. . . . .	43
3.11	The RWP can rotate the polarization ellipses shown in the top illustration to the orientation shown in the bottom to minimize the charge asymmetry . . . . .	45
3.12	Double Wein filters produces fully longitudinal polarization . . . . .	46
3.13	Schematic drawing of instrumentation in Hall A from top view . . . .	47
3.14	The arc section of the beamline . . . . .	49

3.15 The eP beam energy measurement instrumentation . . . . .	50
3.16 The schematic of beam current monitor (BCM) . . . . .	51
3.17 Hall A Møller polarimeter set up . . . . .	54
3.18 A schematic of the Compton polarimeter layout in Hall A . . . . .	56
3.19 A waveform from the GSO calorimeter for an incident photon in the energy range for Compton-scattered photons (for PREX, the maximum scattered photon energy was 38.4 MeV) . . . . .	58
3.20 Beam Position Monitors layout and associated coordinate systems . .	60
3.21 Hall A Beam position Monitor readout electronics . . . . .	61
3.22 Schematic of Hall A beamline including seven coils of beam modulation.	62
3.23 Target configuration during optics/calibration phase . . . . .	64
3.24 Target configuration during production phase . . . . .	64
3.25 Lead/Diamond target configurations and the components . . . . .	65
3.26 A completed Lead/Diamond target with He cooling tube. The liquid He flows around the target foils. . . . .	66
3.27 Septum magnets were installed between the target vacuum and the spectrometers. . . . .	70
3.28 Conceptional drawing of the PREX collimators. The Be plug is shown near the top of the aperture of this collimator. It can be blocked by a remotely actuated tungsten plug. . . . .	71
3.29 A cross sectional view of the experimental Hall A showing details of an HRS . . . . .	72
3.30 Schematic layout of a HRS device . . . . .	73
3.31 VDC schematic layout . . . . .	75
3.32 VDC location as seen from side view and top view . . . . .	76
3.33 HRS layout showing the location of main triggers, S0 and S1. . . . .	77
3.34 The schematic of quartz detectors principle . . . . .	77

3.35 Cherenkov cone of electrons in the quartz. Bold area delimits the arc of the cone which contributes to the PMT signal . . . . .	78
3.36 Circuit diagram of one channel of the 16 bit integrating ADC . . . . .	80
4.1 Sieve slit coordinate system used in optics reconstruction . . . . .	86
4.2 PREX sieve slit used for optics reconstruction (units shown in inches). The two bigger holes are for the ability to identify the orientation of reconstructed data . . . . .	87
4.3 Target coordinate system (TCS) for left HRS. $L$ is the distance from Hall center to the sieve plane, while $D$ is the horizontal displacement of the spectrometer axis from its ideal position. Spectrometer central angle is denoted by $\Theta_0$ . Note that $x_{tg}$ and $x_{sieve}$ are vertically down (into the page) . . . . .	89
4.4 Optimized $\theta_{tg}$ vs $\phi_{tg}$ sieve patterns for left HRS. . . . .	90
4.5 Optimized $\theta_{tg}$ vs $\phi_{tg}$ sieve patterns for right HRS. . . . .	90
4.6 Optimized $y_{tg}$ histogram for left HRS. The horizontal beam position used for this particular run was -2.5 mm (in HCS) . . . . .	91
4.7 Optimized $y_{tg}$ histogram for right HRS. The horizontal beam position used for this particular run was 3 mm (in HCS) . . . . .	91
4.8 Carbon momentum spectrum after the calibration showing the final momentum difference between the ground state and the first excited state of $^{12}\text{C}$ . . . . .	92
4.9 Watercell target momentum spectrum . . . . .	98
4.10 Spectrometer angle ( $\theta_0$ ) comparison between pointing and surveys . .	99
4.11 $Q^2$ distribution on L-HRS . . . . .	101
4.12 $Q^2$ distribution on R-HRS . . . . .	101
4.13 The relationship between calibrated $y_{tg}$ and known beam positions . .	104
4.14 $Q^2$ distribution versus beam position on L-HRS . . . . .	105

4.15 $Q^2$ distribution versus beam position on R-HRS . . . . .	105
4.16 $Q^2$ showing VDC performance at different trigger rate (L-HRS) . . .	106
4.17 $Q^2$ showing VDC performance at different trigger rate (R-HRS) . . .	106
4.18 $Q^2$ dependence on trigger rate (higher values at the same rate are L-HRS). The red dashed line shows the limit of the trigger rate that could be used for $Q^2$ measurement. . . . .	107
4.19 The figures illustrate the procedures to obtain the acceptance of the PREX detectors. The top figure is the energy spectrum of scattered electrons without the ADC cut. Previous white spectrum data (with no ADC cut) taken for HRSs show that the relative acceptance is $100 \pm 3\%$ over the full range shown [40]. The second figure is the energy spectrum of scattered electron with the ADC cut. The last figure shows the acceptance of the detectors, which is the ratio of normalized numbers of events with ADC cut to the number of events without ADC cut in each small bin of energy. The lines labeled $5^-$ and $3^-$ indicate the locations of $^{208}\text{Pb}$ excited states. . . . .	111
4.20 The raster current weighted by the detector events showing the target uniformity for the run 27258 taken on April 4 <sup>th</sup> , 2010 . . . . .	115
4.21 The raster current weighted by the detector events showing the target uniformity for the run 27789 taken on June 11 <sup>th</sup> , 2010 . . . . .	115
4.22 The histogram illustrates the change in the thickness of target 1 . .	118
4.23 The histogram illustrates the change in the thickness of target 2 . .	118
4.24 The histogram illustrates the change in the thickness of target 3 . .	119
4.25 The plot shows the differential cross section of $^{208}\text{Pb}$ and $^{12}\text{C}$ for different 4-momemtum transfer $Q^2$ . The differential cross sections are shown in arbitrary units . . . . .	120

---

4.26 Probabilities of electrons to rescatter in the spectrometers and reach the detectors as a function of scattered momentum [31]. The probability was measured by increasing the spectrometer dipole field to force elastic trajectories to trace those taken by the lower-energy inelastics at the production momentum setting. . . . .	122
4.27 The histogram showing the normalized spectrum of scattered electrons as a function of scattered momentum [31]. The spectrum measurement was performed by lowering the dipole magnet to let lower-energy, inelastically scattered electrons to reach the main detectors. . . . .	123
4.28 The figure shows the examples of the (blinded) raw asymmetries in two different states of double Wien filter and IHWP [4]. . . . .	127
4.29 The beam modulation applied controlled changes of beam position and energy to measure the false beam asymmetries arising from random fluctuations. The traces in red are x-position modulation, blue are y-position modulation and magenta are energy modulation. BPM4a and BPM4b measured fluctuations in beam position, and BPM12x measured fluctuations in beam energy [71]. . . . .	129
4.30 The figure shows the unblinded raw asymmetry for all asymmetry runs. The asymmetry for each run has been multiplied by +1 or -1 depending on the helicity state. The black horizontal line is the average value of the raw asymmetry. The average raw asymmetry shown must be multiplied by -1 to get the corrected sign [72]. . . . .	139
4.31 The figure shows the comparison between the measured $Q_{focal}^2$ (red) and the simulated $Q_{focal}^2$ using HAMC (black). . . . .	141
4.32 The figure shows the comparison between the simulated $Q_{focal}^2$ (red) and the simulated $Q_{vertex}^2$ (black), generated by HAMC. . . . .	141

4.33 The figure shows the acceptance function as a function of scattering angles for PREX using HAMC [47]. . . . .	143
4.34 The figure shows the wood-saxon form of $\rho(r) = \frac{\rho_0}{1+e^{(r-R)/a}}$ . The parameter $\rho_0$ is the maximum of $\rho(r)$ (in this case, 1). The parameter $R$ is the value of $r$ such that $\rho(r) = \rho_0/2$ . The difference in $r$ such that $\rho(r)$ decreases from $0.9\rho_0$ to $0.1\rho_0$ equals to $4.4a$ . . . . .	144
4.35 The figure shows the Helm model of $\rho_W(r) = \int d^3r' f_G(r - r')\rho_0\Theta(R_0 -  r' )$ where $f_G(r) = \frac{1}{(2\pi)^{3/2}\sigma^3}e^{-r^2/2\sigma^2}$ . The parameters used in this plot are; $R_0 = 10$ , $\sigma = 1$ , and $\rho_0 = 1$ . . . . .	147
4.36 Helm model weak charge density $-\rho_W(r)$ of $^{208}\text{Pb}$ that is consistent with the PREX result (solid black line). The brown error band shows the incoherent sum of experimental and model errors. The red dashed curve is the experimental charge density $\rho_{ch}$ and the blue dotted curve shows a sample mean-field result based on the FSUGold interaction [68].	150
4.37 Result of the asymmetry in PREX (red square) versus neutron point radius $R_n$ in $^{208}\text{Pb}$ . The horizontal (vertical) red line shows the error in $A_{PV}(R_n)$ measurement. Distorted-wave calculations for seven mean-field neutron densities are circles while the diamond marks the expectation for $R_n = R_p$ . The blue squares show plane wave impulse approximation results. . . . .	153
5.1 Result of the asymmetry in PREX (red square) vs neutron point radius $R_n$ in $^{208}\text{Pb}$ . The horizontal (vertical) red line shows the error in $A_{PV}(R_n)$ measurement. Distorted-wave calculations for seven mean-field neutron densities are circles while the diamond marks the expectation for $R_n = R_p$ . The blue squares show plane wave impulse approximation results. . . . .	158

---

5.2 Simulated and reconstructed scattering angle for PREX. The data are compared to the original simulation (left) and a corrected simulation (right), where the correction takes into account that the septum current was set too low by 5% such taht the scattering angle cutoff was too high by 5 mrad ( $0.3^\circ$ ). . . . .	159
5.3 Distribution of the asymmetries for a typical run at $70 \mu\text{A}$ . The width of 171 ppm is consistent with counting statistics [46]. . . . .	161
5.4 Rate measured in counting mode versus time in days for the three Pb/D targets. The target with the thinnest diamond backing degraded the fastest. The target with the thickest diamond did not melt and ran for 4 days at $70 \mu\text{A}$ (7.5 days total). . . . .	163
5.5 Simulated rates in one HRS versus $Q^2$ for two assumptions about septum current setting. For $I=729\text{A}$ (PREX-I), the minimum scattering angle was $4.58^\circ$ and was not optimal. For $I=775\text{A}$ , the minimum angle will be $4.35^\circ$ . By setting the septum at $I=775\text{A}$ and reducing the energy to the range of 925-1000 MeV, the rate is expected to increase by a factor of two. . . . .	166
5.6 The PREX asymmetry for the first PREX data, the PREX-II projections, and 8 selected models. . . . .	167
5.7 The figure shows the rates for 1 HRS versus angle for a beam energy of 2.2 GeV and a beam current of $100 \mu\text{A}$ in CREX proposal. . . . .	169
5.8 The figure shows the measured asymmetry versus angle for a beam energy of 2.2 GeV and a beam current of $100 \mu\text{A}$ in CREX proposal. A factor of 0.85 for the beam polarization is included. . . . .	170
5.9 The figure shows the sensitivity of the asymmetry $\epsilon$ versus angle for a beam energy of 2.2 GeV and a beam current of $100 \mu\text{A}$ in CREX proposal. . . . .	170

A.1	Hall A coordinate system (HCS) (top view) . . . . .	174
A.2	Target coordinate system (TCS) for left HRS. $L$ is the distance from Hall center to the sieve plane, while $D$ is the horizontal displacement of the spectrometer axis from its ideal position. Spectrometer central angle is denoted by $\Theta_0$ . Note that $x_{tg}$ and $x_{sieve}$ are vertically down (into the page) . . . . .	175
A.3	Detector coordinate system (DCS)(top view) . . . . .	176
A.4	Detector coordinate system (DCS)(side view) . . . . .	176
A.5	Transport coordinate system (TRCS)(side view) . . . . .	177
A.6	The focal plane (rotated) coordinate system as a function of the focal plane position(side view) . . . . .	178

# Chapter 1

## Introduction

A nucleon (a neutron or a proton) in a nucleus experiences two important forces. One is the attractive force due to the strong nuclear interaction between nucleons. The other force is the repulsive force due to the electrostatic interaction between protons. The nuclear force between nucleons is a derived force from the strong interaction between quarks; similar to Van der Waals force between molecules arising due to electrostatic forces within atoms. The comparison of the two forces in the nucleus is given in Table 1.1. Note that the nuclear force has a short range of about  $10^{-15}$  m and diminishes after that. On the other hand, the strength of the electromagnetic force decreases as  $1/r^2$ .

Interaction	Type	Range (m)
Nuclear	attractive	approximately $10^{-15}$
Electromagnetic	repulsive	infinite ( $\propto 1/r^2$ )

Table 1.1: The table shows the comparison of strong interaction and electromagnetic interaction.

The range of the nuclear force happens to be about the size of a nucleon. As a result, a given nucleon in a nucleus is only attracted by the nuclear force to its nearest neighbors. Therefore, for small nuclei with mass numbers ( $A$ ) up to iron ( $_{26}\text{Fe}$ ), the strength of the nuclear force increases as  $A$  increases. However, in the case of heavier

nuclei, the strength of the nuclear force acting on a nucleon becomes almost a constant and independent of  $A$ . On the other hand, the repulsive electrostatic force acting on a proton keeps increasing as  $Z$  increases. This leads to the reduction in the average binding energy as  $A$  increases and causes the instability of heavy nuclei.

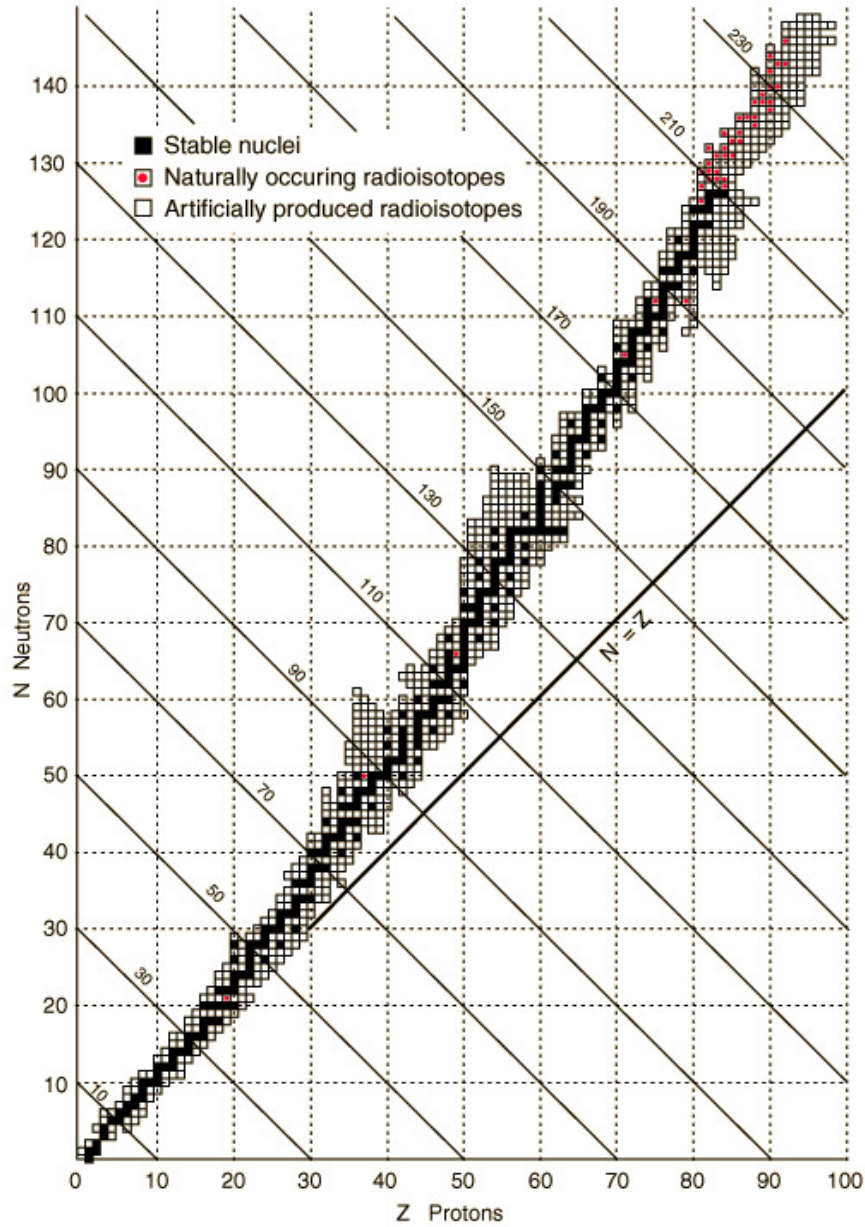


Figure 1.1: The plot shows the stability of various isotopes of different nuclei. The black dots illustrate stable nuclei.

In order to increase the stability of heavier nuclei, the number of neutrons ( $N$ ) in the nucleus must be greater than the number of protons ( $Z$ ) such that it increases the attractive nuclear force to balance the repulsive electrostatic force. As presented in Fig. 1.1, the  $N/Z$  ratio increases as nuclei become heavier. By the time,  $Z \sim 80$ ,  $N/Z \sim 1.5$ . As a result, the radius of neutron distribution,  $R_n$ , is expected to be larger than the radius of the proton distribution,  $R_p$ , in heavy nuclei leading to a “neutron skin” in these nuclei. The goal of the lead ( $^{208}\text{Pb}$ ) radius experiment (PREX) is to measure the thickness of the neutron skin of the  $^{208}\text{Pb}$  nucleus by measuring the neutron radius of  $^{208}\text{Pb}$ , which is the heaviest stable nucleus with 82 protons and 126 neutrons or a ratio of  $N/Z = 1.54$ .

## 1.1 Motivation for the Neutron Radius Measurement

The saturation density of nuclear matter ( $\rho_0$ ) is a fundamental concept central to the study of nuclear structure, the nature of the interactions between nucleons, models of heavy ion collisions, and applications of dense matter in astrophysics. However, present estimates of  $\rho_0$  are based only on known proton density. This leads to significant uncertainties in  $\rho_0$  since we do not have accurate information on the central neutron density. Despite the fact that there have been many measurements of neutron densities with strongly interacting probes such as pion or proton elastic scattering, unfortunately, all such measurements suffer from potentially serious theoretical systematic errors. As a result, no hadronic measurement of neutron densities has been generally accepted. For example, in the case of modern mean field interaction, due to the uncertainties in systematic errors, the interactions are typically fit without using any neutron density information [29]. Hence, an accurate measurement of the neutron radius  $R_n$  will constrain the average interior neutron density and help refine our knowledge of  $\rho_0$  and modern mean field interactions.

One possible way to measure the neutron radius,  $R_n$ , is based on the fact that

the  $Z^0$  boson couples primarily to neutrons<sup>1</sup> and leads to the occurrence of parity violation. Thus, experiments in parity violating elastic electron-nucleus scattering could provide an accurate and model-independent measurement of neutron densities and  $R_n$ .

In order to have very accurate parity violating measurements, very good helicity correlated beams and advanced experimental equipment are required. Fortunately, with the very high quality of beam properties of Continuous Electron Beam Accelerator Facility at Jefferson Lab and equipment in the experimental Hall A, very accurate parity violating experiments are possible. The first measurement of the neutron radius in  $^{208}\text{Pb}$  through parity-violation in elastic electron scattering (PREX) was conducted in Hall A in 2010. The data analysis was completed and final results were published in 2012. The details on PREX will be discussed in this dissertation.

## 1.2 Knowledge of Neutron Density and Radius

### 1.2.1 Neutron Density and Neutron Radius Theory

There are several models to predict the neutron radius of a heavy nucleus. The most well-known models are mean field models and Skyrme force models. A relativistic mean field calculation gives  $R_n - R_p \approx 0.3$  fm, while a nonrelativistic zero range Skyrme force gives  $R_n - R_p \approx 0.1$  fm for the  $^{208}\text{Pb}$  nucleus [58].

Fig. 1.2 shows the difference between neutron radii,  $R_n$ , and proton radii,  $R_p$ , for a range of nuclei based on two typical interactions. One can take the spread between the two methods of calculations as some measure of the uncertainty in  $R_n$ , and, by using these calculations, they both suggest the existence of the neutron skin.

---

<sup>1</sup>The  $Z^0$ -proton coupling depends on the small factor  $1-4\sin^2\Theta_W$ , where  $\sin^2\Theta_W \sim 0.24$ .

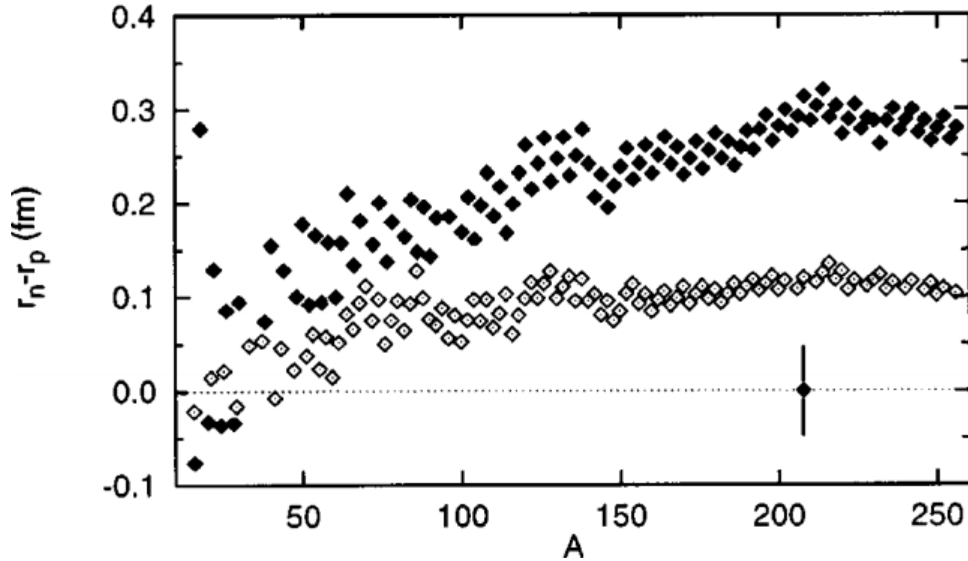


Figure 1.2: The difference between neutron radii and proton radii for several nuclei of different mass number  $A$ . The filled symbols are for the relativistic mean field NL1 interaction while the open symbols are for the nonrelativistic zero range Skyrme skiii interaction. A possible 1% measurement in  $^{208}\text{Pb}$  is indicated by the error bar which has been arbitrarily placed at  $R_n-R_p=0$ .

### 1.2.2 Neutron Density and Neutron Radius Measurement

There have been several experimental approaches to measure the neutron density and neutron radii of nuclei. Originally, neutron radii were extracted from Coulomb energy differences [35]. However, it is now thought that these measurements are actually sensitive to isospin violating interactions rather than neutron skin. Next set of experiments,  $(p, d)$  and  $(d, t)$  stripping reactions, are only sensitive to the tail in the neutron density at very large radius and are not directly sensitive to the interior density, which is much larger than the tail, and contributes significantly to  $R_n$ . Therefore,  $R_n$  cannot be extracted from stripping experiments without making some model assumptions.

Another experimental approach involves elastic proton-nucleus scattering, which is sensitive to both the surface and interior neutron density. Typically, this data is analyzed in an impulse approximation where a nucleon-nucleon interaction is folded

with the nucleon density. Unfortunately, the corrections to the impulse approximation have uncertainties that are difficult to quantify.

Also, it was once purposed that the neutron density could be extracted by comparing the data from elastic scattering of positive and negative pions. However, it was later pointed out that this method was not directly sensitive to the neutron density [18].

As of now, no existing measurement of neutron densities or radii has an established accuracy of 1%. With the possible 1% accuracy and model independence of PREX, this approach can have a major impact on our knowledge of neutron density and neutron radii of nuclei.

In short, PREX used the parity violating elastic electron scattering off  $^{208}\text{Pb}$  nuclei to extract  $R_n$ . The asymmetry,  $A_{PV} = \frac{\sigma_R - \sigma_L}{\sigma_R + \sigma_L}$ , results due to the interference between the  $Z^0$  exchange amplitude (weak neutral current) and the photon exchange amplitude. The asymmetry is mostly sensitive to the neutrons (and hence to  $R_n$ ) because the weak charge of the neutron is much larger than the weak charge of the proton.

## 1.3 Implications of Neutron Radius Measurement

### 1.3.1 Neutron Stars

An accurate determination of  $R_n$  is an important input to calculate the Equation of State (EOS), which describes how pressure varies as a function of density, of neutron rich matters such as neutron stars. A neutron star is a type of stellar remnant that can result from the gravitational collapse of a massive star during a supernova event. Such stars are composed predominantly of neutrons. Neutron stars are very hot and are supported against further collapse by quantum degeneracy pressure due to the

Pauli exclusion principle<sup>2</sup>

On the basis of current models, the matter at the surface of a neutron star is composed of ordinary atomic nuclei crushed into a solid lattice with a sea of electrons flowing through the gaps between them. The “atmosphere” of the star is hypothesized to be at most several micrometers thick, and its dynamic is fully controlled by the star’s magnetic field. Below the atmosphere, one encounters a solid crust. This crust is extremely hard and very smooth because of the extreme gravitational field. Proceeding inward, one encounters nuclei with increasing numbers of neutrons, and to a point called neutron drip where neutron leak out of nuclei and become free neutrons. In this region, there are nuclei, free electrons, and free neutrons. The nuclei become smaller and smaller until the core is reached, where they disappear altogether. The composition of the superdense matter in the core remains uncertain. One model describes the core as superfluid neutron-degenerate matter. More exotic forms of matter are possible, including degenerate strange matter or ultra-dense quark-degenerate matter [27].

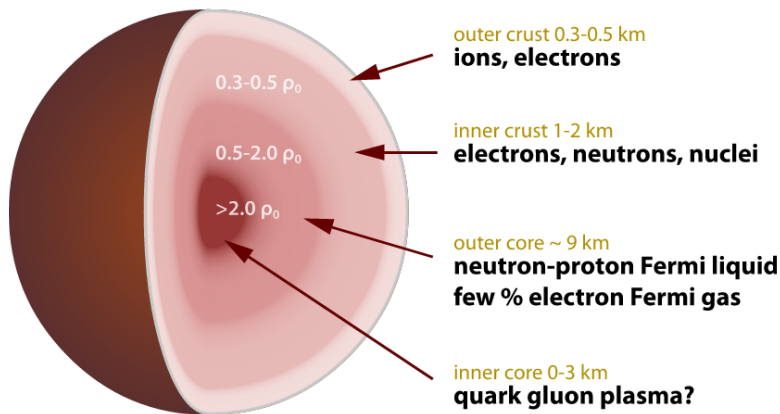


Figure 1.3: Cross sectional of neutron star. Densities are in terms of  $\rho_0$ , the saturation nuclear matter density, which happens when nucleus begin to touch.

The correlation between  $R_n$  and the radius of a neutron star  $r_{NS}$  is also very

---

<sup>2</sup>Pauli exclusion principle states that no two neutrons (fermions) can occupy the same place and quantum state simultaneously.

interesting. In general, a larger  $R_n$  implies a stiffer equation of state (EOS), which will also suggest a larger  $r_{NS}$ . However, it has been determined from the observation of X-ray bursts that  $r_{NS}$  is very small, near 10 km, implying that the EOS softens at high density which is suggestive of a transition to an exotic phase of QCD. In contrast, Steiner *et al.* [66] conclude that  $r_{NS}$  is near 13 km, leading to a prediction that  $R_n - R_p = 0.15 \pm 0.02$  fm for  $^{208}\text{Pb}$ . This implies a stiffer EOS which leaves little room for softening due to a phase transition at high density. This controversy could be resolved once the high accuracy of  $R_n$  information is achievable.

The EOS of neutron-rich matter is also closely related to the symmetry energy <sup>3</sup>,  $S$  [63]. There is a strong correlation between  $R_n$  and the density dependence of the symmetry energy,  $\frac{dS}{d\rho}$ , where  $\rho$  is the baryon density. The symmetry energy,  $S$ , helps determine the composition of a neutron star. A large  $S$  at high density would imply a large proton fraction, which would allow the direct Urca process<sup>4</sup> of rapid neutrino cooling. If  $R_n - R_p$  were large, it is likely that massive neutron stars would cool quickly by the direct Urca process. In addition, the transition density from a solid neutron star crust to the liquid interior is also strongly correlated with  $R_n - R_p$  [28].

### 1.3.2 Atomic Parity Non-Conservation (PNC) Experiments

The atomic PNC experiments allow to test the standard model at low energies. These experiments can be sensitive to new parity violating interactions such as additional heavy  $Z^0$  bosons. Furthermore, by comparing atomic PNC to higher  $Q^2$  measurements, one can study the momentum dependence of standard model radiative corrections. However, as the accuracy of atomic PNC experiments improves, they will require increasingly precise information on neutron densities since the parity violating

---

<sup>3</sup>The symmetry energy is defined as the difference in energy per nucleon between the pure neutron matter and the symmetric nuclear matter containing an equal number of protons and neutrons, i.e. for a nucleus,  $S \propto \frac{(N-Z)^2}{A}$  or  $S \propto \frac{(A-2Z)^2}{A}$ .

<sup>4</sup>In astroparticle physics, an Urca process is a reaction which emits a neutrino and which is assumed to take part in cooling processes in neutron stars and white dwarfs.

interaction is proportional to the overlap between electrons and neutrons. In the future, the most precise low energy standard model tests may involve the combination of an atomic PNC measurement and parity violating electron scattering to constrain the neutron density.

Unfortunately, atomic PNC experiments suffer from atomic theory uncertainties in the electron density at the nucleus. These uncertainties motivate future atomic experiments involving isotope ratios where the atomic theory dependences cancel out. However, these ratios may require even more nuclear structure information on isotope differences of neutron densities. Parity violating electron scattering measurement of isotope differences could be performed in the future to significantly improve the accuracy of atomic PNC experiments.

## Chapter 2

# Theoretical Aspects

This chapter will discuss important theoretical aspects of PREX, including some useful concepts used in PREX, definition and characteristics of the weak interaction, and the relationship between parity violation,  $A_{PV}$  and neutron radius,  $R_n$ .

## 2.1 Underlying Concepts for PREX

### 2.1.1 Elastic Electron Scattering

In scattering theory, elastic scattering is one of the specific forms of scattering where the kinetic energies of the incident particles are conserved in the center-of-mass frame, only their directions of propagation are modified after the scattering.

In particular, elastic electron scattering is used widely in nuclear structure study. Most of electron scattering experiments involve bombarding a beam of electrons on a target made of the atoms under study, and observing the rate of scattering as a function of scattering angle and energy.

For example, considering incident electron energy  $E_1$  and momentum  $\mathbf{k}_1$ , and scattered electron energy  $E_2$  and momentum  $\mathbf{k}_2$ , with scattering angle  $\theta$ , the electron

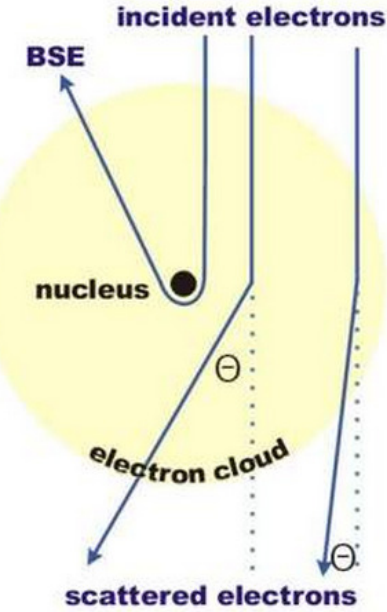
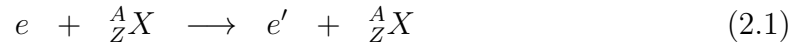


Figure 2.1: The figure shows the schematic of elastic electron scattering off a nucleus. The scattering angle depends on the impact parameters and the strength of the potential from the nucleus and the incident electrons. BSE stands for “back scattered electrons”.

scattering process on a heavy nuclear target [69],



as shown in Fig. 2.1, satisfies the kinematic equations

$$\mathbf{k}_1 - \mathbf{k}_2 = \mathbf{q} \quad (2.2)$$

$$E_1 - E_2 = E \quad (2.3)$$

where  $E$  is the energy transfer to the nucleus; in elastic scattering, the energy transfer equals to the recoil kinetic energy of the target nucleus in the lab frame. The quantity  $\mathbf{q}$  is the momentum transfer of the incident electron. However, a more commonly used term in nuclear physics for the momentum transfer is the four-momentum transfer

squared,  $Q^2$ , which is defined as  $Q^2 = -q^2$  and can be expressed as;

$$Q^2 = 2E_1 E_2 (1 - \cos(\theta)) \quad (2.4)$$

For elastic scattering, the scattered electron energy,  $E_2$ , can also be expressed in terms of  $E_1$  as

$$E_2 = \frac{E_1}{1 + \frac{2E_1 \sin^2(\frac{\theta}{2})}{M_t}} \quad (2.5)$$

where  $E_1$ ,  $E_2$ , and  $\theta$  are beam energy, final energy after scattering, and scattering angle respectively.

Given the relationships shown above, ones can eliminate one of  $E_1$ ,  $E_2$ , and  $\theta$ , and  $Q^2$  can be rewritten as

$$1. Q^2 = 2E_1^2 f_r (1 - \cos(\theta))$$

$$2. Q^2 = 2E_2^2 f'_r (1 - \cos(\theta))$$

$$3. Q^2 = 2m_p(E_1 - E_2)$$

Here  $f_r$  and  $f'_r$  are recoil factors defined as  $f_r = \frac{1}{1 + (\frac{E_1}{m})(1 - \cos(\theta))}$  and  $f'_r = \frac{1}{1 - (\frac{E_2}{m})(1 - \cos(\theta))}$ .

Because of its simplicity and well-studied characteristics of elastic electron scattering, PREX made use of its principles as part of the advanced experimental design to probe the neutron distribution of the  $^{208}\text{Pb}$  nucleus.

### 2.1.2 Helicity and Chirality

Although helicity and chirality are related closely and they are used interchangably in the case of massless particles, in general, these two terms are distinguishable and can be explained in two different ways.

### Helicity

Helicity is the projection of the spin,  $\vec{s}$ , of a particle onto the direction of its momentum,  $\hat{p}$ ,

$$h = \vec{s} \cdot \hat{p} \quad (2.6)$$

Since the eigenvalues of spin with respect to an axis have discrete values, the eigenvalues of helicity are also discrete and range from  $-s$  to  $s$  for a spin  $S$  particle. The helicity of a particle is right-handed if the projection defined above is positive, i.e. the direction of its spin is the same as the direction of its motion, and a particle is left-handed if the projection is negative, i.e. the direction of its spin points in the opposite direction to its momentum.

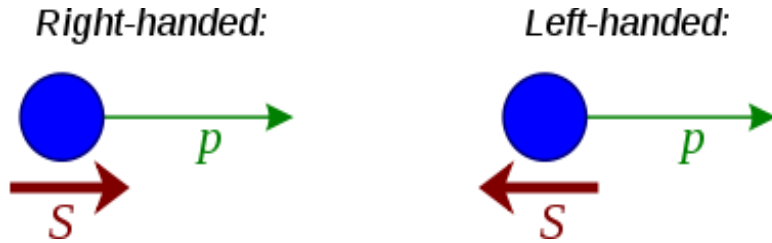


Figure 2.2: The figure illustrates the definitions of the helicity of a particle. A right-handed particle is a particle with the direction of the spin the same as the direction of its motion. A left-handed particle is a particle with the direction of the spin opposite the direction of its motion.

However, in general, the helicity is not an intrinsic property of a particle and depends on a reference frame of an observer. For a massive particle, such as an electron, a quark, or a neutrino, which moves slower than the speed of light, it is possible for an observer to move in such a way that changes the motion direction of the particle as seen by the observer, and thus changing the handedness of a particle. In the case of a massless particle, such as a photon, which moves with a speed of light, an observer will not be able to change the direction of a particle and its helicity becomes an intrinsic property.

In mathematical representation, the helicity operator is defined as

$$\mathcal{H} = \frac{\vec{\sigma} \cdot \vec{p}}{|\vec{p}|} \quad (2.7)$$

where  $\vec{\sigma}$  is the pauli matrices [12].

### Chirality

On the other hand, the chirality of a particle is more abstract. It is determined by whether the particle transforms in a right or left-handed chiral projection operator, which is defined as

$$P_{R,L} = \frac{1}{2}(1 \pm \gamma^5) \quad (2.8)$$

$$\text{where } \gamma^5 = \begin{bmatrix} 0 & 0 & 1 & 0 \\ 0 & 0 & 0 & 1 \\ 1 & 0 & 0 & 0 \\ 0 & 1 & 0 & 0 \end{bmatrix} \text{ or } \gamma^5 = \frac{i}{4!} \epsilon_{\mu\nu\alpha\beta} \gamma^\mu \gamma^\nu \gamma^\alpha \gamma^\beta.$$

The chiral projection operators can decompose every wave function into chiral components,  $\psi = \psi_R + \psi_L$ , where

$$\psi_R = P_R \psi = \frac{1}{2}(1 + \gamma^5)\psi \quad (2.9)$$

$$\psi_L = P_L \psi = \frac{1}{2}(1 - \gamma^5)\psi \quad (2.10)$$

In the case of massless particles,  $\gamma^5$  in the chiral projection operator acts just like the helicity operator, and thus make the chirality and helicity of a massless particle the same.

### 2.1.3 Parity

Parity is characterized by a multiplicative quantum number of a discrete symmetry operation. This symmetry operation, the parity transformation, labeled  $P$ , is the spatial reflection of a physical state at the coordinate origin. In general, the notation for the parity transformed quantity of a quantity  $\psi$  is  $\psi^P$ . For a scalar wave function  $\psi(\vec{x}, t)$ , the parity transformation is given by

$$\psi^P(\vec{x}, t) = P\psi(\vec{x}, t) = \psi(-\vec{x}, t) \quad (2.11)$$

The eigenvalues of the parity operator  $P$  are  $\pm 1$ , and are called “even parity” if the eigenvalue is 1 and are called “odd parity” if the eigenvalue is -1 [21].

It is important to note that the spin state of a particle remains unchanged under parity transformation, but that the momentum undergoes a sign change. This effect transforms a left-handed particle into a right-handed particle, and vice versa, e.g.

$$P|e_L^-> = |e_R^-> \quad (2.12)$$

$$P|e_R^-> = |e_L^-> \quad (2.13)$$

It has been shown experimentally that the strong and the electromagnetic interaction

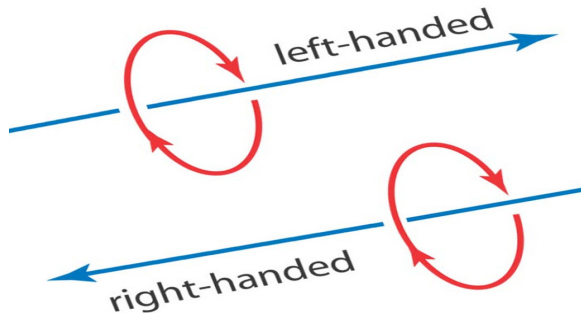


Figure 2.3: The figure illustrates how the parity transformation changes the handedness of a particle. Under the parity transformation, the momentum changes its direction, while spin remains the same, and thus changes the handedness of a particle.

conserve parity, however, the weak interaction does not conserve parity. This means that a reaction which occurs through the weak interaction, does not occur in the same way in its space-inverted form. This was first noticed in 1946, during an experiment involving the decay of  $K$  mesons (the so-called  $\Theta - \tau$  problem) [53]. The more obvious example of the violation of parity, which will be described below, is the left-handedness of neutrinos in beta decay.

### Parity Violation in Beta Decay

In 1956, T.D. Lee and C.N. Yang predicted the nonconservation of parity in the weak interaction [39]. Their prediction was quickly tested when C.S. Wu and her collaborators studied the beta decay of  $^{60}\text{Co}$  in 1957 [9][73]. By lowering the temperature of  $^{60}\text{Co}$  atoms to 0.01K, Wu was able to polarize the nuclear spins along the direction of an applied magnetic field. The directions of the emitted electrons were measured. In the case of parity conservation, the equal numbers of electrons should be emitted parallel and antiparallel to the magnetic field. However, in reality, more electrons were emitted in the direction opposite to the magnetic field and therefore opposite to the nuclear spin, as shown in Fig. 2.4.

This and subsequent experiments have consistently shown that a neutrino always has its spin pointed in the direction opposite to its velocity, i.e. a neutrino is a left-handed particle. Furthermore, antineutrinos have their spins parallel to their velocity and are therefore right-handed.

## 2.2 Weak Interaction

Weak interaction is one of the four fundamental forces in nature. It is responsible for the radioactive decay of subatomic particles by changing quark flavours. In addition, the weak interaction also breaks parity symmetry. The weak interaction is mediated by the exchange of massive  $W^\pm$  and  $Z^0$  bosons, which are much heavier than protons

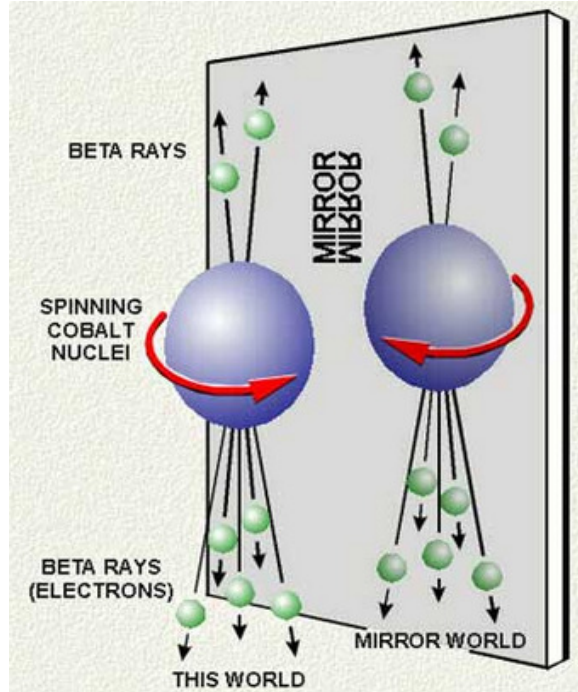


Figure 2.4: Beta emission is preferentially in the direction opposite to the nuclear spin, indicating the violation of parity conservation.

or neutrons:  $M_W = 80.375 \pm 0.023$  GeV [1] and  $M_Z = 91.1876 \pm 0.0021$  GeV [8]. The large masses of these exchange particles account for the very short range of the weak interaction.  $W^\pm$  bosons are charged bosons and are best known as mediators of neutrino absorption and emission, where their charge is associated with electron or positron emission and absorption. On the other hand,  $Z^0$  boson is electrically neutral and is its own antiparticle. The  $Z^0$  boson is most easily detected as a necessary theoretical force-mediator whenever neutrinos scatter elastically from matter. Moreover,  $Z^0$  boson couples mainly to the neutrons in a nucleus, thus it could be used to study neutron structure of nuclei via weak interaction.

A comparison of strong, electromagnetic, and weak interactions is given in the following table:

Interaction	Particles Involved	$\sim \tau$ (s)
Strong	quarks	$10^{-23}$
Electromagnetic	charged leptons and quarks	$10^{-16}$
Weak	all leptons and quarks	$10^{-6} - 10^{-8}$

Table 2.1: The table shows the comparison of strong, electromagnetic, and weak interactions for types of particles involved and lifetimes of decays.

From Table 2.1, the timescales involved in weak decays are much larger than the ones of strong and electromagnetic decays. Since  $\tau \sim 1/\text{coupling}^2$ , the weak coupling, which indicates the strength of the weak interaction, is much smaller than the strong and electromagnetic interactions.

### 2.2.1 Weak Neutral Current

Weak neutral current occurs when the particles interact via the exchange of a virtual  $Z^0$  boson. The contribution of the weak neutral current to the elastic scattering amplitude of  $f f' \rightarrow f f'$  is

$$\mathcal{M}^{NC} \propto J_\mu^{(NC)}(f') J^{(NC)\mu}(f) \quad (2.14)$$

where the neutral currents describing the flow of  $f$  and  $f'$  are given by

$$J^{(NC)\mu}(f) = \bar{u}_f \gamma^\mu \frac{1}{2} (g_V^f - g_A^f \gamma^5) u_f \quad (2.15)$$

where  $g_V^f$  and  $g_A^f$  are the vector and axial vector coupling for fermion  $f$ . Notice that the difference between the electromagnetic current,  $J^{(\gamma)\mu} = \bar{u}_f \gamma^\mu u_f$ , and the weak neutral current is the additional term  $\gamma^5$ , which actually leads to the parity violation.

This behavior can be shown by considering  $\gamma^5$  acting on a left-handed fermion,

$$\begin{aligned}
 \gamma_5 u_L &= \gamma_5 P_L u \\
 &= \gamma_5 \frac{1}{2} (1 - \gamma_5) u \\
 &= -\frac{1}{2} (\gamma_5^2 - \gamma_5) u \\
 &= -\frac{1}{2} (1 - \gamma_5) u \\
 &= -u_L
 \end{aligned} \tag{2.16}$$

The  $\gamma_5$  acts on the left-handed fermion by changing its sign. On the other hand, consider  $\gamma^5$  acting on a right-handed fermion,

$$\begin{aligned}
 \gamma_5 u_R &= \gamma_5 P_R u \\
 &= \gamma_5 \frac{1}{2} (1 + \gamma_5) u \\
 &= \frac{1}{2} (\gamma_5^2 + \gamma_5) u \\
 &= \frac{1}{2} (1 + \gamma_5) u \\
 &= u_R
 \end{aligned} \tag{2.17}$$

The  $\gamma_5$  term leaves the state of the right-handed fermion unchanged. Similarly,  $\gamma_5$  only changes the right-handed antifermions, and leaves the left-handed antifermions unchanged. Since the weak interaction only changes left-handed (right-handed) particles (antiparticles), this property leads to the maximal violation in the parity conservation.

### 2.2.2 Electroweak Interaction

The electroweak interaction is the unified description on the electromagnetic interaction and the weak interaction. Although these two forces are different at low energies, at energy above unification energy, on the order of 100 GeV, they could be

merged into a single principle, called electroweak interaction. The electromagnetic interaction arises from the imposition of local gauge invariance to the free particle Lagrangian, which contains left-handed fermions in weak isospin doublets and right-handed fermions in iso-singlets. The specific gauge group that is chosen is  $SU(2)_L \times U(1)_Y$ , which results in the emergence of 4 electroweak gauge bosons, two charged and two neutral, that mediate the electroweak interaction. The two charged bosons include  $W^+$  and  $W^-$ , while the neutral bosons include the massless photon,  $\gamma$ , with the known electromagnetic couplings to various fermions, and the neutral boson,  $Z^0$  [37].

Many of the parameters of the electroweak interaction are related to each other by the Weak mixing or Weinberg angle ( $\theta_W$ ). For example, the masses of  $W^\pm$  and  $Z^0$  bosons are related by  $M_{W^\pm} = M_{Z^0} \cos(\theta_W)$  and the vertex factor of the  $Z^0$  boson,  $g_{Z^0}$ , is related to the  $W^\pm$  vertex factor,  $g_{W^\pm}$ , by  $g_{Z^0} = g_{W^\pm} \cos(\theta_W)$ . Furthermore, both  $g_{W^\pm}$  and  $g_{Z^0}$  are related to the *QED* coupling constant  $g_e$  by  $g_{W^\pm} = g_e / \sin(\theta_W)$  and  $g_{Z^0} = g_e / \sin(\theta_W) \cos(\theta_W)$ . The value of the Weak mixing angle is measured experimentally to be  $\sin^2(\theta_W) = 0.2380 \pm 0.0016$  at a  $Q^2 = 0.026$  GeV $^2$  [33].

Similar to electromagnetic charge, the electroweak interaction has its own charges called electroweak charges. Table 2.2 shows the resulting neutral electroweak vector and axial-vector charges of the light quarks and leptons.

Particle	$q^{em}$	$g^V$	$g^A$
$\nu$	0	1/4	1/4
$e^-$	-1	$-1/4 + \sin^2(\theta_W)$	-1/4
$u$	2/3	$1/4 - 2/3 \sin^2(\theta_W)$	1/4
$d, s$	-1/3	$-1/4 + 1/3 \sin^2(\theta_W)$	-1/4

Table 2.2: Electromagnetic and neutral weak charges of the electron and light quarks.

Both left-handed and right-handed particles have weak neutral current charges, which can be expressed as vector ( $V$ ) and axial-vector ( $A$ ) charges by  $g^R = g^V + g^A$  and  $g^L = g^V - g^A$ . The other key feature of Table 2.2 is that the relative sizes of the

weak and electromagnetic charges of the quarks are different. Since we are averaging over target particle spin, the vector charge  $g^V$  is the relevant weak charge. The up quark has the strongest electromagnetic charge whereas the down and strange quarks have the strongest weak vector charge.

## 2.3 Parity-Violating Elastic Electron Scattering

Since the weak neutral charges of electrons and light quarks are different for left-handed and right-handed particles, the parity symmetry is violated in the scattering of polarized electrons off unpolarized targets.

### 2.3.1 Potential Scattering

The potential scattering discussed in this section will begin with the Born approximation. Consider that the target is a spinless potential distribution fixed in space while the electron is treated ultra-relativistic. An electron has energy  $E$  scattered by an angle  $\theta$  with momentum transfer  $q = 2E \sin(\theta/2)$ . The spatial charge distribution  $\rho(r)$  is the Fourier transform of the electromagnetic form factor

$$F(q) = \int d^3r \rho(r) e^{i\mathbf{q}\cdot\mathbf{r}} \quad (2.18)$$

The cross section is given by

$$\frac{d\sigma}{d\Omega} = |\mathcal{M}(\theta)|^2 \cos^2(\theta/2) \quad (2.19)$$

where the scattering amplitude  $\mathcal{M}(\theta)$  can be expressed as

$$\mathcal{M}(\theta) = \frac{2\alpha}{q^2} F(q) \quad (2.20)$$

The scattering amplitude consists of two important factors, the form factor ( $F(q)$ ) and  $2\alpha/q^2$ . The  $F(q)$  is related to the spatial distribution of the charge, while  $2\alpha/q^2$  is the amplitude for scattering from a point distribution characterized by the potential  $V(r) = e^2/4\pi r$ . However, to include the weak scattering, the potential must be generalized to

$$V(r) = ke^2g^B g^T \frac{e^{-Mr}}{4\pi r} \quad (2.21)$$

where  $g^B$  is the charge of the incident beam particle,  $g^T$  is the charge of the target particle in the units of the electron charge  $e$ ,  $k$  is the strength of the coupling;  $k = 1$  for the electromagnetic interaction and  $k = (\sin(\theta_W)\cos(\theta_W))^{-2}$  for weak scattering, and  $M$  is the mass of the exchanged particle;  $M = 0$  for the electromagnetic interaction and  $M = M_Z$  for the neutral weak current.

In order to describe various charge distributions, a number density  $\rho_i(r)$  for each quark flavor  $i$  and a corresponding form factor

$$F_i(q) = \int d^3r \rho_i(r) e^{i\mathbf{q}\cdot\mathbf{r}} \quad (2.22)$$

could be used. Then, all electromagnetic and weak scattering from a given potential may be described by the same  $F_i(q)$ . The scattering amplitude  $\mathcal{M}(q)$  is given by the general form

$$\mathcal{M}(q) = -\frac{1}{2\pi} \int d^3r V(\mathbf{r}) e^{i\mathbf{q}\cdot\mathbf{r}} = \frac{2k\alpha g^B g^T}{q^2 + M^2} F(q) \quad (2.23)$$

Similar to the electromagnetic case, each scattering amplitude consists of two factors, a form factor related to the spatial distribution of the quarks and another factor describing the point-like interaction. Then, the cross section is given by the coherent sum of all scattering amplitude  $\mathcal{M}_i(q)$

$$\frac{d\sigma}{d\Omega} = \sum |M_i(\theta)|^2 \cos^2(\theta/2) \quad (2.24)$$

In the case of an ordinary electromagnetic scattering, at  $q \ll M_Z$ , the weak interaction is negligible, and only one combination of the quark form factors survives, i.e. [37]

$$F_\gamma = \sum g_i^{em} F_i = \frac{2}{3} F_u - \frac{1}{3} (F_d + F_s) \quad (2.25)$$

To include the weak interaction, the interpretation of the weak scattering amplitudes is required.

### 2.3.2 Parity Violation

To measure the weak scattering amplitude in electron scattering, the most practical way is to measure the asymmetry of the scattering probability of right-handed ( $d\sigma_R$ ) and left-handed ( $d\sigma_L$ ) electrons,

$$A_{PV} = \frac{d\sigma_R - d\sigma_L}{d\sigma_R + d\sigma_L} \quad (2.26)$$

The scattering probability,  $d\sigma$ , is proportional to the square of the scattering amplitudes, which can be explicitly expressed as:

$$\mathcal{M}^R = \mathcal{M}_\gamma + \mathcal{M}_Z^R \quad (2.27)$$

$$\mathcal{M}^L = \mathcal{M}_\gamma + \mathcal{M}_Z^L \quad (2.28)$$

where

$$\mathcal{M}_\gamma(\theta) = -\frac{2\alpha}{q^2} \sum q_j^{em} F_j(q) \quad (2.29)$$

$$\mathcal{M}_Z^{L(R)}(\theta) = \frac{2\alpha k_Z g^{L(R)}}{M_Z^2} \sum g_j^V F_j(q) \quad (2.30)$$

Thus,

$$|\mathcal{M}^R|^2 = |\mathcal{M}_\gamma|^2 + 2(\mathcal{M}_\gamma)^*(\mathcal{M}_Z^R) + |\mathcal{M}_Z^R|^2 \quad (2.31)$$

$$|\mathcal{M}^L|^2 = |\mathcal{M}_\gamma|^2 + 2(\mathcal{M}_\gamma)^*(\mathcal{M}_Z^L) + |\mathcal{M}_Z^L|^2 \quad (2.32)$$

The ratio of the magnitudes of the three terms in  $|\mathcal{M}^R|^2$  and  $|\mathcal{M}^L|^2$  can be estimated by

$$\begin{aligned} |\mathcal{M}_\gamma|^2 : 2(\mathcal{M}_\gamma)^*(\mathcal{M}_Z^{L,R}) : |\mathcal{M}_Z^{L,R}|^2 &\sim \left(\frac{4\pi\alpha}{Q^2}\right)^2 : 2\left(\frac{4\pi\alpha}{Q^2}\right)\left(\frac{G_F}{2\sqrt{2}}\right) : \left(\frac{G_F}{2\sqrt{2}}\right)^2 \\ &\sim 1 : 10^{-4} : 10^{-9} \end{aligned} \quad (2.33)$$

where  $G_F$  is the Fermi constant,  $\alpha$  is the fine structure constant, and  $Q^2 = -q^2$ .

This implies that the electromagnetic scattering amplitude squared,  $|\mathcal{M}_\gamma|^2$ , dominates the other two terms. Thus, any absolute cross-section measurement would be a measurement of  $\mathcal{M}_\gamma$ . However, the weak neutral current scattering,  $\mathcal{M}_Z^{L,R}$ , interferes with  $\mathcal{M}_\gamma$ , and this term is only a factor of  $\sim 10^{-4}$  smaller than the  $|\mathcal{M}_\gamma|^2$  term, making  $\mathcal{M}_Z^{L,R}$  term accessible to precision measurements.

Then, from Eq. 2.26 and 2.32, the asymmetry from the parity violation can be written as

$$\begin{aligned} A_{PV} &= \frac{|\mathcal{M}^R|^2 - |\mathcal{M}^L|^2}{|\mathcal{M}^R|^2 + |\mathcal{M}^L|^2} \\ &\simeq \frac{\mathcal{M}_\gamma(\mathcal{M}_Z^R - \mathcal{M}_Z^L)}{\mathcal{M}_\gamma^2} \\ &= \frac{\mathcal{M}_Z^R - \mathcal{M}_Z^L}{\mathcal{M}_\gamma} \end{aligned} \quad (2.34)$$

The Eq. 2.34 shows that the weak-electromagnetic interference gives rise to a ratio of amplitudes rather than the ratio of the squares of the amplitudes.

Since  $g^R - g^L = 1/2$ ,  $\mathcal{M}_Z^R - \mathcal{M}_Z^L$  can be reduced to

$$\mathcal{M}_Z^R - \mathcal{M}_Z^L = \frac{\alpha k_Z}{M_Z^2} \sum g_j^V F_j(q) \quad (2.35)$$

Finally, by combining the weak and the electromagnetic scattering amplitude, the asymmetry becomes

$$\begin{aligned} A_{PV} &= \frac{k_Z q^2}{2 M_Z^2} \frac{\sum g_j^V F_j}{\sum q_j F_j} \\ &= -\frac{k_Z q^2}{2 M_Z^2} \left\{ \frac{\left(\frac{1}{4} - \frac{2}{3} \sin^2 \theta_W\right) F_u + \left(-\frac{1}{4} + \frac{1}{3} \sin^2 \theta_W\right) (F_d + F_s)}{\frac{2}{3} F_u - \frac{1}{3} (F_d + F_s)} \right\} \end{aligned} \quad (2.36)$$

The following sections will describe the asymmetry arising from parity violation in elastic electron-nucleon scattering and, then the specific application to the scattering off the  $^{208}\text{Pb}$  nucleus as in the case of PREX.

### 2.3.3 Electron-Nucleon Scattering

To extend the previous method to find  $A_{PV}$  in elastic electron-nucleon scattering, the four-momentum transfer squared  $Q^2$  is used instead of the three-momentum transfer  $q$ . The general current for elastic electron-nucleon scattering is

$$j_\mu^a(\text{nucleon}) = \bar{u}(k\ell, s\ell) \mathcal{O}(Q^2) u(k, s) \quad (2.37)$$

where

$$\mathcal{O}(Q^2) = F_1^a(Q^2) \gamma_\mu + \frac{i}{2M} F_2^a(Q^2) \sigma_{\mu\nu} q^\nu + F_A^a(Q^2) \gamma_\mu \gamma^5 + F_P^a(Q^2) \gamma^5 q_\mu \quad (2.38)$$

and  $F_s^a$  are real Dirac form factors that depend only on  $Q^2$ . There are four currents since the target particle can be a proton or a neutron and the current can be electromagnetic or weak. The index  $a$  is used to denote both characteristics.

The Sachs form factors are usually used to express the cross section and they are defined by

$$G_E^a \equiv F_1^a - \tau F_2^a \quad (2.39)$$

$$G_M^a \equiv F_1^a + F_2^a \quad (2.40)$$

where  $\tau = Q^2/4M^2$ .  $G_E$  is referred to as the electric form factor and  $G_M$  is referred to as the magnetic form factor. The advantage of the Sachs form factor over the Dirac form factors is that, in the center-of-mass frame,  $G_E^\gamma$  and  $G_M^\gamma$  are simply the Fourier transforms of the electric and magnetic charge densities of the nucleon.

The differential cross section for electron scattering from the proton in terms of the Sachs form factors is then

$$\frac{d\sigma}{d\Omega} = \left\{ \frac{\alpha^2}{4E^2 \sin^4(\theta/2)} \right\} \frac{E'}{E} \left\{ \frac{(G^{p\gamma_E})^2 + \tau(G^{p\gamma_M})^2}{1 + \tau} \cos^2(\theta/2) + 2\tau(G^{p\gamma_M})^2 \sin^2(\theta/2) \right\} \quad (2.41)$$

The neutron cross section is given by changing the superscript  $p$  to  $n$ .

The parity-violating asymmetry is then given by

$$A_{PV} = \frac{\sigma_R - \sigma_L}{\sigma_R + \sigma_L} = \left\{ -\frac{G_F Q^2}{\pi \alpha \sqrt{2}} \right\} \frac{\epsilon G_E^{p\gamma} G_E^{pZ} + \tau G_M^{p\gamma} G_M^{pZ} - \frac{1}{2}(1 - 4 \sin^2(\theta_Q)) \epsilon' G_M^{p\gamma} G_A^{pZ}}{\epsilon (G_E^{p\gamma})^2 + \tau (G_M^{p\gamma})^2} \quad (2.42)$$

where  $\epsilon = [1 + 2(1 + \tau) \tan^2(\theta/2)]^{-1}$  is the transverse polarization of the virtual photon exchanged and  $\epsilon' = \sqrt{\tau(1 + \tau)(1 - \epsilon^2)}$ . The above equation involves many form factors, however, in the case of the above mentioned potential scattering, all of

the form factors can be related to flavor form factors as [37]:

$$\begin{aligned} \langle p|j_\mu^a|p\rangle &= \langle p|\sum g_i^{Va}\bar{u}_i\gamma_\mu u_i|p\rangle + \langle p|\sum g_i^{Aa}\bar{u}_i\gamma_\mu\gamma_5 u_i|p\rangle \\ &= \bar{u}_p \sum \left[ g_i^{Va}(F_1^i\gamma_\mu + \frac{i}{2M}F_2^i\sigma_{\mu\nu}q^\nu) + g_i^{Aa}F_A^i\gamma_\mu\gamma_5 \right] u_p \end{aligned} \quad (2.43)$$

where  $g_i^a$  is the coupling of the current by boson  $a$  to quark  $i$ . The spinor of the proton is denoted  $u_p$  and the spinors of the quarks are denoted  $u_i$ . Thus, the flavor form factors are defined as:

$$\langle p|\bar{u}_i\gamma_\mu u_i|p\rangle = \bar{u}_p(F_1^i\gamma_\mu + \frac{i}{2M}F_2^i\sigma_{\mu\nu}q^\nu)u_p \quad (2.44)$$

$$\langle p|\bar{u}_i\gamma_\mu\gamma^5 u_i|p\rangle = \bar{u}_p F_A^i\gamma_\mu\gamma^5 u_p \quad (2.45)$$

Since there are three flavors and three Lorentz invariants, there are a total of nine flavor form factors as:

$$\begin{matrix} F_1^u & F_2^u & F_A^u \\ F_1^d & F_2^d & F_A^d \\ F_1^s & F_2^s & F_A^s \end{matrix}$$

To include neutron scattering with the same set of form factors, the charge symmetry could be used by

$$p \rightarrow n \Rightarrow u \rightarrow d, d \rightarrow u, s \rightarrow s.$$

This implies,

$$\begin{aligned} F_1^u &\equiv F_1^{pu} = F_1^{nd} \\ F_1^d &\equiv F_1^{pd} = F_1^{nu} \\ F_1^s &\equiv F_1^{ps} = F_1^{ns} \end{aligned}$$

The weak and electromagnetic currents may be expressed in terms of these flavor

form factors for the proton as follows:

$$\text{Electromagnetic Current: } j_\mu^\gamma = \frac{2}{3}\bar{u}\gamma_\mu u - \frac{1}{3}\bar{d}\gamma_\mu d + \frac{2}{3}\bar{c}\gamma_\mu c - \frac{1}{3}\bar{s}\gamma_\mu s + \dots \quad (2.46)$$

$$\begin{aligned} \text{Weak Current: } j_\mu^Z &= \left(\frac{1}{4} - \frac{2}{3}\sin^2\theta_W\right)\bar{u}\gamma_\mu u - \left(\frac{1}{4} - \frac{1}{3}\sin^2\theta_W\right)\bar{d}\gamma_\mu d \\ &\quad + \left(\frac{1}{4} - \frac{2}{3}\sin^2\theta_W\right)\bar{c}\gamma_\mu c - \left(\frac{1}{4} - \frac{1}{3}\sin^2\theta_W\right)\bar{s}\gamma_\mu s \\ &\quad - \frac{1}{4}\bar{u}\gamma_\mu\gamma_5 u + \frac{1}{4}\bar{d}\gamma_\mu\gamma_5 d - \frac{1}{4}\bar{c}\gamma_\mu\gamma_5 c + \frac{1}{4}\bar{s}\gamma_\mu\gamma_5 s \end{aligned} \quad (2.47)$$

Eq. 2.46 and Eq. 2.47 implicate that

$$F_i^{p\gamma} = \frac{2}{3}F_i^u - \frac{1}{3}F_i^d - \frac{1}{3}F_i^s \quad (2.48)$$

$$F_i^{n\gamma} = \frac{2}{3}F_i^d - \frac{1}{3}F_i^u - \frac{1}{3}F_i^s \quad (2.49)$$

$$F^{pZ} = \left(\frac{1}{4} - \frac{2}{3}\sin^2\theta_W\right)F_i^u - \frac{1}{4} - \frac{1}{3}\sin^2\theta_W(F_i^d + F_i^s) \quad (2.50)$$

$$F^{nZ} = \left(\frac{1}{4} - \frac{2}{3}\sin^2\theta_W\right)F_i^d - \frac{1}{4} - \frac{1}{3}\sin^2\theta_W(F_i^u + F_i^s) \quad (2.51)$$

The best known form factors for the proton and neutron are  $G_E^\gamma$  and  $G_M^\gamma$ , thus it is traditional to use  $G_{E,M}^{p\gamma}$ ,  $G_{E,M}^{n\gamma}$ , and  $G_{E,M}^s$  as the independent form factors. In terms of these quantities,

$$G_{E,M}^{pZ} = \frac{1}{4}(G_{E,M}^{p\gamma} - G_{E,M}^{n\gamma}) - \sin^2\theta_W G_{E,M}^{p\gamma} - \frac{1}{4}G_{E,M}^s \quad (2.52)$$

An interesting point for nucleon scattering is that the strange form factors are negligible and the asymmetry is well predicted. Thus, any deviation of the measured asymmetry,  $A_{PV}$ , from the prediction could be attributable to non-zero strange form

factors. The equation to extract strange form factors from  $A_{PV}$  is given by

$$A_{PV} = \left[ \frac{G_F M_p^2 \tau}{\pi \alpha \sqrt{2}} \right] \{ (1 - 4 \sin^2 \theta_W) \right. \\ \left. - \frac{[\epsilon G_E^{p\gamma} (G_E^{n\gamma} + G_E^{s\gamma}) + \tau G_M^{p\gamma} (G_M^{n\gamma} + G_M^{s\gamma})]}{\epsilon (G_E^{p\gamma})^2 + \tau (G_M^{p\gamma})^2} \right. \\ \left. - \frac{(1 - 4 \sin^2 \theta_W) \sqrt{\tau(1+\tau)} \sqrt{1 - \epsilon^2} G_M^{p\gamma} (-G_A^{(1)} + \frac{1}{2} F_A^s)}{\epsilon (G_E^{p\gamma})^2 + \tau (G_M^{p\gamma})^2} \right\} \quad (2.53)$$

The recent parity-violating experiment to measure the strange form factor, HAPPEX-III [5], showed that the contribution of strange quarks to the combination of electric and magnetic form factors  $G_E^s + 0.517 G_M^s = 0.003 \pm 0.010(\text{stat}) \pm 0.004(\text{syst}) \pm 0.008(\text{ff})$ , where the third error is due to the limits of precision on the electromagnetic form factors and radiative corrections. With this measurement, the world data on strange contributions to nucleon form factors are seen to be consistent with zero.

### 2.3.4 Electron Scattering off $^{208}\text{Pb}$

This section will describe how the asymmetry from parity violation,  $A_{PV}$ , can be used to find the neutron radius,  $R_n$ . Although, for simplicity, the plane-wave Born approximation will be used and the nucleon form factors will be neglected, this does not invalidate the simple qualitative idea presented here.

The photon has purely vector couplings, and thus only couples to charged leptons and protons at  $Q^2 = 0$ . On the other hand,  $Z^0$  boson couples to all leptons and nucleons. Moreover, the  $Z^0$  has a much larger coupling to the neutron than to the proton. In addition, the  $Z^0$  has large axial coupling to the electron that results in a parity-violating amplitude. Note that, for spinless nuclei such as  $^{208}\text{Pb}$ , the magnetic moment cannot contribute, even though  $Z^0$  has both vector and axial vector couplings. This is because spinless nuclei have a zero net axial coupling and thus the magnetic moment does not contribute to the interaction.

The potential between an electron and a nucleus can be written as

$$\hat{V}(r) = V(r) + \gamma_5 A(r) \quad (2.54)$$

where the electromagnetic vector potential is

$$V(r) = \int d^3 r' \frac{Z\rho(r')}{|\vec{r} - \vec{r}'|} \quad (2.55)$$

and the charge density  $\rho(r)$  is closely related to the point proton density  $\rho_p(r)$  given by

$$Z\rho_p(r) = \sum_p <\psi_p^\dagger(r)\psi_p(r)>. \quad (2.56)$$

Similarly, the axial potential is

$$A(r) = \frac{G_F}{2^{3/2}} [(1 - 4 \sin^2 \theta_W) Z\rho_p(r) - N\rho_n(r)] \quad (2.57)$$

where the neutron density is

$$N\rho_n(r) = \sum_n <\psi_n^\dagger(r)\psi_n(r)>. \quad (2.58)$$

Considering the axial potential in Eq. 2.57,  $A(r)$  depends mainly on the neutron distribution  $\rho_n(r)$  because  $\sin^2 \theta_W \sim 0.23$ , and this makes the term  $(1-4\sin^2 \theta_W)$  small. Another feature of the vector and axial potentials is that the magnitude for the vector potential is much larger than the axial potential<sup>1</sup>, thus it is better to observe the axial potential by measuring parity violation.

The electromagnetic cross section for scattering electrons with momentum transfer

---

<sup>1</sup>  $A(r)$  is in the order of eV, while  $V(r)$  is in the order of MeV

$q = (Q^2)^{1/2}$  is

$$\frac{d\sigma}{d\Omega} = \frac{d\sigma}{d\Omega_{mott}} |F_p(Q^2)|^2 \quad (2.59)$$

where the proton form factor is

$$F_p(Q^2) = \int d^3r j_0(qr) \rho_p(r) \quad (2.60)$$

and  $j_0$  is the zeroth order spherical Bessel function. Similar to the proton form factor,  $F_p(Q^2)$ , which can be used to determine the proton radius,  $R_p$ , of the nucleus, the neutron form factor,  $F_n(Q^2)$ , can be used to determine the neutron radius,  $R_n$ , of the nucleus. The  $F_n(Q^2)$  is given by

$$F_n(Q^2) = \int d^3r j_0(qr) \rho_n(r) \quad (2.61)$$

Finally, in Born approximation, the parity-violating asymmetry involving the interference between  $V(r)$  and  $A(r)$  is

$$A_{PV} = \frac{G_F Q^2}{4\pi\alpha\sqrt{2}} \left[ 1 - 4 \sin^2 \theta_W - \frac{F_n(Q^2)}{F_p(Q^2)} \right]. \quad (2.62)$$

The important feature of Eq. 2.62 is that the asymmetry is proportional to  $G_F Q^2$ , and thus it is also proportional to  $Q^2/M_Z^2$ , which is the ratio of the propagators, since  $G_F \propto 1/M_Z^2$ .

The asymmetry measurement,  $A_{PV}$ , provides a practical method to measure the neutron form factor,  $F_n(Q^2)$ , and neutron radius,  $R_n$ . Since the term  $1 - 4 \sin^2 \theta_W$  is small and the proton form factor,  $F_p(Q^2)$ , is well studied and measured to have a very precise value, the measurement of  $A_{PV}$  directly measures  $R_n$ .

## 2.4 Coulomb Distortions

The Coulomb distortions account for the largest known correction to the asymmetry measurement in the electron scattering off the  $^{208}\text{Pb}$  nucleus, and thus require thorough consideration. The Coulomb distortions are the repeated electromagnetic interactions of the incoming electrons with the target nucleus remaining in its ground state. Since all of the  $Z$  protons in a nucleus can contribute coherently, coulomb distortion corrections are expected to be of order  $Z\alpha/\pi$ , i.e. 20% of the asymmetry in the case of PREX [29].

The calculation of the Coulomb distortions is given in [25]. The Dirac equation was numerically solved for an electron moving in a coulomb and vector-axial weak potentials and, from the phase shifts, all of the elastic scattering observables can be precisely calculated.

To check on the numerics of the calculation, three independent methods were used. First, known cross sections including those at large angles were reproduced by using the calculation values. Second, the code reproduced known plane wave asymmetries. Finally, the sensitivity to the subtraction between helicities was checked by varying the strength of the weak potential. It is expected that the numerical accuracy in the asymmetry is significantly better than 1%, however, the code neglected terms involving the electron mass over the beam energy, which are of order 0.1%.

In summary, Coulomb distortions corrections are larger than the experimental error and they modify the sensitivity to the neutron radius. However, the corrections have been calculated with an accuracy significantly better than the expected 3% experimental error.

## Chapter 3

# The Experiment

Experiment 06-002 or PREX ran in Hall A at the Thomas Jefferson National Accelerator Facility (JLAB) from March to June 2010. PREX measured the parity-violating electroweak asymmetry in the elastic scattering of polarized electrons off  $^{208}\text{Pb}$  at a beam energy of 1.063 GeV and a scattering angle of  $5^\circ$ . Since the  $Z^0$  boson couples mainly to neutrons, this asymmetry provides a clean measurement of the radius of the neutron distribution,  $R_n$ , in the  $^{208}\text{Pb}$  nucleus, which is believed to be different from proton distribution radius,  $R_p$ , by several percent. This chapter describes the choice of target and kinematics, the experimental setup, the instrumentation, and the experiment.

### 3.1 Choice of Target and Kinematics for PREX

There are two nuclei which were of interest for PREX,  $^{208}_{82}\text{Pb}$  and  $^{138}_{56}\text{Ba}$ . They are both neutron rich nuclei with  $n/p$  ratios exceeding 1.4, and are equally accessible experimentally.  $^{208}\text{Pb}$  has the advantage that it has the largest known splitting between the ground state and the first excited state (2.6 MeV) of any heavy nucleus, and thus lends itself well to use of the flux integration technique. Also,  $^{208}\text{Pb}$  is a

doubly magic nucleus<sup>1</sup>, has been well studied, and with its simple structure, it is a good first test case from the point of view of nuclear theory. On the other hand, <sup>138</sup>Ba has the advantage that it is one of the nuclei being used for an atomic physics test of standard model. Furthermore, <sup>138</sup>Ba is also a magic nucleus with 82 neutrons.

The choice of kinematics was guided by the objective of minimizing the running time required for a 1% accuracy. There were three ingredients that entered into the optimization: the cross section ( $\frac{d\sigma}{d\Omega}$ ), the parity violating asymmetry  $A$ , and the sensitivity to the neutron radius  $\epsilon = \frac{dA}{A} = \frac{A_1 - A}{A}$ , where  $A$  is the asymmetry computed from a Mean Field Theory (MFT) calculation and  $A_1$  is the asymmetry from the MFT calculation in which the neutron radius is increased by 1%. Using magnetic spectrometers with high resolution to isolate elastically scattered electrons, the optimal kinematics can be determined from the allowable settings for angle and momentum of the spectrometer by searching for the minimum running time, which is equivalent to maximizing the product,

$$FOM \times \epsilon^2 = R \times A^2 \times \epsilon^2 \quad (3.1)$$

where  $R$  is the detected rate and is proportional to  $\frac{d\sigma}{d\Omega}$ , and  $FOM$  is the conventionally defined Figure Of Merit for parity experiments,  $FOM = R \times A^2$ . Note that rather than only maximizing the conventional  $FOM$ , the experiment took into account the sensitivity ( $\epsilon$ ) to  $R_n$  which varies with kinematics.

To reduce the running time, a thick target was needed. However, there were some other issues which needed to be carefully considered. The main issues were as follows:

1. For a given energy resolution required to discriminate excited states, there is an optimum target thickness ( $\sim 10\%$  radiation length) that maximizes the rate in

---

<sup>1</sup>A magic nucleus has a number of nucleons (either proton or neutrons) such that they are arranged into complete shells within the atomic nucleus. The seven most widely recognised magic numbers are 2, 8, 20, 28, 50, 82, and 126. In the case of <sup>208</sup>Pb, it has 82 protons and 126 neutrons, and thus a doubly magic nucleus.

$$\text{FOM} \times \epsilon^2 = R \times A^2 \times \epsilon^2$$

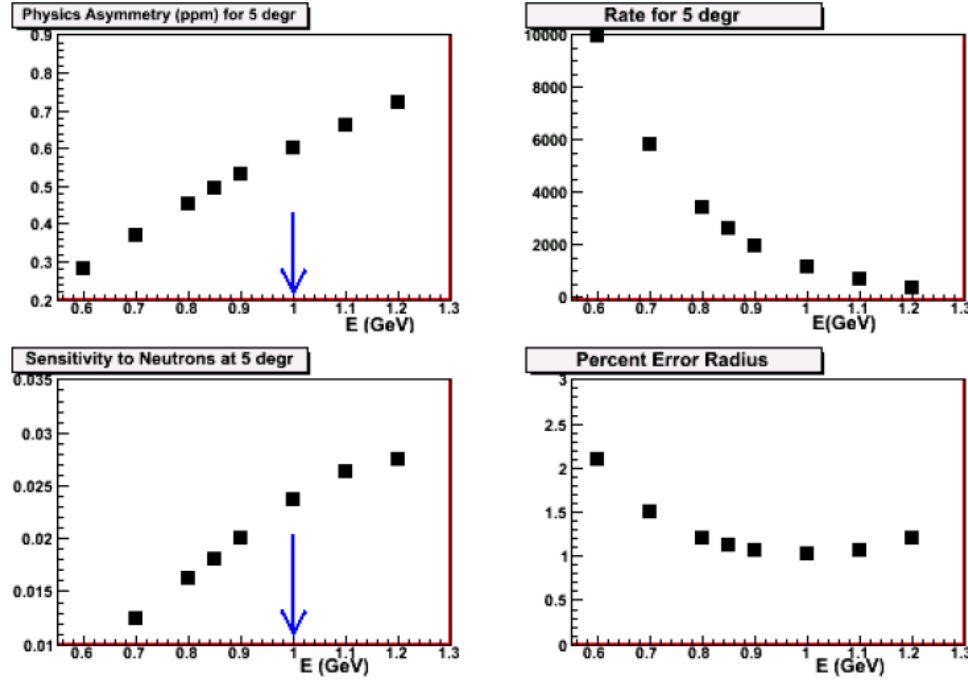


Figure 3.1: Figures of Merit (FOM) for PREX to determine choices of kinematics. This figure shows the FOM from optimizing the  $^{208}\text{Pb}$  target

the detector. As the target becomes thicker, the radiative losses decrease the rate.

2. If, at the low  $Q^2$  where the experiment ran, the rates from the inelastic states closest to the ground state are sufficiently small and understood theoretically, one may tolerate accepting them into the detector, thus allowing one to integrate more of the radiative tail.
3. To improve the heat load capability of the target, a cooling agent such as laminations of diamond has to be interleaved with the target material. However, one must have sufficient knowledge of the effect of this material on the parity signal.

After a very careful consideration, PREX collaboration decided to use  $^{208}\text{Pb}$  as

the target material with a beam energy of 1.06 GeV and at a central scattering angle of  $5^\circ$ . The  $^{208}\text{Pb}$  target thickness was chosen to be 0.5 mm, sandwiched between two 0.15-mm diamond sheets for improving the heat transfer.

### 3.2 Thomas Jefferson National Accelerator Facility (Jefferson Lab)

The Thomas Jefferson National Accelerator Facility or Jefferson Lab (JLAB) is located in Newport News, Virginia. JLAB is funded by the U.S. Department of Energy's Office of Science (DOE). JLAB was previously known as the Continuous Electron Beam Accelerator Facility(CEBAF). In 1995, the first physics experiment was conducted at JLAB. JLAB's primary mission is to conduct basic research that builds a comprehensive understanding of the atom's nucleus at quark level. In addition, the laboratory also conducts applied research with industry and university partners through its nuclear imaging group and a free-electron laser based on technology developed at the laboratory. JLAB consists of a continuous-wave electron accelerator, three existing experimental halls (Hall A, Hall B, and Hall C) and several applied research centers. Since 2009, JLAB has been undergoing an upgrade expected to be completed in 2015 that would double the accelerator beam energy. Also, part of the upgrade is a new experimental area (Hall D) and associated beamline.

### 3.3 The Accelerator

PREX utilized the CEBAF accelerator [76] shown in Fig. 3.3. The two superconducting linear electron accelerators (north and south linacs) are capable of providing up to  $200 \mu\text{A}$  of continuous-wave electron beam. The polarized continuous-wave<sup>2</sup> electrons from the source are first accelerated to 45 MeV, then are injected into the north linac.

---

<sup>2</sup>The beam is actually pulses at 1497 MHz which essentially makes the beam continuous



Figure 3.2: Thomas Jefferson National Accelerator (JLAB)

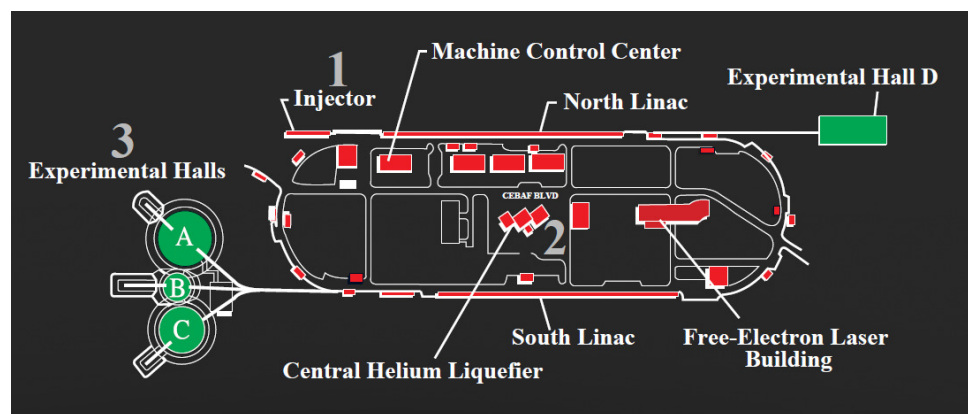


Figure 3.3: Schematic overview of the CEBAF accelerator and a new experimental hall (Hall D)

The north and south linacs are connected by two  $180^\circ$  arcs with a radius of 80 m. These form a “racetrack” recirculating beamline. The two linacs consist of twenty radio-frequency (RF) cryomodules. Each cryomodule contains eight superconducting niobium cavities. Liquid helium keeps the accelerating cavities superconducting at a temperature of 2 K. The electron beam is focused and steered by the field of quadrupole and dipole magnets as the beam passes through each arc. The nominal gain for each linac is 400 MeV but can be tuned up to about 570 MeV per experimental hall’s request. The electron beam can recirculate up to five times, thus providing an extraction of beam energy up to 5.7 GeV.

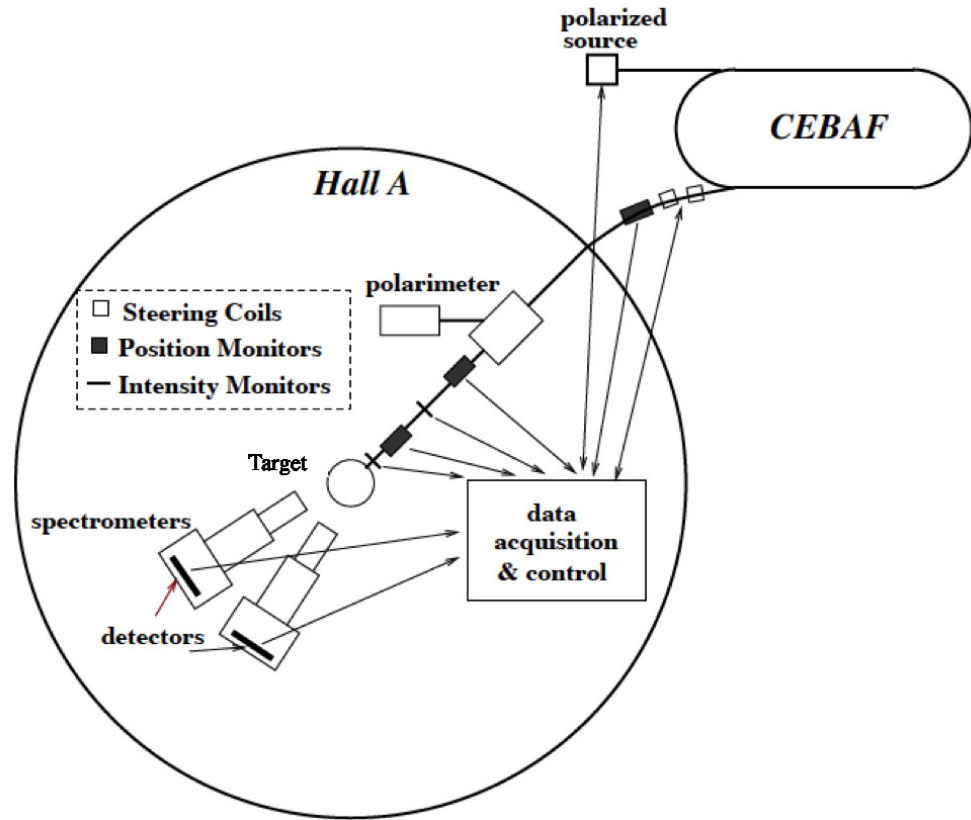


Figure 3.4: Schematic of beam entering the Hall A

After the beam passes through the south linac, it can either circle around the west recirculating arc for another pass around the accelerator, or be directed into an

experimental hall's transport channel using magnetic or RF extraction. The beam received by each hall is made of bunches at a frequency of 499 MHz, with a bunch length of 1.7 ps.

### 3.4 The Polarized Electron Source

PREX measured very small parity-violating asymmetries ( $A_{PV}$ ) of the order of few hundreds parts-per-billion (ppb) with unprecedented accuracy. To meet all the PREX requirements given in Table 3.1, parity-quality of the electron beam had to be improved significantly [20].

Beam Current	Target	Approximate $A_{PV}$ Raw Asymmetry	Maximum Charge Asymmetry	Maximum Position Differences
50 $\mu$ A	$^{208}\text{Pb}$ (0.5 mm)	$500 \pm 15$ ppb	$100 \pm 10$ ppb	$2 \pm 1$ nm

Table 3.1: PREX beam requirements

The ambitious beam quality goals were achieved for the experiment, thanks to the work done at the *Center of Injectors and Sources* at JLAB to improve the quality of the beam by minimizing the helicity-correlated charge asymmetry and position differences. Furthermore, the center also provided a new scheme to cancel systematic errors. The statistical errors were also minimized by providing the required beam current and reducing the target density fluctuations.

#### 3.4.1 The Fiber-based Laser System

The fiber-based laser system [22] installed at the CEBAF photo injector generates 780 nm light directed toward the GaAs superlattice photocathode in the 100 kV DC high voltage photogun. The fiber amplifier produces light with very good spatial beam quality (nearly diffraction limited), which is maintained following frequency doubling. The 30 mm focal length lens at the output of the periodically poled lithium niobate

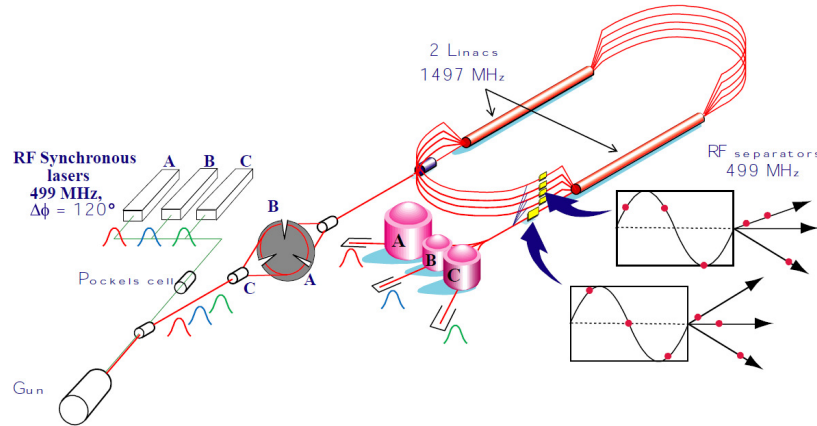


Figure 3.5: Schematic overview of the polarized electron source and the accelerator

(PPLN) crystal is used to adjust the collimation of the laser beam. A 2 m focal length lens near the photogun vacuum chamber window creates a  $500 \mu\text{m}$  diameter (FWHM) focused spot at the photocathode. In order to provide the beam to three experimental halls simultaneously, a water-cooled copper plate with three apertures in photogun spaces  $120^\circ$  apart is used.

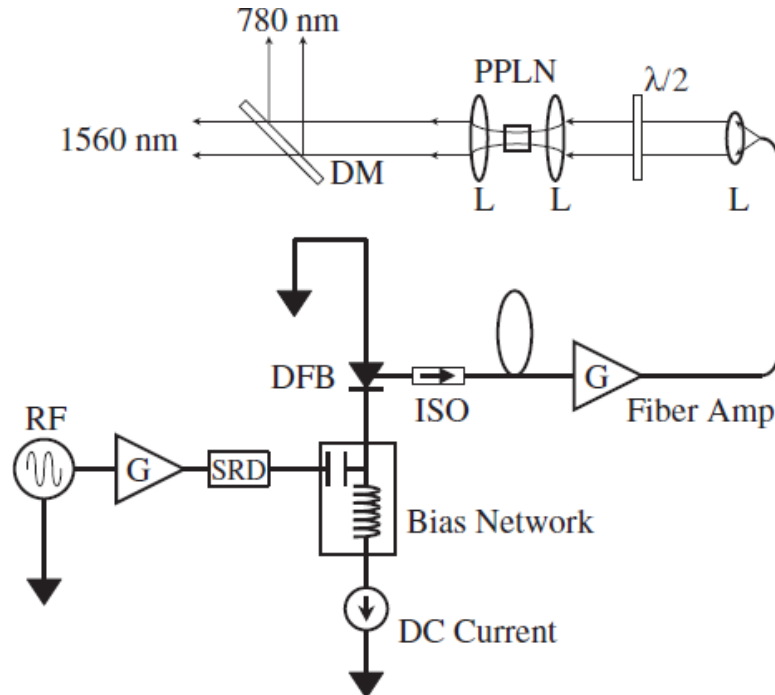


Figure 3.6: Schematic of the fiber-based laser system

The fiber-based laser system was used for PREX with high beam polarization and good beam current stability. The system proved that it could enhanced reliability compared to diode master-oscillator-power-amplifier (MOPA) systems and mode-locked Ti-sapphire lasers previously used in other parity violating experiments.

### 3.4.2 Intensity Attenuator System

The Intensity Attenuator (IA) is a system devised to control the amount of light that traverse through the laser table optical elements, in a helicity correlated manner. For PREX, the IA was used for diagnostic study. Its main component is a Pockels Cell that operates at a lower voltage than the main Pockels Cell. The voltage is varied for specific helicity states by supplying a digital-to-analog (DAC) control offset voltage to the high voltage supply. A rotatable  $\lambda/10$ -plate, just upstream of the cell, provides a mean of control over the maximum amount of attenuation that the system provides, and thus allows the change in the system's lever arm over the helicity-correlated laser intensity asymmetry. Linear polarizers are used before and after this system to clean up the linear polarization.

### 3.4.3 GaAs Photocathode

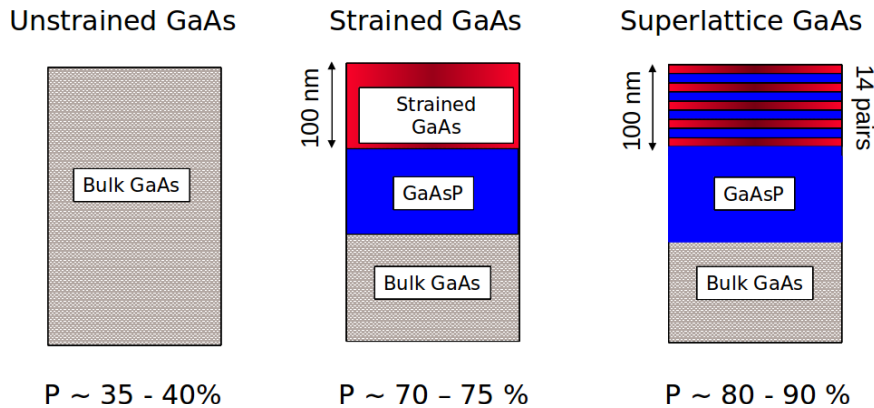


Figure 3.7: Various types of GaAs photocathode. PREX used the superlattice photocathode due to its higher polarization.

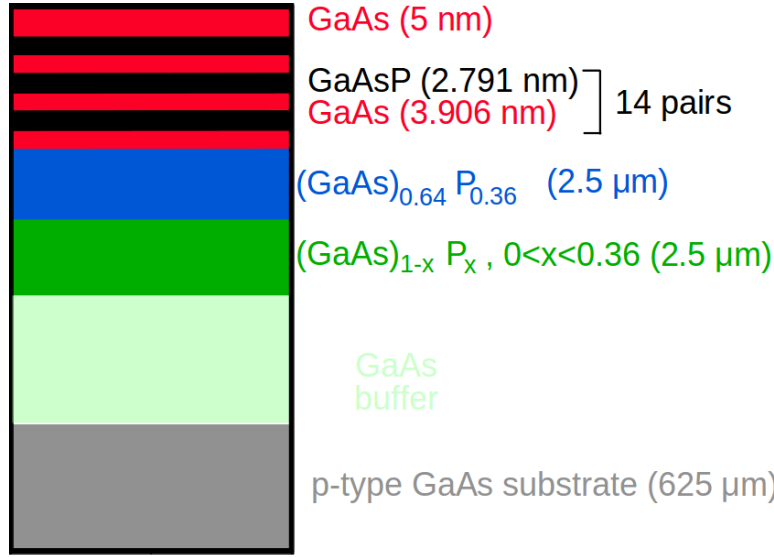


Figure 3.8: Details of superlattice photocathode used in PREX

The polarized electrons are released from a superlattice GaAs photocathode. The cathode is created by growing layers of various GaAs combinations, as shown in Fig. 3.7. The superlattice cathode is made up of 14 pairs of GaAs and  $\text{GaAs}_{0.64}\text{P}_{0.36}$  only 100 nm thick grown on a 2.5  $\mu\text{m}$  thick layer of GaAsP. At the bottom of the superlattice photocathode is a bulk of GaAs. The shorter lattice spacing of GaAsP causes the natural spacing of the GaAs to shrink slightly, hence creates strain [43]. The strain induces a gap in the different sublevels of the  $P_{3/2}$  electrons in the valence band of the GaAs. By tuning a left-handed circularly polarized laser (helicity -1) to the proper frequency, electrons from the  $P_{3/2} m=3/2$  state can be excited to the  $S_{1/2} m=1/2$  state of the conduction band. In this case, the energy gap between the valence and conduction bands is 1.59 eV. From there, the polarized electrons diffuse to the surface and escape into the surrounding vacuum. Since the strain creates a sufficiently wide gap ( $\sim 50$  meV) between the  $P_{3/2}$  sublevels, the electrons from  $P_{3/2} m=1/2$  state will not be excited by the tuned laser. Thus, the electrons escaping from the surface are all from the  $S_{1/2} m=1/2$  state and are theoretically 100% polarized, although typically measured around 80%-90%.

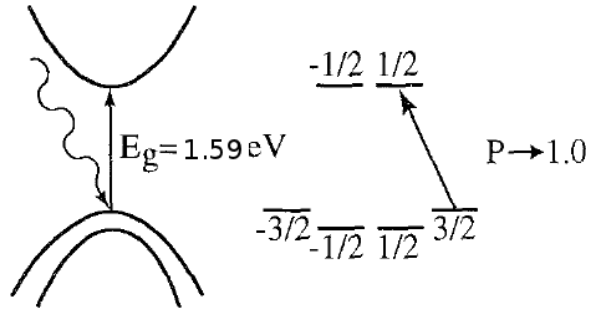


Figure 3.9: A diagram of the bandgap and energy levels for superlattice GaAs. The arrow indicates the allowed transitions for left-helicity photons

### 3.4.4 Helicity Pockels Cell

PREX used the Helicity Pockels Cell (HPC) as a Fast Helicity Reversal. HPC was a voltage-controlled, rapidly switching  $\lambda/4$ -plate to convert linearly polarized light into circularly polarized light. The degree to which the beam wavelength is retarded can be adjusted through application of an appropriate high voltage to provide control over the phase difference between the outgoing polarization states.

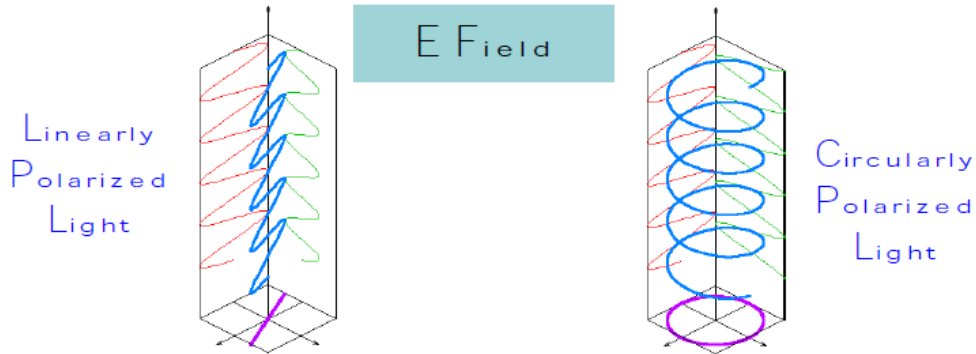


Figure 3.10: Helicity Pockels Cell converts linearly polarized electron beam to circularly polarized.

PREX used 120 Hz and later 240 Hz helicity reversal rate during the run. This rates were higher than normal operation (30 Hz) due to the problems of noise at low frequencies such as lead target density fluctuations and beam current fluctuations. Running at the higher reversal rates reduced the widths of helicity correlated distributions by a factor of 4 [67].

### 3.4.5 Insertable Half-wave Plate

In addition to the fast reversal of the electron polarization by the HPC, an insertable half-wave plate (IHWP) is inserted into or extracted from the laser beamline on a much larger timescale ( $\sim 1/\text{day}$ ). Thus, this is also called “slow reversal of electron polarization”. The purpose of this device is to rotate the linear polarization state incident on the HPC by  $90^\circ$ , therefore reversing the final circular polarization of the laser, and thus the polarization of the electron beam, relative to the voltage applied to the HPC [52]. This action would flip the sign of the measured parity violating asymmetry observed in the hall. Furthermore, many possible helicity-correlated systematics are insensitive to the change in IHWP state, so this procedure also provides means for systematic cancellation. Also, IHWP provides a powerful mean to check for a false asymmetry, since the physics asymmetries measured with and without this IHWP should have the opposite sign.

### 3.4.6 Rotatable Half-wave Plate

Strain in the superlattice layers causes a quantum efficiency (QE)<sup>3</sup> that is dependent on the orientation of linearly polarized light. This effectively creates an “analyzing” power with respect to an axis lying in the plane of the cathode’s surface. Residual linear polarization aligned with this axis can therefore lead to a charge asymmetry. The rotatable half-wave plate (RHWP) can eliminate the charge asymmetry by choosing a RHWP angle that rotates the residual linear polarization produced by the HPC to be at  $45^\circ$  to the cathode analyzing power as in Fig.3.11. Furthermore, the RHWP can be rotated such that the sensitivity of the HPC birefringence to the cathode analyzing power is eliminated. In practice, the RHWP angle is chosen such that there is

---

<sup>3</sup>Quantum efficiency (QE) is defined as the number of electrons emitted from the cathode relative to the intensity of light incident on the cathode.

small, but non-zero Polarization-Induced Transport Asymmetry (PITA)<sup>4</sup> slope. Having some sensitivity to analyzing power allows us to used PITA voltage to cancel the effects of residual linear polarization produced by the vacuum window or the RWP itself [34].

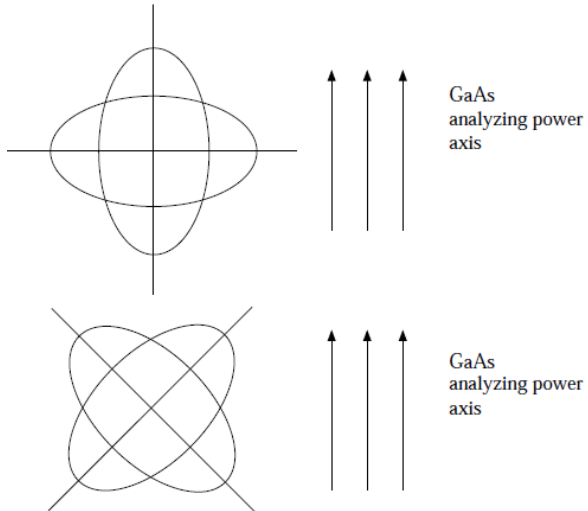


Figure 3.11: The RWP can rotate the polarization ellipses shown in the top illustration to the orientation shown in the bottom to minimize the charge asymmetry

### 3.4.7 Spin Precession and Double Wien Filters

The presence of the recirculating arcs in the accelerator and the bending arc along the Hall A beamline introduces a Thomas precession of the beam polarization. This effect takes place whenever there is a component of acceleration perpendicular to the velocity of the particle. To eliminate this spin precession, the maximization of the longitudinal polarization observed must be met. Although the photogun produces longitudinally polarized electrons, in order to receive fully longitudinal polarization, double Wien filters are needed. The first Wien filter rotates the spin by 90° in the vertical direction. The two solenoids rotate the spin back to the horizontal plane transverse to the beam motion. By changing the current direction in these two solenoids,

---

<sup>4</sup>PITA effect is from the imperfect circular polarization produced by the HPC. It causes an analyzing power of the optical system to arise.

the spin is rotated either to right or left of beam. Then, the second Wien filter rotates the spin in the horizontal plane to account for the spin precession in the accelerator such that the experiment receives fully longitudinal polarization after taking into account the spin precession through the accelerator. Also, the double Wien filters allow us to flip the helicity about once a week using an arrangement of solenoids that flips the helicity without changing the beam trajectory.

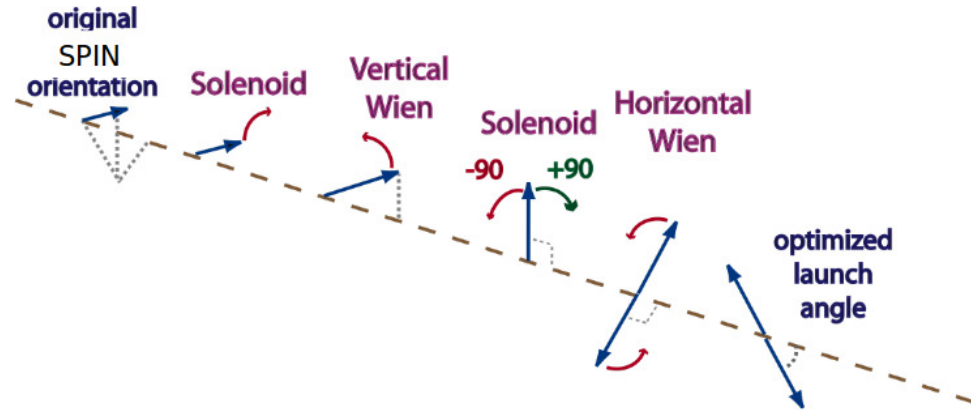


Figure 3.12: Double Wein filters produces fully longitudinal polarization

### 3.4.8 Electron Guns and the Injector

JLAB has two identical electron guns, Gun # 2 and Gun # 3, to inject electrons into the accelerator. Gun # 2 had a strained-layer cathode installed in it and Gun # 3 had a superlattice cathode installed. The electron gun is situated at an angle of 15° with respect to the accelerator beamline. The injector consists of a solenoid which is used to bend the electrons into the accelerator. The injector accelerates the electrons up to an energy of 45 MeV before they enter the main accelerator.

### 3.5 Hall A Overview

Hall A is the biggest experimental hall among the three existing experiment halls at JLAB, with a diameter of 53 m.

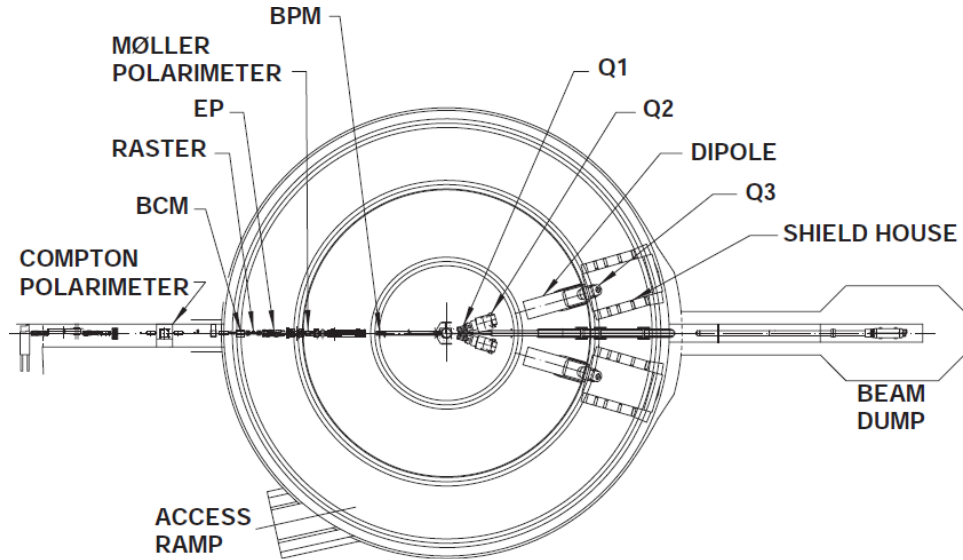


Figure 3.13: Schematic drawing of instrumentation in Hall A from top view

Fig. 3.13 shows major instrumentation of Hall A. This includes beamline equipment, target, and the two high resolution spectrometers. One of commonly used coordinate system is the Hall Coordinate System (HCS). The origin of the HCS is at the center of the hall, which is defined by the intersection of the electron beam and the vertical symmetry axis of the target system.  $\hat{z}$  is along the beamline and points in the direction of the beam dump, and  $\hat{y}$  is vertically up.

### 3.6 Hall A Beamline

The beamline in Hall A starts after the arc section and ends at the beam dump. The arc section can be used for beam energy measurement. The beamline consists of a Compton beam polarimeter, two beam current monitors (BCM) between which located an Unser monitor (for absolute beam current measurement), a fast raster,

the eP device for beam energy measurement, a Møller beam polarimeter, and beam position monitors (BPMs).

### 3.6.1 Beam Energy Measurement

During the run, beam energy was measured continuously using the Tiefenbach method, which had been calibrated using the Arc and the eP measurements. The advantage of using the Tiefenbach measurement over the latter two measurements is that the Tiefenbach measurement can be done without disturbing data taking while the other two methods require stopping the run to perform the measurement. The precision of the Tiefenbach measurement is of the order of  $\delta E_{beam}/E_{beam} \sim 1 \times 10^{-3}$ .

#### Arc Measurement

The Arc measurement uses the fact that an electron beam would be deflected by a known angle when it passes through a magnetic field. This measurement is performed in the arc region of the beamline. This region consists of eight dipole magnets that bend the electron beam from linac by  $34.3^\circ$  into Hall A. When the beam is tuned into the so-called “dispersive” mode in this region, the momentum  $p$  of the beam is determined by

$$p = c \frac{\int \vec{B} \times d\vec{l}}{\theta} \quad (3.2)$$

where  $c = 0.299792 \text{ GeV}\cdot\text{rad/Tm}$  is the speed of light, the numerator is the dipole field integral, and  $\theta$  is the bend angle.

The Arc measurement is made up of concurrent measurements of the magnetic field integral and bend angle. An identical ninth dipole, separate from the beamline, is used to measure the field integral. The bend angle is measured by using wire scanners (SuperHarps)<sup>5</sup> to determine the position of the beam throughout the arc.

---

<sup>5</sup>When the beam strikes a wire, the particles scattering off the wire are collected by a simple ion chamber, hence a current is generated and the beam’s position is generated and the beam position is recorded.

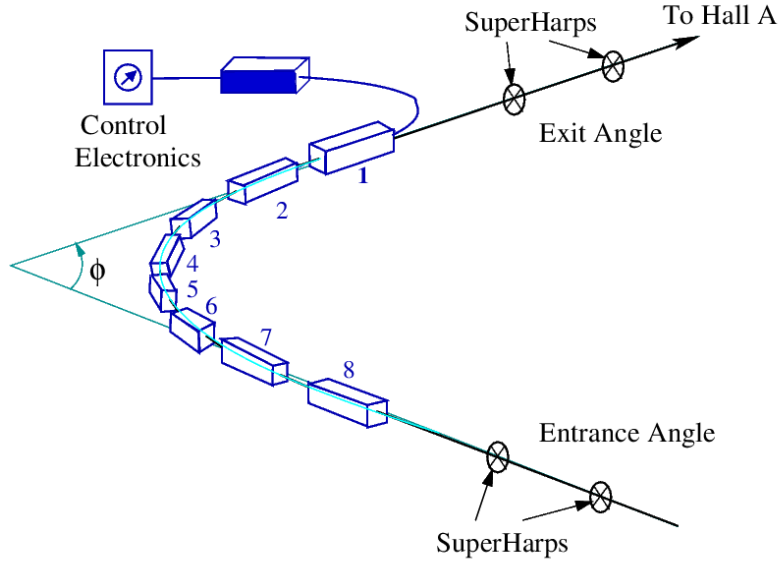


Figure 3.14: The arc section of the beamline

The Arc measurement provides the precision in beam energy measurement of the order of  $\delta E_{beam}/E_{beam} \sim 2 \times 10^{-4}$ .

### eP Measurement

The eP measurement makes use of the fact that, for the elastic  $e + p$  reaction, the scattering angles of the electron and proton ( $\theta_e$  and  $\theta_p$ ) are related to the energy  $E$  of the incoming electron by,

$$E = M_p \frac{\cos(\theta_e) + \sin(\theta_e)/\tan(\theta_p) - 1}{1 - \cos(\theta_p)} + \mathcal{O}\left(\frac{m_e^2}{E'^2}\right) \quad (3.3)$$

Thus, by measuring  $\theta_e$  and  $\theta_p$ , one can find the beam energy precisely.

Fig. 3.15 illustrates the layout of the eP measurement devices. The target is a  $\text{CH}_2$  film enclosed by an aluminum cover. Two identical arms, each consisting of an electron and a proton detector system, are placed symmetrically with respect to the beam direction on the vertical plane. By simultaneously measuring the beam energy with both arms, any error due to misalignment of the detectors is canceled in the first

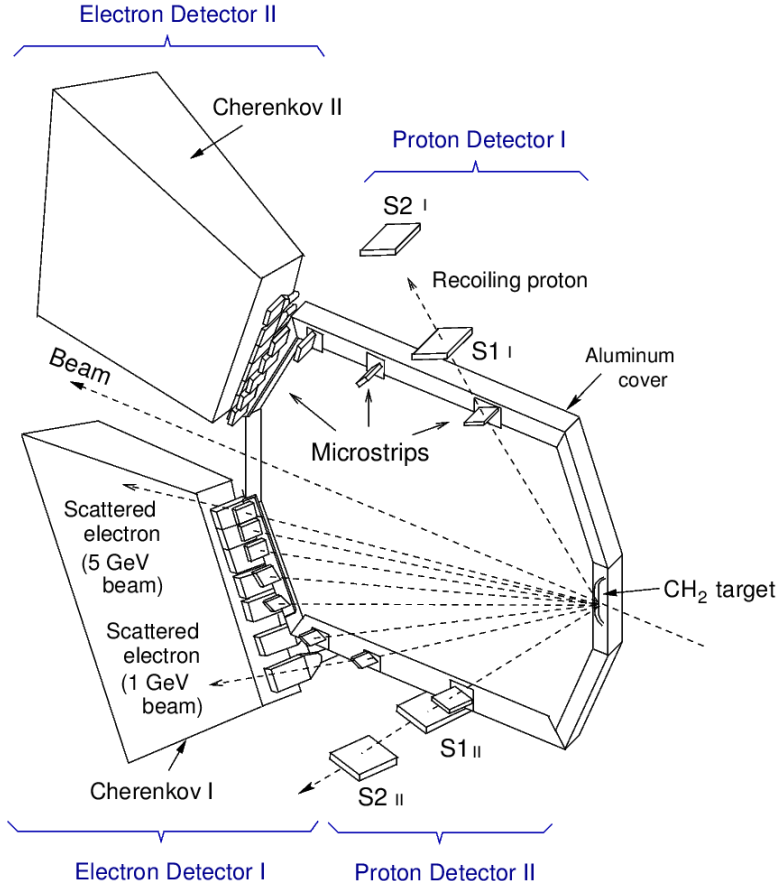


Figure 3.15: The eP beam energy measurement instrumentation

order. The proton detectors are fixed at  $60^\circ$  while the electron detectors can be moved from  $9^\circ$  to  $41^\circ$ , corresponding to an energy range of 0.5 to 6.0 GeV. The proton detector consists of two scintillator planes, combined with a silicon strip detector (SSD), while the electron detector consists of a scintillator plane and a Cherenkov counter in addition to a silicon strip detector [65] [76]. Although the eP measurement was not used during the experiment, it was used to verify the accuracy of the Tiefenbach measurement.

### The Tiefenbach Measurement

The Tiefenbach beam energy measurement uses the current values of Hall A arc *Bdl* and Hall A arc beam position monitors (BPMs) to calculate the beam energy. This

number is continuously recorded in the data stream and is calibrated against the Arc energy of the 9<sup>th</sup> dipole regularly. Since the Tiefenbach measurement is continuously performed along the data taking, the method provides a tool to acknowledge the beam fluctuations that might occur during the run. The precision from the Tiefenbach measurement is of the order of  $\delta E_{beam}/E_{beam} \sim 1 \times 10^{-3}$ .

### 3.6.2 Beam Current Measurement

The beam current in Hall A is measured using an Unser monitor and two RF cavities called beam current monitors (BCM). The devices are contained within a temperature controlled, magnetically shielded enclosure about 25 m upstream of the target. The two cavities are placed symmetrically upstream and downstream of the Unser.

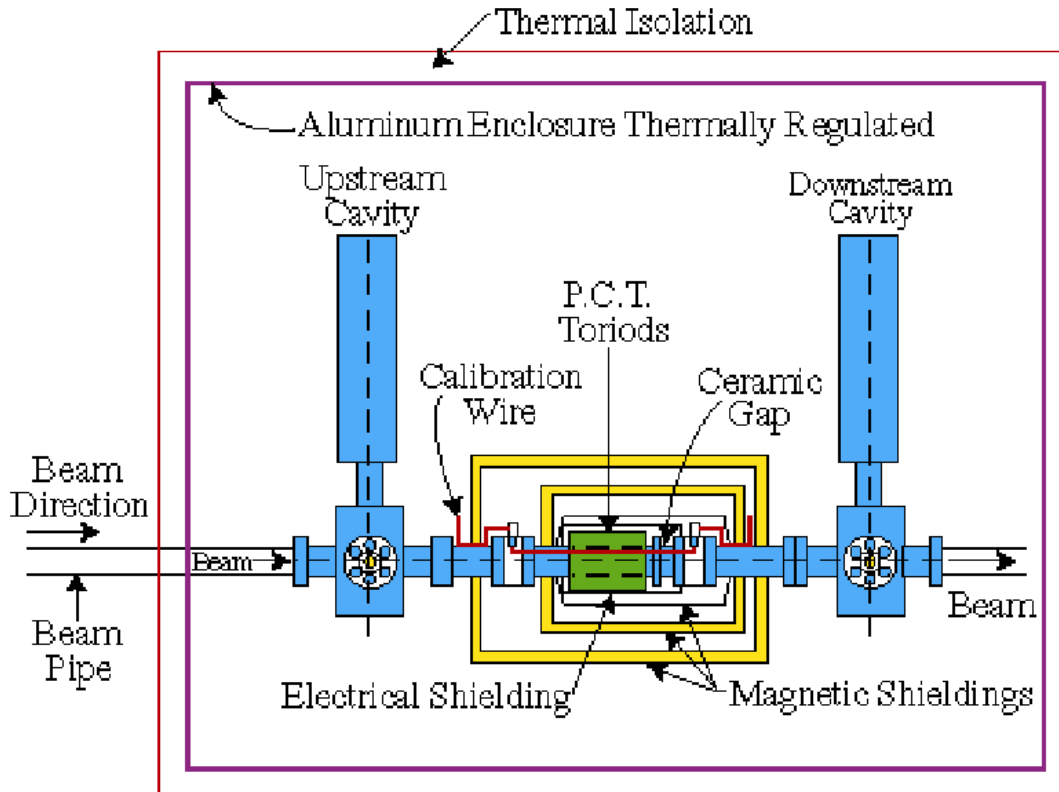


Figure 3.16: The schematic of beam current monitor (BCM)

The Unser monitor [52] is a parametric current transformer that provides an ab-

solute measure of the beam current. Since the output signal of the Unser is unstable over a period of a few minutes, it is unreliable as a continuous measure of the beam current. Hence, the Unser is used for calibrating the RF cavities.

The cavities are made of stainless steel cylinders, 15.48 cm in diameter and 15.24 cm in length, and are resonantly tuned to the beam frequency of 1497 MHz. The electron beam excites the resonant transverse mode  $TM_{010}$  of the cavity at 1497 MHz. This is picked up by the antennae creating an RF output signal whose voltage is proportional to the beam current. This signal is processed through a down-converter to obtain a 1 MHz signal, to avoid attenuation from the long cable length to the counting house. At this point, the signal is split into two paths [65]. One signal will be integrated and recorded by the scalers, the other signal will be sampled and leads to the EPICS data stream. The signal in the counting house is passed to a RMS-to-DC converter which outputs a DC voltage proportional to the beam current. The constant voltage is input to a Voltage-To-Frequency (VTOF) converter which outputs a signal with a frequency proportional to the input voltage. This sinusoidal wave is fed to the 200 MHz VME scalers which simply count each incident pulse. The accumulated number of scaler counts will be proportional to the total charge. In practice, the RMS-to-DC converter is non-linear below  $5\mu A$ , so the signal is amplified by a factor of 1, 3 and 10 before the converter. Therefore, two cavities each output 3 signals, referred to as X1, X3, and X10 respectively.

The RF cavities provide a relative value and must be calibrated with an absolute measurement. The Unser, which is a toroidal parametric transformer, serves this purpose. The toroid responds to the DC magnetic field created by the presence of the beam. It can provide an absolute measurement at large currents, but at lower currents, the absolute uncertainty ( $\sim 250$  nA) becomes prohibitive and the offset drifts significantly over the course of a few minutes. The Unser is calibrated with an internal reference wire carrying a current of 2 mA from a precision current source. Then it, in

turn, is used to calibrate the cavities by making a measurement of the beam current at the highest available current, typically about 50  $\mu\text{A}$ . The beam is cycled on and off at one minute intervals to compensate for the drifting offset. The measurement typically takes about two hours and interrupts beam delivery to all experimental halls.

The cavities and their associated electronics are highly linear, so once they have been calibrated at high current, the calibration can be extrapolated reliably to the lower currents. The overall system is estimated to be accurate to better than 1% down to 1  $\mu\text{A}$  and  $\sim$ 2-3% down to 50 nA.

### 3.6.3 Beam Polarization Measurement

The longitudinal polarization of an electron beam may be defined as

$$P_e = \frac{N_e^+ - N_e^-}{N_e^+ + N_e^-} \quad (3.4)$$

where  $N_e^{+(-)}$  is the number of electrons with spin parallel (antiparallel) to the beam direction.

Since PREX is a parity-related experiment, polarization of the beam is extremely crucial to the experiment. In Hall A, the polarization of beams at GeV energies is measured via Møller scattering ( $e^-e^- \rightarrow e^-e^-$ ) or via Compton scattering ( $e^-\gamma \rightarrow e^-\gamma$ ), both of which are sensitive to the relative spins of the incident particles.

#### Møller Polarimeter

Møller polarimeter [19] measures the process of Møller scattering of the polarized electron beam off electrons in a thin magnetized iron target,  $e^- + e^- \rightarrow e^- + e^-$ . The Hall A Møller polarimeter was developed to measure the polarization of electron beams over the energy range of 0.8 to 6.0 GeV. It consists of a small spectrometer

with a series of three quadrupole magnets which provide an angular selection, and a dipole magnet for energy analysis.

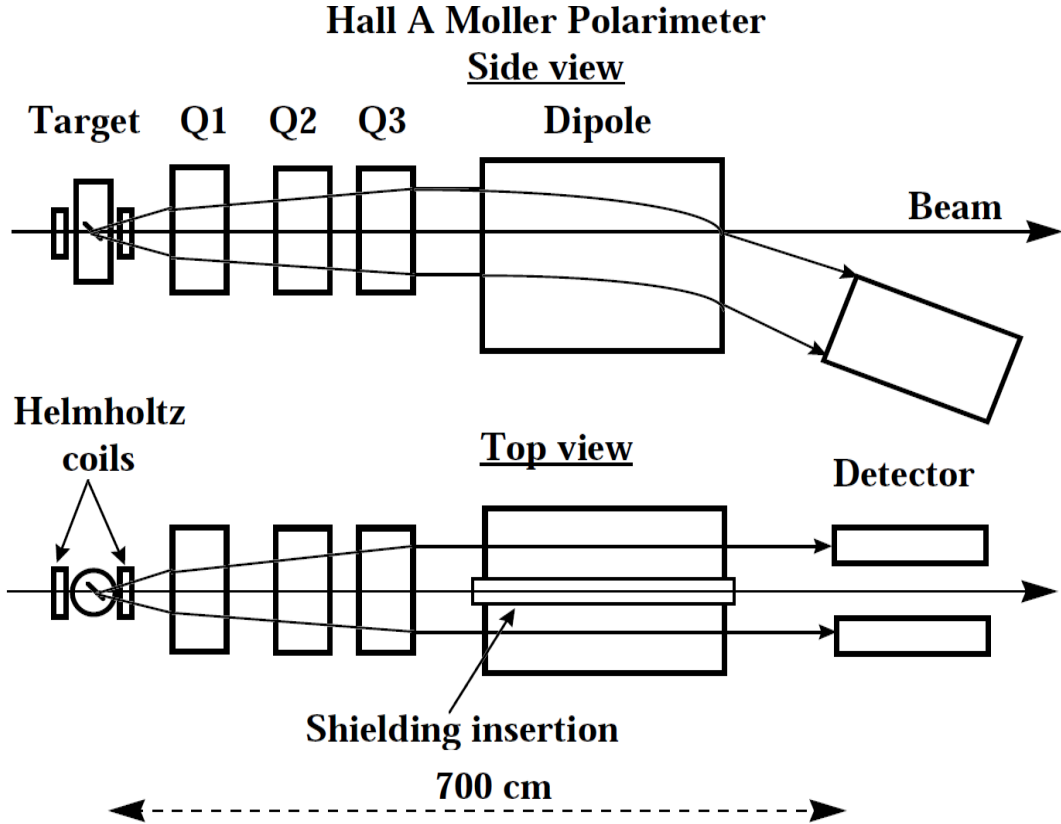


Figure 3.17: Hall A Møller polarimeter set up

The Møller scattering cross section depends on the beam and target polarizations ( $P_b$  and  $P_t$ ) as

$$\sigma \propto (1 + \sum_{i=X,Y,Z} A_{ii} P_{b,i} P_{t,i}) \quad (3.5)$$

where  $i = X, Y, Z$  defines the projections of the polarizations. The analyzing power  $A_{ii}$  depends on the scattering angle in the center of mass (CM) frame ( $\theta_{CM}$ ). Assuming that the beam direction is along the Z-axis and that the scattering happens in

the XZ plane,

$$A_{ZZ} = -\frac{\sin^2 \theta_{CM}(7 + \cos^2 \theta_{CM})}{(3 + \cos^2 \theta_{CM})^2} \quad (3.6)$$

$$A_{XX} = -A_{YY} = -\frac{\sin^4 \theta_{CM}}{(3 + \cos^2 \theta_{CM})^2} \quad (3.7)$$

At  $\theta_{CM} = 90^\circ$ , the analyzing power has its maximum  $A_{ZZ} = 7/9$ . A beam polarization transverse to the scattering plane also leads to an asymmetry, though the analyzing power is lower:  $A_{XX,max} = A_{ZZ,max}/7$ .

The polarimeter is schematically presented in Fig. 3.17. The polarimeter reaction plane is parallel to the horizontal plane in Hall A. The polarimeter consists of the polarized electron target, three quadrupole magnets, a dipole magnet and a detector. The polarimeter quadrupole magnets make it possible to keep the position of all polarimeter elements unchanged within the whole range of JLAB energies. Their primary purpose is to focus the divergent trajectories of Møller electrons in the scattering plane into an envelope of paired trajectories aligned with the axis of the beam at the exit of the last quadrupole. The dipole is the main element of the polarimeter magnetic system. It provides the energy analysis, thus separating the Møller scattered electrons having energy of  $E_0/2$  and scattering angle of  $\theta_{CM}$  from electrons coming from the Mott scattering peak, which has energy of  $E \sim E_0$  at the same scattering angle and thereby suppressing the background. It also bends the Møller electrons from the reaction plane, allowing their detection away from the electron beam. The dipole has a magnetic shielding insertion in the center of the magnetic gap. The Møller electrons pass through the dipole on the left and right sides of this shielding insertion. The primary electron beam passes through a 4 cm diameter hole bored in the shielding insertion letting its passage to the Hall A target and then to the beam dump with small influence of the dipole magnetic field.

The Møller polarimeter detector is located in the shielding box downstream of

the dipole and consists of two modules (left and right) for coincidence measurements. Each part of the detector includes an aperture detector made of plastic scintillator and four blocks of lead glass. In order for PREX to achieve 1% accuracy in beam polarization, the Møller target system was upgraded by increasing the high magnetic field on the target to 4 Tesla with the help of a super conduction split-coil solenoid. The increase in magnetic field reduced the uncertainty arising from the determination of target polarization.

For PREX, the beam polarization measured by Møller polarimeter was found to be  $90.32 \pm 0.07(\text{stat}) \pm 1.12(\text{sys}) \%$ .

### Compton Polarimeter [57]

For head-on Compton scattering between electrons with longitudinal polarization  $P_e$  and photons with circular polarization  $P_\gamma$ , one may form an asymmetry between the energy-weighted, integrated Compton signal  $S$  for time intervals in which the polarizations are parallel ( $\uparrow\uparrow$ ) and antiparallel ( $\uparrow\downarrow$ ):

$$A_{\text{meas}} = \frac{S^{\uparrow\uparrow} - S^{\uparrow\downarrow}}{S^{\uparrow\uparrow} + S^{\uparrow\downarrow}} = P_e P_\gamma \langle A_s \rangle \quad (3.8)$$

where  $\langle A_s \rangle$ , the analyzing power, is the signal asymmetry that would be measured if the incident electron and photon beams were 100% polarized.

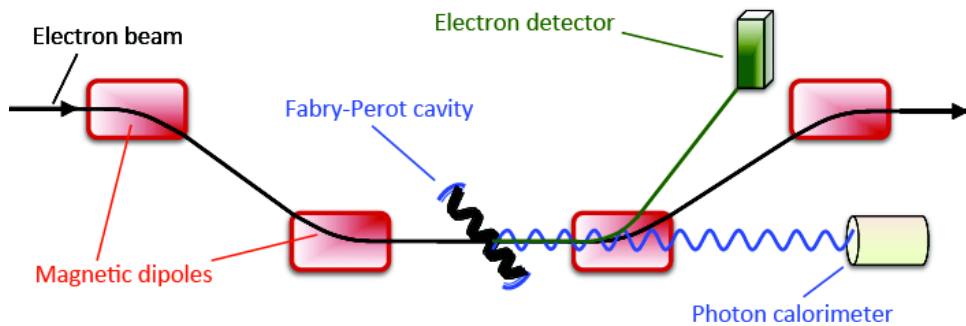


Figure 3.18: A schematic of the Compton polarimeter layout in Hall A

Fig. 3.18 illustrates a schematic representation of the polarimeter's layout. The beam entering from the left is routed through a chicane formed by four magnetic dipoles. At the center of the chicane, electrons undergo Compton scattering with circularly polarized photons in resonance in a Fabry-Pérot cavity fed by green light ( $\lambda = 532$  nm) which has been upgraded from an infrared laser ( $\lambda = 1064$  nm) in 2010. The crossing angle between the two beams is 23 mrad. The photon polarization is periodically flipped between right- and left-circular in order to control for systematic effects; during a flip, background processes are characterized by shutting off the Pound-Drever-Hall feedback loop between the cavity and the interaction point. Unscattered electrons, separated from the Compton-scattered particles by the third dipole in the chicane, continue on into the hall for the primary experiment.

The Compton photon calorimeter consists of a single cylinder of cerium-doped  $\text{Gd}_2\text{SiO}_5$  (GSO). With a 6-cm diameter and 15-cm length, this crystal is large enough to contain most of the shower from an incident photon, without the extended cross-calibration and gain matching required for a crystal array. The calorimeter is located approximately 6 m downstream of the Compton interaction point, and is mounted on a motorized table with remote-controllable motion along both axes (horizontal and vertical) transverse to the beam direction. Two narrow converter-scintillator pairs allow precise centering on the beam of Compton-scattered photons, which form a cone with higher-energy photons at the center.

To compute an asymmetry from the Compton polarimeter, the photon signals are detected in the energy-weighted integral mode, rather than in the raw counting rates. In such an integral, the greatest contributions to the asymmetry will be made by photons in the energy range where the analyzing power is at a maximum. Furthermore, since this integral is less sensitive to low-energy uncertainties in the detector response function, the method is well-suited to stand-alone photon detector running: accurate asymmetries may be measured even without calibration against the scattered-electron

detector. Therefore, a data acquisition system (DAQ) has been designed and commissioned with both integrating and counting capability.

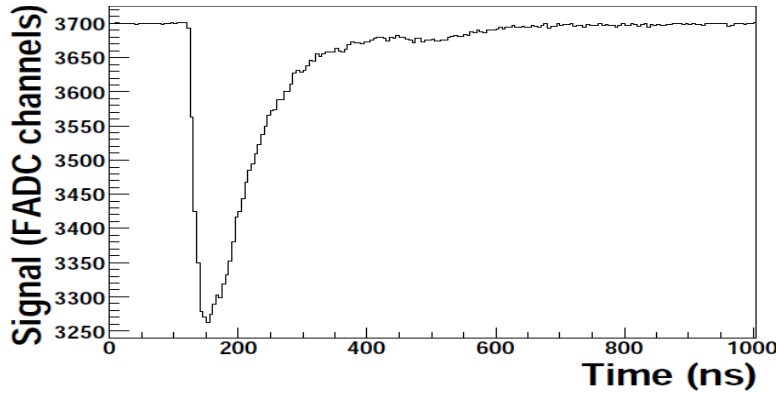


Figure 3.19: A waveform from the GSO calorimeter for an incident photon in the energy range for Compton-scattered photons (for PREX, the maximum scattered photon energy was 38.4 MeV)

The new DAQ is based on a 12-bit FADC. A photon pulse registers as a negative waveform relative to a programmable pedestal level, as in Fig. 3.19. The signal from the photon detector is sampled at 200 MHz and integrated in a digital summing accumulator for a single helicity window<sup>6</sup>, an interval in which the electron beam helicity is well-defined. Then, the sum of the signal between intervals where incident particles have opposite polarization configurations forms an asymmetry in the pedestal-subtracted. According to Eq. 3.8, this energy-weighted integral is proportional to the degree of longitudinal polarization of the electron beam.

The measurement of the background signal  $B$  allows the correction of the Compton signal by accounting for the dilution of the asymmetry due to background processes (primarily bremsstrahlung and synchrotron radiation):

$$A_{meas} = \frac{(S^{\uparrow\uparrow} - B^{\uparrow\uparrow}) - (S^{\uparrow\downarrow} - B^{\uparrow\downarrow})}{(S^{\uparrow\uparrow} - B^{\uparrow\uparrow}) + (S^{\uparrow\downarrow} - B^{\uparrow\downarrow})} = P_e P_\gamma \langle A_s \rangle \quad (3.9)$$

Ideally,  $B^{\uparrow\uparrow} = B^{\uparrow\downarrow}$ , but in practice, there may be so-called false asymmetries due to

<sup>6</sup>In the case of PREX, the helicity window was at 120 Hz, and later at 240 Hz

helicity-dependent changes in beam tune [16]. The average analyzing power,  $\langle A_S \rangle$ , can be found by using GEANT4 to simulate the analyzing power as a function of scattered photon signal, and performing an energy-weight integral of the function.  $P_\gamma$ , the circular polarization of photon, is measured from the light transmitted through the cavity when it is in resonance. Two powermeters are placed at the outputs of a polarizing beam splitter in the optical path, and their relative readings are combined with the cavity transfer function to compute the photon polarization at the Compton interaction point.

The major advantage of Compton polarimetry compared to Møller polarimetry is its negligible effect on the electron beam as a whole; approximately one electron in  $10^9$  undergoes Compton scattering. Since the measurement is nondestructive, the beam polarization can be continuously monitored throughout the course of an experiment. For PREX, the beam polarization measured by Compton polarimeter was found to be  $88.20 \pm 0.12(\text{stat}) \pm 1.04(\text{sys}) \%$ .

### 3.6.4 Beam Position Measurement

To determine the position and direction of the beam at the target location, PREX used two Beam Position Monitors (BPMs) and a low current cavity monitor.

#### Beam Position Monitors

The Beam Position Monitors (BPMs) is a 4 wire antenna array located at 7.524 m (IPM1H03A or BPMA) and 1.286 m (IPM1H03B or BPMB) upstream of the target [6]. The absolute position of the beam can be determined from the BPMs by calibrating them with respect to wire scanners<sup>7</sup> (SuperHarps) which are located adjacent to each of the BPMs (7.353 m and 1.22 m upstream of the target). To obtain the beam position information, three different kinds of parameters are involved [30]:

---

<sup>7</sup>The wire scanners are surveyed with respect to the Hall A coordinates at regular intervals and the results are reproducible at the level of  $200\mu\text{m}$ .

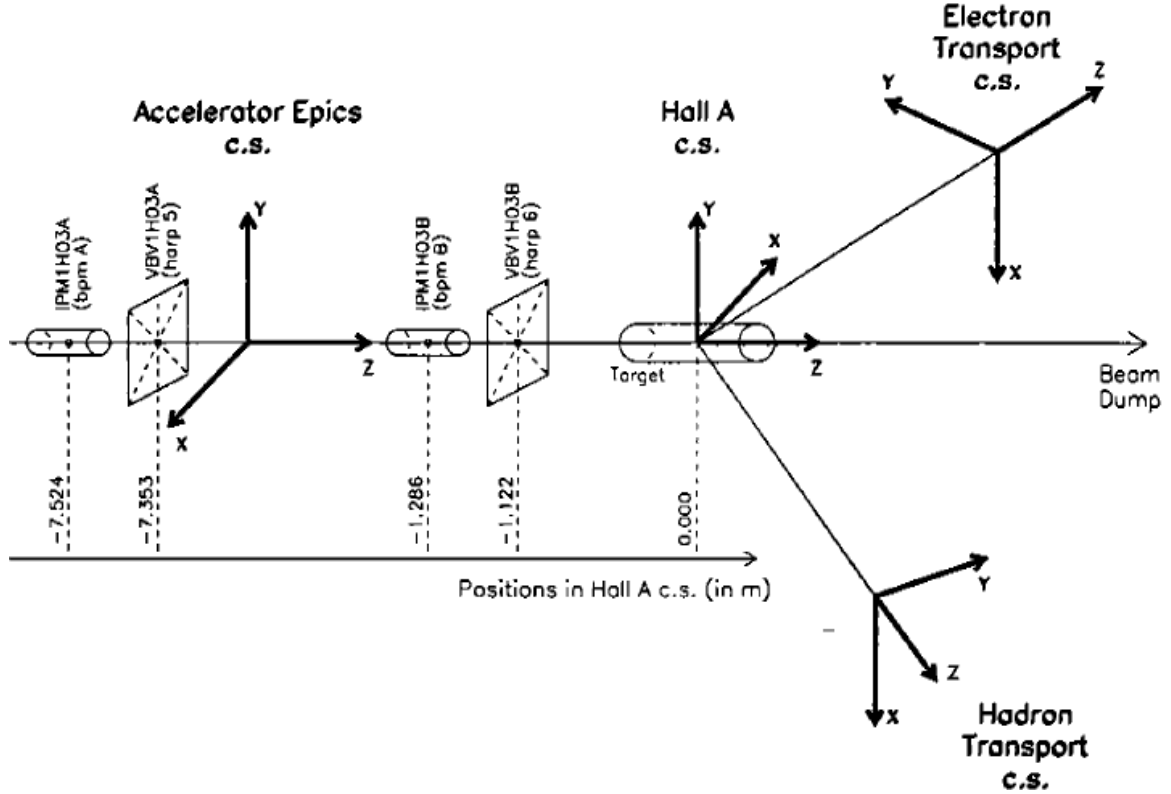


Figure 3.20: Beam Position Monitors layout and associated coordinate systems

1. the offsets of the four channels  $X_p^{off}$ ,  $X_m^{off}$ ,  $Y_p^{off}$  and  $Y_m^{off}$
2. their relative gains  $\alpha_X$  and  $\alpha_Y$
3. the absolute conversion factors  $\kappa_X$  and  $\kappa_Y$ .

The detection method is based on comparing the signals induced by the beam passing in two opposite antennas (p and m). From the recorded signals  $X_p$ ,  $X_m$ ,  $Y_p$  and  $Y_m$ , the beam coordinates  $X_{bpm}$  and  $Y_{bpm}$  are reconstructed as follows:

$$X_{bpm} = \kappa_X \times (18.87 \text{ mm}) \times \frac{(X_p - X_p^{off}) - \alpha_X \times (X_m - X_m^{off})}{(X_p - X_p^{off}) + \alpha_X \times (X_m - X_m^{off})} \quad (3.10)$$

$$Y_{bpm} = \kappa_Y \times (18.87 \text{ mm}) \times \frac{(Y_p - Y_p^{off}) - \alpha_Y \times (Y_m - Y_m^{off})}{(Y_p - Y_p^{off}) + \alpha_Y \times (Y_m - Y_m^{off})} \quad (3.11)$$

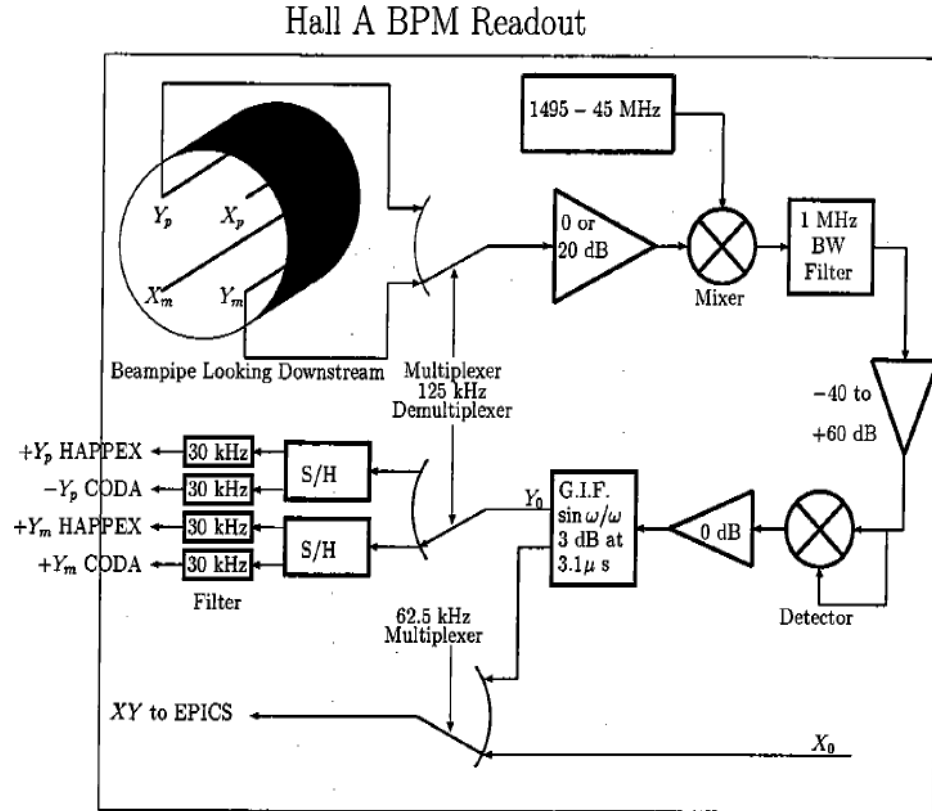


Figure 3.21: Hall A Beam position Monitor readout electronics

The BPMs measure the beam position with respect to a coordinate system rotated 45° counterclockwise with respect to the EPICS Hall A coordinate system, and 135° clockwise with respect to the Hall A Transport coordinate system.

### 3.6.5 Raster

At high beam intensity, the intrinsic size of the beam ( $\sim 100 \mu\text{m}$ ) can produce local heating within the target, with the possibility of melting the lead target leading to large fluctuations and even target breakdown. These fluctuations increase the detected asymmetry width beyond what is expected for counting statistics. To reduce the effects of target heating, the heat load is swept over a small area of the target by use of a device called the raster.

The raster [74] consists of two magnetic coils located upstream of the Compton

polarimeter and four beamline quadrupoles. The two magnetic coils are air-core windings made of Litz cables. The advantage of air-core magnet over the iron-core magnet is that it can operate at relatively higher frequencies with low-field integral value for applications of small bending power. Also, the response between the excitation current and the induced magnetic field is spontaneous. The coils are oriented to provide a horizontal and vertical deflection. Each coil current is driven with triangle waveforms at different frequencies, with amplitudes set to deliver a rectangular pattern at the target. For PREX, the raster dimensions used were approximately 4 mm×3 mm.

### 3.6.6 Beam Modulation

Beam modulation, also referred to as “dithering”, is a technique used by the experiment to measure the change in the detector flux for a known change in beam position and beam energy on target.

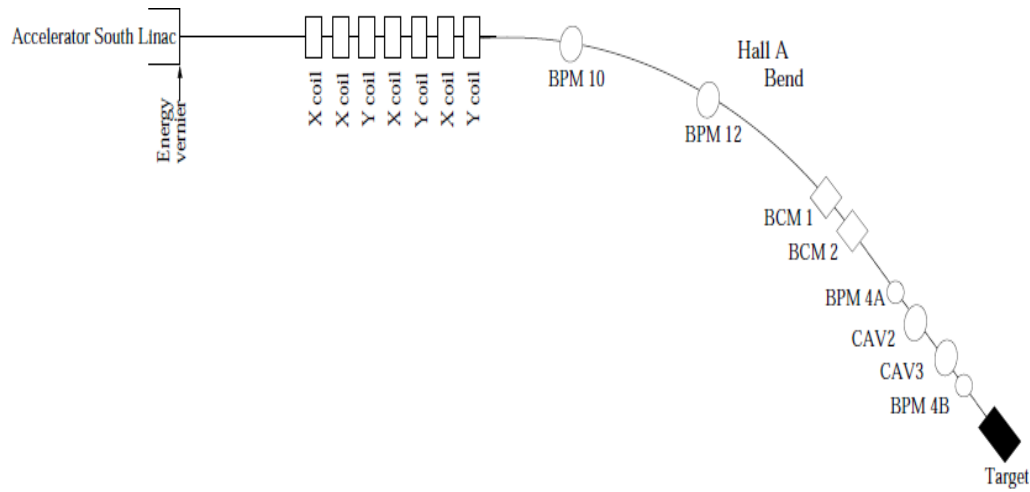


Figure 3.22: Schematic of Hall A beamline including seven coils of beam modulation.

Beam modulation system consists of seven magnetic coils (four X coils and three Y coils) located several meters upstream of the main bend in the Hall A beamline (after an energy vernier of a cryo-module in the south linac of the accelerator). The beam

modulation is capable of applying small changes in the beam position ( $\leq 300 \mu\text{m}$ ) and energy ( $\leq 300 \text{ keV}$ ) at the target. The energy vernier [36]<sup>8</sup> is the last activity in the south linac of the accelerator and affects all three experimental halls. However, an effort was made to ensure that the changes in energy has a minimal effect on the data taking in Hall B and Hall C. Since the beam modulation causes abrupt changes in beam position, the Fast Feedback, which maintains a steady beam position, in the accelerator had to be turned off during the procedure.

## 3.7 Targets

The lead/diamond (Pb/D) target used as a main target for PREX was carefully studied, manufactured, and tested. In 2008, the Pb/D target was tested in Hall A with the beam. Despite the successful results from the test run, we found that the Pb/D target could be damaged when exposed to the beam for extended periods of time. To have the Pb/D targets ready to use throughout the experiment, three Pb/D targets were prepared for the experiment(called #1, #2, and #3<sup>9</sup>). Besides Pb/D targets, other targets such as BeO viewer,  $^{181}\text{Ta}$ ,  $^{12}\text{C}$ , thin lead ( $^{208}\text{Pb}$ ), and water cell ( $\text{H}_2\text{O}$ ), were also used for optics/calibration studies,  $Q^2$  measurements, and studies of systematic errors.

### 3.7.1 Target Configurations

Fig. 3.23 and Fig. 3.24 illustrate target configurations for both optics/calibration and production phases of the experiment. The PREX target ladder had the optics sled at the top, followed by the Pb/D assembly, with auxiliary target ladder at the bottom. During the optics/calibration phase, the auxiliary target ladder consisted of a BeO viewer,  $^{181}\text{Ta}$ , thin  $^{12}\text{C}$ , and water cell. There was no liquid-He cooling during this

---

<sup>8</sup>The functions of the energy vernier are to stabilize the average energy of the emerging beam and to set the RF phases in the cavities in a way that minimizes the energy spread.

<sup>9</sup>#1 is the top assembly

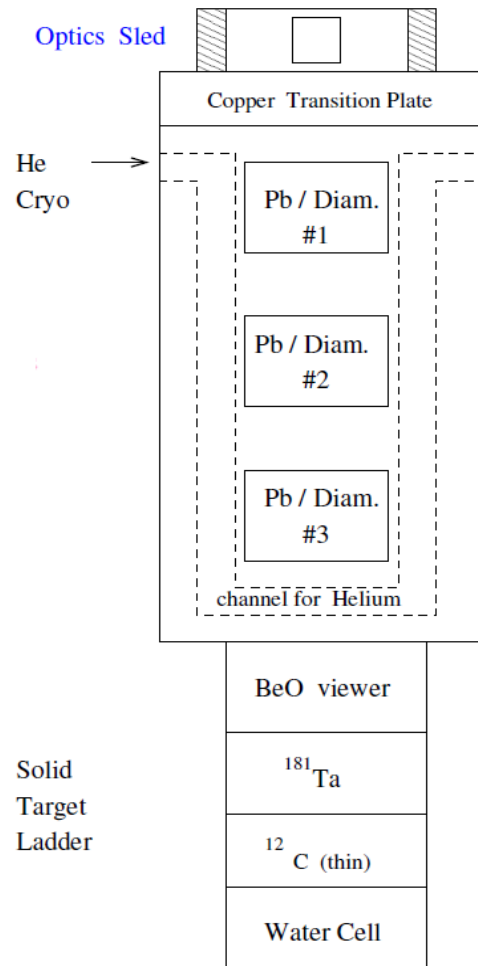


Figure 3.23: Target configuration during optics/calibration phase

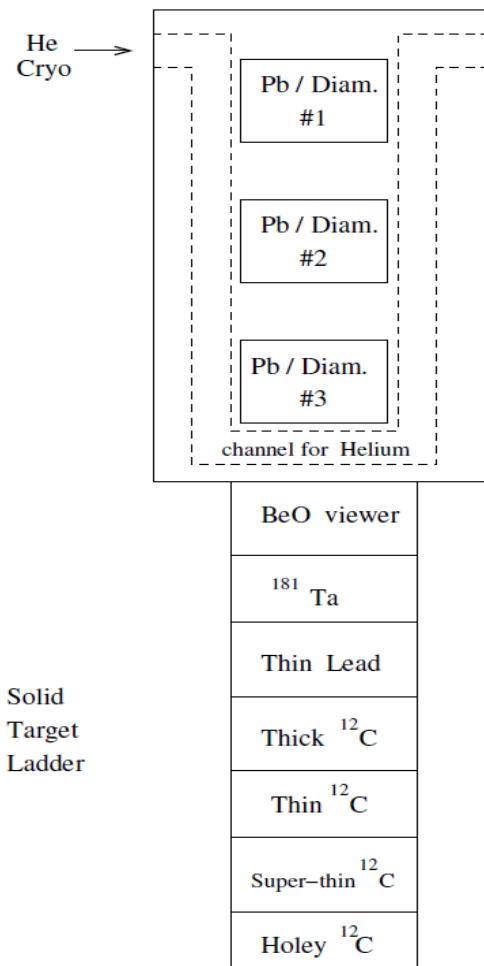


Figure 3.24: Target configuration during production phase

phase. After the optics commissioning, the auxiliary target ladder was removed and replaced with another ladder that had a BeO viewer,  $^{181}\text{Ta}$ , thin lead, thick  $^{12}\text{C}$ , thin  $^{12}\text{C}$ , super-thin  $^{12}\text{C}$ , and  $^{12}\text{C}$  hole target [50].

### 3.7.2 Lead/Diamond Target

Pure lead ( $^{208}\text{Pb}$ ) has a rather poor thermal conductivity ( $\sim 35.3 \text{ W}\cdot\text{m}^{-1}\cdot\text{K}^{-1}$ ) and a low melting point ( $\sim 600 \text{ K}$ ). This can lead to a major problem of overheating and melting of the target even with the liquid helium cooling. To increase the heat transfer capability, sheets of pure diamond ( $^{12}\text{C}$ ), which has significantly better thermal conductivity ( $\sim 900\text{-}2300 \text{ W}\cdot\text{m}^{-1}\cdot\text{K}^{-1}$ ) and higher melting point ( $\sim 3773 \text{ K}$ ), was used to help the heat flow in addition to the He cooling channel.

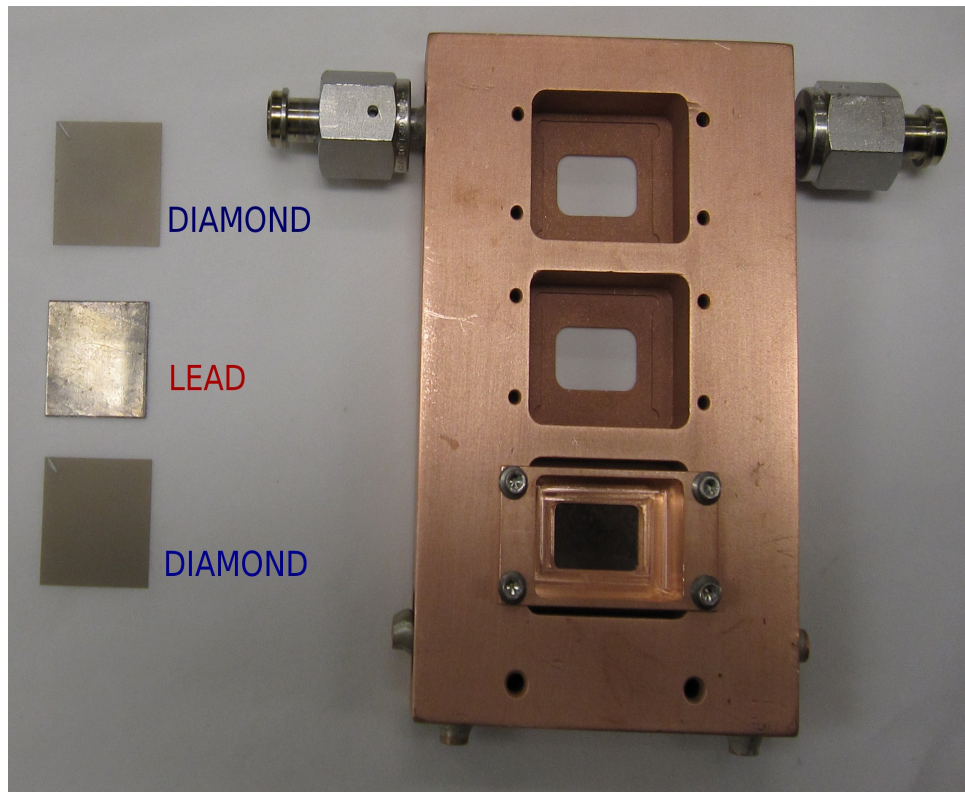


Figure 3.25: Lead/Diamond target configurations and the components

The lead/diamond (Pb/D) target was a stack of diamond + lead + diamond. The lead was isotopically pure  $^{208}\text{Pb}$ . The lead foil was 0.5 mm thick and was sandwiched between the two diamond foils. These foils were initially proposed to be approximately 0.15 mm thick. However, it was later decided to increase the thicknesses of the diamond foils of target #1 and #3 to improve the heat transfer. The

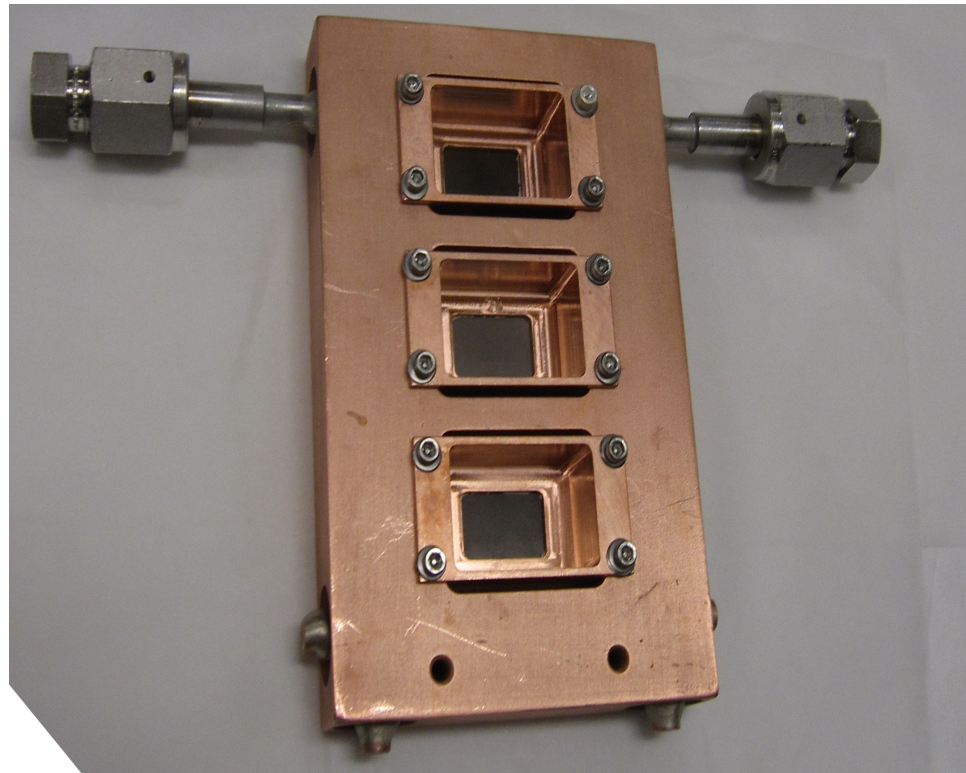


Figure 3.26: A completed Lead/Diamond target with He cooling tube. The liquid He flows around the target foils.

actual measurements of both lead and diamond are given in Table 3.2 and Table 3.3<sup>10</sup>. There were three Pb/D target slots to use for the entire experiment. The beam current limit of Pb/D target was  $100 \mu\text{A}$  and needed to have raster on when the beam current was above  $1 \mu\text{A}$ .

Target #	Mass (g)	Area ( $\text{mm}^2$ )	Average Thickness ( $\text{g}/\text{cm}^2$ )
1	3.223	$24.23 \times 24.08$	$0.552 \pm 0.001$
2	3.298	$23.52 \times 24.00$	$0.584 \pm 0.001$
3	3.223	$24.13 \times 24.13$	$0.554 \pm 0.001$

Table 3.2: Lead foils' mass and dimensions measurement

---

<sup>10</sup>Front side means facing the beam first.

Target #	Side	Mass (g)	Area (mm <sup>2</sup> )	Average Thickness (g/cm <sup>2</sup> )
1	front	0.467	25.40×25.40	0.072 ± 0.001
1	back	0.467	25.40×25.43	0.072 ± 0.001
2	front	0.257	25.35×25.37	0.040 ± 0.001
2	back	0.262	25.30×25.35	0.041 ± 0.001
3	front	0.292	25.40×25.40	0.045 ± 0.001
3	back	0.340	25.40×25.43	0.053 ± 0.001

Table 3.3: Diamond foils' mass and dimensions measurement

### 3.7.3 Other Targets

Besides Pb/D targets, several other targets were also used for optics commissioning,  $Q^2$  measurements, and systematic error studies. The BeO viewer<sup>11</sup> was used to get a visual spot of the beam on the target that could be seen on a monitor in the Hall A counting house. The water cell target was used for the precision measurement of the spectrometer angles, which will be described in detail in Chapter 4. There were two target ladders; water cell target ladder and standard solid target ladder. The water cell target ladder was only installed when the water cell was in operation (optics phase). The ladder had different spacing and positions to accommodate the water cell. The water cell had two thin windows made from stainless steel shim-stock. The following table gives the actual thickness of targets in water cell target ladder.

Target name	Material	Purity	Average Thickness (g/cm <sup>2</sup> )
BeO	BeO	99.0%	0.149 ± 0.001
Tantalum	<sup>181</sup> Ta	99.9%	0.122 ± 0.001
Super Thin C	<sup>12</sup> C	99.8%	0.009 ± 0.001
Water Cell	H <sub>2</sub> O	99.9%	~5 mm

Table 3.4: Characteristics of targets in water cell target ladder. The last column gives the average thickness of the target foil (average over the area of the foil)

The standard solid target ladder was installed for production running and included

<sup>11</sup>The Beryllium oxide (BeO) is capable of storing energy upon exposure to ionizing radiation. The energy is stored in the form of charge carriers trapped in defects in the crystalline structure of BeO and can be released by thermal or optical stimulation, providing the basis for use of the material as an ionizing radiation dosimeter [75].

varieties of lead and carbon targets. The Table 3.5 lists the solid targets and their thicknesses.

Target name	Material	Purity	Average Thickness (g/cm <sup>2</sup> )
BeO	BeO	99.0%	0.149 ± 0.001
Tantalum	<sup>181</sup> Ta	99.9%	0.122 ± 0.001
Thin Lead	<sup>208</sup> Pb		0.055 ± 0.001
Thick Carbon	<sup>12</sup> C	99.95%	0.442 ± 0.001
Thin Carbon	<sup>12</sup> C		0.027 ± 0.001
Super Thin Carbon	<sup>12</sup> C	99.8%	0.009 ± 0.001
Carbon Hole	<sup>12</sup> C	99.95%	0.084 ± 0.001

Table 3.5: Characteristics of targets in standard solid target ladder. The last column gives the average thickness of the target foil (average over the area of the foil)

The optics target, used during the optics phase, consisted of 5 carbon foils cut from the same sheet. The foils were 99.5% chemically carbon. Each foil was  $0.042 \pm 0.001$  g/cm<sup>2</sup>. Upstream face of each foil was located at 0 cm, ±7.5 cm and ±15 cm nominally (as measured from the target center) along the beam direction.

### 3.8 Luminosity Monitor

It was clear from the SLAC parity violating electron scattering experiments (E122 and E158) that a beam luminosity monitor is very important for high precision parity experiments. The luminosity monitor could help the experiment by:

- measuring the noise of electronics in the accelerator environment
- measuring the changes in beam parameters or target density

The luminosity monitor's sensitivity to beam parameters exceeds the sensitivity of the experiment, and the monitor is segmented to unfold the different parameters (position, angle, etc).

Each luminosity monitor used for PREX was made of quartz Cherenkov detectors. The quartz is radiation hard ( $\geq 1$  GRad) material, cut and polished into rectangular

bars attached via a light guide to well-shielded PMTs. There were two monitor stations, one at a “larger” angle ( $2^\circ$  for PREX), and another at a very small angle ( $\sim 0.5^\circ$  for PREX).

The large-angle monitor was exposed to a very high rate from low-energy particles. For PREX, the rate seen by this monitor was at least an order of magnitude higher than that seen by the main detector in the spectrometer, and therefore had a much smaller pulse-to-pulse noise due to counting statistics. This provided a stringent test on the ability of the electronics to measure a sufficiently small pulse-to-pulse noise of order 50 ppm in the accelerator environment.

The second, small-angle detector, was exposed primarily to higher energy particles. Thus it was more directly sensitive to beam position and angle. The small-angle detector was segmented into eight pieces placed symmetrically about the beam. The segmentation permitted us to unfold the different beam parameters (position, angle) in detail [45].

### 3.9 Septum Magnet

PREX measured parity-violating electroweak asymmetry at a scattering angle of  $5^\circ$ , however, due to size of the High Resolution Spectrometers (HRS), the minimum horizontal angle they can provide in the standard configuration is  $12.5^\circ$ . A pair of septum magnets was used to bend the scattered electrons from  $5^\circ$  into the HRS aperture at  $12.5^\circ$  for PREX.

The existing superconducting septum magnets in Hall A would not have worked at the high luminosity of PREX due to beam induced radiation heating of the superconducting coils. Since PREX required less than half the magnetic field in the septum compared to other experiments running at higher energies, an inexpensive normal conducting septum magnet with lower full field was used for PREX. This magnet was much more robust with respect to heat loads than the superconducting septa.

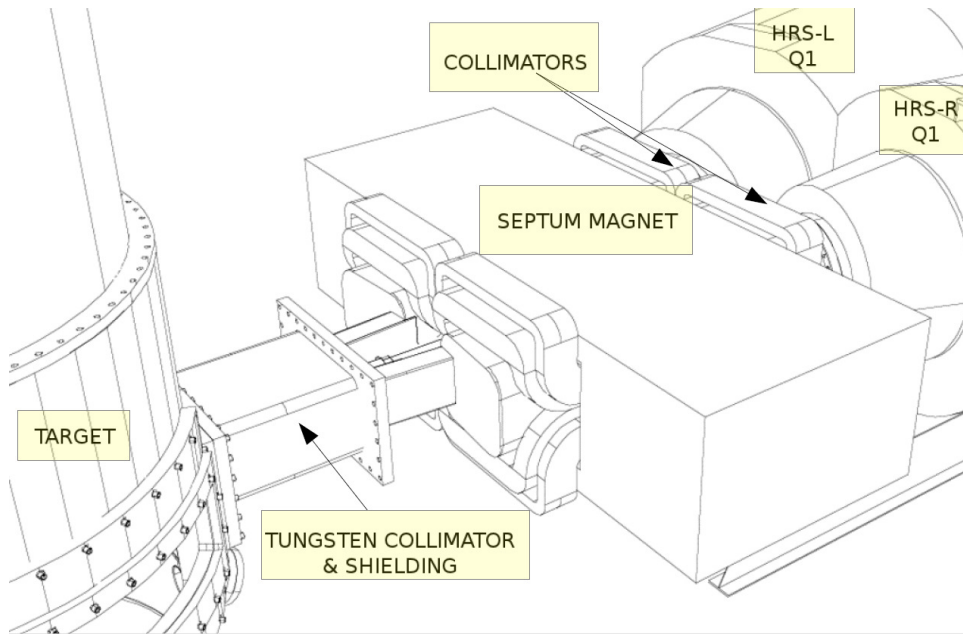


Figure 3.27: Septum magnets were installed between the target vacuum and the spectrometers.

The design was magneto-statically produced using TOSCA and resulting maps of the expected magnetic fields were used in a ray-tracing study to ensure that the hardware resolution needed to separate the elastic peak in lead from the the first excited state was achieved.

### 3.10 Collimator

For parity experiments, it is highly desirable to have symmetry in the apparatus as “seen” by electrons coming from the target. Ideally, the angle profiles should be identical on the left HRS and on the right HRS. Furthermore, there should be good up/down symmetry. These symmetries reduce systematic errors. A collimator pair installed in front of  $Q_1$  magnets was used to achieve these condition.

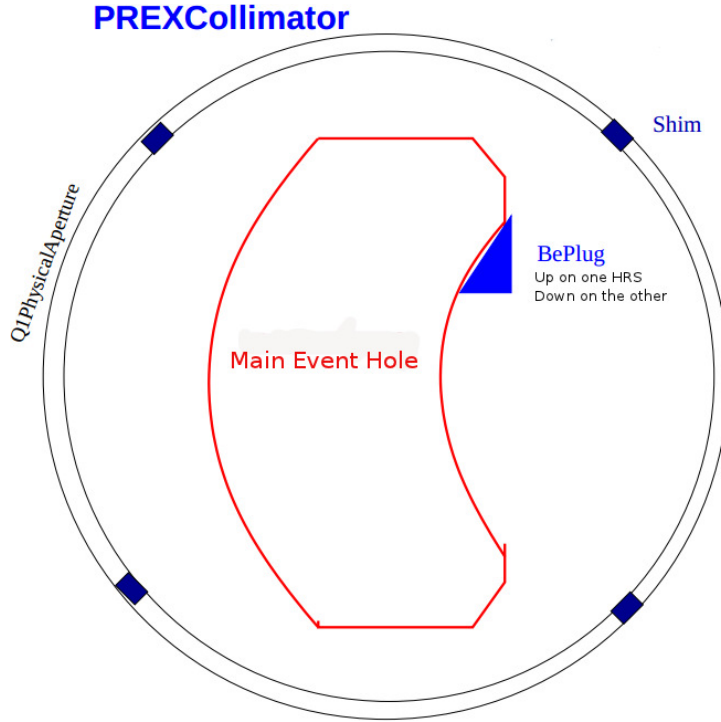


Figure 3.28: Conceptional drawing of the PREX collimators. The Be plug is shown near the top of the aperture of this collimator. It can be blocked by a remotely actuated tungsten plug.

Fig. 3.28 shows the PREX collimator for one HRS. One collimator had a Beryllium plug placed in the upper smaller-angle corner, while in the other collimator, a plug was placed in the lower smaller-angle corner. The most important requirement for the two collimators was that they had to be symmetric as much as possible, both left/right and up/down. The equivalent placement tolerance was  $\pm 1$  mm for the location of the center of the collimator [49].

### 3.11 High Resolution Spectrometers (HRS)

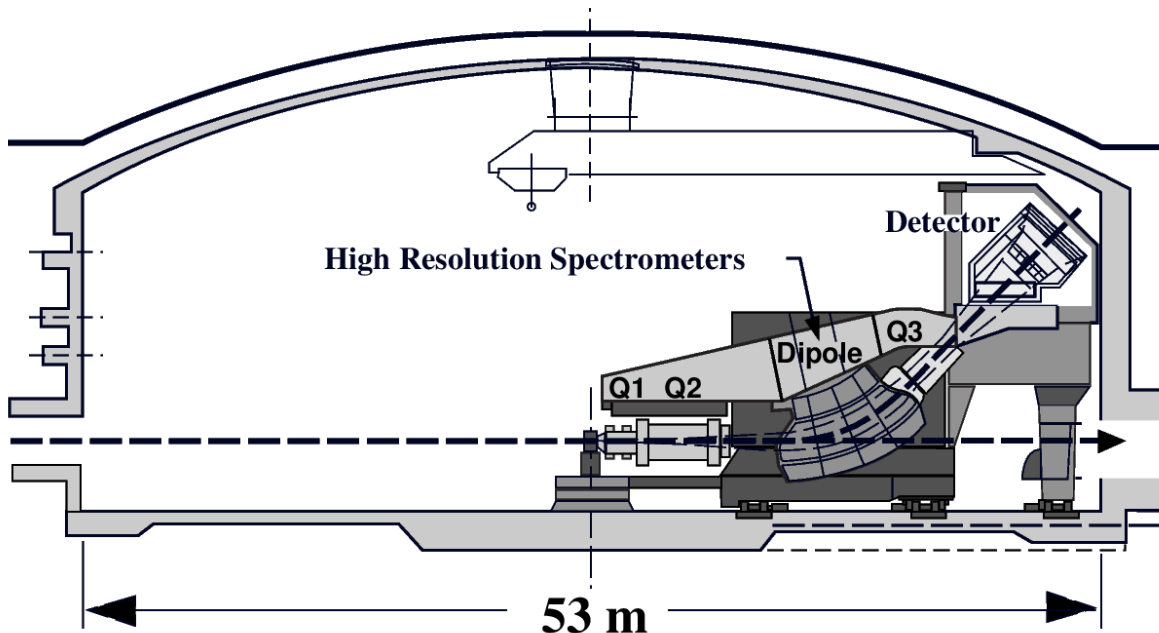


Figure 3.29: A cross sectional view of the experimental Hall A showing details of an HRS

#### 3.11.1 Magnets

Hall A consists of two identical 4 GeV spectrometers. Each vertically bending spectrometer has a combination of three quadrupoles(Q1, Q2, and Q3) and a dipole magnets to bend and to focus the electrons. The pair of superconducting  $\cos(2\theta)$  quadrupoles, Q1 and Q2, are followed by the 6.6 m long dipole magnet with focusing entrance and exit pole faces and including additional focusing from a field gradient, n, in the dipole. Following the dipole is the third superconducting  $\cos(2\theta)$  quadrupole, Q3. The second and third quadrupoles of each spectrometer are identical in design and construction because they have similar field and size requirements.

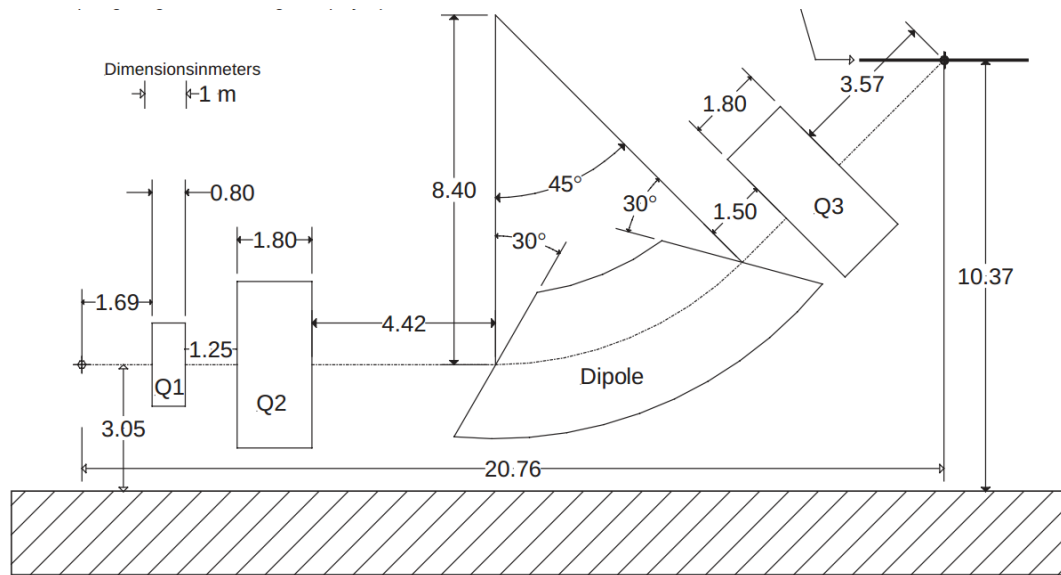


Figure 3.30: Schematic layout of a HRS device

Configuration	$\text{QQD}_n\text{Q}$ vertical bend
Bending angle	$45^\circ$
Optical length	23.4 m
Momentum range	0.3-4.0 GeV
momentum acceptance	$-4.5\% < \delta p/p < +4.5\%$
Momentum resolution	$1 \times 10^{-4}$
Dispersion at the focus (D)	12.4 m
Radial linear magnification (M)	-2.5
D/M	5.0
Angular range	
HRS-L	$12.5^\circ - 150^\circ$
HRS-R	$12.5^\circ - 130^\circ$
Angular acceptance	
Horizontal	$\sim \pm 30$ mrad
Vertical	$\sim \pm 60$ mrad
Angular resolution	
Horizontal	0.5 mrad
Vertical	1.0 mrad
Solid angle at $\delta p/p=0, y_0=0$	$\sim 6$ msr
Transverse length acceptance	$\pm 5$ cm
Transverse position resolution	1 mm

Table 3.6: Main design characteristics of the Hall A high resolution spectrometers; the resolution values are for the FWHM [6]

As stated in Table 3.6, the bending angle is  $45^\circ$ , which is a compromise between cost and performance. A larger bend angle would produce a better momentum resolution capability and a more favorable focal plane angle, ensuring a better momentum resolution at the extremes of the momentum acceptance. However, with a 4 GeV central momentum, the cost of a bending magnet, particularly in a spectrometer with a relatively large vertical acceptance, grows rapidly with bend angle. The  $45^\circ$  bending is the optimum choice for both considerations.

### 3.11.2 HRS Detectors

The HRS standard detector package was used for PREX calibration and  $Q^2$  determination runs.

#### Vertical Drift Chambers (VDC)

The VDCs for the HRS pair were constructed, commissioned, and installed by the Nuclear Interactions Group from MIT. Each HRS detector is equipped with a VDC package for the detection of particle tracks. A VDC package consists of two VDCs.

The lower VDC is located near the nominal focal surface. The second VDC is placed 50 cm downstream in the dispersive direction such that the nominal central ray of the spectrometer passes through the centers of both VDCs.

A VDC has two wire planes made of 20- $\mu\text{m}$  thin conducting wires [13]. Each wire plane is between two conducting planes (cathodes), separated by 2.6 cm. The cathode surface is kept at a negative high voltage, while the wires are maintained at ground voltage, thus results in the drift electric field that guides electrons towards wires. Near the wire, the field is radial and increase as  $\frac{1}{r}$ . Away from the wire, the field is parallel and uniform. When a charged particle travels through the chamber, it ionizes the gas inside and leaves behind a track of electrons and ions along its way. The total number of electron-ion pairs produced depends on the ionization properties

of the gas and is proportional to the amount of energy deposited [40].

In the electric field of the drift cell, the liberated electrons accelerate towards the wire along the field lines. However, this acceleration does not result in increasing the average drift velocity since an electron loses the acquired energy as it collides with the gas atoms. In the strong electric field very close to the thin wire, an electron gathers enough energy between two collisions to ionize another gas atom. This creates an avalanche effect, with the number of electrons multiplying at each collision. As the avalanche approaches the wire, the positive ions drift away from the wire. The depletion of positive ions from the vicinity of the wire induces a detectable negative signal on the wire.

The VDCs are operated at 4.0 kV with a chamber gas mixture of 65% Argon and 35% Ethane.

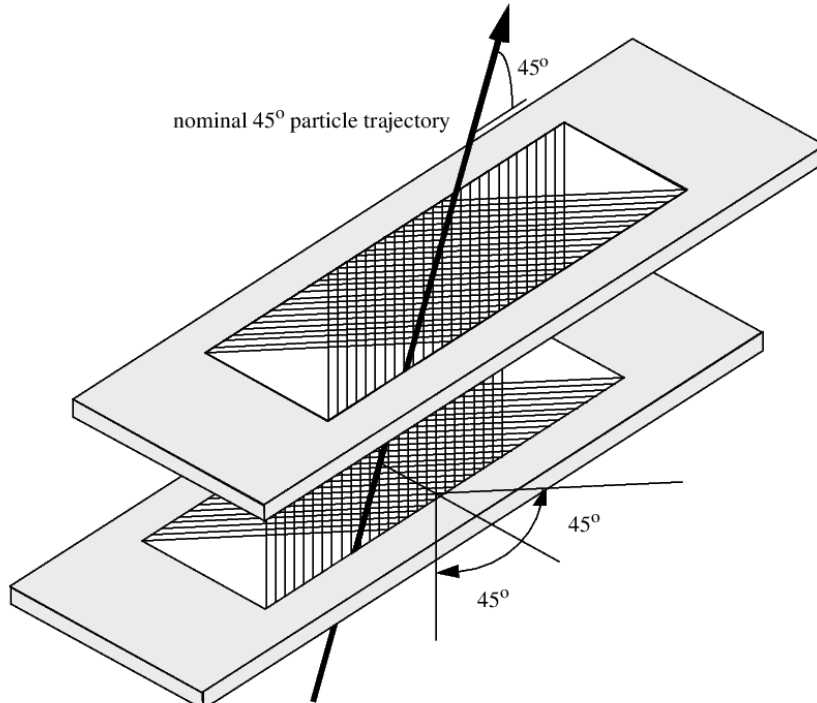


Figure 3.31: VDC schematic layout

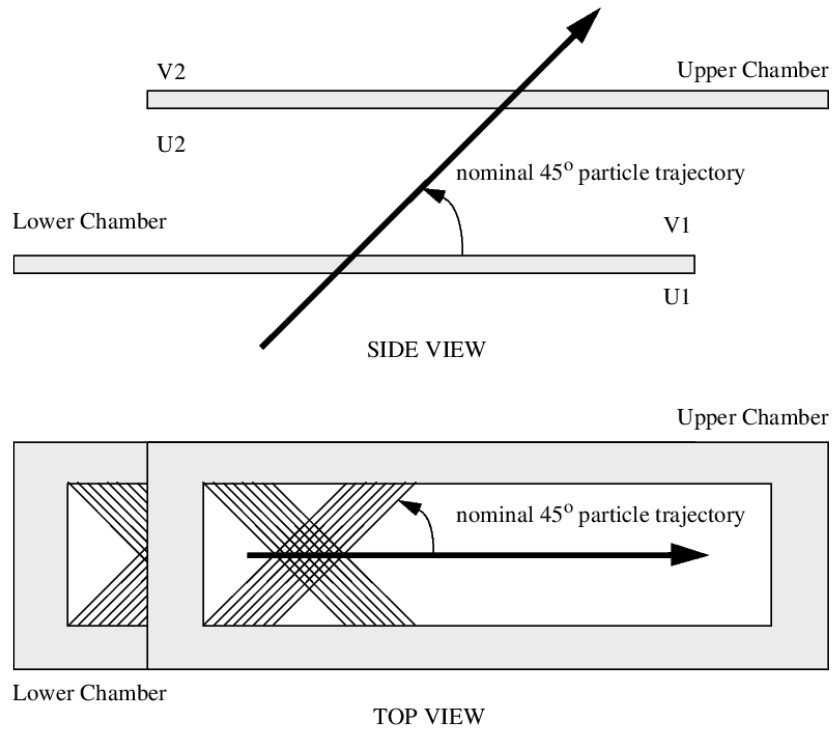


Figure 3.32: VDC location as seen from side view and top view

### Trigger

The main spectrometer trigger, used occasionally during PREX for optics calibration,  $Q^2$  measurements, and spot++, was from scintillators in each spectrometer. The first scintillator, S0, was placed horizontally just above the VDCs. This trigger was called T1. The second scintillator, S1, was placed above the quartz detector with  $45^\circ$  orientation, and thus perpendicular to central ray of scattered electrons. The trigger from S1 was called T5. T5 was used most of the  $Q^2$  runs during the experiment.

S1 scintillator consists of six plastic scintillator paddles. The paddles are arranged in such a way that their long axes are perpendicular to the spectrometer dispersive direction. A 5 mm overlap of the neighboring paddles is used to ensure the complete coverage of the plane. A photo-multiplier tube is mounted on either end of each paddle.

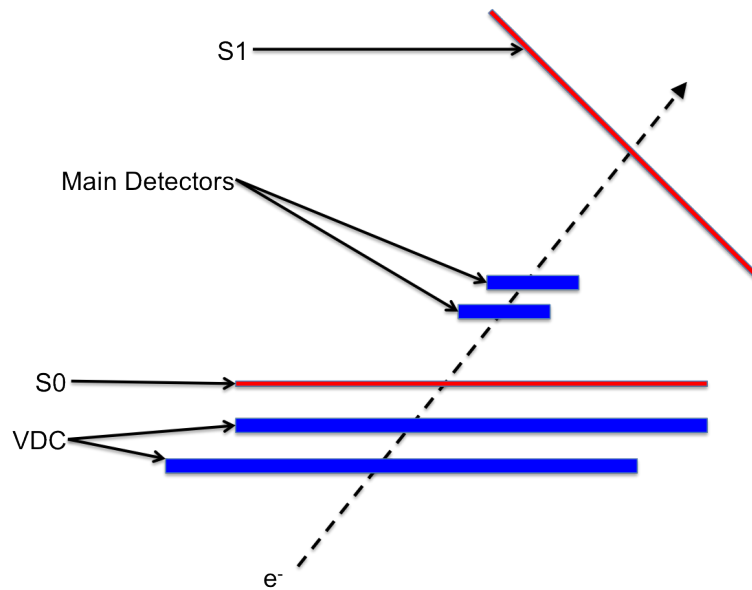


Figure 3.33: HRS layout showing the location of main triggers, S0 and S1.

### PREX Detector (Quartz Detector)

PREX used quartz detectors to collect the asymmetry information. These detectors were based on the principle that when scattered electrons enter the absorber, they would start an electromagnetic shower. When the secondary charged particles of the shower go across the optical medium, they radiate Cherenkov photons, which travel to the photomultiplier tube (PMT) resulting in signals that are processed by the DAQ system. The total light flux was integrated over a helicity window.

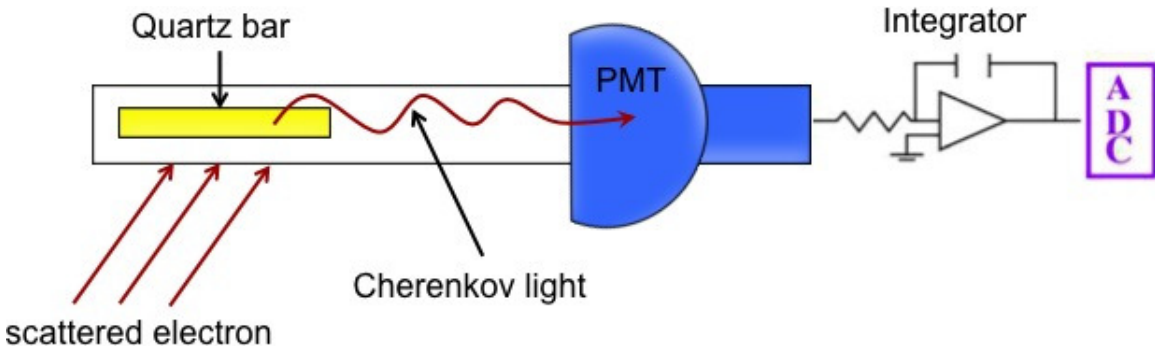


Figure 3.34: The schematic of quartz detectors principle

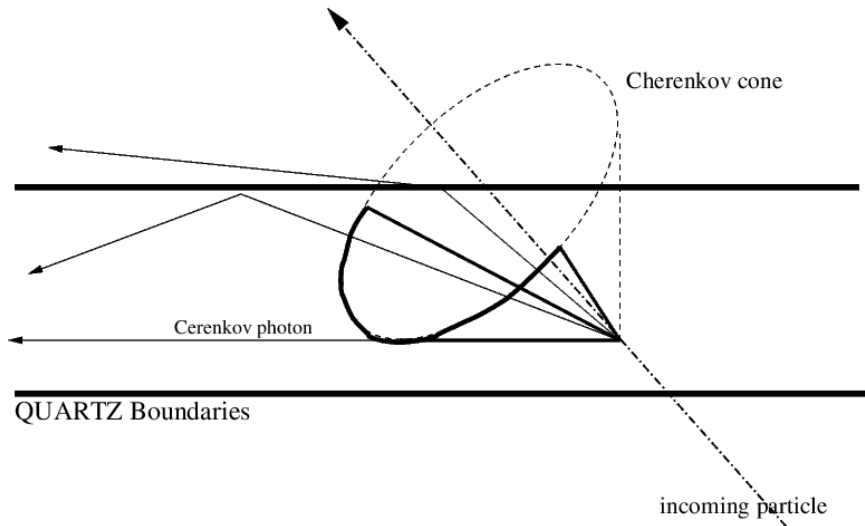


Figure 3.35: Cherenkov cone of electrons in the quartz. Bold area delimits the arc of the cone which contributes to the PMT signal

Quartz detectors consisted of a thin bar of silicon dioxide,  $\text{SiO}_2$ , or “quartz” as the radiating element. This was different from the HAPPEX-I detector, which was a sandwich of lead and lucite, because of the much higher radiation levels in PREX and the concern that the lucite would turn yellow and degrade the performance

Each HRS consisted of two quartz detectors. Each quartz detector had a  $14\text{cm} \times 3.5\text{cm}$  active area and a 0.6 cm (1 cm) thickness for lower (upper) quartz detector. Both quartz detectors were parallel to the VDC planes with a distance of  $52.0$  ( $23.0$ )  $\pm 0.3$  cm, measured from the lower edge of the lower quartz detector to the top plane of VDC, for the first (second) half of the experiment. The distance between the two detectors was kept at 10 cm [44].

### 3.12 Data Acquisition System (DAQ)

The PREX data acquisition (DAQ) system is unique from the standard Hall A DAQ since PREX required high precision measurements of signals integrated over a helicity pulse (8.33 ms), or over a fraction as small as  $1/20^{th}$  of a helicity pulse, this latter

case is called “oversampling”. The signals consisted of PMT outputs from detectors (current sources) or a voltage levels (voltage sources) from various devices such as beam position monitors (BPM) or beam current monitors (BCM). The reason for using signal integration as opposed to signal counting was that in order to see the small parity violating signal in a reasonable amount of beam time, the event rate has to be very high (GHz range). This required rate is far too high to count individual events, so the integration of the signals had to be used.

Quantity	Specification
Bit Resolution	18 bits
Rate Capacity	10 kHz
Input Signals	PMT signals (current) or Voltages
input Polarity	One sign, but reversible
Gain Adjustment	Factor of 100
Max Input (Low Gain)	10 V
Differential Nonlinearity	$\leq 2 \times 10^{-5}$
Integral Nonlinearity	$\leq 5 \times 10^{-5}$
Pedestal Noise	$\leq 100 \mu\text{V}$ or $\leq 2.5 \text{ ADC chan FWHM}$

Table 3.7: ADC specifications for PREX

The integrated ADCs were designed to achieve high resolution (18 bits) with small nonlinearity. Each ADC channel consisted of an input amplifier, an integrating circuit, two sample-and-hold circuits, a difference amplifier, a summing circuit, and a 16 bit ADC chip. The input amplifier converted the input voltage to a scaled current which was integrated in the next stage; for current signals such as PMT outputs, this amplifier stage was bypassed and the signal was integrated directly. The integrator output was sampled and held once  $700 \mu\text{s}$  after the beginning of the helicity pulse, and again 32 ms later near the end of the pulse, for non-oversampling mode. This timing was determined by an external ADC Timing Board built by the JLAB Electronics Group. The difference between these two signals was the integrated result. To achieve the nonlinearity specification, a pseudo-random DAC voltage (“DAC noise”) was added to this integrated result prior to digitization by the ADC, then subtracted

later in analysis. The DAC noise smeared the data over many ADC channels, this reduced systematic errors from bit resolution [48].

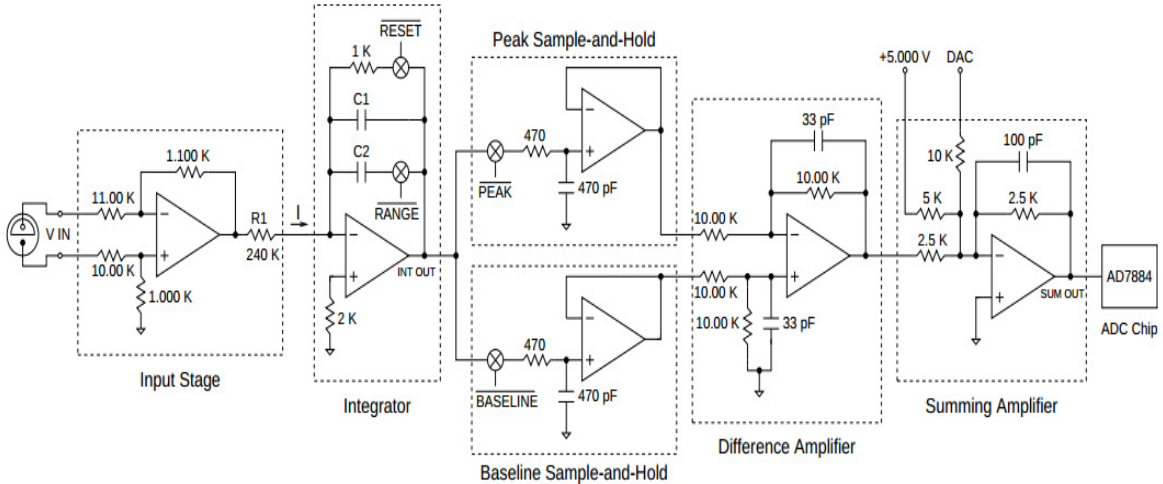


Figure 3.36: Circuit diagram of one channel of the 16 bit integrating ADC

The DAQ was controlled by a VME computer using the JLAB DAQ software CODA. The VME controller handled communication between the DAQ and other system parameters. The counting-house crate was used to control the intensity feedback, RWP scans, and beam modulation. The DAQ also recorded many EPICS variables (which were recorded on a 4 s timescale) into the data stream such as the status of the polarized source optics, accelerator systems, target and raster parameters, septum and HRS magnet properties, and detector HV.

### 3.13 Contributions of Author to the Experiment

In addition to extensive involvement in daily planning, taking shifts, and collaborating with other JLAB staff, the author was also involved in hardware installation during the experiment and played a major role in data analysis after the experiment.

### 3.13.1 Contributions to Hardware Installations

The concern that the high rate in detectors ( $>500$  MHz) might cause a reduction in VDC efficiency led to a second, back-up plan to measure positions and angles of scattered electrons during  $Q^2$  runs. Under this back up scheme, two sets of Gas Electron Multiplier (GEM) [61] detectors were installed, above the VDCs, to be used in case the VDCs did not perform well. This was the very first time GEM detectors were part of an experiment in Hall A. The GEM detectors are capable of running at much higher rate compared to wire chambers and also have high spatial resolution. However, it was found out after the analysis that the VDCs performed reasonably well when the trigger rates were under 100 kHz. Thus, the results from GEM detectors were not used for  $Q^2$  measurement and other kinematic analysis. Nonetheless, the GEM data collected showed the feasibility for using GEMs in this future higher-rate experiments.

### 3.13.2 Contributions to Data Analysis

The author performed all of the kinematic analysis for PREX; this included the analysis of  $Q^2$  measurements, spectrometer calibrations, background analysis, and finite acceptance of the spectrometers. The details of each analysis task will be presented in Chapter 4.

## 3.14 The Summary of Experimental Procedures

The PREX measurement was carried out in Hall A at the Jefferson Lab. A 50 to 70  $\mu\text{A}$  continuous-wave beam of longitudinally polarized 1.06 GeV electrons was incident on a 0.5 mm thick isotopically pure  $^{208}\text{Pb}$  target foil. Two 150  $\mu\text{m}$  diamond foils sandwiched the lead foil to improve thermal conductance to a copper frame cooled to 20K with cryogenic helium. Also, a 4 mm  $\times$  4 mm square beam raster reduced the

probability for target melting.

The polarized electron beam originated from a strained GaAsP photocathode illuminated by circularly polarized light. The sign of laser circular polarization determined the electron helicity; this was held constant for periods of 8.33 ms, referred to as “windows”. The accelerated beam was directed into Hall A, where its intensity, energy, polarization, and trajectory on target were inferred from the responses of several monitoring devices. The addition of a pair of dipole septum magnets between the target and the HRSs allowed us to achieve a forward scattering angle of  $\theta_{lab} \sim 5^\circ$ . Elastically scattered electrons were focused onto thin quartz detectors in the twin HRSs. The momentum resolution ensured that only elastic events (and a negligible fraction of inelastic events from the 2.6 MeV first excited state) were accepted by the quartz detectors. This would create Cherenkov light from each quartz bar. The Cherenkov light then traversed through air light guides and were detected by quartz-window photomultiplier tubes (PMT).

The integrated responses of detector PMTs and beam monitors were digitized by an 18-bit ADC and recorded for each window. Two “window quadruplet” patterns of helicity states (+ - - + or - + + -) ensured complementary measurement at the same phase relative to the 60 Hz line power, thus canceling power-line noise from the asymmetry measurement. The right-left helicity asymmetry in the integrated detector response, normalized to the beam intensity, was computed for sets of complementary helicity windows in each quadruplet to form the raw asymmetry  $A_{raw}$ . The sequence of these patterns was chosen with a pseudo-random number generator [2].

## Chapter 4

# Data Analysis

PREX measured the parity-violating electroweak asymmetry in the elastic scattering of polarized electrons off a  $^{208}\text{Pb}$  target. Since the expected asymmetry was of the order of a few hundred ppb, PREX required careful data analysis in order to extract useful and accurate information. This chapter discusses the details of spectrometer calibration, the determination of the central 4-momentum transfer squared ( $Q^2$ ), and the determination of background contamination. Also included in this chapter are the analyses of asymmetry and its corrections, and the calculation of weak charge radius and neutron radius.

### 4.1 High Resolution Spectrometer (HRS) Calibrations

Direction and final momentum of scattered electrons were measured using the two high resolution spectrometers (HRSs) in Hall A. In order to have accurate information, the two HRSs had to be calibrated. In the past, the two HRSs had been calibrated in their standard (no septum) configuration with a momentum resolution (FWHM) of  $1 \times 10^{-4}$  and angular resolutions (FWHM) of  $0.034^\circ$  ( $0.114^\circ$ ) for horizontal (vertical) angle. However, with the addition of septum magnets, the HRSs needed to be recalibrated. The calibration involved two main processes:

1. spatial and angular ( $y_{tg}$ ,  $\theta_{tg}$ , and  $\phi_{tg}$ ) calibration
2. momentum ( $\delta_{tg}$ ) calibration

For each event, four focal plane variables<sup>1</sup> are measured at the focal plane of the spectrometer. The position of the particle and the tangent of the angle made by its trajectory along the dispersive direction are given by  $x_{fp}$  and  $\theta_{fp}$ , while  $y_{fp}$  and  $\phi_{fp}$  give the position and tangent of the angle perpendicular to the dispersive direction. These variables are used to determine  $\theta_{tg}$ ,  $y_{tg}$ ,  $\phi_{tg}$ , and  $\delta_{tg}$ <sup>2</sup> at the target.

The relationship between the focal plane variables and target variables is expressed in a matrix form (in first-order approximation) with a Transport Tensor linking the two systems.

$$\begin{bmatrix} \delta_{tg} \\ \theta_{tg} \\ y_{tg} \\ \phi_{tg} \end{bmatrix} = \begin{bmatrix} < x_{fp} | x_{fp} > & < x_{fp} | \theta_{fp} > & 0 & 0 \\ < \theta_{fp} | x_{fp} > & < \theta_{fp} | \theta_{fp} > & 0 & 0 \\ 0 & 0 & < y_{fp} | y_{fp} > & < y_{fp} | \phi_{fp} > \\ 0 & 0 & < \phi_{fp} | y_{fp} > & < \phi_{fp} | \phi_{fp} > \end{bmatrix} \cdot \begin{bmatrix} x_{fp} \\ \theta_{fp} \\ y_{fp} \\ \phi_{fp} \end{bmatrix}. \quad (4.1)$$

The null tensor elements result from the mid-plane symmetry of the spectrometer.

In practice, the expansion of the focal plane coordinates was performed up to the fifth order<sup>3</sup>. A set of tensors  $Y_{jkl}$ ,  $T_{jkl}$ ,  $P_{jkl}$ , and  $D_{jkl}$  link the focal plane variables to

---

<sup>1</sup>See more details of Hall A coordinate systems in Appendix A

<sup>2</sup> $\delta = \frac{P - P_0}{P}$  where  $P_0$  is the central momentum of the spectrometer

<sup>3</sup>Higher orders might cause the oscillation of the optimized variables.

target variables as:

$$y_{tg} = \sum_{j,k,l} Y_{jkl} \theta_{fp}^j y_{fp}^k \phi_{fp}^l \quad (4.2)$$

$$\theta_{tg} = \sum_{j,k,l} T_{jkl} \theta_{fp}^j y_{fp}^k \phi_{fp}^l \quad (4.3)$$

$$\phi_{tg} = \sum_{j,k,l} P_{jkl} \theta_{fp}^j y_{fp}^k \phi_{fp}^l \quad (4.4)$$

$$\delta_{tg} = \sum_{j,k,l} D_{jkl} \theta_{fp}^j y_{fp}^k \phi_{fp}^l \quad (4.5)$$

where the superscripts denote the power of each focal plane variable. The tensors  $Y_{jkl}$ ,  $T_{jkl}$ ,  $P_{jkl}$ , and  $D_{jkl}$  are polynomials in  $x_{fp}$  as:

$$Y_{jkl} = \sum_{i=1}^m Y_{jkl,i} x_{fp}^i \quad (4.6)$$

$$T_{jkl} = \sum_{i=1}^m T_{jkl,i} x_{fp}^i \quad (4.7)$$

$$P_{jkl} = \sum_{i=1}^m P_{jkl,i} x_{fp}^i \quad (4.8)$$

$$D_{jkl} = \sum_{i=1}^m D_{jkl,i} x_{fp}^i \quad (4.9)$$

To perform the calibration, one needs a sieve slit collimator to serve as a reference of particle tracks before they enter the spectrometer. For PREX, the sieve slits were made of 5-mm thick stainless steel plates and were placed in front of the septum magnets with the distance  $L$  of 798.02 (796.64) mm for left (right) HRS measured from the ideal target location to the central hole of the sieve slit<sup>4</sup>.

---

<sup>4</sup>We defined the spectrometer axis as a line passing from the ideal target location to the central sieve slit hole.

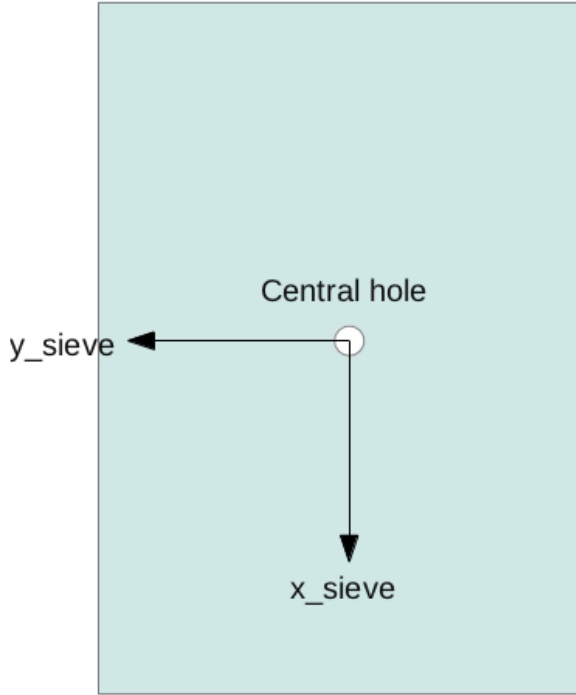


Figure 4.1: Sieve slit coordinate system used in optics reconstruction

Fig. 4.2 shows the sieve slit used in PREX. The central hole was defined as (0,0). To be consistent with the target coordinate system (TCS), the following sieve-slit coordinates were defined<sup>5</sup>:

1. The origin (0,0) was at the central sieve slit hole
2.  $y_{sieve}$  was pointing horizontally to the left
3.  $x_{sieve}$  was pointing vertically down, along the dispersive direction.

#### 4.1.1 Spatial and Angular Calibration

In general, the basic spatial and angular variables ( $y_{tg}$ ,  $\theta_{tg}$ , and  $\phi_{tg}$ ) do not form a good set of variables to work with. For a foil target not located at the origin of the target coordinate system,  $y_{tg}$  varies with  $\phi_{tg}$ . In the case of a multi-foil target,  $\phi_{tg}$  calculated for a given sieve slit hole depends on  $y_{tg}$ . Also, all three variables depend on

---

<sup>5</sup>As seen from the front of the sieve slit

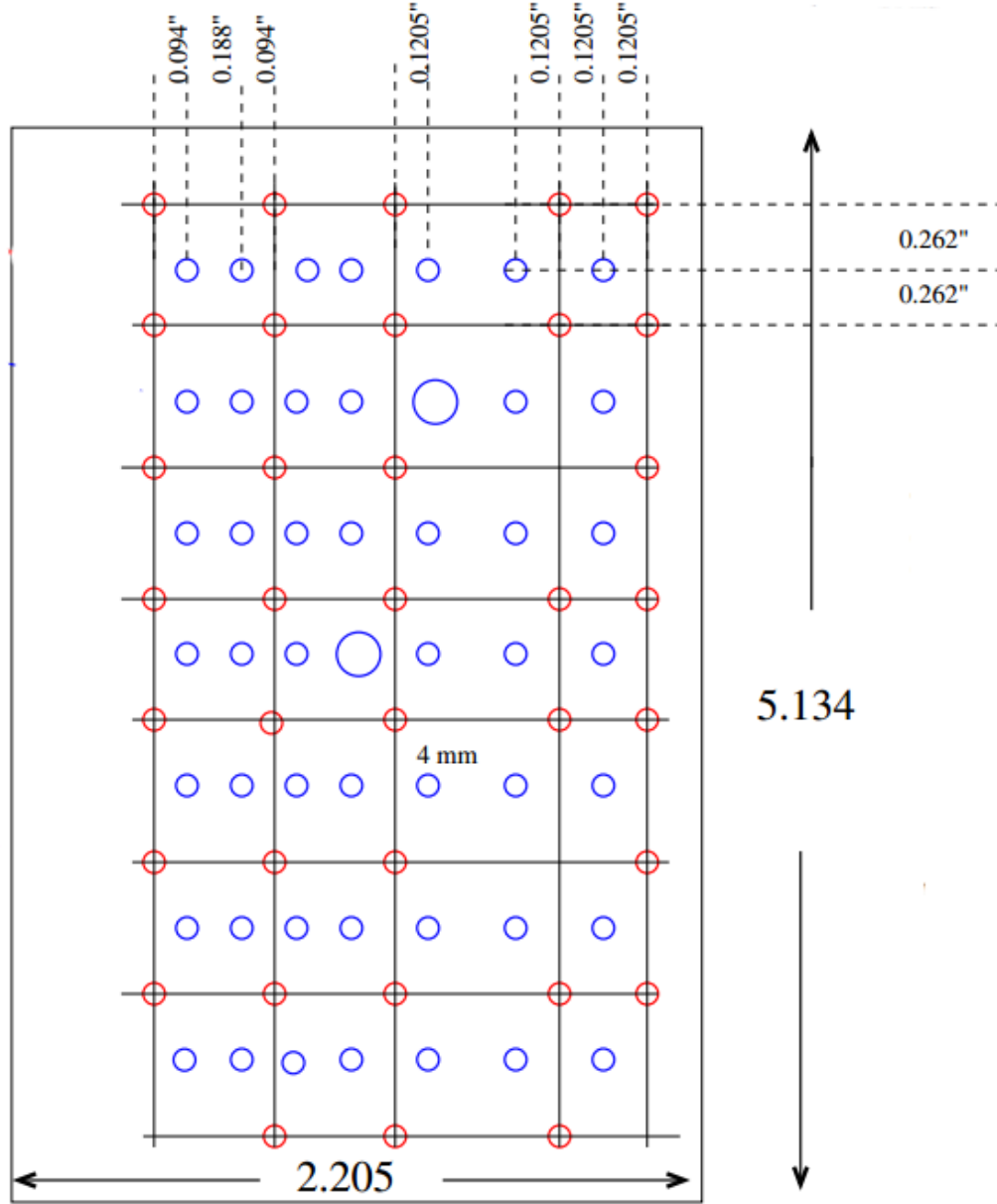


Figure 4.2: PREX sieve slit used for optics reconstruction (units shown in inches). The two bigger holes are for the ability to identify the orientation of reconstructed data

the beam positions ( $x_{beam}$  and  $y_{beam}$ <sup>6</sup>). Another important quantity is the interaction position along the beam,  $z_{react}$ .  $z_{react}$  is crucial for extended targets, but since PREX used a single thin  $^{208}\text{Pb}$  as a target, the calibration of  $z_{react}$  was less important than  $y_{tg}$ ,  $\theta_{tg}$ , and  $\phi_{tg}$  and was checked to be close to zero.

<sup>6</sup>The beam positions are measured in the hall coordinate system (HCS)

Equations that relate sieve-slit variables to target variables are:

$$z_{react} = -(y_{tg} + D) \frac{\cos(\phi_{tg})}{\sin(\theta_0 + \phi_{tg})} + x_{beam} \cot(\theta_0 + \phi_{tg}) \quad (4.10)$$

$$y_{sieve} = y_{tg} + L \tan(\phi_{tg}) \quad (4.11)$$

$$x_{sieve} = x_{tg} + L \tan(\theta_{tg}) \quad (4.12)$$

where  $\theta_0$  is the spectrometer central angle,  $L$  is the distance from target location to central sieve slit hole, and  $D$  is the distance of the actual target location to ideal target location. The vertical coordinate  $x_{tg}$  in the TCS is calculated using the beam position in the vertical direction  $y_{beam}$ , vertical displacement of the spectrometer from its ideal position,  $\theta_{tg}$ , and  $z_{react}$ .

For PREX, Eq. 4.10-4.12 can be rearranged to:

$$\theta_{tg} = \tan^{-1} \left( \frac{x_{sieve}}{L} \right) \quad (4.13)$$

$$\phi_{tg} = \tan^{-1} \left( \frac{y_{sieve} - x_{beam} \cos(\theta_0) + D}{L - x_{beam} \sin(\theta_0)} \right) \quad (4.14)$$

$$y_{tg} = y_{sieve} - L \left( \frac{y_{sieve} - x_{beam} \cos(\theta_0) + D}{L - x_{beam} \sin(\theta_0)} \right) \quad (4.15)$$

These equations assume that  $Z_{react}$  and  $x_{tg}$  are zero.

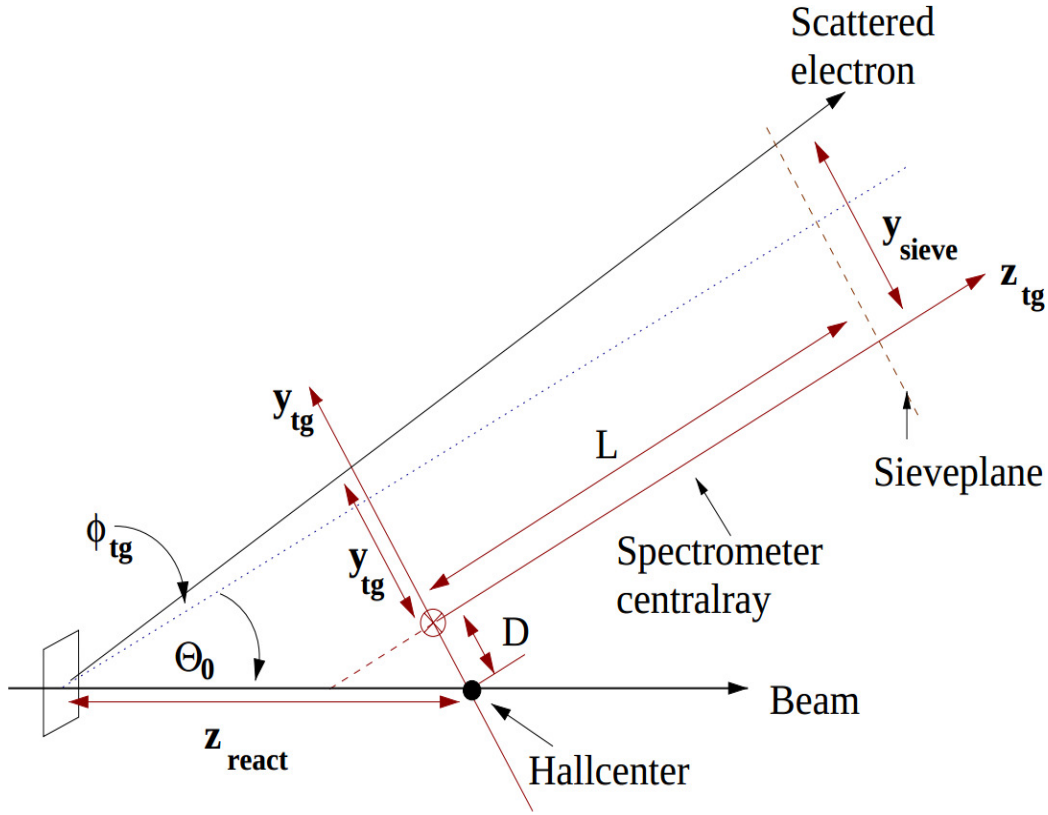


Figure 4.3: Target coordinate system (TCS) for left HRS.  $L$  is the distance from Hall center to the sieve plane, while  $D$  is the horizontal displacement of the spectrometer axis from its ideal position. Spectrometer central angle is denoted by  $\Theta_0$ . Note that  $x_{\text{tg}}$  and  $x_{\text{sieve}}$  are vertically down (into the page)

The procedures to perform the spatial and angular calibrations are described in Appendix B.1.

Fig. 4.4 and Fig. 4.5 show the sieve patterns after the angular calibration. The cross points between vertical and horizontal lines are the expected location of sieve holes. By comparing the average locations with the expected values, the average uncertainties for angular reconstruction are calculated.

HRS	$\sigma_{\theta_{\text{tg}}}$	$\sigma_{\phi_{\text{tg}}}$
Left	$0.066^\circ$ (1.2 mrad)	$0.017^\circ$ (0.3 mrad)
Right	$0.091^\circ$ (1.6 mrad)	$0.011^\circ$ (0.2 mrad)

Table 4.1: Angle errors obtained after angular calibration

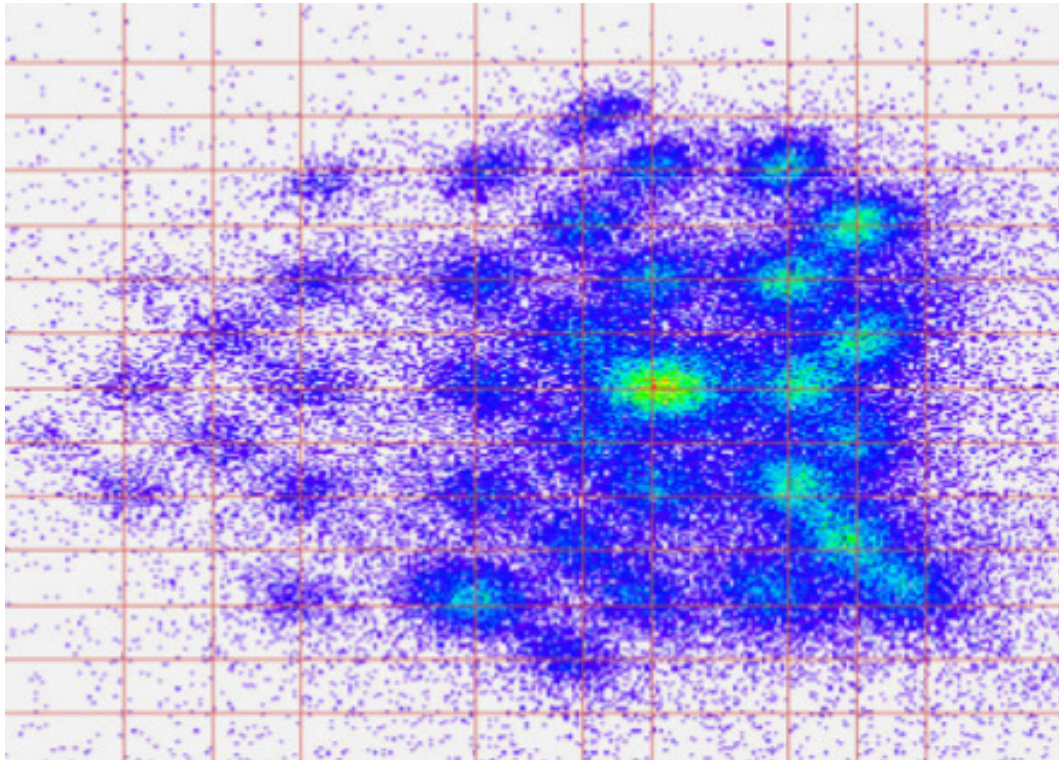


Figure 4.4: Optimized  $\theta_{tg}$  vs  $\phi_{tg}$  sieve patterns for left HRS.

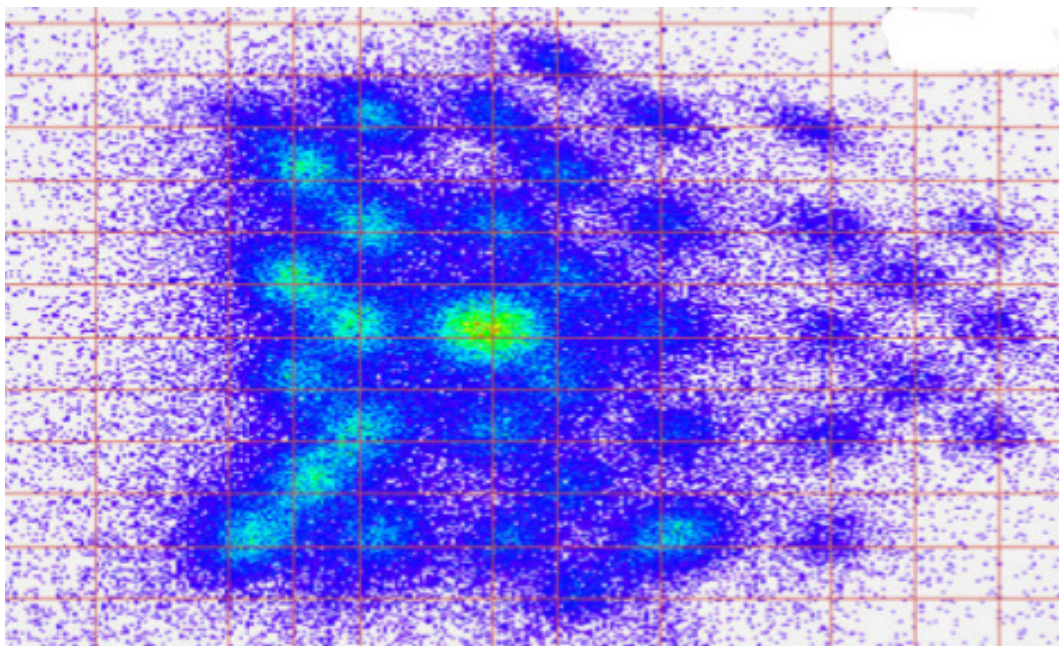


Figure 4.5: Optimized  $\theta_{tg}$  vs  $\phi_{tg}$  sieve patterns for right HRS.

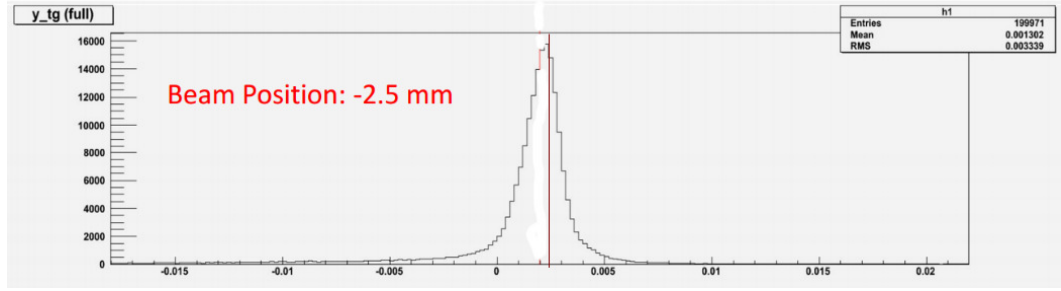


Figure 4.6: Optimized  $y_{tg}$  histogram for left HRS. The horizontal beam position used for this particular run was -2.5 mm (in HCS)

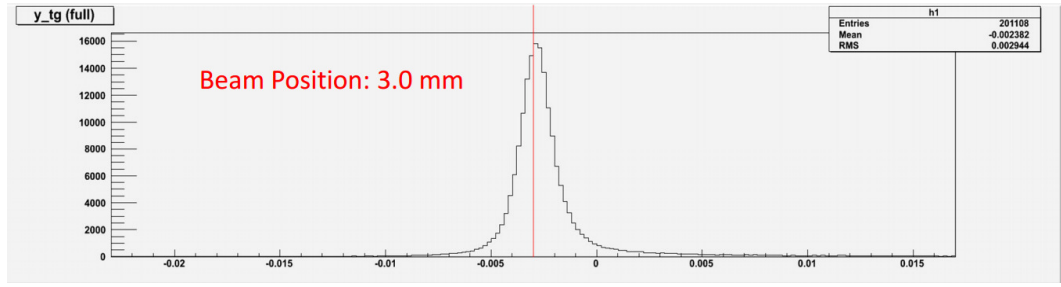


Figure 4.7: Optimized  $y_{tg}$  histogram for right HRS. The horizontal beam position used for this particular run was 3 mm (in HCS)

Fig. 4.6 and Fig. 4.7 shows the  $y_{tg}$  histograms for both HRSs. The vertical red lines are the expected location of  $y_{tg}$ . One can see that  $y_{tg}$  is closely related to the horizontal beam position, as expected from the condition that  $Z_{react} = 0$ .

#### 4.1.2 Momentum Calibration

In order to extract the final momentum of scattered electrons ( $\delta_{tg}$ ) with the required accuracy, the momentum calibration had to be performed for each HRS. The calibration could be done with or without the sieve slit inserted. However, the advantage of having the sieve slit inserted is that the momentum calibration is independent from spatial and angular reconstruction, which reduces the uncertainty significantly. On the other hand, the multiple scattering at the edges of sieve holes could reduce the momentum resolution. The procedure to perform momentum calibration are described in Appendix B.2.

After the calibration, the quality of momentum reconstruction across the focal plane could be checked by measuring the energy difference between the ground state and the first excited state of  $^{12}\text{C}$  ( $\Delta E_C$ ) at three different central momentum settings of the spectrometer and compareing it to the well-measured value of  $\Delta E_C = 4.442 \pm 0.001$  MeV.

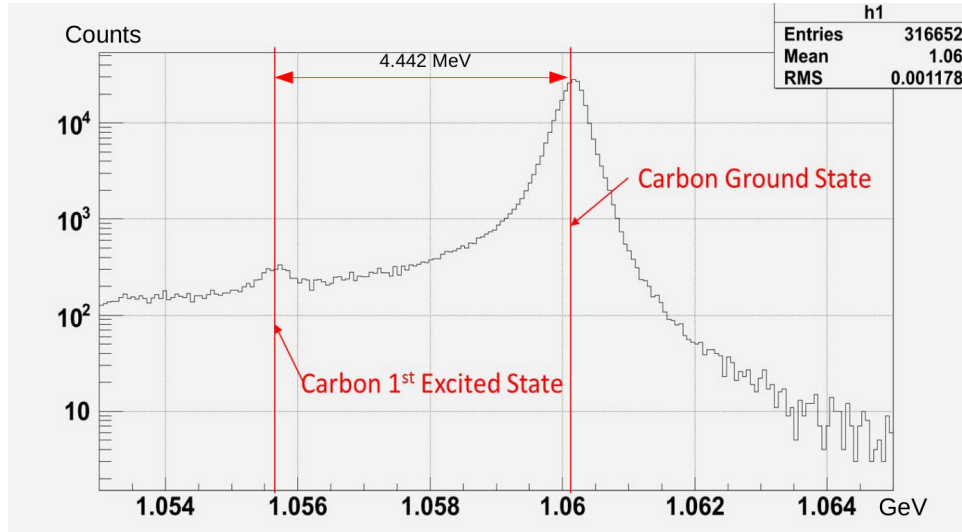


Figure 4.8: Carbon momentum spectrum after the calibration showing the final momentum difference between the ground state and the first excited state of  $^{12}\text{C}$ .

Run	Spectrometer Momentum Setting ( $P_0$ )	$E_f^{ground} - E_f^{first}$ (MeV)
6274	1.063	4.413
6279	1.058	4.497
6289	1.047	4.446

Table 4.2:  $E_f^{ground} - E_f^{first}$  for carbon target on right HRS

Fig. 4.8 and Table 4.2 show the difference in energies of the ground state and the  $4.442 \pm 0.001$  MeV. This comparison indicated that the overall accuracy of the momentum reconstruction was  $\pm 30$  keV.

## 4.2 $Q^2$ Measurement

### 4.2.1 $Q^2$ Components

The four-momentum transfer squared is

$$Q^2 = 2EE'(1 - \cos(\theta)) \quad (4.16)$$

where  $E$  is the incident energy,  $E'$  is the final momentum of scattered electron and  $\theta$  is the scattering angle. In the case of elastic electron scattering, one may eliminate one of the three variables and the  $Q^2$  can be written as

$$Q^2 = 2E^2 f_r(1 - \cos(\theta)) \quad (4.17)$$

$$Q^2 = 2E'^2 f'_r(1 - \cos(\theta)) \quad (4.18)$$

$$Q^2 = 2m_p(E - E') \quad (4.19)$$

Here  $f_r$  and  $f'_r$  are recoil factors defined as  $f_r = \frac{1}{1+(\frac{E}{m})(1-\cos(\theta))}$  and  $f'_r = \frac{1}{1-(\frac{E'}{m})(1-\cos(\theta))}$ . Ideally, any of these three equations could be used to calculate  $Q^2$  and the other two equations would serve as tools for consistency check. However, for PREX, the difference between  $E$  and  $E'$  was only about 20 keV (after the correction for energy losses occurred before and after the scattering) while the uncertainties in  $E$  and  $E'$ ,  $\delta E$  and  $\delta E'$ , were  $\sim 200$  keV at best<sup>7</sup>. These lead to a large  $\delta Q^2$  in Eq. 4.19. Consequently, we could use only Eq. 4.17 and Eq. 4.18 for  $Q^2$  calculation and consistency check.

In order to accurately measure  $Q^2$ , the first component needed is the beam energy. The beam energy was continuously measured to the accuracy of  $1 \times 10^{-3}$  during the run using the Tiefenbach method which had been previously calibrated using two energy measuring apparatus, ARC and eP. Second component needed is the final momentum of scattered electrons. This quantity is well measured to  $\sim 5 \times 10^{-4}$

---

<sup>7</sup>The fractional uncertainty in both  $E$  and  $E'$  is  $\sim 2 \times 10^{-4}$ ; while the approximate values of both  $E$  and  $E'$  for the case of elastic scattering off Pb in PREX was  $\sim 1.063$  GeV in both  $E$  and  $E'$ .

using the high resolution spectrometers (HRS) in Hall A. The last component is the scattering angle. There are two steps involved in measuring the scattering angle:

1. Obtain the spectrometer central angle ( $\theta_0$ ).
2. Obtain the angle of a scattered particles with respect to the spectrometer central angle.

The uncertainty from scattering angle measurement was the main source of the uncertainty in  $Q^2$ .

### **Beam Energy Measurement**

The nominal beam energy for PREX was 1.063 GeV and was continuously measured by the Tiefenbach measurement which had been calibrated using two independent apparatus, ARC and eP. ARC measurement uses the fact that an electron beam would be deflected by a known angle when it passed through a magnetic field. By applying the right magnetic field and fixing angle at  $34.3^\circ$ , one could measure the beam energy precisely. The eP measurement makes use of the fact that, for the elastic  $e + p$  reaction, the scattering angles of the electron and proton were related to the energy of the incoming electron. The two measurements are accurate to  $3 \times 10^{-4}$  level. However, since PREX only used the Tiefenbach measurement, beam energy accuracy was limited to  $\sim 0.1\%$  level and contributed  $\sim 0.1\%$  to systematic error in  $Q^2$ .

### **Scattered Electron Momentum Measurement**

The final momentum of scattered electrons was measured using the two high resolution spectrometers (HRS) in Hall A. The standard HRS absolute momentum accuracy range of 0.3-4.0 GeV is  $\sim 3 \times 10^{-4}$  [6]. However, with the installation of a new septum magnet for PREX, the HRS had to be recalibrated. This recalibration was

checked using elastic scattering off a thin tantalum target. The momentum accuracy was found to be better than  $\sim 0.1\%$  level and contributed  $\sim 0.1\%$  to systematic error in  $Q^2$ .

### Scattering Angle

Scattering angle is the angle between the direction of a scattered electron and the direction of electron beam. Scattering angle measurement consists of two parts: spectrometer central angle ( $\theta_0$ ) and spectrometer (optics) reconstruction (target angles). Scattering angle ( $\theta$ ) relates to  $\theta_0$  and target angles ( $\theta_{tg}$  and  $\phi_{tg}$ ) by

$$\theta = \frac{\cos(\theta_0) - \phi_{tg} \sin(\theta_0)}{\sqrt{1 + \theta_{tg}^2 + \phi_{tg}^2}} \quad (4.20)$$

### Spectrometer Central Angle

Spectrometer central angle ( $\theta_0$ ) is the angle between the spectrometer axis and the ideal beam line. There are two methods to measure  $\theta_0$ . One way is to perform a **survey**. A survey measures the angle between two imaginary lines: the first line along the ideal spectrometer axis and the second line along the ideal beam line. However, target angles  $\theta_{tg}$  and  $\phi_{tg}$  are defined with respect to the line from the target center to the central sieve-slit hole. Therefore, translating the central angle from the spectrometer axis to the sieve central line requires surveys of both the target position and the sieve-slit position. The uncertainties from these measurements combine to make the final uncertainties of the surveyed angle as much as  $0.046^\circ$  (0.7 mrad). This leads to more than 2% uncertainty in  $Q^2$ .

A better method to determine  $\theta_0$  is to perform a **pointing** measurement using the differential recoil in elastic scattering. Consider the equation for elastic scattering off

a target of mass  $M_t$

$$E' = \frac{(E - E_{loss1})}{1 + \frac{2(E - E_{loss1}) \sin^2(\frac{\theta}{2})}{M_t}} - E_{loss2} \quad (4.21)$$

Here,  $E$ ,  $E'$ ,  $\theta$ ,  $E_{loss1}$  and  $E_{loss2}$  are beam energy, final momentum, scattering angle, energy loss occurred before the scattering, and energy loss occurred after the scattering respectively. Pointing method makes use of the fact that  $E$  and  $M_t$  are well known. By accurately measuring  $E'$ , one could precisely calculate  $\theta$ . The accuracy of this method could be greatly enhanced by considering the difference in  $E'$  for elastic scattering off Hydrogen and oxygen nuclei in a water target. In this case, the energy loss terms drop out and the angle measurement is not too sensitive to the absolute values of  $E$  or  $E'$  anymore.

$E_{beam} - E'_{Pb} - E_{loss,Pb}$ (MeV)	1.0
$E_{beam} - E'_{O} - E_{loss,water}$ (MeV)	1.7
$E_{beam} - E'_{H} - E_{loss,water}$ (MeV)	5.8

Table 4.3:  $E_{beam} - E' - E_{loss}$  for various nuclei in PREX at the central scattering angle of  $5^\circ$

Type	$E_{loss}$
Pb	0.8 MeV
Water	1.0 MeV

Table 4.4: Average  $E_{loss}$  for two types of target materials used for measuring spectrometer central angle.

For PREX, which ran at a nominal angle of  $5^\circ$ , Table 4.3 gives the values for  $E_{beam} - E' - E_{loss}$  for different target used. In this case,  $\theta$  depends on  $E'_2 - E'_H$ . Since these energy differences were  $\sim 4$  MeV for PREX, the accuracy of  $\theta$  measurement depends on how well the spectrometer could measure these energy differences. This was accomplished by calibrating momentum reconstruction, as described in Section 4.1.

A second major uncertainty could arise due to the energy loss ( $E_{loss}$ ) in the target. This energy loss was approximately 1 MeV at the center of target. Thus, any

uncertainty from  $E_{loss}$  estimation could affect the accuracy of pointing measurement significantly. However, we were able to adequately eliminate this uncertainty by using the difference in  $E'$  for two nuclei that are in the same target, where  $E_{loss}$  cancels out. The watercell target which consists of  $^{16}\text{O}$  and  $^1\text{H}$  can serve for this purpose. Furthermore, this also eliminated any possible uncertainty due to a beam energy shifted from one run to another. For the watercell target, the difference between oxygen and hydrogen elastic peaks is given by:

$$\Delta E' = E'_O - E'_H = E \left( \frac{1}{1 + \frac{2E \sin^2(\frac{\theta}{2})}{M_O}} - \frac{1}{1 + \frac{2E \sin^2(\frac{\theta}{2})}{M_H}} \right) + \text{correction} \quad (4.22)$$

where *correction* is the negligible correction term accounting for the difference between  $M_O$  and  $M_H$  in  $E_{loss}$  terms. This term is approximately  $\sim 0.1\%$  compared to the first term of  $E'_O - E'_H$ .

In order to determine  $\theta_0$ , we only selected events going through the central sieve slit hole. We avoided using runs without sieve slit so that the  $\theta_0$  measurement did not depend on optics reconstruction. However, they could still be used as a consistency check.

Run	Momentum Setting ( $P_0$ )	$E'_O - E'_H$ (MeV)
26800	1.063	4.24
26822	1.058	4.21
26824	1.047	4.27

Table 4.5:  $E'_O - E'_H$  for watercell target on left HRS

Run	Momentum Setting ( $P_0$ )	$E'_O - E'_H$ (MeV)
6205	1.063	4.09
6233	1.058	4.16
6235	1.047	4.11

Table 4.6:  $E'_O - E'_H$  for watercell target on right HRS

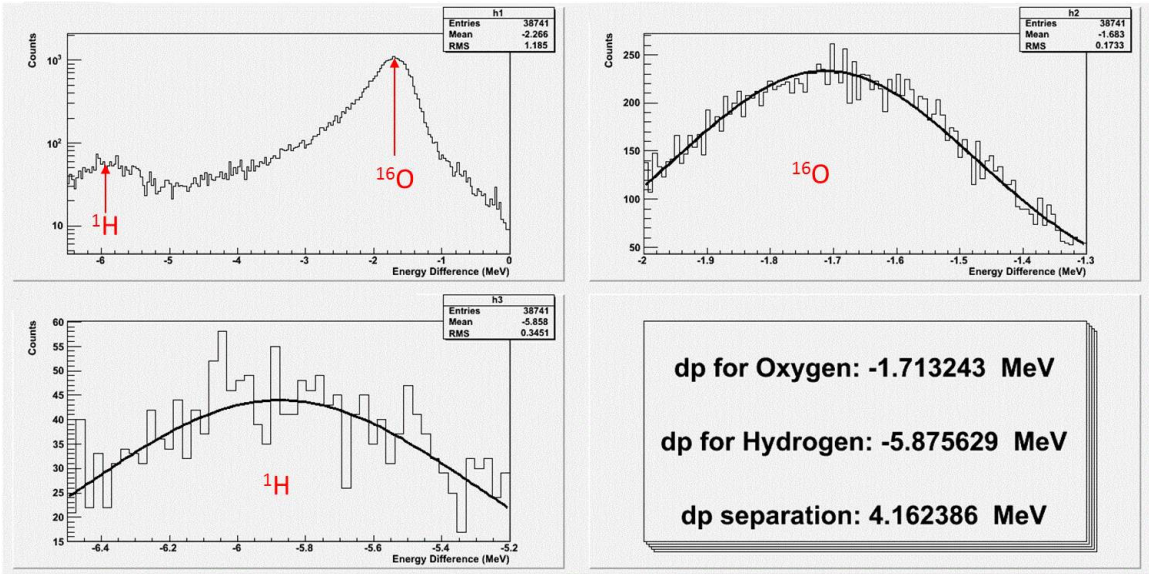


Figure 4.9: Watercell target momentum spectrum

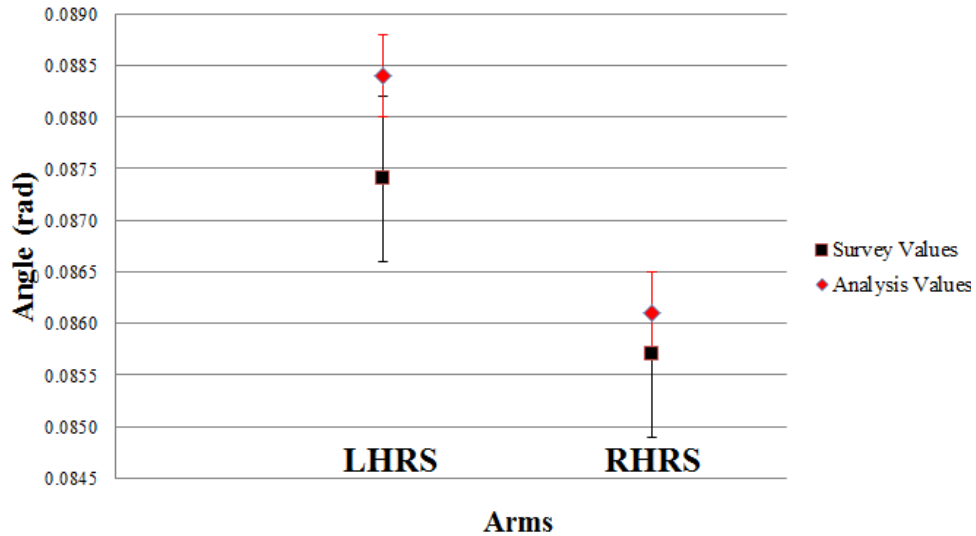
Pointing measurement was done with three central momentum settings of HRS to increase the accuracy. The oxygen and hydrogen peaks were located in three different areas of the HRS focal plane for the three different momentum settings. Each of the three settings provided an independent measurement of the separation between oxygen and hydrogen peaks. To accurately measure the energy differences, the shifts in locations of peaks due to the radiative tails must be thoroughly considered. The most important was a possible shift of the hydrogen peak which was on top of the radiative tail of the oxygen peak. However, we found that this effect was negligible since the radiative tail of the oxygen peak was relatively flat and the shift in the hydrogen peak is negligible. Fig. 4.9 shows the momentum distribution of the watercell target for one of the spectrometer momentum settings. Table 4.5 and Table 4.6 show the values of  $E'_O - E'_H$  from both left and right HRS, and for the three central momentum settings. These values were used to calculate  $\theta_0$  by using the least squares method, which was defined as  $(\Delta E'_{calc} - \Delta E'_{meas})^2$ .  $\Delta E'_{calc}$  was calculated using Eq. 4.21, treating  $\theta$  as the parameter to be optimized.

Arm	Pointing values ( $^{\circ}$ )	Surveys values ( $^{\circ}$ )
Left	$5.065 \pm 0.020$	$5.007 \pm 0.046$
Right	$4.933 \pm 0.020$	$4.910 \pm 0.046$

Table 4.7: Spectrometer angles for PREX

The final spectrometer angles determined from this method are given in Table 4.7. Here the spectrometer angle is defined as the angle between the ideal beamline and the line connecting target center and central sieve slit hole.

In summary, the accuracy for pointing measurement was  $0.020^{\circ}$  (0.3 mrad), while the accuracy for surveys was  $0.046^{\circ}$  (0.8 mrad). Thus, the pointing measurement improved the angle determination accuracy by about a factor of two.

Figure 4.10: Spectrometer angle ( $\theta_0$ ) comparison between pointing and surveys

### Target Angles

Once the pointing measurement has been done, we can obtain  $Q^2$  with the required accuracy at  $\theta_0$ . However, PREX requires the average  $Q^2$  from the entire acceptance calculated using scattering angles of all possible tracks. This requires the optics reconstruction of angles of the scattered electron tracks. The procedure to perform

the calibration is described in Section 4.1. The following tables show uncertainties for all angle measurements and of scattering angles.

Arm	$\sigma_{\theta_0}$ (°)	$\sigma_{\theta_{tg}}$ (°)	$\sigma_{\phi_{tg}}$ (°)
Left	0.020	0.066	0.017
Right	0.020	0.091	0.011

Table 4.8: Errors from all angle measurements

Combining all uncertainties from  $\theta_0$ ,  $\theta_{tg}$  and  $\phi_{tg}$ , the average systematic error from scattering angle would be:

Arm	$\sigma_\theta$ (°)	$\sigma_\theta/\theta$ (%)
Left	0.024	0.49
Right	0.021	0.43

Table 4.9: Errors of scattering angles

These errors in scattering angle measurement contributed  $\sim 0.9\%$  to  $\delta Q^2$ .

#### 4.2.2 Average $Q^2$ Analysis

During PREX production runs, where the integration mode of the PREX detectors was used to collect data, the vertical drift chambers (VDCs) were off and no  $Q^2$  data were recorded. This was due to the fact that the particle flux during production runs was too high for the VDCs to operate. Approximately once a week, a series of  $Q^2$  runs was taken in the counting mode by lowering the beam current and turning on the VDCs to verify the  $Q^2$  distribution.

PREX only selected events that passed through the four PREX detectors, two on each spectrometer. To ensure that the  $Q^2$  runs only collected hits with the same acceptance as production runs,  $Q^2$  events were required to have non-zero ADC amplitudes after pedestal subtraction.

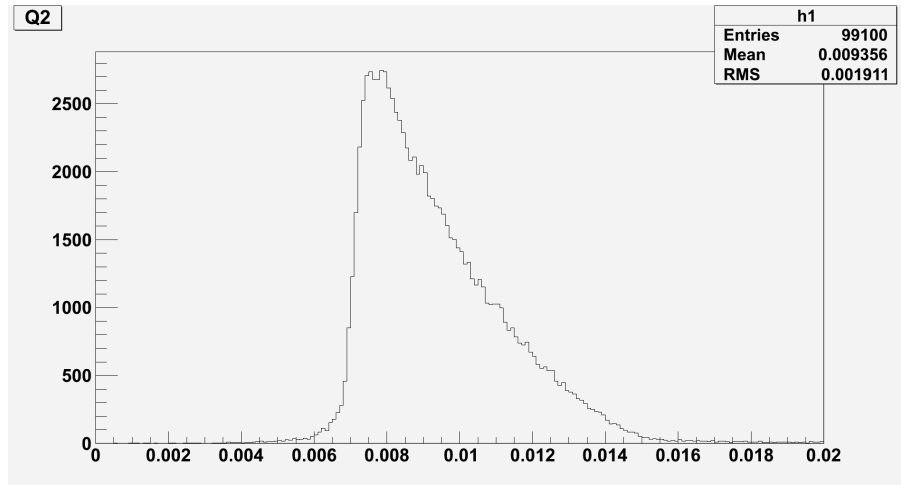
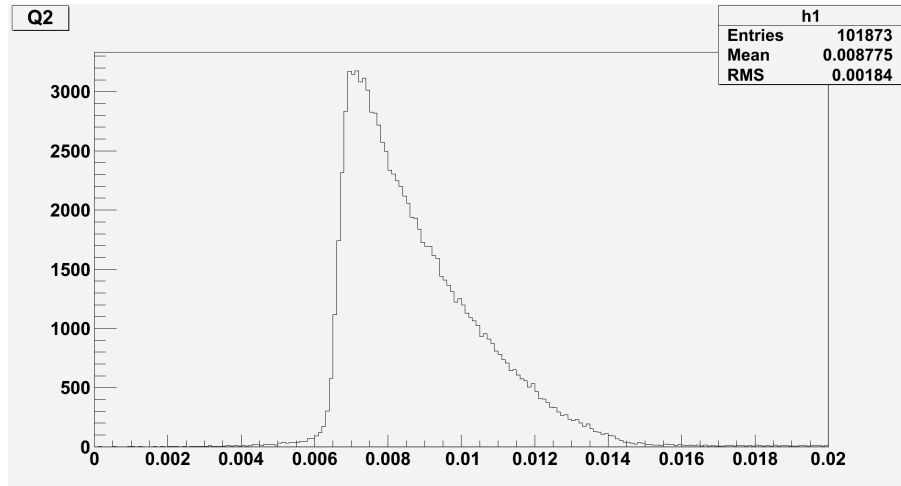
Figure 4.11:  $Q^2$  distribution on L-HRSFigure 4.12:  $Q^2$  distribution on R-HRS

Fig. 4.11 and 4.12 show  $Q^2$  distributions from two such runs on both left and right spectrometers after applying the ADC amplitude cut. One might notice that the left HRS produced larger  $Q^2$  than the right HRS. This was consistent with the fact that the the spectrometer angle for left HRS was larger than the right HRS, leading to a higher momentum transfer.

The following tables show the summary of  $Q^2$  measurement data and the measured

values of  $Q^2$  for each  $Q^2$  run.

Run Number	Date	$Q^2$ ( $GeV^2$ )
27421	4/18/2010	0.00934
27422	4/18/2010	0.00935
27423	4/18/2010	0.00932
27426	4/18/2010	0.00929
27427	4/18/2010	0.00933
27507	4/25/2010	0.00930
27508	4/25/2010	0.00927
27511	4/25/2010	0.00931
27610	5/07/2010	0.00938
27697	5/19/2010	0.00939
27698	5/19/2010	0.00931
27700	5/19/2010	0.00934
27701	5/19/2010	0.00934
27722	6/04/2010	0.00930
27723	6/04/2010	0.00931
27922	6/18/2010	0.00923

Table 4.10:  $Q^2$  values for left HRS. The uncertainty of each  $Q^2$  value is  $\pm 0.00009$   $GeV^2$

Run Number	Date	$Q^2$ ( $GeV^2$ )
6714	4/18/2010	0.00875
6715	4/18/2010	0.00875
6716	4/18/2010	0.00875
6719	4/18/2010	0.00874
6720	4/18/2010	0.00875
6741	4/25/2010	0.00877
6742	4/25/2010	0.00876
6745	4/25/2010	0.00874
6824	5/19/2010	0.00871
6825	5/19/2010	0.00870
6826	5/19/2010	0.00876
6827	5/19/2010	0.00876
6828	5/19/2010	0.00876
6839	6/04/2010	0.00872
6840	6/04/2010	0.00872
6965	6/18/2010	0.00880

Table 4.11:  $Q^2$  values for right HRS. The uncertainty of each  $Q^2$  value is  $\pm 0.00009$   $GeV^2$

HRS	Average $Q^2$ (GeV $^2$ )
Left	$0.00933 \pm 0.00009$
Right	$0.00875 \pm 0.00009$

Table 4.12: average  $Q^2$  values for left and right HRSs, which is calculated by a simple average over all the  $Q^2$  runs.

To get the average  $Q^2$  from both arms, three sets of data; both arms, left arm only, and right arm only, were considered. In the case of both arms, the relative detector strengths between the left and the right arms must be taken into consideration. Even though the PREX quartz detectors on the two spectrometers were tuned through high voltage (HV) adjustments periodically such that their gain were kept roughly equal, there were still some small imbalances. Using the average ratio of the right detector sum of ADC amplitudes to the left detector sum of ADC amplitudes,  $R$ , obtained from each  $Q^2$  run, the average left and right weights could be calculated.

The left weight was  $\frac{1}{1+R}$  and the right weight was  $\frac{R}{1+R}$ . These were averaged with the statistical weights of the “both-arms-up” runs,  $\frac{N}{\sigma^2}$ , where  $N$  is the number of  $Q^2$  runs and  $\sigma$  is the standard deviation of the ADC spectrum. This yields the weights of 0.5020 and 0.4980 for left and right respectively.

The three data sets were weighted together, run-by-run using aforementioned  $Q^2$  for “both-arms-up” data and the individual  $Q^2$  for the left and right arm data. This yielded a grand average of 0.00906 GeV $^2$ . The effective ratio of left arm to right arm data was 1.213.

We also observed shifts in  $Q^2$  by as much as 1% between runs. These shifts could be explained by the shifts in average beam position for detected events. The shifts in average beam position could be due to two reasons:

1. After taking the beam for several days, some parts of target melted away and became non-uniform. This reduced the yield for those thinner parts and, with the raster on, the average beam position seen by the detectors changed.

2. Due to the low beam currents during  $Q^2$  runs, the beam position locks were not in place. This may have caused the actual beam position to change.

The change in beam position to one side would increase  $Q^2$  on one spectrometer and decrease  $Q^2$  on the other spectrometer. Since the beam position monitors did not operate during PREX  $Q^2$  runs due to low beam current ( $\sim 50$  nA), we had to extract the beam position by using the measured  $y_{tg}$  instead. Note that

$$z_{react} = -(y_{tg} + D) \frac{\cos(\phi_{tg})}{\sin(\theta_0 + \phi_{tg})} + x_{beam} \cot(\theta_0 + \phi_{tg}) \quad (4.23)$$

where  $z_{react}$  and  $x_{beam}$  are the interaction position along the beam and horizontal beam position at the target respectively. For PREX,  $z_{react}=0$ , and so,  $x_{beam}$  could be extracted directly from  $y_{tg}$ , given that  $y_{tg}$  is properly calibrated. The following figure illustrates how well  $y_{tg}$  was calibrated compared to known beam positions from high current, counting mode, runs for which both beam position monitors and VDCs were on. The beam position data from BPMs were obtained using EPICS information.

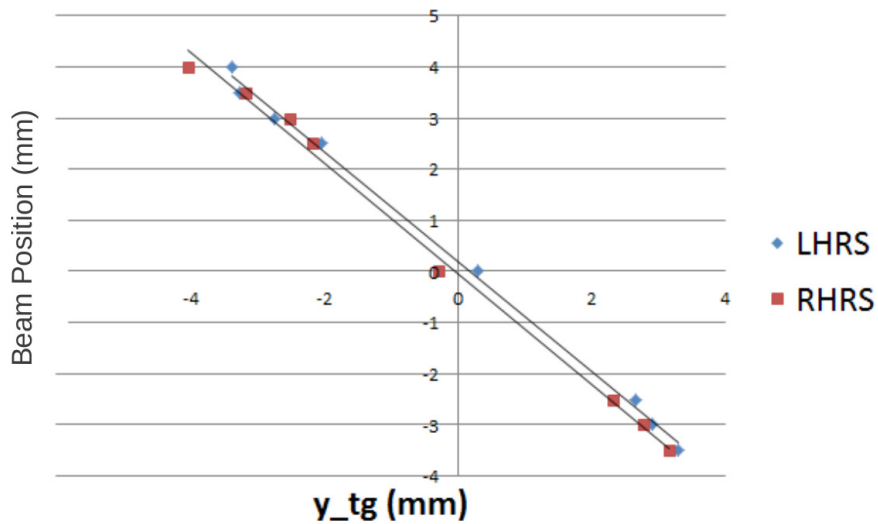
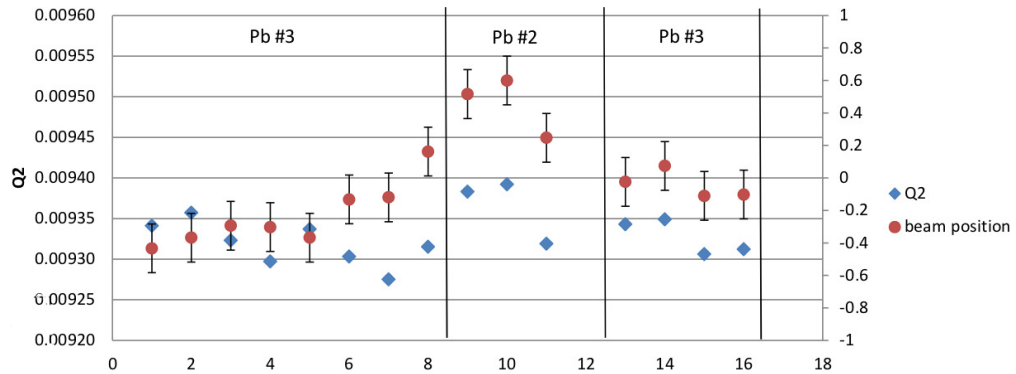
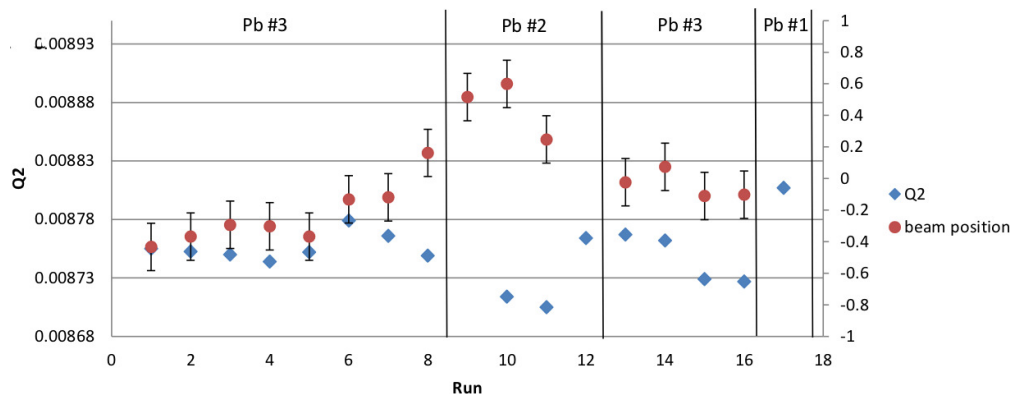


Figure 4.13: The relationship between calibrated  $y_{tg}$  and known beam positions

Figure 4.14:  $Q^2$  distribution versus beam position on L-HRSFigure 4.15:  $Q^2$  distribution versus beam position on R-HRS

As seen in figs. 4.14 and 4.15, once the average beam position moved to one side,  $Q^2$  on one spectrometer increased while decreased on the other spectrometer.

#### 4.2.3 Other Systematic Errors on the $Q^2$ Measurement

##### Pileup

Pileup effects could occur from running at too high trigger rates which decreased the performance of vertical drift chambers (VDC). To determine the size of this effect, we took a series of  $Q^2$  runs with trigger rates varying over a large range from 300 Hz to 500 kHz and considered the VDC performance from  $Q^2$  distributions.

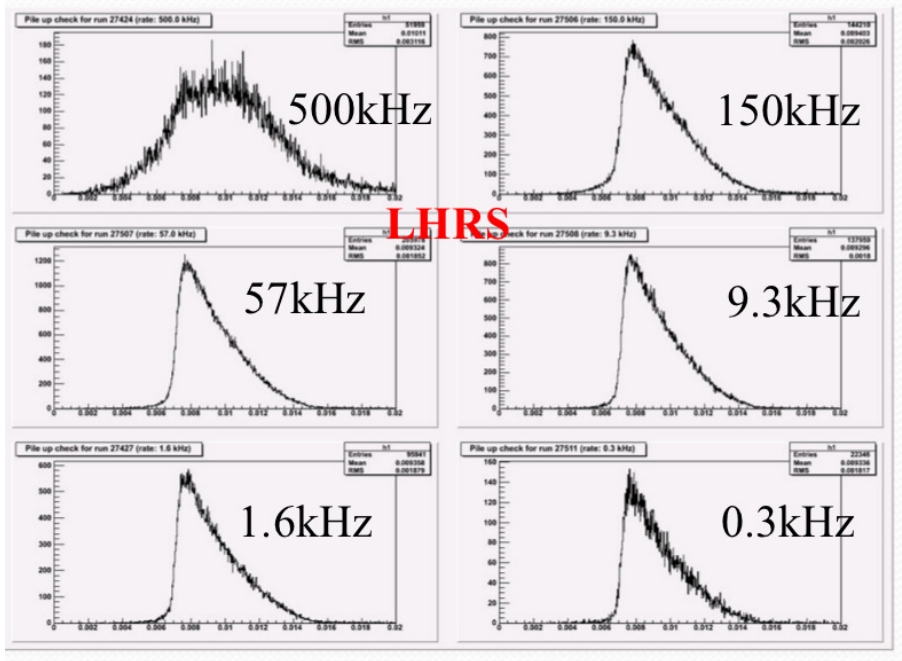


Figure 4.16:  $Q^2$  showing VDC performance at different trigger rate (L-HRS)

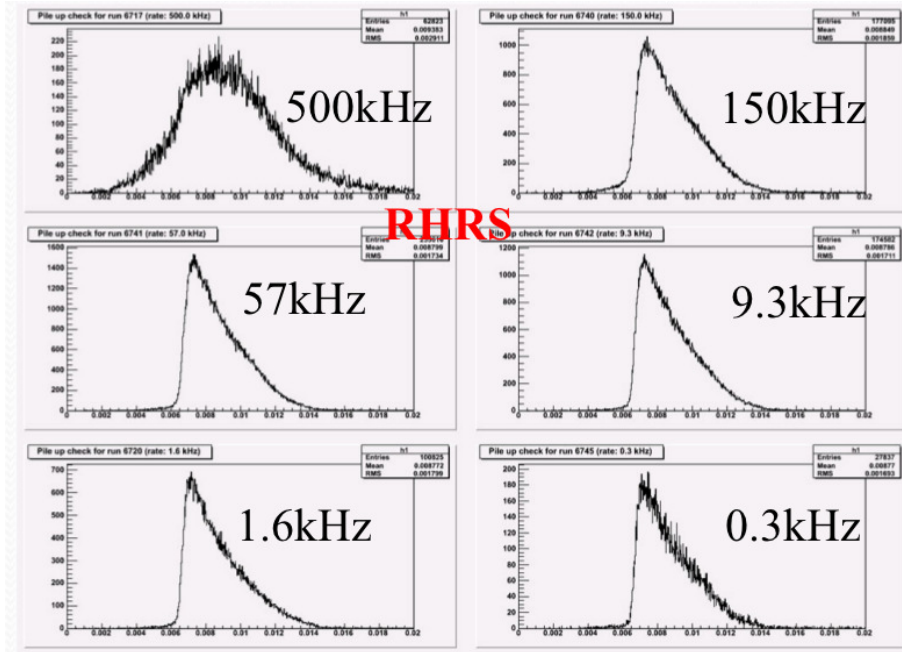


Figure 4.17:  $Q^2$  showing VDC performance at different trigger rate (R-HRS)

Clearly, pileup occurred when we ran at very high rate (500 kHz). Fig. 4.18 shows how the average value of  $Q^2$  depended on trigger rates.

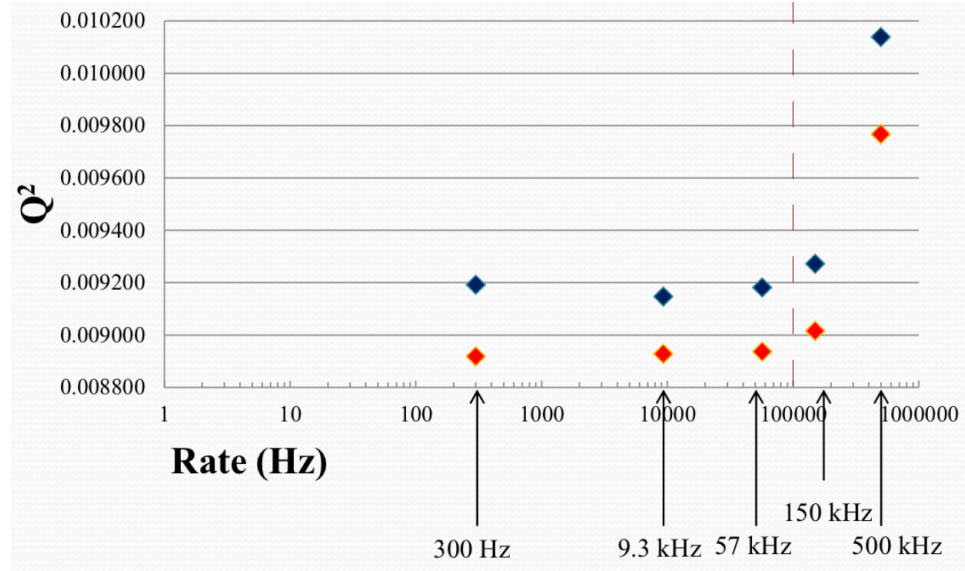


Figure 4.18:  $Q^2$  dependence on trigger rate (higher values at the same rate are L-HRS). The red dashed line shows the limit of the trigger rate that could be used for  $Q^2$  measurement.

To reduce the effect of pileup on the  $Q^2$  measurement, we only selected  $Q^2$  runs with the trigger rates lower than 100 kHz. However, even at low trigger rates, pileup effects still occurred. The effect could be estimated by comparing  $Q^2$  for different cuts on the number of tracks in the event. Using a 1-track cut versus allowing multiple tracks makes a shift of  $-0.06 \pm 0.05\%$  average shift on  $Q^2$ . We will take this variation in this as a systematic error.

### Trigger Bias

PREX used two types of trigger: T1 and T5. T1 was the scintillator above the VDC planes while T5 was the scintillator placed just above the PREX detector. T5 trigger was used as the main trigger during the experiment for the  $Q^2$  measurement. By comparing  $Q^2$  values collected from the same run but using different trigger types, it

was revealed that T5 triggered events had a  $Q^2$  value  $\sim 0.2\%$  higher than the  $Q^2$  value of T1 triggered events. We took this difference as a systematic error from trigger bias to account for the T1-only triggered  $Q^2$  measurement runs.

### $Q^2$ Results and Conclusions

Beam Energy (GeV)	$1.063 \pm 0.001$
L-HRS $\theta_0$ ( $^\circ$ )	$5.065 \pm 0.024$
R-HRS $\theta_0$ ( $^\circ$ )	$4.933 \pm 0.021$
Average L-HRS $Q^2$ (GeV $^2$ )	$0.00933 \pm 0.00009$
Average R-HRS $Q^2$ (GeV $^2$ )	$0.00875 \pm 0.00009$
L-HRS $Q^2$ Weight	$0.5020 \pm 0.0005$
L-HRS $Q^2$ Weight	$0.4980 \pm 0.0005$
Average $Q^2$ (GeV $^2$ )	$0.00906 \pm 0.00009$

Table 4.13: Summary of  $Q^2$  and useful information for PREX

Error Source	Error (in source units)	Percent Error in $Q^2$
Beam Energy	1 MeV	0.1%
Final Momentum	1 MeV	0.1%
Scattering Angle	$0.023^\circ$	0.9%
Pileup		<0.1%
Trigger Bias		0.2%
<b>Total Systematic Error</b>		1.0%
<b>Statistical Error</b>		<0.1%
<b>Total Error</b>		1.0%

Table 4.14: Summary of errors in  $Q^2$  for PREX

Table 4.13 and Table 4.14 summarize the results and uncertainties for the  $Q^2$  measurement. The systematic errors of  $Q^2$  add in quadrature to 1.0% error. The largest error was from scattering angle measurement.

## 4.3 Background Analysis

The ability to estimate asymmetries arising from backgrounds was very crucial for parity violating experiments, especially with the integrating technique used in PREX, which did not allow for the separation of background events from the desired elastic events in the data.

The twin High Resolution Spectrometers (HRS) served as powerful devices to focus the elastically scattered electrons into the quartz detectors. However, a small fraction of the data collected in the quartz detectors could be due to the following background events:

- Elastically scattered events of  $^{12}\text{C}$  from the diamond backing of the target.
- Events from the 1<sup>st</sup> excited state of  $^{208}\text{Pb}$ .
- Inelastically scattered events rescattered into the acceptance of the quartz detectors.

In principle, one could measure with enough energy resolution to avoid excited state contributions. However, in practice, there may be a gain in rate by running with lower resolution and allowing a small contamination from excited states such as using a thicker target with a larger energy loss to increase the rate from  $^{208}\text{Pb}$ . By design, the contaminations from backgrounds were expected to be small. This section will estimate the contamination of background events in the desired elastic events.

### 4.3.1 Contamination due to Excited States of $^{208}\text{Pb}$

$^{208}\text{Pb}$  has several excited states as indicated in the Table 4.15 [23]. The cross section data for these excited states are available. However, in order to estimate the contamination due to each state, the acceptance fraction for that state to be accepted in the PREX detector had to be measured.

State	$\Delta E$ (MeV)
$3^-$	2.615
$5^-$	3.198
$5^-$	3.709
$5^-$	3.961
$7^-$	4.037
$2^+$	4.085
$4^+$	4.323
$6^+$	4.424
$8^+$	4.610

Table 4.15: Energy differences between the ground state and some excited states of  $^{208}\text{Pb}$ 

The counting mode  $Q^2$  runs could be used to extract the number of excited state events included in the data sample. During the  $Q^2$  analysis of these runs, in order to ensure that the events analyzed were detected by four quartz detectors, the “ADC cut”, which selected events that had ADC values greater than pedestal values, were applied to all runs. The pedestal value used for each detector is shown in Table 4.16.

Arm	Detector Position	Pedestal
Left	Upper	470
Left	Lower	645
Right	Upper	520
Right	Lower	500

Table 4.16: Pedestal values for each quartz detector that were applied for “ADC cut”

Another important quantity for background analysis is the ratio of normalized numbers of event with and without the ADC cut for each small energy bin to determine the acceptance of that bin. For data taken with the standard HRS trigger and no ADC cut, the acceptance has been measured to be flat over a momentum range of  $\pm 3\%$  of the central momentum. This flat acceptance region includes all excited states shown in Table 4.15. Therefore, the ratio of events with and without ADC cut indicates the probability of an electron with a certain scattered energy to be detected

by the quartz detector.

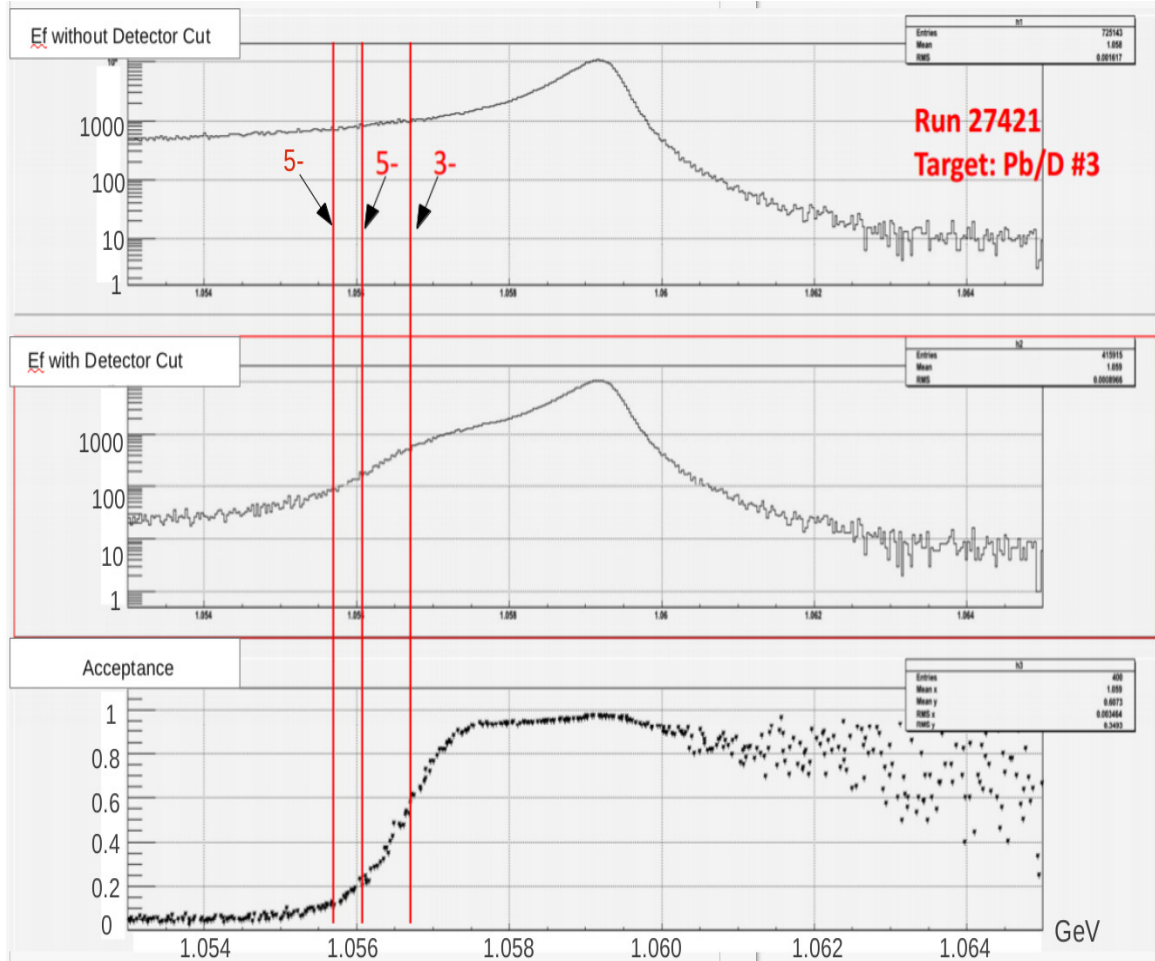


Figure 4.19: The figures illustrate the procedures to obtain the acceptance of the PREX detectors. The top figure is the energy spectrum of scattered electrons without the ADC cut. Previous white spectrum data (with no ADC cut) taken for HRSs show that the relative acceptance is  $100 \pm 3\%$  over the full range shown [40]. The second figure is the energy spectrum of scattered electron with the ADC cut. The last figure shows the acceptance of the detectors, which is the ratio of normalized numbers of events with ADC cut to the number of events without ADC cut in each small bin of energy. The lines labeled 5<sup>-</sup> and 3<sup>-</sup> indicate the locations of  $^{208}\text{Pb}$  excited states.

Fig. 4.19 shows the acceptance fraction of the detectors for HRSs. One clearly sees that the acceptance drops sharply once the scattered energy goes below 1.057 GeV, corresponding to the edge of the quartz detector. The reason that the acceptance does

not drop completely to zero beyond the edge is due to the rescatter of inelastic events into the quartz detector. The following table illustrates the percentage acceptance at some of the important excited states of  $^{208}\text{Pb}$ .

State	Acceptance (%)
Ground	$\sim 100$
$3^-$	$\sim 60$
$5^-$	$\sim 20$
$5^-$	$\sim 10$

Table 4.17: The acceptance values for some excited states of  $^{208}\text{Pb}$

The interpretation for the Table 4.17 is that the elastically scattered electrons had a relative probability of  $\sim 100\%$  to be detected by the quartz detectors while the first excited state,  $3^-$ , had a relative probability of  $\sim 60\%$  to be detected by the detectors, etc...

Next, we need to consider the ratio of cross sections for excited states and ground state. From [54], the cross section ratios of the first excited state to the ground state for different effective momentum transfers  $q_{eff}$ <sup>8</sup> are:

$q_{eff}$	$\frac{\sigma_{3^-}}{\sigma_{elastic}} (\%)$
0.550	0.123
0.692	0.804
0.837	1.066
0.974	0.954
1.117	2.226
1.226	6.380
1.258	6.309
1.436	3.867
1.631	7.347

Table 4.18: The cross section ratios of the first excited state and the ground state of  $^{208}\text{Pb}$

From Table 4.18, in the case of PREX which has  $q = 0.47 \text{ fm}^{-1}$  or  $q_{eff} = 0.482 \text{ fm}^{-1}$ ,

---

<sup>8</sup> $q_{eff} = q(1 + \frac{4Z\alpha}{3E_i R_{rms}})$

$\frac{\sigma_{3^-}}{\sigma_{elastic}} \sim 0.1\%$ . By combining this result with the acceptance at the location of the  $3^-$  state, the actual contamination due to this state is only  $\sim 0.06\%$ .

In addition to the negligible contamination amount, the asymmetry from  $3^-$  state, which is adjacent to the elastic peak calculated by C. J. Horowitz [29], is similar to the elastic asymmetry:

$$A(3^-) \approx 1.25A(\text{elastic}) \quad (4.24)$$

These make the contamination of the first excited state of  $^{208}\text{Pb}$  in asymmetry correction negligible. Contamination due to higher excited states are even lower, as the acceptance drops rapidly after  $3^-$  state. As a result, although no actual estimation of their asymmetries is given, it is safe to neglect the contamination due to these higher states.

### 4.3.2 $^{12}\text{C}$ Contamination

Since  $^{208}\text{Pb}$  has a low melting temperature of  $\sim 327.5^\circ\text{C}$ , a 0.5 mm foil of  $^{208}\text{Pb}$  was sandwiched between two 0.15 mm sheets of pure  $^{12}\text{C}$  diamond in order to improve the heat transfer. However, the addition of diamond sheets contaminates asymmetry used to calculate the radius of  $^{208}\text{Pb}$ . This section will describe the analysis of  $^{12}\text{C}$  contamination and its affect on the measured asymmetry.

The asymmetry from the ground state of  $^{12}\text{C}$  and its corresponding cross section are well understood and could be estimated with sufficient precision. In order to accurately extract asymmetry from  $^{208}\text{Pb}$ , the correction of the  $^{12}\text{C}$  contamination was applied to the measured asymmetry by:

$$A_{Pb} = \frac{1}{P} \frac{A_{meas} - PfA_C}{1 - f} \quad (4.25)$$

where

$$f = \frac{N_C}{N_{Pb}} = \frac{Z_C \times t_C \times \sigma_C}{Z_{Pb} \times t_{Pb} \times \sigma_{Pb}} \quad (4.26)$$

$$A_C = \frac{G_F Q^2 \sin^2 \theta_W}{\pi \alpha \sqrt{2}} \quad (4.27)$$

where  $A_C$  is the standard model prediction for raw asymmetry from  $^{12}\text{C}$ . The terms used in Eq. 4.25 - Eq. 4.27 are:

Variable	Definition
$A_{meas}$	Asymmetry actually measured
$A_{Pb}$	Raw asymmetry from $^{208}\text{Pb}$
$f$	The background fraction of electrons scattered off $^{12}\text{C}$
$P$	Beam polarization
$N_C$	Number of events from $^{12}\text{C}$
$N_{Pb}$	Number of events from $^{208}\text{Pb}$
$Z_C$	Atomic number of $^{12}\text{C}$
$Z_{Pb}$	Atomic number of $^{208}\text{Pb}$
$N_C$	Number of events from $^{12}\text{C}$
$N_{Pb}$	Number of events from $^{208}\text{Pb}$
$Z_C$	Atomic number of $^{12}\text{C}$
$Z_{Pb}$	Atomic number of $^{208}\text{Pb}$
$t_C$	Thickness of $^{12}\text{C}$ target
$t_{Pb}$	Thickness of $^{208}\text{Pb}$ target
$\sigma_C$	Cross section of $^{12}\text{C}$
$\sigma_{Pb}$	Cross section of $^{208}\text{Pb}$
$G_F$	Fermi constant
$Q^2$	Four-momentum transfer squared
$\theta_W$	Weinberg angle or weak mixing angle
$\alpha$	Fine-structure constant

Table 4.19: Explanations of terms in Eq. 4.25 - Eq. 4.27

In order to calculate  $f$ , two important ratios ( $\frac{t_C}{t_{Pb}}$  and  $\frac{\sigma_C}{\sigma_{Pb}}$ ) must be accurately estimated. The details of the analysis for the ratios are explained below.

**Thickness Ratio of Diamond  $^{12}\text{C}$  to  $^{208}\text{Pb}$** 

Since  $^{208}\text{Pb}$  has a low melting temperature, even with the diamond sheets, some parts of the  $^{208}\text{Pb}$  target melted away. This changed the ratio of the thicknesses between  $^{12}\text{C}$  Diamond and  $^{208}\text{Pb}$  during the experiment.<sup>9</sup> The next two figures illustrate the change in the uniformity of the same target.

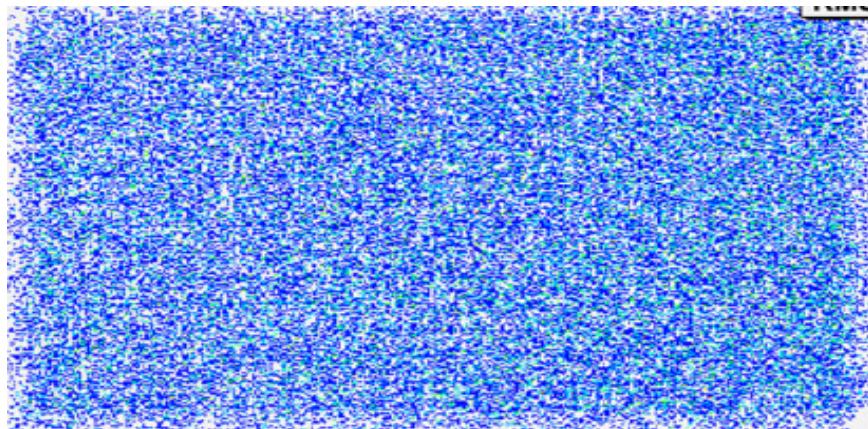


Figure 4.20: The raster current weighted by the detector events showing the target uniformity for the run 27258 taken on April 4<sup>th</sup>, 2010

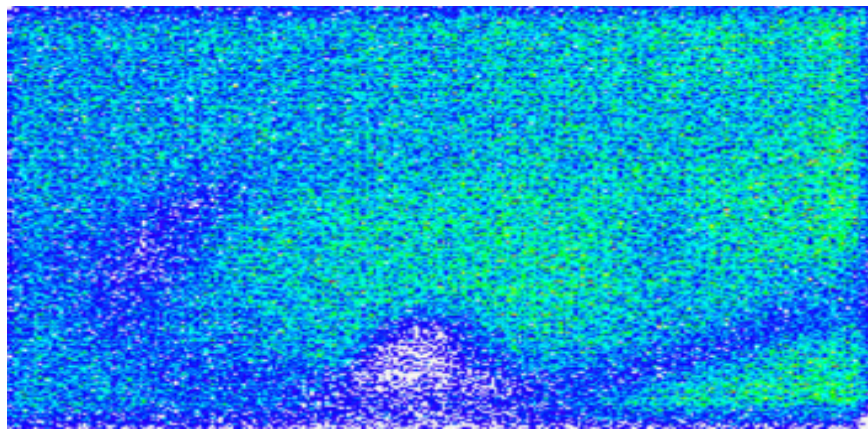


Figure 4.21: The raster current weighted by the detector events showing the target uniformity for the run 27789 taken on June 11<sup>th</sup>, 2010

---

<sup>9</sup>Since diamond has a much better ability to transfer heat generated from the beam and a much higher melting point than  $^{208}\text{Pb}$ , the thickness of diamond was relatively constant throughout the experiment.

As clearly seen in Fig. 4.21, a hole appeared at the bottom of the target. This non-uniformity led to a decrease in the average thinkness of  $^{208}\text{Pb}$  target seen by the electron beam. As a consequence, the ratio of the thickness between diamond  $^{12}\text{C}$  and  $^{208}\text{Pb}$  increased.

In order to find the average thickness of the  $^{208}\text{Pb}$  target, we divided a 2D plot of event weighted raster current into small square bins. Under the assumption that the thickness remained the same at the edge of the target where heat dissipation was most effective, we could use runs taken at the very early stage of the experiment, when the target was still uniform, as a reference for the number of events in each bin. The decrease in the ratio of number of events in later runs compared to number of events in reference runs represents the decrease in the thickness of the target. Then the average thickness for the target as seen by the beam was calculated by taking the weighted average over all bins. The equation to obtain the average thickness is

$$\text{Average Thickness} = \frac{\sum t_i}{N_b} \quad (4.28)$$

where  $t_i$  is the ratio of the number of events of the later run and of the reference run normalized by the ratio of the bin at the edge of the target, and  $N_b$  is the total number of small squared bins used for calculation.

The following tables and figures show the changes in the thickness and their statistical errors, which equal to  $1/\sqrt{N}$ , where  $N$  is the total number of events in each run.

As shown on Table 4.20 and Fig. 4.22, the target thickness of target 1 was relatively constant throughout the experiment. This was because target 1 had the thickest total diamond backing ( $\sim 0.46$  mm), while the others only had  $\sim 0.25$  mm, thus significantly improved the heat dissipation from the target. However, with thicker diamond sheets, the contamination of  $^{12}\text{C}$  in the measured asymmetries increases. The ratios of the thickness were applied to each asymmetry run by interpolating runs in between the

Number	Date	Run Number	Thickness	Error(%)
1	06/13/2010	27870	1.00	1.93
2	06/15/2010	27884	1.01	2.42
3	06/15/2010	27887	0.98	1.64
4	06/15/2010	27895	0.99	1.51
5	06/19/2010	27932	1.00	2.74
6	06/20/2010	27944	1.01	1.68

Table 4.20: Changes in the target thickness of Pb/D target 1

Number	Date	Run Number	Thickness	Error(%)
1	05/02/2010	27551	1.00	1.09
2	05/02/2010	27557	1.01	1.35
3	05/07/2010	27601	0.96	1.23
4	05/07/2010	27622	0.94	2.03
5	05/09/2010	27642	0.94	1.74
6	05/14/2010	27659	0.94	2.16
7	05/19/2010	27698	0.86	1.19

Table 4.21: Changes in the target thickness of Pb/D target 2

Number	Date	Run Number	Thickness	Error(%)
1	04/03/2010	27258	1.00	2.33
2	04/04/2010	27283	0.99	2.23
3	04/06/2010	27329	0.97	1.77
4	04/18/2010	27433	0.97	2.25
5	04/19/2010	27434	0.92	2.26
6	04/20/2010	27448	0.92	2.37
7	04/23/2010	27480	0.92	2.46
8	04/24/2010	27483	0.94	2.40
9	05/02/2010	27545	0.91	2.16
10	05/02/2010	27546	0.92	2.85
11	05/02/2010	27549	0.92	1.83
12	05/14/2010	27645	0.92	1.88
13	05/14/2010	27656	0.93	2.38
14	06/04/2010	27719	0.23	1.72
15	06/06/2010	27754	0.92	1.67
16	06/07/2010	27767	0.92	1.69
17	06/11/2010	27789	0.92	1.85

Table 4.22: Changes in the target thickness of Pb/D target 3

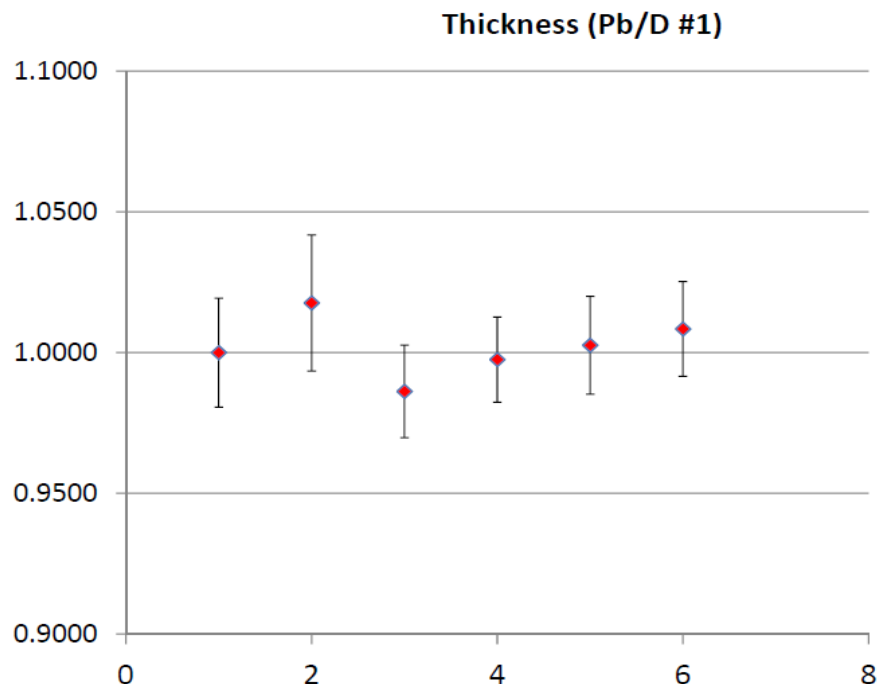


Figure 4.22: The histogram illustrates the change in the thickness of target 1

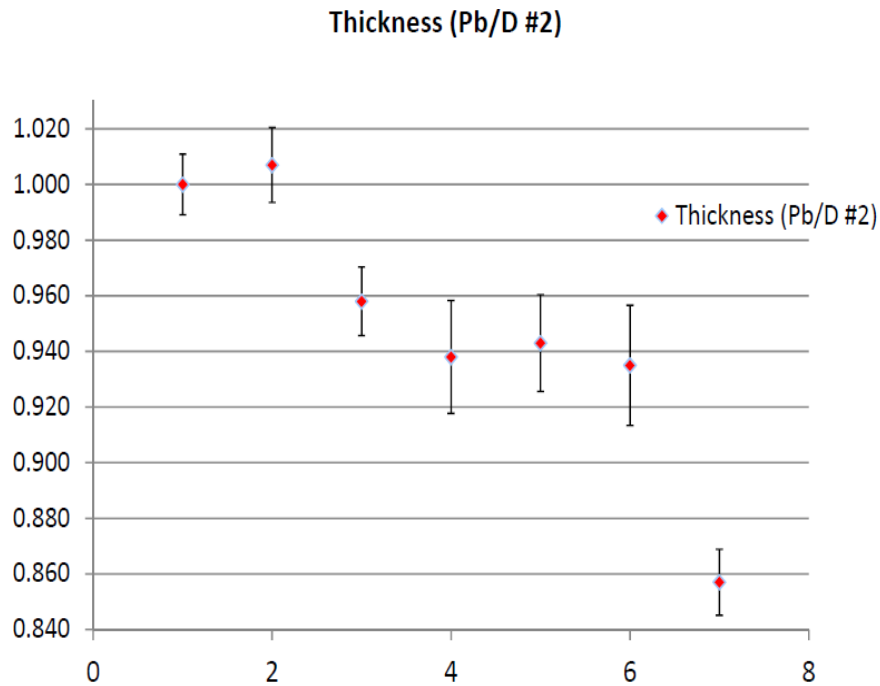


Figure 4.23: The histogram illustrates the change in the thickness of target 2

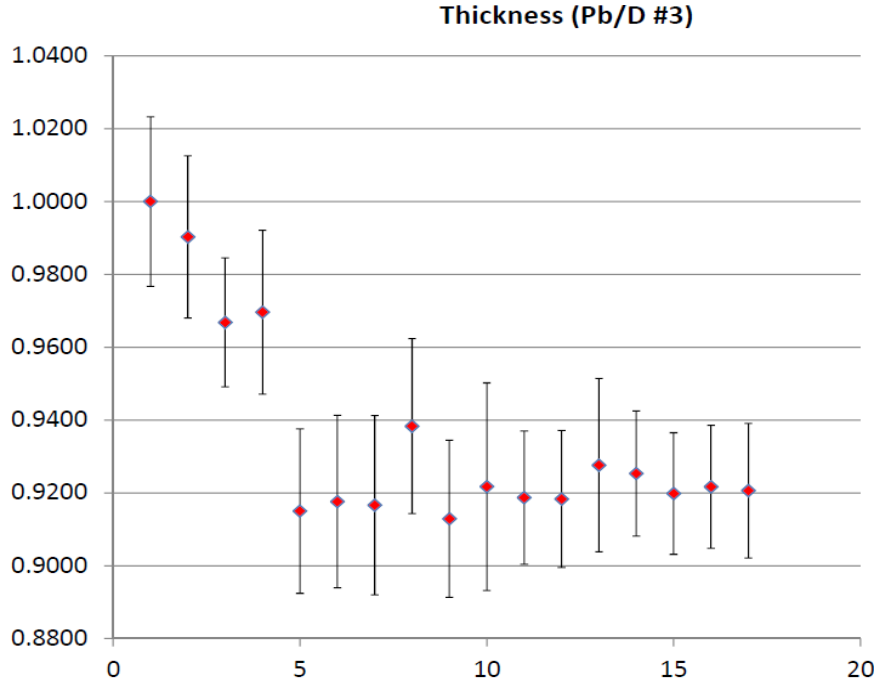


Figure 4.24: The histogram illustrates the change in the thickness of target 3

above calibrated runs in Table 4.20, 4.21, and 4.22.

#### Elastic Cross Section Ratio of $^{12}\text{C}$ Diamond to $^{208}\text{Pb}$

The elastic cross section ( $\sigma$ ) for each type of nucleus depends very strongly on the momentum transfer ( $Q^2$ ) and can be expressed as

$$\frac{d\sigma}{d\Omega} = \left(\frac{d\sigma}{d\Omega}\right)_{Mott} \times F^2(Q^2) \quad (4.29)$$

where the Mott cross section,  $(\frac{d\sigma}{d\Omega})_{Mott}$ , describes the elastic cross section of electrons scattered off a point-like particle and can be expressed as

$$\left(\frac{d\sigma}{d\Omega}\right)_{Mott} = \frac{4Z^2\alpha^2(\hbar c)^2 E'^2}{|qc|^4} \cos^2(\theta/2) \quad (4.30)$$

and  $F(Q^2)$  is the form factor.

The following figure shows the yield of the differential cross sections ( $\frac{d\sigma}{d\Omega}$ ) using a Hall A Monte Carlo (HAMC) simulation for  $^{208}\text{Pb}$  and  $^{12}\text{C}$ , which takes the acceptance of the spectrometers and multiple scattering into account.

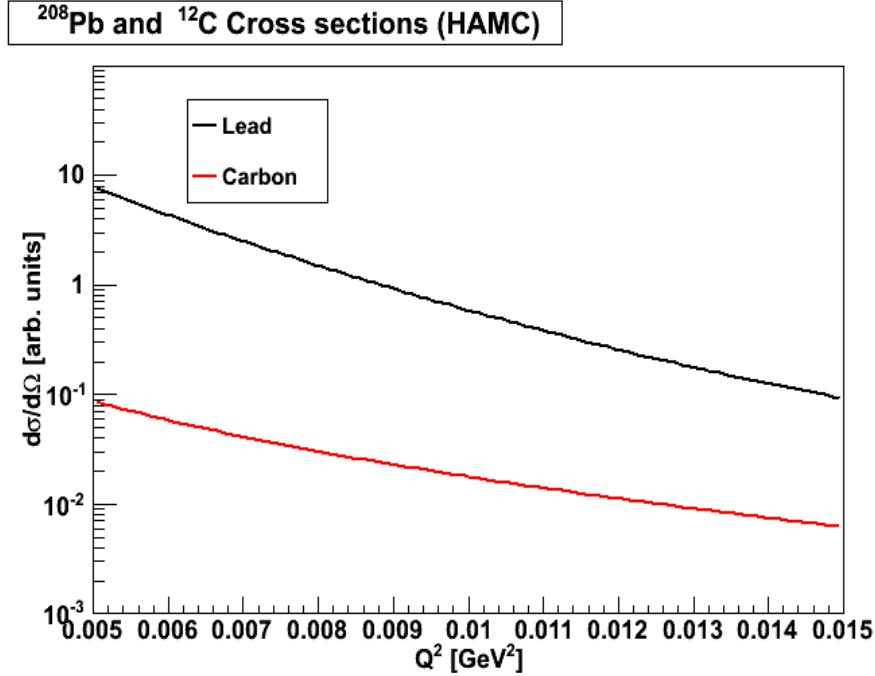


Figure 4.25: The plot shows the differential cross section of  $^{208}\text{Pb}$  and  $^{12}\text{C}$  for different 4-momentum transfer  $Q^2$ . The differential cross sections are shown in arbitrary units

As shown in Fig. 4.25, the yield in differential cross section for  $^{208}\text{Pb}$  drops much faster than for  $^{12}\text{C}$ . This is due to the fact that the  $^{208}\text{Pb}$  nucleus is significantly bigger than the  $^{12}\text{C}$  nucleus, and thus, the elastic form factor for  $^{208}\text{Pb}$  drops faster with increasing  $Q^2$  than the  $^{12}\text{C}$  elastic form factor. One can not simply use the average  $Q^2$  from Pb/D target to obtain the ratio of the cross section since the average  $Q^2$  from a pure  $^{208}\text{Pb}$  target and the average  $Q^2$  from a pure  $^{12}\text{C}$  target are not the same due to the different  $Q^2$  dependence of  $^{208}\text{Pb}$  and  $^{12}\text{C}$ . Therefore, the cross section for each target material needs to be evaluated at the  $Q^2$  averaged for a target of that material alone. In order to calculate the ratio, we measured the average  $Q^2$  from a thin  $^{12}\text{C}$  target and a thin  $^{208}\text{Pb}$  target separately. The average  $Q^2$  from  $^{12}\text{C}$  and

$^{208}\text{Pb}$  and the ratio of their cross sections evaluated at these corresponding  $Q^2$  values, are shown in the Table 4.23.

Average $Q^2$ from $^{12}\text{C}$ ( $\text{GeV}^2$ )	0.01010
Average $Q^2$ from $^{208}\text{Pb}$ ( $\text{GeV}^2$ )	0.00933
$\frac{\sigma_C}{\sigma_{Pb}}$	0.01863

Table 4.23: Average  $Q^2$  from  $^{12}\text{C}$  and  $^{208}\text{Pb}$  and its corresponding  $\frac{\sigma_C}{\sigma_{Pb}}$

Using these values in Eq. 4.26 and Eq. 4.27, we obtained the corrections due to carbon contamination as:

Quantity	Value	Percent Error to Asymmetry
$f$	0.063	0.2%
$A_C$	817 ppb	0.4%

Table 4.24: Table shows the values of  $^{12}\text{C}$  background fraction,  $f$ , and asymmetry of this background,  $A_C$ .

The asymmetry correction arising due to  $^{12}\text{C}$  backing was -8.8 ppb. This number was determined with an accuracy of 2.6 ppb (or 0.4% relative uncertainty) contribution to the final asymmetry.

### 4.3.3 Rescattering in the HRS

Electrons which inelastically scatter in the target can reach the detector if they rescatter off the spectrometer walls. These rescattered electrons could generate signals in the detectors. The fraction of the rescattered events can be expressed using the following integral [11]:

$$f_s = \int_0^{E_{elastic}} dE' P_{rs}(E') R(E') \quad (4.31)$$

where  $E'$  is the energy of the scattered electron,  $P_{rs}$  is the ADC weighted probability of an electron with this energy to rescatter in the spectrometer and produce a signal

in the detector, and  $R(E')$  is the ratio of the inelastic cross section to the elastic cross section:

$$R(E') = \frac{\left(\frac{d\sigma}{d\Omega dE'}\right)_{inelastic}}{\left(\frac{d\sigma}{d\Omega}\right)_{elastic}} \quad (4.32)$$

Measurement of  $P_{rs}(E')$  was performed by increasing the spectrometer dipole field to force the elastic trajectories to trace those taken by the lower-energy inelastics at the production momentum setting.  $R(E')$  was then measured by decreasing the dipole field such that the inelastic events are directed at the PREX detector. The resulting product between these two functions was integrated from  $E' = 0$  to the elastic energy<sup>10,11</sup>

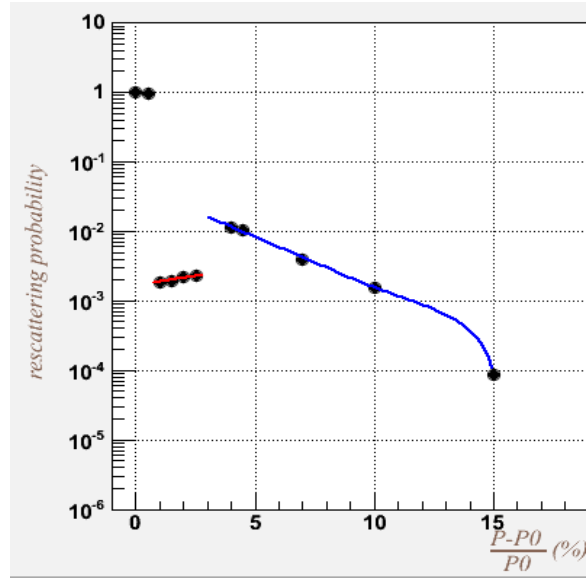


Figure 4.26: Probabilities of electrons to rescatter in the spectrometers and reach the detectors as a function of scattered momentum [31]. The probability was measured by increasing the spectrometer dipole field to force elastic trajectories to trace those taken by the lower-energy inelastics at the production momentum setting.

<sup>10</sup>In reality, the measurement was performed down to  $E' \sim 0.8$  GeV since the number of electrons with lower energy is negligible.

<sup>11</sup>The rescattering in the HRS for PREX was analyzed by Chun-Min Jen, Syracuse University and all figures were taken from Jen's analysis

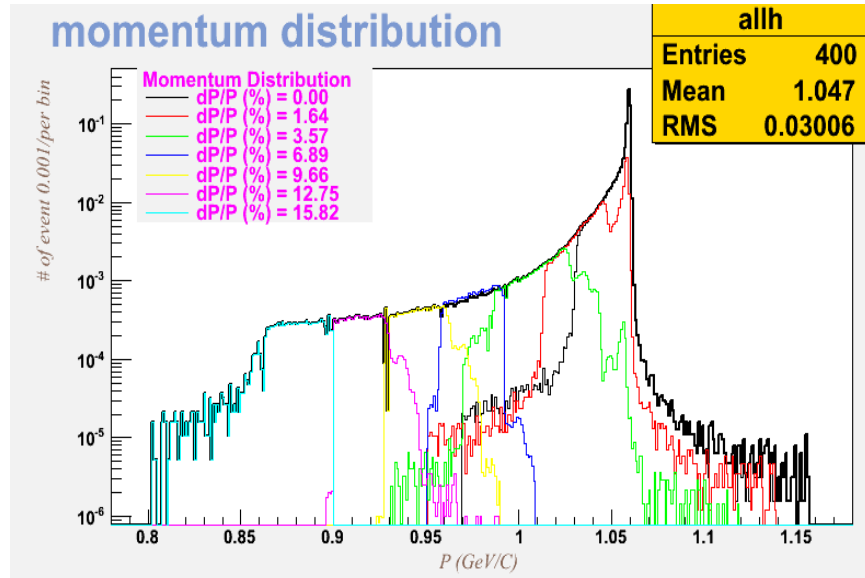


Figure 4.27: The histogram showing the normalized spectrum of scattered electrons as a function of scattered momentum [31]. The spectrum measurement was performed by lowering the dipole magnet to let lower-energy, inelastically scattered electrons to reach the main detectors.

Fig. 4.27 and Fig. 4.26 indicate that the rescattering fraction was small. The corresponding correction to the asymmetry was less than 0.1%.

#### 4.3.4 Summary of Corrections and Uncertainties from Background

Three main sources of background in PREX were carbon contamination, excited states of  $^{208}\text{Pb}$  contamination, and rescattering of inelastic electrons. Their corrections to the final asymmetry and their uncertainties are:

Source	Contamination (% in source)	Correction (ppb)	Error (ppb)
Carbon contamination	$6.3 \pm 0.6$	-8.8	2.6
Excited states of $^{208}\text{Pb}$	$<0.1$	0.0	0.0
Rescattering	$<0.1$	0.0	0.0

Table 4.25: Main sources of background in PREX and their corresponding corrections and errors to the final parity-violating asymmetry.

## 4.4 Asymmetry Analysis

PREX used the integrating technique to measure the asymmetry. The data were collected with the IHWP state being reversed once every 12 hours. Furthermore, a double Wien filter, which also performed as a slow helicity reversal, reversed its state once every few days. A total of 21 slugs<sup>12</sup> were collected during the experiment. The final data set consisted of a total of  $2 \times 10^7$  helicity-quadruplets. The corrected sign of the measured asymmetry depended on states of IHWP and double Wien filter. The sign of the asymmetry can be corrected by multiplying -1 if the state of the IHWP is in or the double Wien filter is left<sup>13</sup>.

The parity-violating asymmetry can be expressed as [64]

$$A_{PV} = \frac{1}{P_b} \frac{A_{corr} - P_b \sum_i A_i f_i}{1 - \sum_i f_i}. \quad (4.33)$$

The corrected detector asymmetry,  $A_{corr}$ , is given as

$$A_{corr} = A_{raw} - A_F \quad (4.34)$$

where  $A_{raw}$  is the helicity-correlated (HC) raw detector asymmetry and was normalized for beam intensity on a pulse-by-pulse basis. Thus any HC beam intensity asymmetry,  $A_I$ , caused by the beam intensity fluctuations has been already removed. R-HRS in  $A_{raw}$ .  $A_F$  is the false asymmetry and can be expressed as

$$A_F = A_{Fb} + A_{FT} \quad (4.35)$$

where  $A_{Fb}$  is the false asymmetry caused from differences in beam position, angle, and energy, while  $A_{FT}$  is the false asymmetry caused by the imperfect cancellation

---

<sup>12</sup>A slug is a period of time between two successive IHWP or Wien reversals

<sup>13</sup>The double Wien filter is left when the solenoid is  $90^\circ$ . On the other hand, the double Wien filter is right when the solenoid is  $-90^\circ$ .

of the asymmetry due to transverse beam polarization.  $P_b$  is the longitudinal beam polarization and  $f_i$  is the fractional background with asymmetry  $A_i$ . As discussed in the previous section, the only significant background for PREX was due to  $^{12}\text{C}$  contamination when  $f_i = 0.063$  and  $A_i = 817$  ppb. In this section, the asymmetry analysis will be discussed.

#### 4.4.1 Blinded Analysis

A blinded asymmetry analysis was performed in order to control experimenter's bias in extracting the physics asymmetry from the data. A hidden blinding offset was applied to the asymmetry in the analysis software, PAN, such that the true measured asymmetry was hidden from the experimenter to avoid the tempting to correct the result to achieve the "right answer". A character string was provided as an input to PAN and was used as an initial seed to a random number generator to produce a blinding offset  $B$  with a value between -1 and 1. The blinding offset was then scaled by a constant  $C$ , typically larger than the expected error on the asymmetry. The PAN database was supplied the sign of the slow reversal so that the blinding offset properly changed sign with the measured asymmetry. Thus, the blinded asymmetry used in all analysis was given by:

$$A_{blind} = A_{true} + (-1)^s BC \quad (4.36)$$

$s$  was 0 or 1 depending on the IHWP state. The blinding effect was only removed after all analysis had been completed.

#### 4.4.2 Raw Asymmetry ( $A_{raw}$ )

In PREX, the raw asymmetry ( $A_{raw}$ ) was formed from helicity-quartets<sup>14</sup>. To calculate  $A_{raw}$ , average hilicity-pairs were formed by averaging responses from the same

---

<sup>14</sup>The quartet will be in a pattern of RLLR or LRRL

helicity state in each quartet. Then, these averaged helicity-pairs were used to calculate  $A_{raw}$  by using the equation

$$A_{raw} = \frac{D_R/I_R - D_L/I_L}{D_R/I_R + D_L/I_L} \quad (4.37)$$

where  $D_{R(L)}$  are the integrated detector responses of the right (left) helicity state in a helicity-pair.  $I_{R(L)}$  are the beam current monitor (BCM) responses of the right (left) helicity state in a helicity-pair.

The asymmetry data were collected by the four focal plane detectors labeled det1, det2, det3, and det4. det1 was the lower detector in R-HRS, det2 was the upper detector in R-HRS, while det3 was the lower detector in L-HRS, and det4 was the upper detector in L-HRS. Not only the raw asymmetries from an individual detector were calculated but also combinations of detectors such as detectors in L-HRS(R-HRS) alone (detL(R)), upper(lower) two detectors alone (detUp(Lo)), and all four detectors (detAll) were used to calculate the raw asymmetries by using the equation

$$A_{raw}^X = \frac{\sum_i S_R^i w^i - \sum_i S_L^i w^i}{\sum_i S_R^i w^i + \sum_i S_L^i w^i} \quad (4.38)$$

where  $X = \{L,R,Up,Lo,All\}$ ,  $S_{R(L)}^i$  is the normalized  $i^{th}$  detector response integrated over the right (left) helicity window.  $w^i$  is the weight and equals 1 for PREX<sup>15</sup>.

The average detector asymmetry from each run was weighted by the width of the asymmetry distribution after the correction of beam modulation and the normalized beam intensity.

The  $A_{raw}^{all}$  measured during PREX (at an average  $Q^2 = 0.00906$  GeV $^2$ ) was

$$A_{raw}^{all} = +554.6 \pm 62.7 \text{ ppb} \quad (4.39)$$

---

<sup>15</sup>The weights corrected for differences in the size of the detector responses that arose primarily because of differences in the electronics used to read out the detectors. Unlike HAPPEX-III, which used both 16-bit and 18-bit ADC, all detectors in PREX were read out into a 18-bit ADC and gave approximately the same ADC channels at similar electron flux. Hence, the weight equals to 1 for PREX.

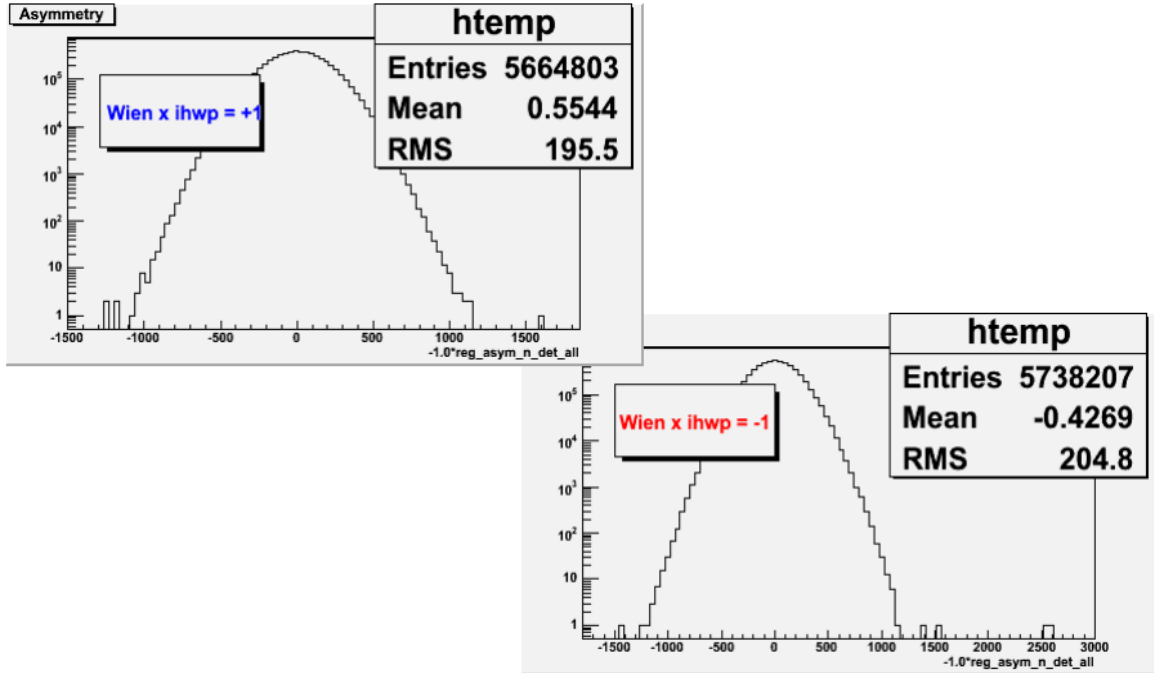


Figure 4.28: The figure shows the examples of the (blinded) raw asymmetries in two different states of double Wien filter and IHWP [4].

#### 4.4.3 Beam Intensity Asymmetry ( $A_I$ )

The beam intensity asymmetry,  $A_I$ , results due to the fluctuations in the beam intensity and can be expressed as

$$A_I = \frac{I_R - I_L}{I_R + I_L} \quad (4.40)$$

where  $I_{R(L)}$  is the integrated responses of the beam cavity monitors (BCM) for the right(left) helicity state of a helicity-pair. The raw asymmetry,  $A_{raw}$ , would include a false asymmetry due to  $A_I$ . To corrected for  $A_I$ , the  $A_{raw}$  was normalized by the integrated response of the BCM for each helicity state on a pulse-by-pulse basis as in Eq. 4.37.

For PREX, the beam intensity asymmetry,  $A_I$ , was measured to be

$$A_I = 84.0 \pm 1.3 \text{ ppb} \quad (4.41)$$

#### 4.4.4 False Beam Asymmetry from Beam Fluctuations ( $A_{Fb}$ )

The random fluctuations in the beam position, angle, and energy, changes the scattering cross section and thus lead to rate variations at the detectors. This leads to the increase in noise level in the data. Furthermore, if the fluctuations have a helicity correlated component, it can cause a false asymmetry,  $A_{Fb}$ . The random fluctuations in the beam parameters were the largest source of noise beyond counting statistics in  $A_{raw}$ . Typical beam jitter between complementary states in the window-quadruplets was less than 2 ppm in energy and 20  $\mu\text{m}$  in position. For PREX,  $A_{Fb}$  was extracted using the techniques of beam modulation (BM) and linear regression.

##### Beam Modulation (BM)

The beam modulation (BM) applied measured changes of the beam position, angle, and energy, and then measured the corresponding responses of the detectors and BPMs to these changes. These responses were expressed as

$$B_{i,j} = \frac{\partial M_i}{\partial C_j} \quad (4.42)$$

$$D_{k,j} = \frac{\partial d_k}{\partial C_j} \quad (4.43)$$

where  $i$  runs over the five beam parameters  $M_i(x, y, x', y', E)$  extracted from the responses of BPMs 4ax, 4ay, 4bx, 4by, and 12x respectively,  $j$  runs over the eight modulation coils, and  $k$  runs over the responses of the four detectors (det1, det2, det3, and det4), normalized to the response of the BCM ( $d_k = D_k/I_k$ ).

The responses of the BPMs and the  $k^{th}$  detector were used to calculate  $A_{Fb}$  in the

$k^{th}$  detector asymmetry as

$$(A_{Fb})_k = \frac{1}{2\bar{d}_k} \sum_{i=1}^5 \beta_{ik} \Delta M_{LR,i} \quad (4.44)$$

where  $\beta_{ik} = \partial d_k / \partial M_i$  or the BM coefficient is the average (normalized) response of the detector to the response of the  $i^{th}$  BPM to fluctuations in the beam parameters  $M$ .  $\Delta M_{LR,i}$  is the position difference ( $\Delta x, \Delta y$ ) obtained from the response of the  $i^{th}$  BPM to the fluctuations in the beam parameters  $M$ . The fluctuations in  $E$  was measured by BPM12x as HC position difference.  $\bar{d}_k = \frac{1}{2} \langle d_{R,k} + d_{L,k} \rangle$  is the response of the  $k^{th}$  detector averaged over the helicity states of a helicity-pair.

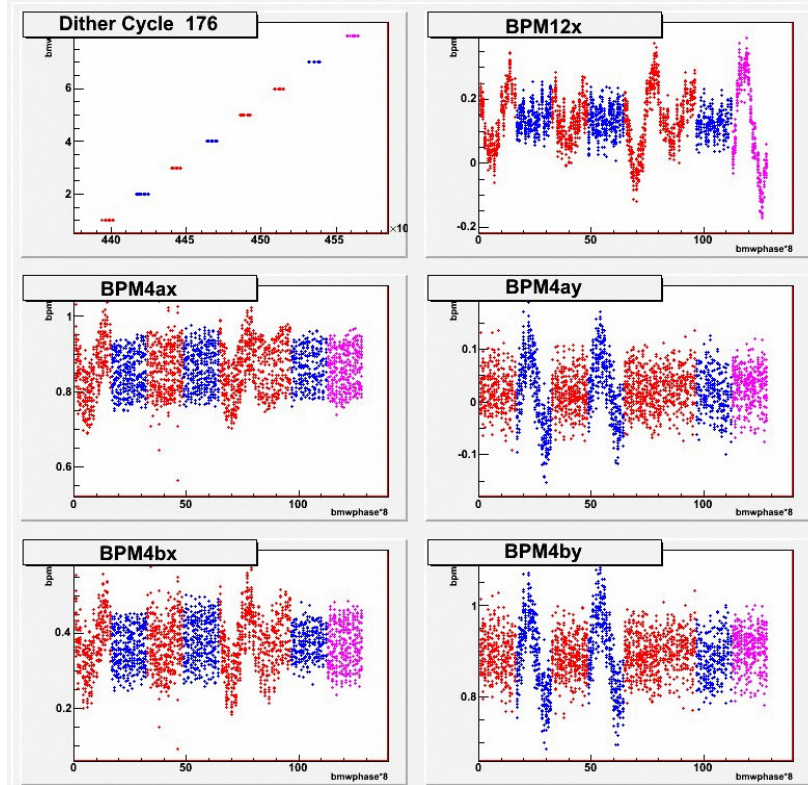


Figure 4.29: The beam modulation applied controlled changes of beam position and energy to measure the false beam asymmetries arising from random fluctuations. The traces in red are x-position modulation, blue are y-position modulation and magenta are energy modulation. BPM4a and BPM4b measured fluctuations in beam position, and BPM12x measured fluctuations in beam energy [71].

Fig. 4.29 illustrates the typical BPM responses during the beam modulation cycle. A complete cycle comprised of the beam excursion horizontally four times (red traces), vertically three times (blue traces), and in energy once (magenta trace). The responses of the target BPM4a and BPM4b were then used to extrapolate the beam position and angle responses at the target. The responses of the raw asymmetry due to the beam modulation would then be observed and related to the change in the beam position and energy at the target.

### Linear Regression

The regression technique uses a linear regression algorithm to minimize the correlation of the detector responses to the “natural” beam motion inferred from the responses of the beam monitors, and correct  $A_{raw}$  for  $A_{Fb}$ .

This method is referred to as the linear regression method because the slope of each beam parameter is determined using a least-squares (or linear  $\chi^2$  minimization) algorithm. For a one parameter regression, the slope is calculated as [52]:

$$b = \frac{\sum_i (y_i - \langle y \rangle)(x_i - \langle x \rangle)}{\sum_i (x_i - \langle x \rangle)^2} \quad (4.45)$$

where  $y$  is the dependent variable, in this case  $A_{PV}$ , and  $x$  is the independent variable such as the beam position or energy. The dependent variable is now regressed by removing its above calculated sensitivity to  $x$ :

$$y_i^{reg} = y_i - bx_i \quad (4.46)$$

For a two or more parameter regression, an iteration of this algorithm may be done, utilizing the regressed dependent variable in each step. For example, a three

parameter regression:

$$y_i^{reg2} = y_i^{reg} - b_1(x_1)_i \quad (4.47)$$

$$y_i^{reg3} = y_i^{reg2} - b_2(x_2)_i \quad (4.48)$$

These multiparameter linear regression accounts for corrections between independent variables.

#### **Summary of the False Beam Asymmetry from Beam Fluctuations ( $A_{Fb}$ )**

After the  $A_{Fb}$  correction from both beam modulation and linear regression, the noise in the resulting asymmetry  $A_{raw} - A_{Fb}$  was about 210 (180) ppm per quadruplet, when the beam current was of 50 (70)  $\mu\text{A}$ . This remaining noise was dominated by counting statistics, corresponding to a rate of about 1 GHz at a beam current of 70  $\mu\text{A}$ .

For PREX, the final  $A_{Fb}$  was measured to be

$$A_{Fb} = -39.0 \pm 5.9 \text{ ppb} \quad (4.49)$$

The uncertainty above was based on the self-consistency of the beam modulation and regression results, along with the resolution of the BPMs.

#### **4.4.5 False Beam Asymmetry from Transverse Beam Polarization ( $A_{FT}$ )**

Any transverse polarization present in the electrons results in a transverse beam asymmetry,  $A_T \cos \phi$ , where  $\phi$  is the HRS angle. In the case that the HRSs are not perfectly symmetric to cancel the  $A_T \cos \phi$  between the two HRSs, the transverse polarization of the beam will cause the false asymmetry  $A_{FT}$ . To observe  $A_{FT}$ , the electron beam-spin vector  $\vec{P}_e$  must have a component normal to the scattering plane defined by the unit vector  $\hat{k}$  perpendicular to the plane, where  $\hat{k} = \vec{k}/|\vec{k}|$ ;  $\vec{k} = \vec{k}_e \times \vec{k}_{out}$ ,

where  $\vec{k}_e$  and  $\vec{k}_{out}$  are the incident and scattered electron momenta respectively. The transverse beam asymmetry is then defined as

$$A_{FT} = \frac{\sigma_\uparrow - \sigma_\downarrow}{\sigma_\uparrow + \sigma_\downarrow} \quad (4.50)$$

where  $\sigma_{\uparrow(\downarrow)}$  is the cross section for beam electron spin parallel (antiparallel) to  $\hat{k}$ . For PREX, notches of Beryllium (Be) and additional detectors were used to determine the size of the transverse asymmetry [32]. Two 4 g Beryllium plugs were inserted up on HRS collimators, one on each spectrometer; in the top inside corner of the R-HRS collimator and in the bottom inside corner of the L-HRS collimator. These plugs induced energy losses in the elastically scattered electrons. As a result, the electrons transmitted through the plug followed a slightly different trajectory inside the HRSs than the elastically scattered electrons transmitted through the semi-circle opening, and were incident at a different physical location on the focal plane, where an additional detector was placed 1.2 m downstream of the focal plane on each arm to measure the transverse beam asymmetry. These detector measurements labeled *flumi1* and *flumi2* were included in the data streams for R-HRS and L-HRS respectively. Even though the values of *flumi1* and *flumi2* were close to zero, the  $A_{FT}$  detector location was found to be in the radiative tail of the elastically scattered electrons and hence, the measurement had hard-to-quantify uncertainty.

In order to measure  $A_{FT}$  with more accuracy, electron polarization entering the hall was changed from longitudinal polarization to transverse polarization by changing the double Wien filter settings. Then, the transverse asymmetry was measured using the two main quartz detectors in each arm. The results of  $A_{FT}$  quoted in the publication were from this method of measurement [3].

Since the main target in PREX was a combination of  $^{12}\text{C}$  and  $^{208}\text{Pb}$ , the net transverse asymmetry,  $A_{FT}$ , included the total effects from both  $^{12}\text{C}$  and  $^{208}\text{Pb}$  transverse

asymmetries. In addition to the Pb/D target, dedicated runs using a pure  $^{12}\text{C}$  and a pure  $^{208}\text{Pb}$  as targets were used to measure  $A_{FT}^C$  and  $A_{FT}^{Pb}$  respectively.

The transverse beam polarization asymmetries were measured to be

$$A_{FT}^{Pb} = +280 \pm 210 \text{ (stat)} \pm 140 \text{ (syst) ppb} \quad (4.51)$$

$$A_{FT}^C = -6490 \pm 360 \text{ (stat)} \pm 100 \text{ (syst) ppb} \quad (4.52)$$

The asymmetry from  $^{208}\text{Pb}$  is essentially zero within the uncertainties. As a result, the false asymmetry from the imperfect cancellation of  $A_{FT}^{Pb}$  between the two HRS detectors,  $A_{FT}$ , was negligible.

#### 4.4.6 Helicity-Correlated Beam Asymmetry and Position Differences

The helicity-correlated (HC) beam position difference of a helicity pair was calculated as

$$\Delta x = x_R - x_L \quad (4.53)$$

where  $x_{R(L)}$  is the beam position of the right (left) helicity state [64].

A statistically weighted average HC position difference was evaluated for the data collected during the whole experiment as

$$\langle \Delta x \rangle = \frac{\sum_i \epsilon_i \langle \Delta x \rangle_i w t_i}{\sum_i w t_i} \quad (4.54)$$

where  $i$  runs over the acceptable data runs. The parameters  $\epsilon_i = \pm 1$  accounts for the sign reversal in  $A_{raw}$  arising from IHWP state reversal.  $\langle \Delta x \rangle_i$  is the average HC position difference and  $w t_i$  is the statistical weight of the  $i^{th}$  run in the measurement

of  $A_{PV}$ , calculated as

$$wt_i = (\Sigma_j wt_j)_i = \left( \Sigma_j \frac{1}{(\sigma_{raw})_j^2} \right)_i \quad (4.55)$$

where  $j$  runs over data collected with only the L-HRS functional, only the R-HRS functional, and both HRSs functional for the  $i^{th}$  run.

The uncertainty in HC position differences is determined by the BPM resolution,  $BPM_{res}$ , as

$$\sigma_{\Delta\langle x \rangle} = \frac{BPM_{res}}{\sqrt{N}} \quad (4.56)$$

where  $N$  is the total number of helicity-pairs collected over the experiment. Since  $BPM_{res} \sim 2\mu m$ ,  $\sigma_{\Delta\langle x \rangle}$  is essentially negligible.

BPM	Position Differences (nm)
BPM4ax(nm)	3.78
BPM4ay(nm)	-0.17
BPM4bx(nm)	2.34
BPM4by(nm)	-0.20
BPM12x(nm)	0.42

Table 4.26: The table shows the helicity-correlated (HC) position differences averaged over the experiment.

As Table 4.26 indicates, the cumulative average for each BPM is small due to cancellations as a consequence of the slow helicity reversals, the IHWP reversal and the Wien filter adjustments. The slow helicity reversals reversed the sign of the physics asymmetry while leaving certain beam asymmetries unchanged. The differences in the beam position and energy, averaged over the course of PREX, were under 4 nm and 0.6 ppb respectively [64].

#### 4.4.7 Normalizations and Corrections to $A_{PV}$

##### Beam Polarization

During PREX, the beam polarization was measured using two independent methods, the Compton and the Møller polarimeters, as described in Section 3.6.3.

The average beam polarizations measured by the two methods were

Compton:  $88.20 \pm 0.12(\text{stat}) \pm 1.04(\text{syst}) \%$

Møller:  $90.32 \pm 0.07(\text{stat}) \pm 1.12(\text{syst}) \%$

Average:  $89.2 \pm 1.1 \%$

##### Non-Linearity

Non-linearities in instrumentation can result in the false asymmetries and systematic uncertainties in  $A_{PV}$  since the responses of the BCMs and BPMs determine  $A_I$ ,  $A_F$ , and  $A_{raw}$ . The non-linearities in the measurements of  $A_I$ ,  $A_F$ , and  $A_{raw}$  increases the systematic uncertainties in  $A_{PV}$  by [64]

$$(\sigma_{A_{PV}})_{alin} = \left( \sqrt{\sigma_{A_{raw}}^2 + \sigma_{A_I}^2 + \sigma_{A_F}^2} \right)_{alin} \quad (4.57)$$

with

$$(\sigma_{A_j})_{alin} = A_j \times (\text{inst})_{alin} \times \alpha \quad (4.58)$$

where  $A_j = \{A_{raw}, A_I, A_F\}$ ,  $(\text{instr})_{alin}$  is the amount of non-linearity in the apparatus that measured  $A_j$ , and  $\alpha$  is given by

$$\alpha = \frac{1}{P_b} \left( \frac{1}{1 - \sum_i f_i} \right) \quad (4.59)$$

where  $P_b$  is the beam polarization and  $f_i$  is the fractional background. The two main non-linearities arose from:

1. *Detector Non-Linearity*: The non-linearity in the detector photo-multiplier tubes (PMTs) was measured *in-situ* during the experiment, and *in bench* tests before and after the experiment, that mimicked running conditions. To check the non-linearity of the detector, a pair of LEDs were used. The first LED, the baseline, was cycled through 0% - 100% filters (in 20% increments). The second LED was pulsed at the helicity flip rate. All pulses from LEDs were kept constant for all filters. In principle, the asymmetry should be independent of filter sizes since the difference between two windows mechanically is the pulsed LED and that should be linear. Hence, for each high voltage setting on the PMTs, a line was fitted to the plot of the response of the detector and the filter size, and checked for a slope, which correlated to the non-linearity. For PREX, detector non-linearity was less than 1%.
2. *Beam Current Monitors (BCM) Non-Linearity*: The BCM non-linearity was extracted by plotting the double-difference (DD) of the HC beam intensity asymmetry measured by BCMs 1 and 2 ( $DD_{12}$ ) for various beam currents against the HC intensity asymmetry determined from the responses of either the detectors or the BPMs.  $DD_{12}$  is defined as:

$$DD_{12} = A_{BCM1} - A_{BCM2} \quad (4.60)$$

where  $A_{BCM1(BCM2)}$  is the charge asymmetry measured by the upstream (downstream) BCM. The detector or the BPM asymmetry was used to avoid correlations with the BCM measurements. The non-linearity in the response of the beam current monitors was determined to be less than 1.5%.

Source	Non-Linearity (% in source)	Correction (ppb)	Error (ppb)
Detectors	1.0	0.0	7.6
BCMs	1.5	0.0	1.5
<b>Total</b>	-	0.0	7.7

Table 4.27: The table shows the non-linearities in PREX and their associated correction and systematic uncertainties.

As indicated in Table 4.27, no correction was made for non-linearities of detectors or BCMs because these corrections were negligible. However, their corresponding systematic errors were included in the overall uncertainty of  $A_{PV}$ .

#### Summary of $A_{PV}$ Corrections and Systematic Errors

Source	Corr. (ppb)	Corr. (%)	Syst. Error (ppb)	Syst. Error (ppb)
<b>False Asymmetry</b>	<b>45.0</b>	<b>6.9</b>	<b>7.4</b>	<b>1.1</b>
$A_I$	84.0	12.8	1.5	0.2
$A_{Fb}$	-39.0	-5.9	7.2	1.1
$A_{FT}$	0.0	0.0	1.2	0.2
<b>Polarization</b>	<b>70.9</b>	<b>10.8</b>	<b>8.3</b>	<b>1.3</b>
<b>Background</b>	<b>-8.8</b>	<b>-1.3</b>	<b>2.6</b>	<b>0.4</b>
$^{12}\text{C}$	-8.8	-1.3	2.6	0.4
Excited States of $^{208}\text{Pb}$	0.0	0.0	0.0	0.0
Rescattering	0.0	0.0	0.0	0.0
<b>Linearity</b>	<b>0.0</b>	<b>0.0</b>	<b>7.7</b>	<b>1.2</b>
<b>Total</b>	<b>17.1</b>	<b>2.6</b>	<b>13.7</b>	<b>2.1</b>

Table 4.28: The table shows the corrections and their systematic errors in  $A_{PV}$  from various sources.

The total systematic uncertainty was only 2.1% of the  $A_{PV}$ , indicating that the systematic uncertainties were well under control during the experiment and the total systematic uncertainty was smaller than the proposed uncertainty of 3%.

#### 4.4.8 Corrected Asymmetry ( $A_{corr}$ )

The corrected asymmetry,  $A_{corr}$ , for PREX was calculated using Eq. 4.34.  $A_{corr}$  was corrected for false beam asymmetries,  $A_{Fb}$  and  $A_{FT}$ .  $A_{raw}$  already included correction for  $A_I$  as described in Section 4.4.3. False beam asymmetry ( $A_F$ ) only had the correction from the beam fluctuation asymmetry ( $A_{Fb}$ ) since the transverse beam asymmetry ( $A_{FT}$ ) was zero within uncertainty. Thus,  $A_F = A_{Fb}$ . As a result, the corrected asymmetry is  $A_{corr} = A_{raw} - A_{Fb}$  and the asymmetries evaluated via beam modulation and linear regression corrections were already the corrected asymmetries.

$\lambda/2$ plate	Spin Rotator	$A_{corr}$	$\delta A_{corr}$	$\chi^2/d.o.f$
OUT	RIGHT	606	113	1.03
IN	RIGHT	492	107	0.74
OUT	LEFT	565	95	1.12
IN	LEFT	687	92	1.03

Table 4.29: Values of  $A_{corr}$  and the statistical error, for each helicity reversal state and for the grand average. The  $\chi^2$  per degree of freedom for each average is also shown.

The corrected asymmetry,  $A_{corr}$ , was calculated to be

$$A_{corr} = +593.6 \pm 50.4 \text{ (stat)} \pm 9.4 \text{ (syst) ppb} \quad (4.61)$$

The helicity-pair distribution of the asymmetries for the complete data sample had negligible non-Gaussian tails over more than four orders of magnitude, indicating that the asymmetry distribution width was dominated by counting statistics.

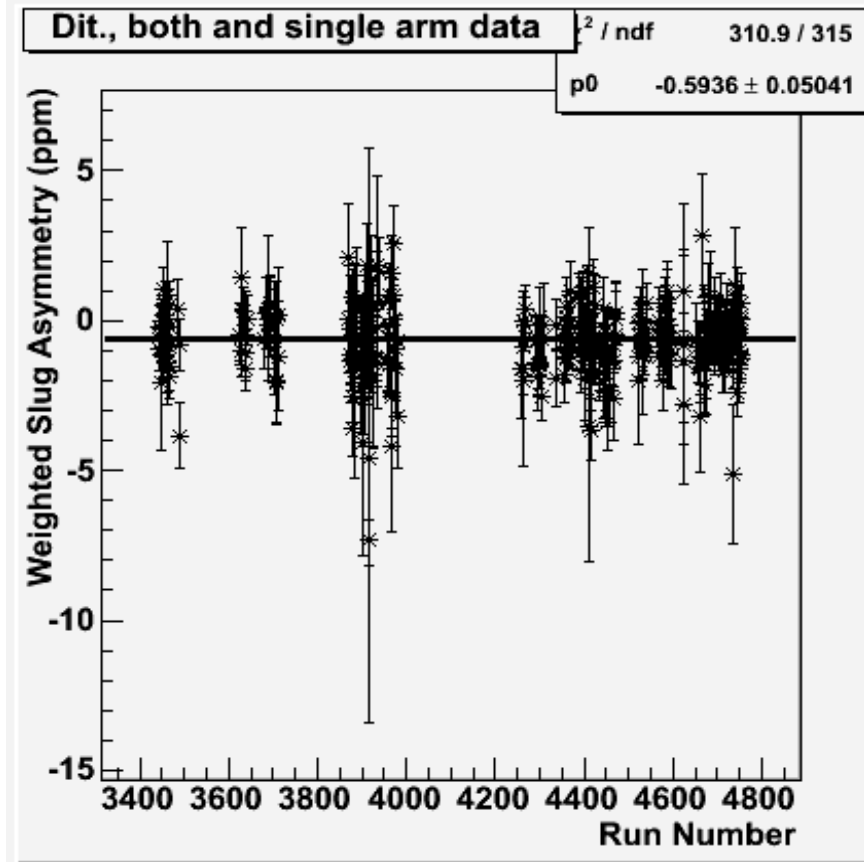


Figure 4.30: The figure shows the unblinded raw asymmetry for all asymmetry runs. The asymmetry for each run has been multiplied by +1 or -1 depending on the helicity state. The black horizontal line is the average value of the raw asymmetry. The average raw asymmetry shown must be multiplied by -1 to get the corrected sign [72].

#### 4.4.9 Calculation of $A_{PV}$

The parity-violating asymmetry was calculated using Eq. 4.33. The related quantities used in the calculation are summarized in the Table 4.30.

These values yield the final parity violating asymmetry for PREX at the average

Quantity	Value
$A_{corr}$	+593.6 ppb
Beam Polarization ( $P_b$ )	0.892
$f_C$	0.063
$A_C$	+817.0 ppb

Table 4.30: The table shows the values for quantities used to calculate a parity-violating asymmetry ( $A_{PV}$ )

$Q^2$  value of  $0.00880 \pm 0.00011$  GeV $^2$ <sup>16</sup> as

$$A_{PV} = +656 \pm 60 \text{ (stat)} \pm 14 \text{ (syst)} \text{ ppb} \quad (4.62)$$

$$= +656 \pm 9\% \text{ (stat)} \pm 2\% \text{ (syst)} \text{ ppb} \quad (4.63)$$

#### 4.4.10 Finite Acceptance Effects and Energy Loss Correction for $Q^2$

For PREX, the HRSs accepted elastically scattered electrons over a solid angle of approximately 5 msr. Due to this, the asymmetry measured is a combination of asymmetries over a range of  $Q^2$  values across the acceptance, which average to the  $Q^2$  value quoted above. Furthermore, the average  $Q^2_{focal}$  and the average  $Q^2_{vertex}$  are different in such a way that the average  $Q^2_{focal}$  contains the effects of energy losses in the target and during transporting to the detectors through the HRSs, while the average  $Q^2_{vertex}$  does not contain any of these energy losses. The average value of  $Q^2_{vertex}$  was calculated by using Hall A Monte Carlo (HAMC) simulation.

##### Energy Loss Correction for $Q^2$

As indicated in Fig. 4.31, the agreement between the measured  $Q^2_{focal}$  and the simulated  $Q^2_{focal}$  using HAMC is better than 2%. This demonstrates that the experimental setup and the particle transport through the spectrometer is accurately simulated in HAMC. Based on this, HAMC was used to calculate the effect on average  $Q^2$  due

---

<sup>16</sup>The average  $Q^2$  quoted here is after the finite acceptance correction and lower than the measured average  $Q^2 = 0.00906$  GeV $^2$ . Details of the correction are described in Section 4.4.10.

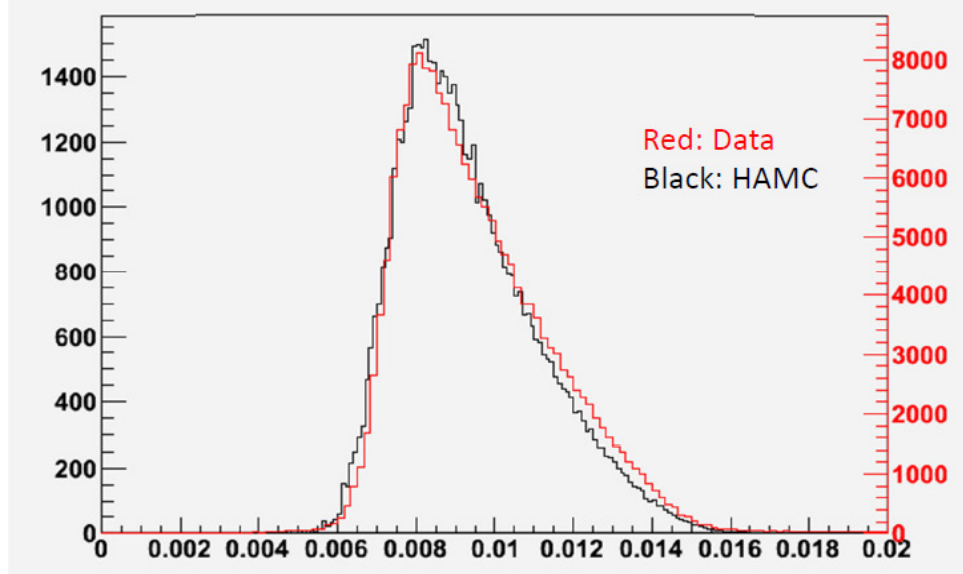


Figure 4.31: The figure shows the comparison between the measured  $Q^2_{focal}$  (red) and the simulated  $Q^2_{focal}$  using HAMC (black).

to energy loss and multiple scattering. Fig. 4.32 shows the HAMC simulated  $Q^2_{focal}$  and  $Q^2_{vertex}$ .

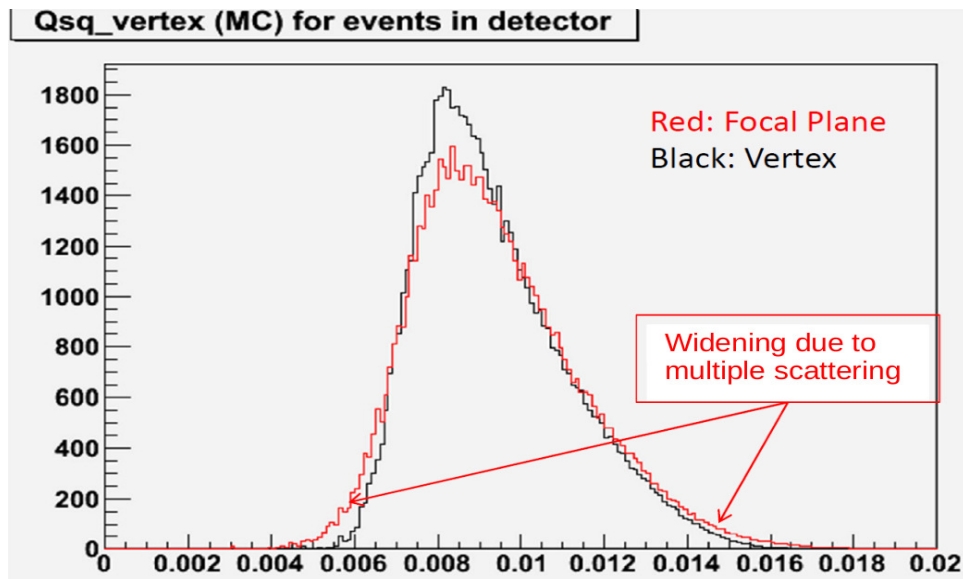


Figure 4.32: The figure shows the comparison between the simulated  $Q^2_{focal}$  (red) and the simulated  $Q^2_{vertex}$  (black), generated by HAMC.

As the Fig. 4.32 indicates, the  $Q_{focal}^2$  was widened, with respect to  $Q^{vertex}$ , due to multiple scattering of the electrons. This caused an increase in the average  $Q^2$  from the vertex ( $Q_{vertex}^2 = 0.00880 \text{ GeV}^2$ ) to the focal plane ( $Q_{focal}^2 = 0.00906 \text{ GeV}^2$ ) by [59] [60]

$$\frac{Q_{focal}^2 - Q_{vertex}^2}{Q_{vertex}^2} = \frac{0.00906 - 0.00880}{0.00880} = 3.0\% \quad (4.64)$$

### Finite Acceptance Effects for $A_{PV}$

The asymmetry values we present in this work are the average asymmetries, averaged over the experimental acceptance. The spectrometer acceptance function  $\epsilon(\theta)$  characterizes the probability, as a function of scattering angle  $\theta$ , for an electron to reach the detector after elastically scattering off  $^{208}\text{Pb}$ . The asymmetry averaged over the acceptance is [2]

$$\langle A \rangle = \frac{\int d\theta \sin \theta A(\theta) \frac{d\sigma}{d\Omega} \epsilon(\theta)}{\int d\theta \sin \theta \frac{d\sigma}{d\Omega} \epsilon(\theta)} \quad (4.65)$$

where  $\frac{d\sigma}{d\Omega}$  is the cross section. The observed distribution of events corrected for the cross section, the background from the carbon backing, and the effects of multiple scattering was used to extract  $\epsilon(\theta)$  by HAMC. The corrections for energy loss in the target were negligible.

The acceptance function,  $\epsilon(\theta)$ , was used to calculate  $\langle A \rangle$  in Eq. 4.65 for several mean-field models, which would be used in the  $R_n$  calculation described in the following section.

## 4.5 Calculation of Weak Charge Radius and Neutron Radius

The distorted wave electron scattering was used to extract the weak charge form factor  $F_W(\bar{q})$ , the weak charge radius  $R_W$ , the neutron radius  $R_n$  of  $^{208}\text{Pb}$ , and the

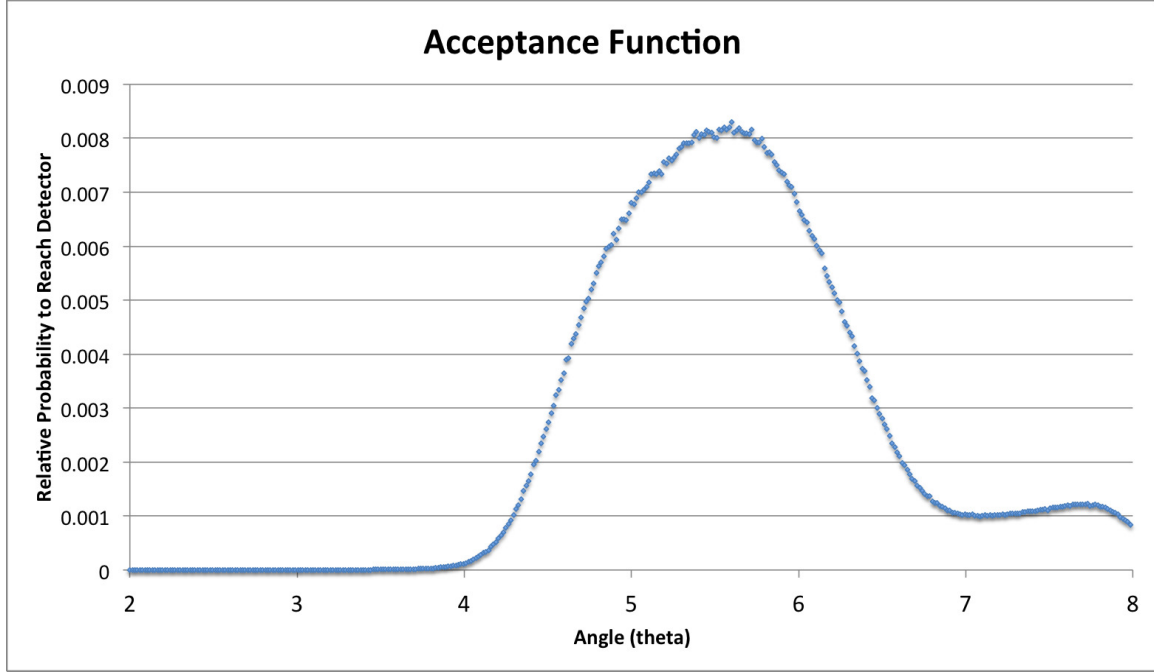


Figure 4.33: The figure shows the acceptance function as a function of scattering angles for PREX using HAMC [47].

neutron skin  $R_n - R_p$  of  $^{208}\text{Pb}$ . This section will describe the methods used to extract these quantities.

#### 4.5.1 Weak Charge Radius

In the Born approximation, one can determine the weak form factor directly from the measured  $A_{PV}$ . However, Coulomb distortions make  $A_{PV}$  sensitive to the weak form factor for a range of momentum transfer  $q$  [26]. Thus, the ability to understand the relationship between the shape of the weak form factor and the momentum transfer  $q$  in order to determine the value of the form factor at the average momentum transfer  $\bar{q}$  is very important. In the case of PREX, which had the scattering angles in the range of  $3.5^\circ$  to  $8^\circ$ ,

$$\bar{q} = \langle Q^2 \rangle^{1/2} = 0.475 \pm 0.003 \text{ fm}^{-1} \quad (4.66)$$

The starting point for the procedures to extract  $R_W$  is the definition of the weak form factor,  $F_W(q)$ , as the Fourier transform of  $\rho_W(q)$ ,

$$F_W(q) = \frac{1}{Q_W} \int d^3r \frac{\sin(qr)}{qr} \rho_W(r) \quad (4.67)$$

where  $Q_W$  is the weak charge of  $^{208}Pb$  and  $\rho_W(r)$  is the weak charge density of  $^{208}Pb$ , initially assumed to have a Wood-Saxon form<sup>17</sup> with parameters  $\rho_0$ ,  $R$ , and  $a$ ,

$$\rho_W(r) = \frac{\rho_0}{1 + e^{(r-R)/a}} \quad (4.68)$$

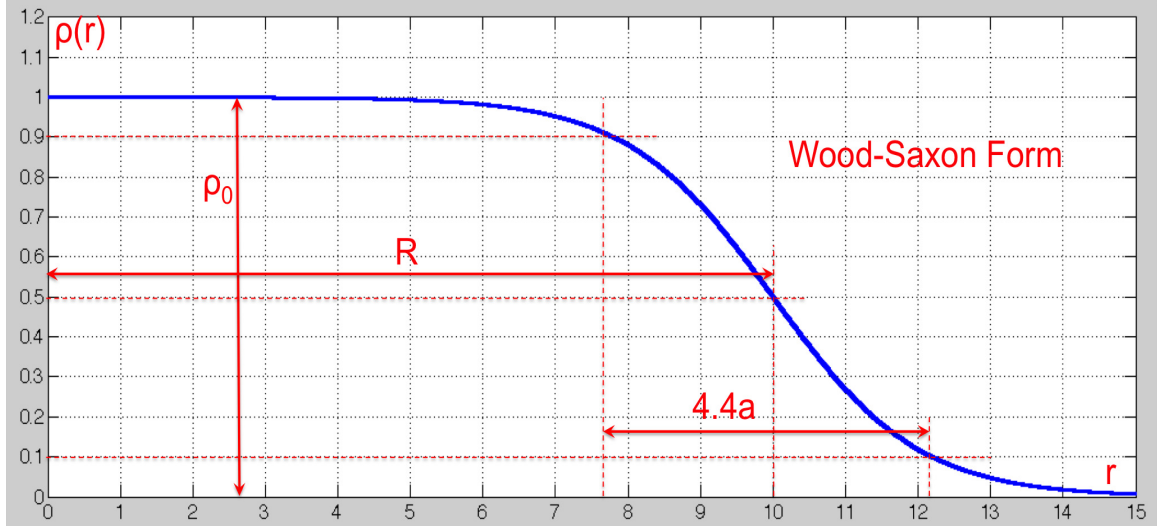


Figure 4.34: The figure shows the wood-saxon form of  $\rho(r) = \frac{\rho_0}{1+e^{(r-R)/a}}$ . The parameter  $\rho_0$  is the maximum of  $\rho(r)$  (in this case, 1). The parameter  $R$  is the value of  $r$  such that  $\rho(r) = \rho_0/2$ . The difference in  $r$  such that  $\rho(r)$  decreases from  $0.9\rho_0$  to  $0.1\rho_0$  equals to  $4.4a$ .

The weak density is normalized to the weak charge such that  $Q_W = \int d^3r \rho_W(r)$  and the weak form factor is normalized such that  $F_W(q = 0) = 1$ . The procedure is to calculate  $A_{PV}(\theta)$ , including full Coulomb distortion, assuming  $\rho_W(r)$  from Eq. 4.68 [25]. Then,  $A_{PV}(\theta)$  is averaged over laboratory scattering angle  $\theta$  using the

<sup>17</sup>This form is used only to access the sensitivity to the shape of the form factor and our results will be independent of this assumed form.

experimental acceptance  $\epsilon(\theta)$ ,

$$\langle A \rangle = \int \frac{d\theta \sin(\theta) \epsilon(\theta) \frac{d\sigma}{d\Omega} A_{PV}}{d\theta \sin(\theta) \epsilon(\theta) \frac{d\sigma}{d\Omega}} \quad (4.69)$$

where  $\frac{d\sigma}{d\Omega}$  is the unpolarized elastic cross section. Then,  $R$  is adjusted until the calculated  $\langle A \rangle$  agrees with the experimental result. The following table shows the value of  $R$  and  $a$  as predicted by the least squares fits of Wood Saxon form to theoretical mean field model weak charge densities<sup>18</sup>.

Mean Field Force	$R$ (fm)	$a$ (fm)
Skyrme I	6.655	0.564
Skyrme III	6.820	0.613
Skyrme SLY4	6.700	0.668
FSUGold	6.800	0.618
NL3	6.896	0.623
NL3p06	6.730	0.606
NL3m05	7.082	0.605
<b>Average</b>		<b>0.61±0.05</b>

Table 4.31: Least squares fits of Wood Saxon parameters to theoretical mean field model weak charge densities.

For a central value of  $a = 0.6$  fm, the central value of  $R$  is 6.982 fm. From Eq. 4.68, which reproduces  $A_{PV}^{Pb}$ ,  $F_W(\bar{q})$  is calculated using Eq. 4.67. This procedure fully includes Coulomb distortions and depends slightly on the assumed surface thickness  $a$ . Using a central value of  $a = 0.6$  fm,

$$F_W(\bar{q}) = 0.204 \pm 0.028 \text{ (exp)} \pm 0.001 \text{ (mod)} \quad (4.70)$$

The first experimental error is from adding the statistical and systematic errors in quadrature. The second model error is from varying  $a$  by  $\pm 0.05$  fm. This small error in model assumption shows that the extracted form factor is independent of the assumed shape of the weak charge density, in this case, the Wood Saxon form.

---

<sup>18</sup>These models span a very large range of neutrons radii  $R_n$ .

### Calculation of Weak Charge Radius by the Wood-Saxon Form

To calculate the weak charge radius by the Wood-Saxon form, the central value of  $a = 0.6$  fm and the central value of  $R = 6.982$  fm are used. The RMS radius of the weak charge density,  $R_W$ , can be expressed by

$$R_W^2 = \frac{1}{Q_W} \int d^3r r^2 \rho_W(r) \quad (4.71)$$

where  $Q_W = \int d^3r \rho_W(r)$  and  $\rho_W(r)$  is expressed in Eq. 4.68.

The value of the weak charge radius calculated by the Wood-Saxon form using above conditions is

$$R_W = 5.850 \pm 0.181 \text{ (exp)} \pm 0.070 \text{ (mod)} \text{ fm} \quad (4.72)$$

Here, the first experimental error is from adding the statistical and systematic errors of the  $A_{PV}$  measurement in quadrature. The second model error is from varying  $a$  by  $\pm 0.05$  fm.

### Calculation of Weak Charge Radius by the Helm Model

The Helm model, which has proven very useful for analyzing unpolarized electron scattering form factors, could be used to extract  $R_W$  with a smaller model uncertainty than the model uncertainty from the Wood-Saxon form. In this model, the diffraction radius and surface thickness extracted from the density form factor are mainly sensitive to the nucleonic distribution in the surface region, and they are practically independent of shell fluctuations in the nuclear interior. The robustness of the Helm-model parameters and their simple geometric interpretation make this model a very attractive tool when characterizing density distributions [51].

In Helm model, the nucleonic density is approximated by a convolution of a sharp-

surface density,  $\Theta(r)$ , with radius  $R_0$  with the Gaussian profile, i.e.,

$$\rho_W(r) = \int d^3r' f_G(r - r') \rho_0 \Theta(R_0 - |r'|) \quad (4.73)$$

where

$$f_G(r) = \frac{1}{(2\pi)^{3/2}\sigma^3} e^{-r^2/2\sigma^2} \quad (4.74)$$

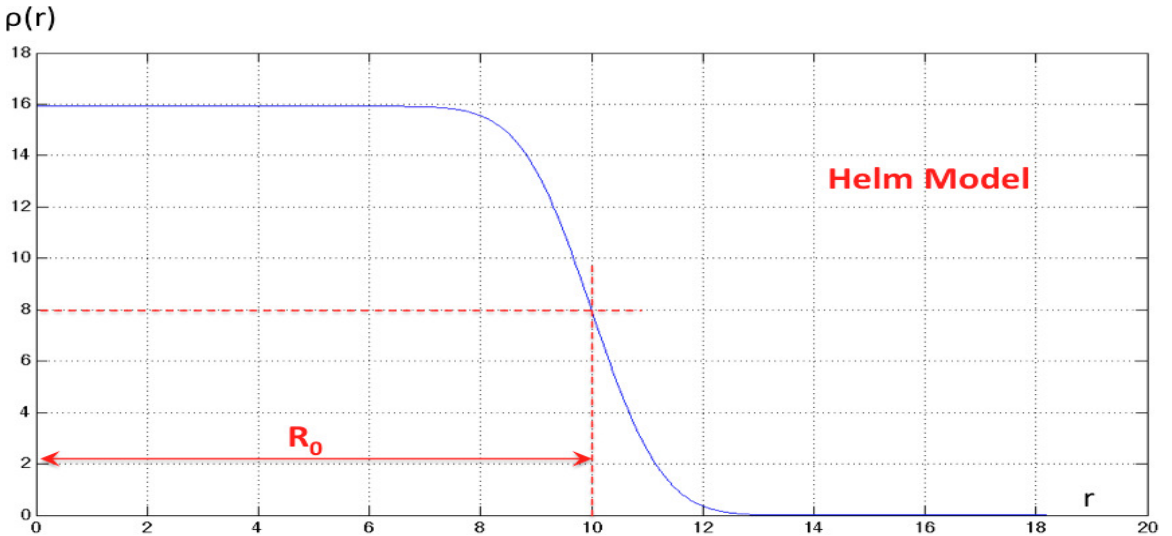


Figure 4.35: The figure shows the Helm model of  $\rho_W(r) = \int d^3r' f_G(r - r') \rho_0 \Theta(R_0 - |r'|)$  where  $f_G(r) = \frac{1}{(2\pi)^{3/2}\sigma^3} e^{-r^2/2\sigma^2}$ . The parameters used in this plot are;  $R_0 = 10$ ,  $\sigma = 1$ , and  $\rho_0 = 1$ .

The radius in  $R_0$  is the diffraction (box-equivalent) radius, and the folding width  $\sigma$  models the surface thickness. The density  $\rho_0$  is given by

$$\rho_0 = \frac{3N}{4\pi R_0^3} \quad (4.75)$$

hence the Helm density is normalized to the particle number  $N$ . The advantage of the Helm model is that folding becomes a simple product in Fourier space, thus

yielding [26],

$$F_W(q) = \frac{3}{qR_0} j_1(qR_0) e^{-\sigma^2 q^2/2} \quad (4.76)$$

where  $j_1(x) = \sin(x)/x^2 - \cos(x)/x$  a spherical Bessel function. The width  $\sigma$  includes the contributions from both the surface thickness of the point nucleon densities and the single-nucleon form factor. The weak charge density can be expressed in coordinate space as,

$$\rho_W(r) = \frac{3Q_W}{8\pi R_0^3} \left\{ \operatorname{erf}\left(\frac{R_0+r}{\sqrt{2}\sigma}\right) - \operatorname{erf}\left(\frac{r-R_0}{\sqrt{2}\sigma}\right) + \sqrt{\frac{2}{\pi}} \frac{\sigma}{r} \left( e^{-\frac{1}{2}(\frac{r+R_0}{\sigma})^2} - e^{-\frac{1}{2}(\frac{r-R_0}{\sigma})^2} \right) \right\} \quad (4.77)$$

The RMS radius of the weak charge density  $R_W$  is

$$R_W^2 = \frac{1}{Q_W} \int d^3r r^2 \rho_W(r) \quad (4.78)$$

The above expression can be reduced to

$$R_W^2 = \frac{3}{5}(R_0^2 + 5\sigma^2) \quad (4.79)$$

Within the Helm model, if one determined the location of the zero of the form factor  $q_0$  in addition to Eq. 4.70, this would uniquely fix both  $R_0$  and  $\sigma$ , and so determine  $R_W$ . The following table shows the values of  $\sigma$  determined by the least squares fits of the Helm density to seven mean field models.

The average of  $\sigma$  for seven mean field densities is  $1.02 \pm 0.09$  fm. Thus,

$$R_W = 5.826 \pm 0.181 \text{ (exp)} \pm 0.027 \text{ (mod)} \text{ fm} \quad (4.80)$$

The larger experimental error is from adding the statistical and systematic errors in

Mean Field Force	$R_0$ (fm)	$\sigma$ (fm)
Skyrme I	6.792	0.943
Skyrme III	6.976	1.024
Skyrme SLY4	6.888	1.115
FSUGold	6.961	1.028
NL3	7.057	1.039
NL3p06	6.886	1.010
NL3m05	7.231	1.012
<b>Average</b>		<b>1.02±0.09</b>

Table 4.32: Least squares fits of Helm parameters to theoretical mean field model weak charge densities.

quadrature, which the model error comes from the coherent sum of the assumed  $\pm 0.09$  fm uncertainty in  $\sigma$  and the  $\pm 0.001$  model error in  $F_W$ . This suggests that the uncertainties in surface thickness are much less important for  $R_W$  than the present experimental error.

Comparison of  $R_W$  values in Eq. 4.72 and Eq. 4.80 show that the two values agree within uncertainties. However, the Helm model gives smaller model error, as expected, by about a factor of three. Thus, the value of the  $R_W$  calculated by the Helm model will be used for later analyses in this chapter.

By comparing Eq. 4.80 to the experimental charge radius of the  $^{208}\text{Pb}$  nucleus,  $R_{ch} = 5.503 \pm 0.006$  fm [17], this implies a “weak charge skin” of thickness

$$R_W - R_{ch} = 0.323 \pm 0.181 \text{ (exp)} \pm 0.027 \text{ (mod)} \text{ fm} \quad (4.81)$$

Fig. 4.36 shows a Helm model weak charge density that is consistent with the PREX measurement. The figure shows an uncertainty range from the experimental error and model uncertainty from the assumed  $\pm 0.09$  fm uncertainty in  $\sigma$ .

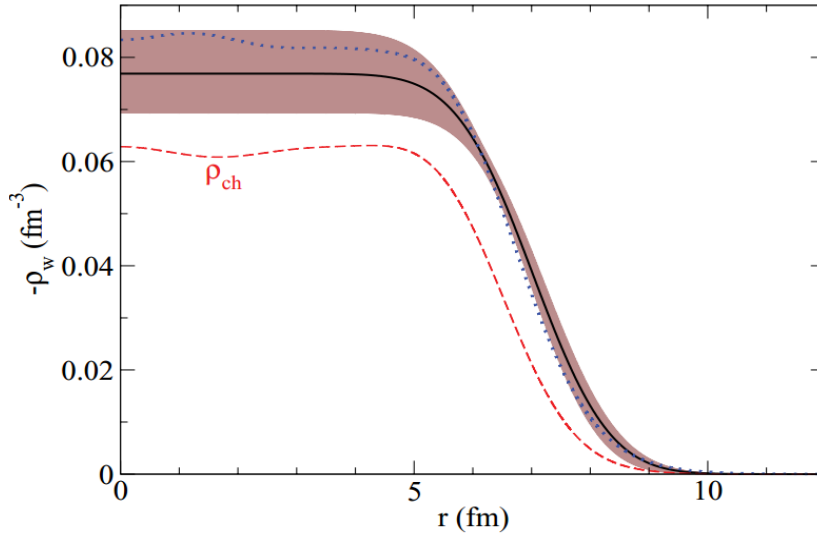


Figure 4.36: Helm model weak charge density  $-\rho_W(r)$  of  $^{208}\text{Pb}$  that is consistent with the PREX result (solid black line). The brown error band shows the incoherent sum of experimental and model errors. The red dashed curve is the experimental charge density  $\rho_{ch}$  and the blue dotted curve shows a sample mean-field result based on the FSUGold interaction [68].

#### 4.5.2 Neutron Radius

Two methods were used to extract the values of the neutron radius  $R_n$  in PREX. One is to calculate  $R_n$  using the previous calculated  $R_W$  and the Helm model representing theoretical mean-field densities. The second method is to directly use the least squares fit of the parity-violating asymmetry  $A_{PV}$  versus the neutron radius  $R_n$  predicted by the distorted-wave calculations for seven mean-field neutron densities.

##### Neutron Radius by Helm Model

To extract  $R_n$  for  $^{208}\text{Pb}$  from  $R_W$ , the relationship between the point proton radius  $R_p$  of the  $^{208}\text{Pb}$  nucleus and the measured charge radius  $R_{ch}$  [56] can be expressed by

$$R_{ch}^2 = R_p^2 + \langle r_p^2 \rangle + \frac{N}{Z} \langle r_n^2 \rangle + \frac{3}{4M^2} + \langle r^2 \rangle_{so} \quad (4.82)$$

The charge radius of a single proton is  $\langle r_p^2 \rangle = 0.769 \pm 0.002 \text{ fm}^2$  and that of a neutron is  $\langle r_n^2 \rangle = -0.116 \pm 0.005 \text{ fm}^2$  [62]. The contribution of spin-orbit currents to  $R_{ch}$  is small because of cancellations between protons and neutrons,  $\langle r^2 \rangle_{so} = -0.028 \text{ fm}^2$ , while  $M$  is the nucleon mass, which makes the Darwin contribution  $3/4M^2$  also small.

For  $^{208}\text{Pb}$ ,  $R_{ch} = 5.503 \pm 0.006 \text{ fm}$ , and from  $R_{ch}^2 = R_p^2 + 0.5956 \text{ fm}^2$  [15] [17],

$$R_p = 5.449 \pm 0.006 \text{ fm} \quad (4.83)$$

For the weak charge density of a spin-zero nucleus, neglecting meson exchange and spin-orbit currents, the density can be expressed as,

$$\rho_W(r) = 4 \int d^3r' [G_n^Z(|\vec{r} - \vec{r}'| \rho_n(r') + G_p^Z(|\vec{r} - \vec{r}'| \rho_p(r'))] \quad (4.84)$$

Here, the density of weak charge in a single proton  $G_p^Z(r)$  or neutron  $G_n^Z(r)$  is the Fourier transform of the nucleon (electric) Sachs form factor  $G_p^Z(Q^2)$  and  $G_n^Z(Q^2)$ . These describe the coupling of a  $Z^0$  boson to a proton or a neutron,

$$4G_p^Z = q_p G_E^p + q_n G_E^n - G_E^s, \quad (4.85)$$

$$4G_n^Z = q_n G_E^p + q_p G_E^n - G_E^s \quad (4.86)$$

At tree level, the weak nucleon charges are  $q_n^0 = -1$  and  $q_p^0 = 1 - 4 \sin^2(\theta_W)$ . The radiative corrections are included using the values  $q_n = -0.9878$  and  $q_p = 0.0721$  based on the up  $C_{1u}$  and down  $C_{1d}$  quark weak charges [26].  $G_E^p(r)$  and  $G_E^n(r)$  are the Fourier transform of the proton and neutron electric form factors respectively and have the total charge  $\int d^3r G_E^p(r) = 1$  and  $\int d^3r G_E^n(r) = 0$ .  $G_E^s$  describes strange quark contributions to the nucleon's electric form factor.

The point neutron RMS radius,  $R_n$ , can then be related to  $R_W$  by

$$R_n^2 = \frac{Q_W}{q_n N} R_W^2 - \frac{q_p Z}{q_n N} R_{ch}^2 - \frac{Z}{N} \langle r_n^2 \rangle + \frac{Z + N}{q_n N} \langle r_s^2 \rangle \quad (4.87)$$

where  $\langle r_s^2 \rangle = \int d^3r' r'^2 G_E^s(r')$  is the square of the nucleon strangeness radius and  $Q_W = \int d^3r \rho_W(r) = N q_n + Z q_p = -118.55$ . This yields

$$R_n^2 = 0.9525 R_W^2 - 1.671 \langle r_s^2 \rangle + 0.7450 \text{ fm}^2 \quad (4.88)$$

The strangeness radius of the nucleon  $\langle r_s^2 \rangle^{1/2}$  is constrained by experimental data and their global analysis. For  $Q^2 < 0.11 \text{ GeV}^2$  gives  $\langle r_s^2 \rangle = -6fG_E^s/dQ^2 = 0.02 \pm 0.04 \approx \pm 0.04 \text{ fm}^2$ .

Hence, the neutron radius measured by PREX is

$$R_n = 5.751 \pm 0.175 \text{ (exp)} \pm 0.026 \text{ (mod)} \pm 0.005 \text{ (str)} \text{ fm} \quad (4.89)$$

The small third uncertainty is from possible strange quark contributions. The neutron radius  $R_n$  is slightly smaller than  $R_W$  because of the nucleon's size. Again, the neutron radius  $R_n$  is larger than the proton radius  $R_p$ , and this confirms the existence of the neutron skin. The thickness of the neutron skin extracted using the Helm model is

$$R_n - R_p = 0.302 \pm 0.175 \text{ (exp)} \pm 0.026 \text{ (mod)} \pm 0.005 \text{ (str)} \text{ fm} \quad (4.90)$$

### Neutron Radius by the Least Squares Fit

Seven nonrelativistic and relativistic mean-field models that have charge densities and binding energies in good agreement with PREX were chosen. These models span a large range in  $R_n$ . The process to extract  $R_n$  starts by solving the Dirac equation for an electron scattering from  $\rho_W$  and the experimental  $\rho_{ch}$ , and the resulting  $A_{PV}(\theta)$  integrated over the acceptance. The results are shown as open circles in the Fig. 4.37.

The importance of Coulomb distortions is emphasized by indicating results from plane-wave calculations, which are not all contained within the vertical axis range.

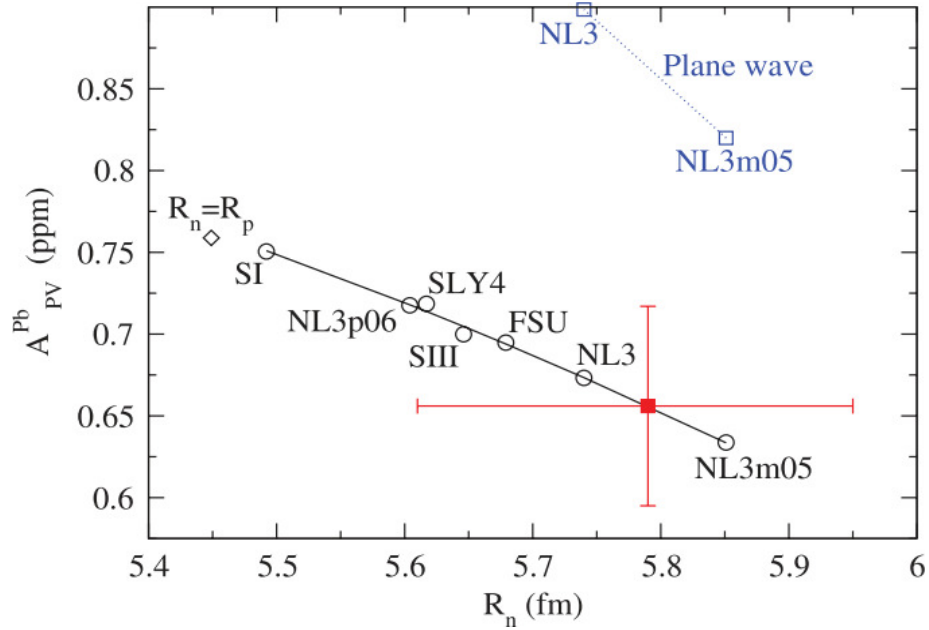


Figure 4.37: Result of the asymmetry in PREX (red square) versus neutron point radius  $R_n$  in  $^{208}\text{Pb}$ . The horizontal (vertical) red line shows the error in  $A_{PV}$  ( $R_n$ ) measurement. Distorted-wave calculations for seven mean-field neutron densities are circles while the diamond marks the expectation for  $R_n = R_p$ . The blue squares show plane wave impulse approximation results.

The least squares fit of the model results yields

$$R_n \approx 6.156 + 1.675\langle A \rangle - 3.420\langle A \rangle^2 \text{ fm} \quad (4.91)$$

where  $\langle A \rangle$  is in ppm.

By using the measured  $A_{PV}$ , the neutron radius is calculated to be

$$R_n = 5.78_{-0.18}^{+0.16} \text{ fm} \quad (4.92)$$

Since a point-proton radius,  $R_p$ , is accurately measured to be  $5.45 \pm 0.01$  fm, this

implies a neutron skin of

$$R_n - R_p = 0.33_{-0.18}^{+0.16} \text{ fm} \quad [2] \quad (4.93)$$

The small difference between the values of  $R_n$  calculated by the least squares fit and by the Helm model arises because of small limitations of the Helm model in representing theoretical mean-field densities. For example, the Helm model does not have the correct exponential behavior at large distances.

PREX successfully measured values of  $R_n$  and  $R_n - R_p$  and becomes the first electroweak experiment to use the parity-violating elastic electron scattering to measure these quantities. Not only PREX measured  $R_n$  with high precision but also confirmed the existence of the neutron skin as predicted for neutron-rich matters. The results have a wide useful range in applications to astronomy and high energy physics.

## Chapter 5

# Results and Conclusions

This chapter presents results and conclusions from PREX, the corresponding weak charge radius, the neutron radius, and the neutron skin of  $^{208}\text{Pb}$ . Also included in this chapter is a discussion on accomplishments and important issues occurred during the experiment, and possible improved parity-violating experiments in the future.

### 5.1 Parity-Violating Asymmetry ( $A_{PV}$ )

The in-depth details on the asymmetry analysis are given in Section 4.4. The final parity-violating asymmetry for PREX after the corrections for the false asymmetries was

$$A_{PV} = +656 \pm 60 \text{ (stat)} \pm 14 \text{ (syst)} \quad \text{ppb} \quad (5.1)$$

$$= +656 \pm 9\% \text{ (stat)} \pm 2\% \text{ (syst)} \quad \text{ppb} \quad (5.2)$$

at the average  $Q^2 = 0.00880 \pm 0.00011 \text{ GeV}^2$ .

The systematic errors and their corrections to the  $A_{PV}$  are summarized in the following table.

Source	Corr. (ppb)	Corr. (%)	Syst. Error (ppb)	Syst. Error (ppb)
<b>False Asymmetry</b>	<b>45.0</b>	<b>6.9</b>	<b>7.4</b>	<b>1.1</b>
$A_I$	84.0	12.8	1.5	0.2
$A_{Fb}$	-39.0	-5.9	7.2	1.1
$A_{FT}$	0.0	0.0	1.2	0.2
<b>Polarization</b>	<b>70.9</b>	<b>10.8</b>	<b>8.3</b>	<b>1.3</b>
<b>Background</b>	<b>-8.8</b>	<b>-1.3</b>	<b>2.6</b>	<b>0.4</b>
$^{12}\text{C}$	-8.8	-1.3	2.6	0.4
Excited States of $^{208}\text{Pb}$	0.0	0.0	0.0	0.0
Rescattering	0.0	0.0	0.0	0.0
<b>Linearity</b>	<b>0.0</b>	<b>0.0</b>	<b>7.7</b>	<b>1.2</b>
<b>Total</b>	<b>17.1</b>	<b>2.6</b>	<b>13.7</b>	<b>2.1</b>

Table 5.1: The table shows the corrections and their systematic errors in  $A_{PV}$  from various sources.

## 5.2 Weak Charge Radius, Neutron Radius, and Neutron Skin

### 5.2.1 Weak Charge Radius

The weak charge radius  $R_W$  is calculated using the Helm model explained in Section 4.5.1. The calculation yields the value of  $R_W$ ,

$$R_W = 5.826 \pm 0.181 \text{ (exp)} \pm 0.027 \text{ (mod)} \text{ fm} \quad (5.3)$$

where the experimental error is from adding the statistical and systematic errors in quadrature. The second error comes from the coherent sum of the assumed uncertainties in surface thickness  $\sigma$  and model error in calculating the weak charge form factor  $F_W$ .

This value of  $R_W$  confirms the existence of the weak charge skin,  $R_W - R_{ch}$ <sup>1</sup>,

$$R_W - R_{ch} = 0.323 \pm 0.181 \text{ (exp)} \pm 0.027 \text{ (mod) fm} \quad (5.4)$$

### 5.2.2 Neutron Radius and Neutron Skin

The neutron radius,  $R_n$ , is calculated using two methods:

1. The least squares fit from the  $A_{PV}$  versus  $R_n$  predicted by the distorted-wave calculations for seven mean-field densities.
2. Using the value of  $R_W$  and the Helm model representing theoretical mean-field densities.

The values of the neutron radius,  $R_n$ , and the neutron skin thickness,  $R_n - R_p$ , calculated from each method are presented in the following table.

Quantity	Method 1	Method 2
$R_n$ (fm)	$5.78^{+0.16}_{-0.18}$	$5.75 \pm 0.175 \text{ (exp)} \pm 0.026 \text{ (mod)} \pm 0.005 \text{ (str)}$
$R_n - R_p$ (fm)	$0.33^{+0.16}_{-0.18}$	$0.30 \pm 0.175 \text{ (exp)} \pm 0.026 \text{ (mod)} \pm 0.005 \text{ (str)}$

Table 5.2: The table shows the calculations of  $R_n$  and  $R_n - R_p$  from the two methods.

From Eq. 5.4 and Table 5.2, one can see that  $R_W > R_n$ . This comes from the fact that protons have a small but nonzero weak charge, which contribute to the weak charge distribution. On the other hand, protons do not contribute to  $R_n$  distribution and this makes  $R_n$  smaller than  $R_W$ .

The nonzero value of  $R_n - R_p$  provides the first electroweak observation of the neutron skin as expected in a heavy, neutron-rich nucleus. The errors from both

---

<sup>1</sup> $R_{ch} = 5.503 \pm 0.006$  fm. [14] The error for  $R_{ch}$  is very small compared to the error from measuring  $R_W$  and thus is negligible.

methods are of the order of  $\pm 0.18$  fm. The differences in values of  $R_n$  and  $R_n - R_p$  calculated from both methods are due to small limitations of the Helm model such as the lack of the correct exponential behavior at large distances.

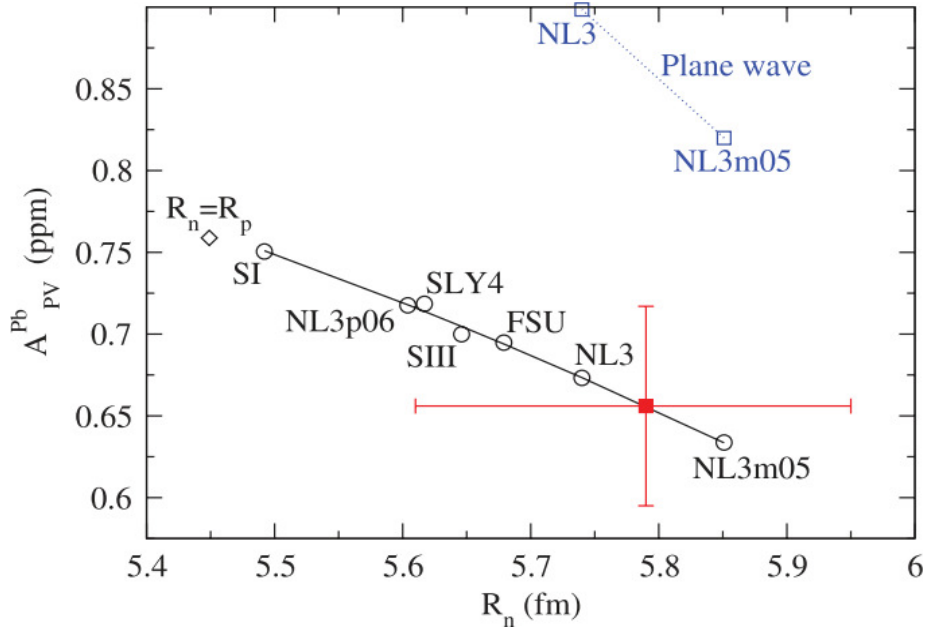


Figure 5.1: Result of the asymmetry in PREX (red square) vs neutron point radius  $R_n$  in  $^{208}\text{Pb}$ . The horizontal (vertical) red line shows the error in  $A_{PV}$  ( $R_n$ ) measurement. Distorted-wave calculations for seven mean-field neutron densities are circles while the diamond marks the expectation for  $R_n = R_p$ . The blue squares show plane wave impulse approximation results.

## 5.3 Technical Accomplishments and Issues Faced in PREX

### 5.3.1 Septum Magnet

The room-temperature septum magnets installed in both spectrometers performed effectively well despite the fact that the septum magnet settings were slightly too low at 729A, instead of the optimal 775A. These too low settings reduced the rates by about a factor of two. The reduction in rate reduced the figure of merit (*FOM*) by 16% [46].

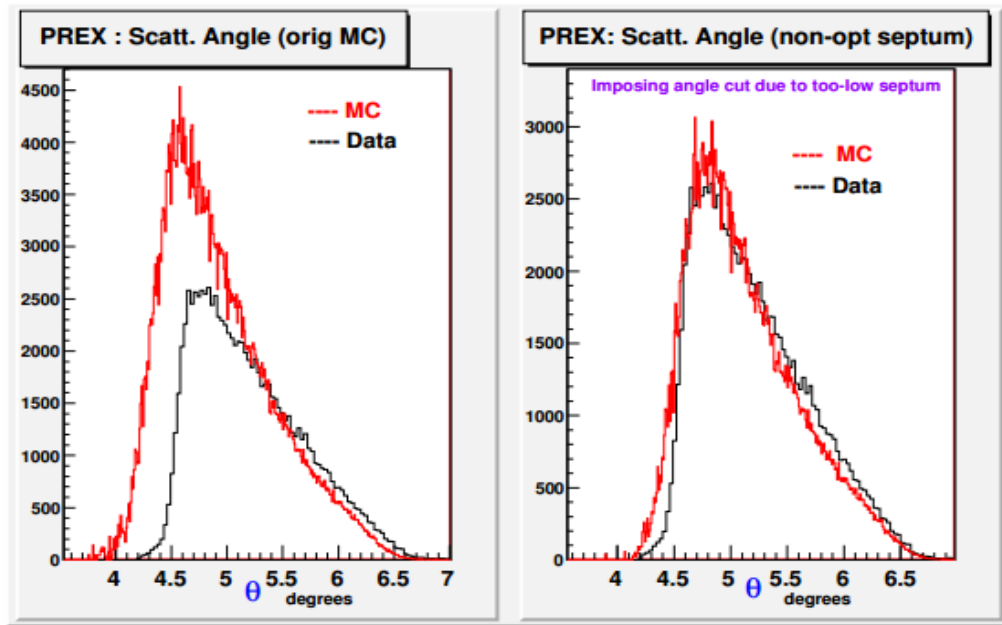


Figure 5.2: Simulated and reconstructed scattering angle for PREX. The data are compared to the original simulation (left) and a corrected simulation (right), where the correction takes into account that the septum current was set too low by 5% such that the scattering angle cutoff was too high by 5 mrad ( $0.3^\circ$ ).

Fig. 5.2 shows the angle distribution of the data compared to simulations using both the actual septum current of 729 A and the optimal current at 775 A. We found that, at the 729 A setting, the bending by each septum was  $\sim 5$  mrad less than expected, hence losing 5 mrad ( $0.3^\circ$ ) in the small-angle side of the acceptance. An analysis of the septum current scans performed during the experiment showed that the full acceptance at the correct  $Q^2$  could be achieved by running the septum magnet at 775A combined with moving the PREX detector to one side by 2.5 cm in the focal plane. This experience allows us to improve the procedure to monitor and to adjust the setup at the start of future experiments.

### 5.3.2 Double Wien Filter

The double Wien filter used an arrangement of solenoids to flip the helicity without changing the beam trajectory. More details on the functions of the double Wien filter are given in Section 3.4.7.

For PREX, two kinds of slow helicity-reversals were used: insertable halfwave plate (IHWP) and the Wien filter. Without any flips, position differences were observed to be in order of 10 to 20 nm. With all the flips, these systematics cancelled at the 5 nm level, making corrections small compared to the statistical error and the systematic error due to beam asymmetries. An advantage of the double Wien filter flip is demonstrated by the additional suppression of the “first order” effects. Furthermore, the double Wien filter has the additional advantage of being able to suppress possible “higher order” effects such as a helicity-correlated spot size.

### 5.3.3 Transverse Asymmetry Systematic

A possible systematic errors resulting from the product of transverse polarization of the beam and vector analyzing power for transverse asymmetry in elastic electron scattering was a main concern before the experiment. However, this concern was eliminated after the finding of two important results, which were:

1. The transverse asymmetry was measured to be  $+0.28 \pm 0.21(\text{stat}) \pm 0.14(\text{syst})$  ppm on the  $^{208}\text{Pb}$  target, which made it a non-problem for the experiment.
2. We found a location in the HRSs focal plane to place an auxiliary detector such that it was sufficiently sensitive to a transverse asymmetry due to higher order terms in the HRSs.

### 5.3.4 Statistical Noise

In order to obtain the necessary statistical precision, the cumulative pulse-pair width (in 30 ms) had to be  $< 200$  ppm. PREX successfully achieved this requirement by, when running at  $70 \mu\text{A}$ , having a width of 171 ppm in the measured asymmetry as illustrated in the following figure.

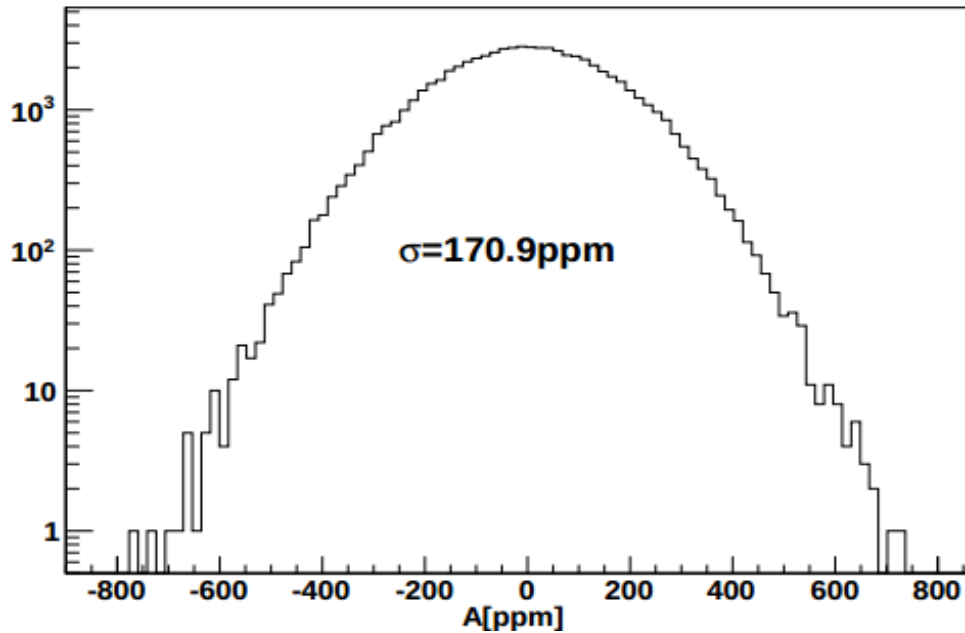


Figure 5.3: Distribution of the asymmetries for a typical run at  $70 \mu\text{A}$ . The width of 171 ppm is consistent with counting statistics [46].

### 5.3.5 Main Target

The main target for PREX consisted of a thin sheet of  $^{208}\text{Pb}$  sandwiched between two sheets of diamond. A major design consideration for the  $^{208}\text{Pb}$  target was the need to operate at high beam currents without melting.

The three sets of Pb/D targets, prepared as discussed in section 3.7, performed efficiently and were just enough to be used for the entire experiment. However, there existed two main problems that need to be addressed for future experiments. These

problems were:

1. After about one day of running, the thickness of the target became non-uniform, resulting in degradation of the pulse-pair width and thus reduced the instantaneous statistical precision due to the use of a raster.
2. After about a week of beam-on-target running, two of the three targets failed due the melting of the lead foil.

The immediate solution to problem 1 was to developed a precision lock for the raster, which completely eleminated the noise. The lock ensured that the raster executed the same orbit between two helicity cycles, cancelling when one took the differences.

In the case of problem 2, it had been predicted by test runs prior to PREX that the lifetime was in an order of one week. The target group found that the main uncertainty in the target's lifetime was due to the thermal contact between lead and diamond, which defined the heat conduction of the target. To ensure a good contact during the construction, three additional processes were introduced:

1. A thin ( $\sim 25 \mu\text{m}$ ) layer of “Apiezon L vacuum grease” was applied to the Pb/D interface.
2. Belleville (“spring-like”) washers were used during the clamping assembly to maintain a force to squeeze the lead and diamond during its thermal cycling.
3. A silver-based paste compound used as a heat sink in the semi-conductor industry was applied between diamond and the copper target holder (but was not in the central area where the beam impacted the target)

The target performance for PREX is shown in the Fig. 5.4, which shows the measured rates for each target as a function of calendar time. The target with the thinnest diamond (4.5% background contamination) degraded the fastest. This target and the

target with the medium thickness diamond back up (6% background contamination) failed, and the last target, which had the thickest diamond (8% background contamination) did not fail and ran successfully during the last four days of the run at 70  $\mu\text{A}$  with high running efficiency. As shown in section 4.3.2, an 8-10% contamination from diamond background is not a problem for the background subtraction.

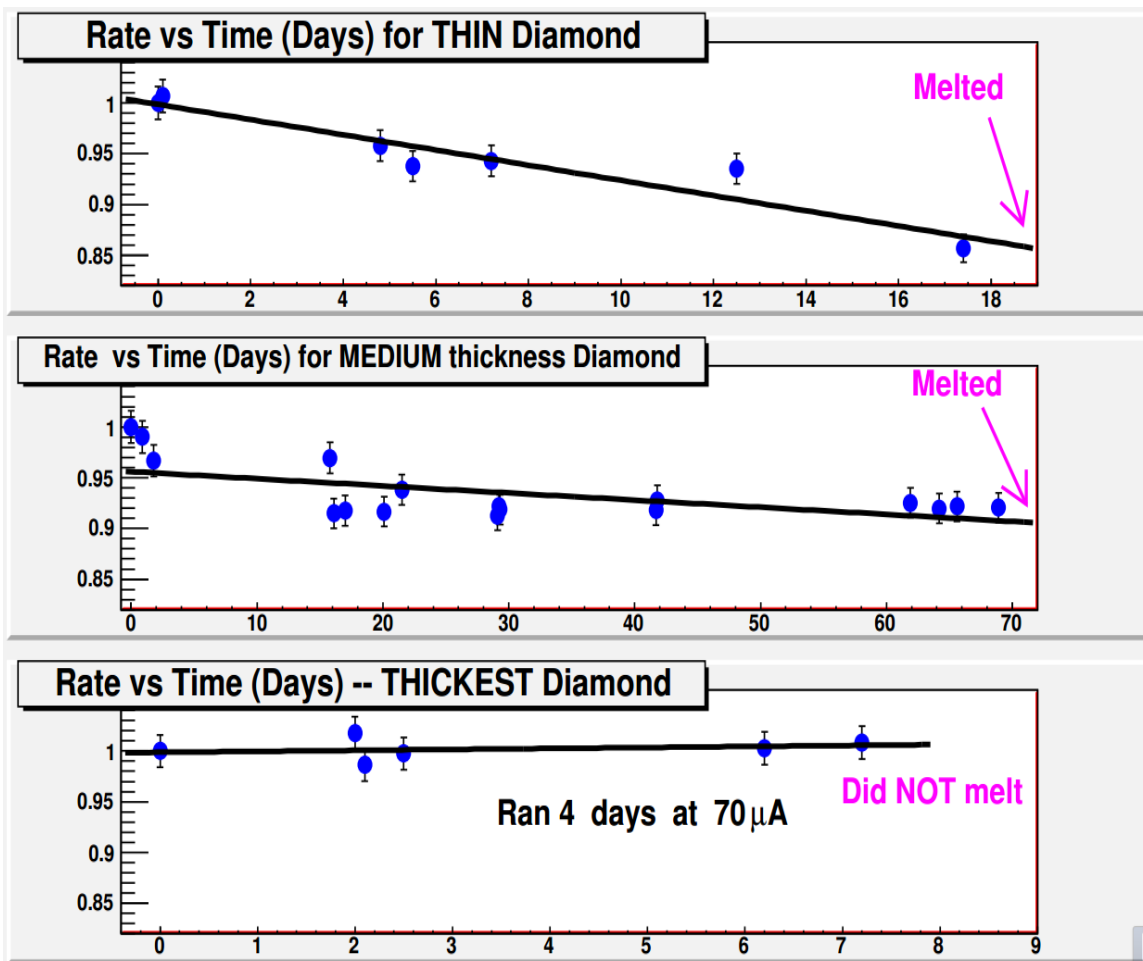


Figure 5.4: Rate measured in counting mode versus time in days for the three Pb/D targets. The target with the thinnest diamond backing degraded the fastest. The target with the thickest diamond did not melt and ran for 4 days at 70  $\mu\text{A}$  (7.5 days total).

### 5.3.6 Radiation Damages

Radiation damage to different components of the experimental setup was the main reason that caused PREX to lose a significant portion of its runtime. The largest downtime was due to the radiation induced failure of a soft O-Ring that was part of the vacuum coupling of the scattering chamber to the exit beam pipe. Furthermore, the high level of radiation inside the hall caused significant failure of the controls systems resulting in loss of running efficiency. The main source of the radiation was neutrons from photonuclear reactions resulting from the interaction of elastically scattered electrons from the lead target, with materials downstream. The tungsten (W) collimator around the downstream beamline, which was not shielded during PREX, became a major source of neutrons from photonuclear reactions. Most of the neutrons generated in PREX were up to few MeV in energy.

## 5.4 Possible Improved Strategies for Future Experiments

### 5.4.1 Target Modifications

As indicated before, the lifetime of the main targets was in the order of one week. The target with the thickest diamond backing could stand a four-day long run at  $70 \mu\text{A}$  without melting. Hence, it is suggested that the next experiment should run with thick diamond ( $\sim 8\%-10\%$  background contamination) and prepare enough targets (about 10) to run 25 days at high current. Moreover, the target group at JLAB has suggested ways to improve the thermal contact between  $^{208}\text{Pb}$  and  $^{12}\text{C}$  by

- Sputtering lead onto diamond or diamond onto lead.
- Using rigid graphite as a backing.
- Using multiple layers of thinner diamond and lead.

These suggestions will be carefully considered to improve the target performance.

### 5.4.2 Radiation Load and Septum Modifications

Since the high level of radiation damage was a critical issue for PREX, reducing the radiation deposition in Hall A by at least a factor of 10 is an important goal for future PREX-like experiments. Furthermore, ways to make Hall A instrumentation more radiation hard are also pursued.

The radiation damage is mostly caused by neutrons with energies in the range of 0.1-10 MeV. The damage to electronics due to thermal electrons is much smaller. So minimizing neutron radiation damage would be accomplished by thermalizing the generated neutrons. One challenge in shielding against low energy neutrons is due to the elastic scatterings of neutrons, where they deviate by large angles from their original paths. As a result, neutrons behave more like a gas (with molecules in random motion) that could readily diffuse out through cracks in a wall, rather than as a beam of high energy particles travelling roughly along the same direction. This allows many neutrons to escape through the holes in shielding reducing the effectiveness of shielding.

Possible methods to reduce the radiation load include installing a new tungsten (W) collimator right after the target to block the electrons and photons from the target at  $0.78^\circ < \theta < 3^\circ$ . This collimator will need to be water-cooled and shielded with at least 20 cm of polyethelene or a polyethelene-concrete mix to thermalize the neutrons. Polyethelene could be encased in aluminum to address the possibility of polyethelene overheating and crumbling. To reduce the holes in shielding and around the septum magnet, which neutrons can leak through, polyethelene in aluminum could be used to fill in the holes.

## 5.5 Proposed Future PREX-Like Experiments

### 5.5.1 PREX-II (E12-11-101)

The PREX collaboration has used the valuable lessons learnt during the experiment to design and propose PREX-II; an improved experiment to measure the neutron radius of  $^{208}\text{Pb}$  [46]. In addition to the improvements suggested in Section 5.4, by using the optimal setting of the septum magnet and a slightly lower energy, the design in PREX-II can reduce the statistical errors by a factor of 3 compared to PREX. The following figure illustrates how the HRS rate varies with the septum current and  $Q^2$ . By setting the septum at  $I=775\text{A}$  and reducing the energy to the range of 925-1000 MeV, the rate is expected to increase by a factor of two.

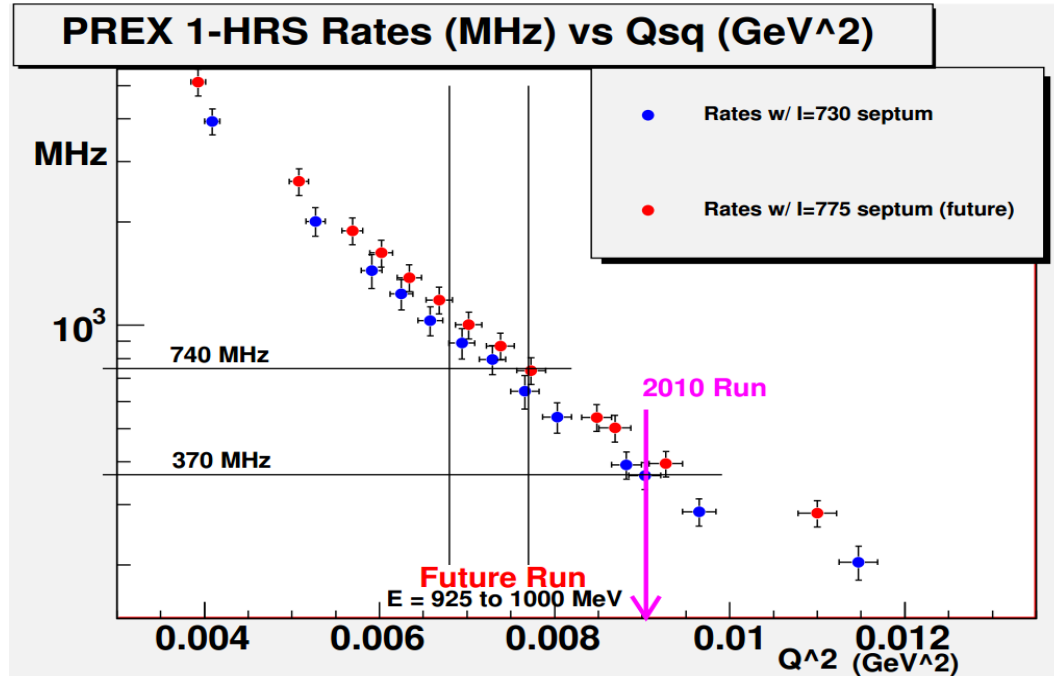


Figure 5.5: Simulated rates in one HRS versus  $Q^2$  for two assumptions about septum current setting. For  $I=729\text{A}$  (PREX-I), the minimum scattering angle was  $4.58^\circ$  and was not optimal. For  $I=775\text{A}$ , the minimum angle will be  $4.35^\circ$ . By setting the septum at  $I=775\text{A}$  and reducing the energy to the range of 925-1000 MeV, the rate is expected to increase by a factor of two.

As a result, a 1% statistical error could be achieved for  $R_n$  in 25 days of running.

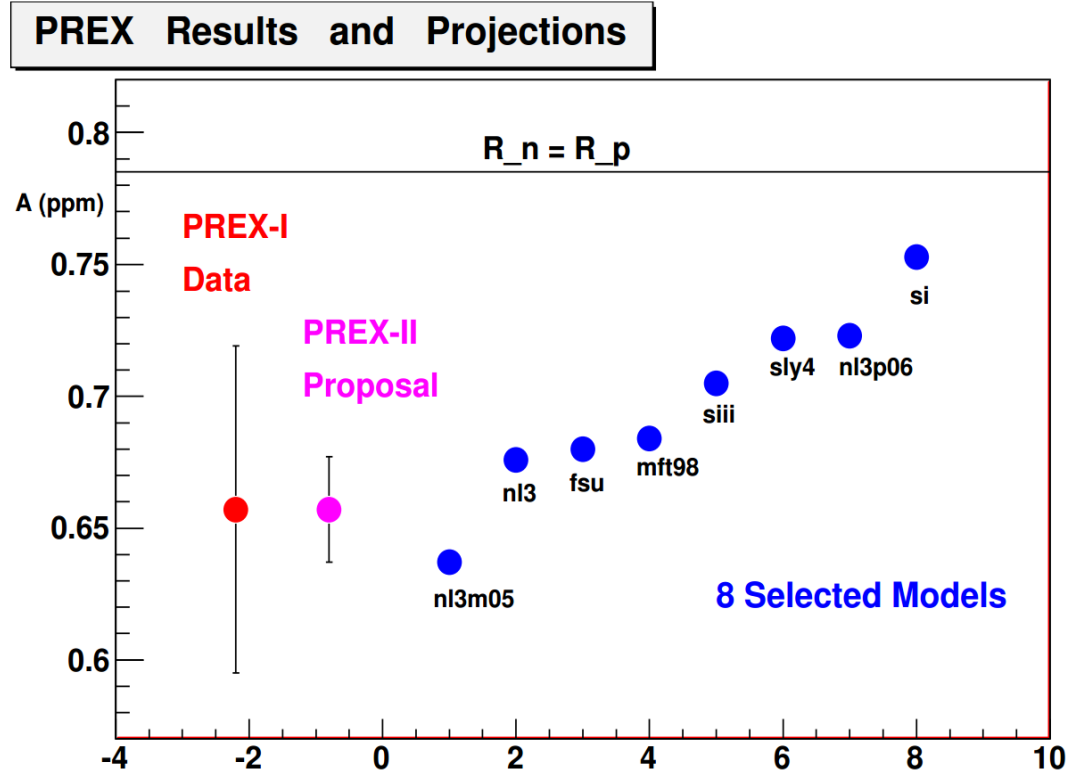


Figure 5.6: The PREX asymmetry for the first PREX data, the PREX-II projections, and 8 selected models.

Fig. 5.6 shows how the PREX-II result would compare to the first PREX result and to various models (NL3M05, NL3, NL3P06 [38], FSU [68], MFT98 [24], SIII [7], SLY4 [10], and SI [70]).

The PREX-II proposal was submitted to the Jefferson lab Program Advisory Committee (PAC)-38 and was approved with an A rating. Table 5.3 shows the parameters of this approved experiment.

Measured Asymmetry	0.51 ppm
Beam Energy	925-1000 MeV
Beam Current	70 $\mu$ A
Statistical Accuracy (combine with PREX-I)	3%
Detected Rate (each HRS)	740 MHz
PREX-II Production	25 days
Setup, Calibration, etc...	10 days
<b>Total Time Request</b>	<b>35 days</b>

Table 5.3: The table shows the important parameters for the approved PREX-II experiment.

### 5.5.2 CREX (E12-12-004)

In a similar measurement to PREX, CREX will measure the parity-violating longitudinal single-spin asymmetry for elastic scattering off  $^{48}\text{Ca}$ . CREX aims to measure the neutron radius with a 0.03-fm accuracy [42]. Like  $^{208}\text{Pb}$ ,  $^{48}\text{Ca}$  is a doubly magic nucleus and has a large neutron excess (28 neutrons and 20 protons). The smaller size of  $^{48}\text{Ca}$  compared to  $^{208}\text{Pb}$  allows the experiment to run at a higher  $Q^2$  and energy<sup>2</sup>, where the *FOM* is larger. Furthermore, while the larger  $^{208}\text{Pb}$  nucleus is a better approximation of infinite nuclear matter, the structure of  $^{48}\text{Ca}$  can be addressed in detailed using microscopic models that are not presently feasible for  $^{208}\text{Pb}$ . The independent electroweak measurements of  $R_n^{Ca}$  and  $R_n^{Pb}$  would provide a test of existing nuclear structure models over a range of  $A$ .

The simulations indicate that a small scattering angle maximizes the *FOM* and the scattering angle is constrained by the septum magnet to bend the scattered electrons to the spectrometers. The preliminary result shows that the optimized angle is at  $4^\circ$  and the beam energy is fixed at 2.2 GeV, which is a natural 1-pass beam energy for CEBAF operations in the 12 GeV era.

The proposed target for CREX will be a 1 gm/cm<sup>2</sup> isotropically pure  $^{48}\text{Ca}$  target and will run at 100  $\mu\text{A}$ . Thermal calculations show that, with a standard raster

---

<sup>2</sup>Since  $^{48}\text{Ca}$  has smaller size than  $^{208}\text{Pb}$ , the form factor of  $^{48}\text{Ca}$  drops slower in momentum space. This results in larger cross section for  $^{48}\text{Ca}$ , and hence the rate, for the same value of  $Q^2$ .

pattern to distribute the heat from the beam, the target temperature will not exceed the melting point ( $842^{\circ}$ ) and stay at  $120^{\circ}$  if the temperature on the border of the target can be fixed at room temperature.

The proposed CREX detectors will be similar to detectors used in PREX, where quartz will be used to detect Cerenkov photons. These will be connected to PMTs and the signal will be integrated in an existing data acquisition system previously used in other parity experiments.

For the proposed running conditions, a beam current of  $100\ \mu\text{A}$  with energy  $2.2\ \text{GeV}$ ,  $85\%$  beam polarization, and a  $5\%$  radiation length ( $1\ \text{g/cm}^2$ ) target, the rate, measured asymmetry, and asymmetry sensitivity to the neutron radius  $\epsilon$  are plotted in Fig. 5.7, 5.8, and 5.9, adapted from the CREX proposal.

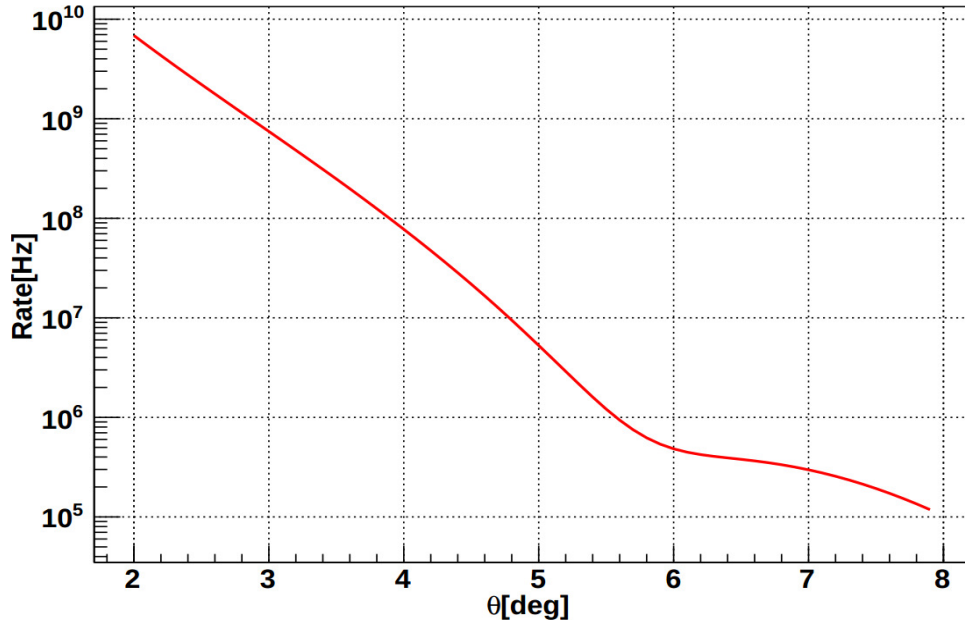


Figure 5.7: The figure shows the rates for 1 HRS versus angle for a beam energy of  $2.2\ \text{GeV}$  and a beam current of  $100\ \mu\text{A}$  in CREX proposal.

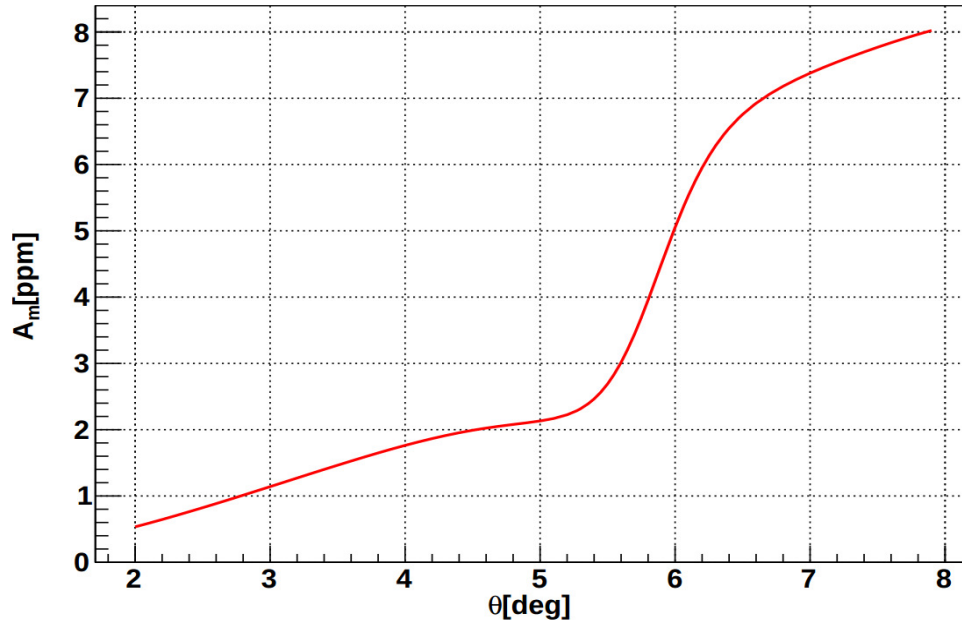


Figure 5.8: The figure shows the measured asymmetry versus angle for a beam energy of 2.2 GeV and a beam current of 100  $\mu$ A in CREX proposal. A factor of 0.85 for the beam polarization is included.

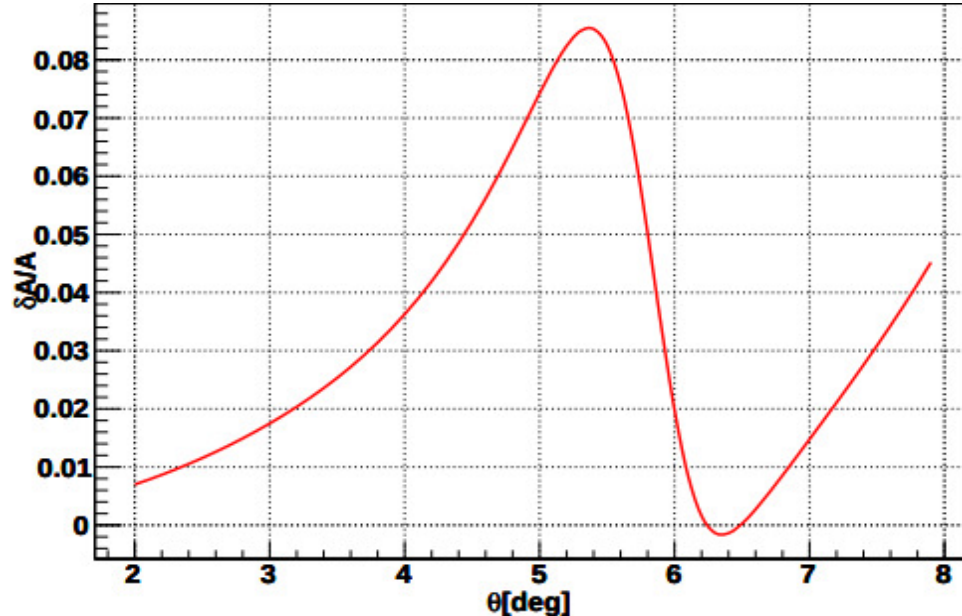


Figure 5.9: The figure shows the sensitivity of the asymmetry  $\epsilon$  versus angle for a beam energy of 2.2 GeV and a beam current of 100  $\mu$ A in CREX proposal.

The CREX proposal experiment was conditionally approved by PAC 39. The following table shows important details for the experiment.

Measured Asymmetry	2 ppm
Beam Energy	2.2 GeV
Scattering Angle	4°
Beam Current	100 $\mu$ A
Statistical Uncertainty of $A_{PV}$	2.8%
Systematic Uncertainty of $A_{PV}$	1.8%
Statistical Uncertainty of $A_T$	0.4 ppm
Detected Rate (each HRS)	80 MHz
CREX Production	30 days
Setup, Calibration, etc...	10 days
<b>Total Time Request</b>	<b>40 days</b>

Table 5.4: The table shows the important details in the CREX proposal.

## 5.6 Conclusions

PREX measured the asymmetry,  $A_{PV}$ , for parity-violating elastic electron scattering off  $^{208}\text{Pb}$  to extract the value of the radius,  $R_n$ , of the neutron distribution of the  $^{208}\text{Pb}$  nucleus. The result  $A_{PV} = 0.656 \pm 0.060(\text{stat}) \pm 0.014(\text{syst})$  ppm corresponds to the neutron skin,  $R_n - R_p = 0.302 \pm 0.175(\text{exp}) \pm 0.026(\text{mod}) \pm 0.005(\text{str})$  fm obtained by Helm model and  $R_n - R_p = 0.33^{+0.16}_{-0.18}$  fm obtained by the least squares fit of seven mean field models that have the same conditions as PREX. The two results of  $R_n - R_p$  agree within the experimental uncertainties. The small difference is due to the small limitation of the Helm model in representing theoretical mean field densities. The non-zero value of  $R_n - R_p$  measured in PREX confirms the existence of neutron skin expected in a heavy, neutron rich nuclei such as  $^{208}\text{Pb}$ . Furthermore, PREX becomes the first electroweak parity violating experiment to successfully confirm the neutron skin. The value of the neutron radius of  $^{208}\text{Pb}$  has important implications for models of nuclear structure and their application in atomic physics and astrophysics such as

atomic parity violation (APV) and neutron stars.

During the experiment, PREX collaboration achieved many technical milestones including the successful application of the double Wein filter, the systems to measure transverse asymmetry, and the methods to reduce statistical noise, which significantly improve systematic uncertainties for PREX. Despite the success in many technical areas, some difficulties including the issue of the high level of radiation, which reduced a significant number of days in runtime, and the failure of the main targets (two of the three main targets melted within a week of runtime) that occurred during the experiment will need to be addressed for future PREX-like experiments. Many possible solutions have been proposed and considered to resolve these issues. The new PREX-like experiments including PREX-II ( $^{208}\text{Pb}$  target) and CREX ( $^{48}\text{Ca}$  target) have been approved from the Jefferson Lab Program Advisory Committee (PAC) to be conducted in the near future, after the completion of 12-GeV upgrade at Jefferson Lab.

## Appendix A

# Hall A Coordinate Systems

Several coordinate systems have been defined in Hall A depending on the types of applications they are referred to. All systems presented in this appendix are Cartesian. Note that an angular coordinate in this section refers to the tangent of the angle [41][55].

### A.1 Hall Coordinate System (HCS)

The origin of the HCS is at the center of the hall, which is the intersection of the ideal electron beamline and the vertical axis of the target system.  $\hat{z}$  is along the beamline and points in the direction of the beam dump.  $\hat{y}$  is vertically up as defined by gravity and  $\hat{x}$  points to the left of the beamline, looking downstream from the target system to the beam dump.

Angles are defined with respect to this origin and a ray pointing along the positive  $\hat{z}$ . Here, the angle  $\theta$  is 0 along  $\hat{z}$  and covers a  $0^\circ$  to  $180^\circ$  range in  $\hat{x} - \hat{z}$  plane. The angle  $\phi$  is the out-of-plane angle formed between the vector under consideration and its projection on the  $\hat{x} - \hat{z}$  plane.

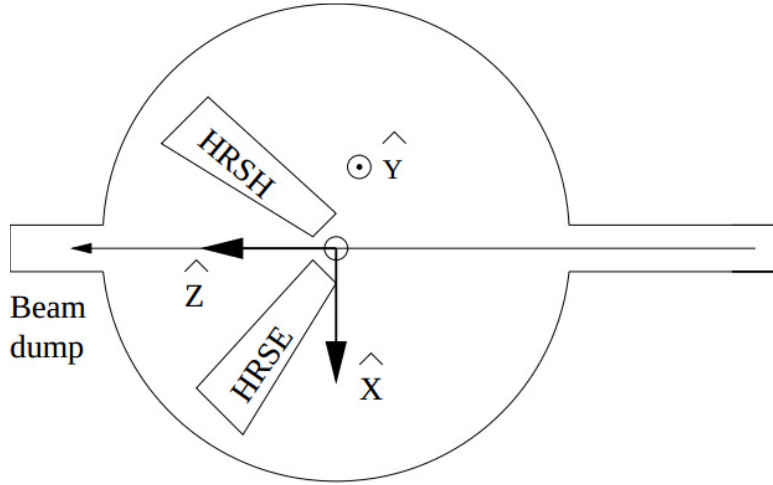


Figure A.1: Hall A coordinate system (HCS) (top view)

## A.2 Target Coordinate System (TCS)

Each of the two HRSs has its own TCS. A line perpendicular to the sieve slit surface of the HRS and going through the midpoint of the central sieve slit hole defines the  $\hat{z}$  of the TCS for a given HRS.  $\hat{z}_{tg}$  points away from the target. In the ideal case where the spectrometer is pointing directly at the hall center and the sieve slit is perfectly centered on the spectrometer, the  $z_{tg}$  axis passes through the hall center. The distance from the hall center to the midpoint of the central sieve slit hole is defined to be the constant  $Z_0$  for the spectrometer. The origin of the TCS is defined as a point at a distance  $Z_0$  from center of the central sieve-slit hole. The  $x_{tg}$  axis is parallel to the sieve slit surface and points vertically down and  $y_{tg}$  axis is also parallel to the sieve slit surface and points to the left of the  $z_{tg}$  axis. The out-of-plane angle ( $\theta_{tg}$ ) and the in-plane angle ( $\phi_{tg}$ ) are given by  $\frac{dx_{tg}}{Z_0}$  and  $\frac{dy_{tg}}{Z_0}$  respectively.

## A.3 Detector Coordinate System (DCS)

The origin of the DCS is defined by the intersection of wire 184 in the first wire plane (U1) and the projection on the first wire plane of wire 184 in the second plane

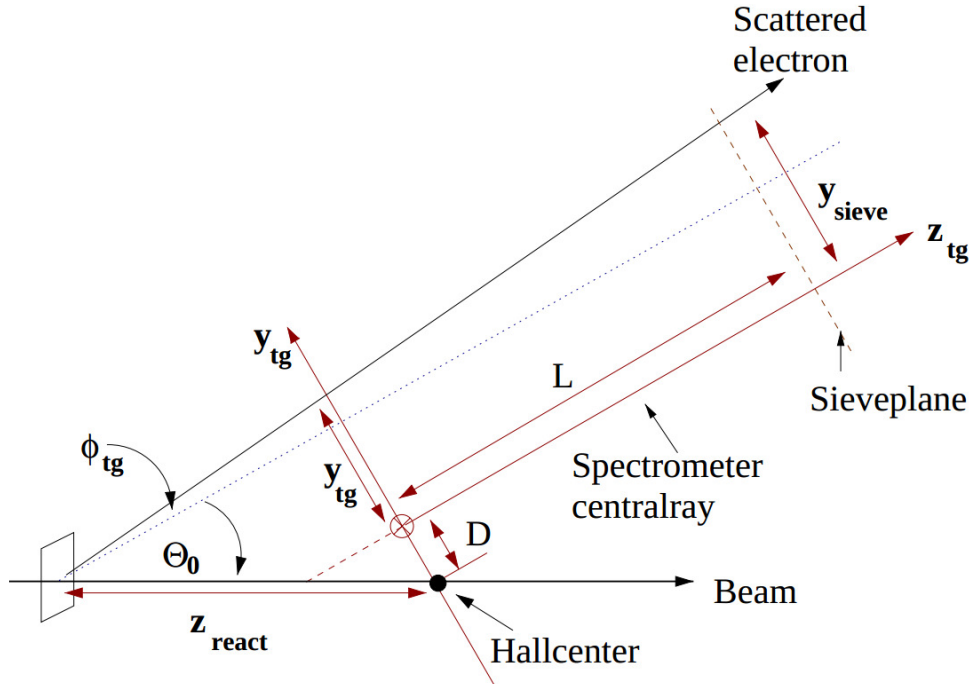
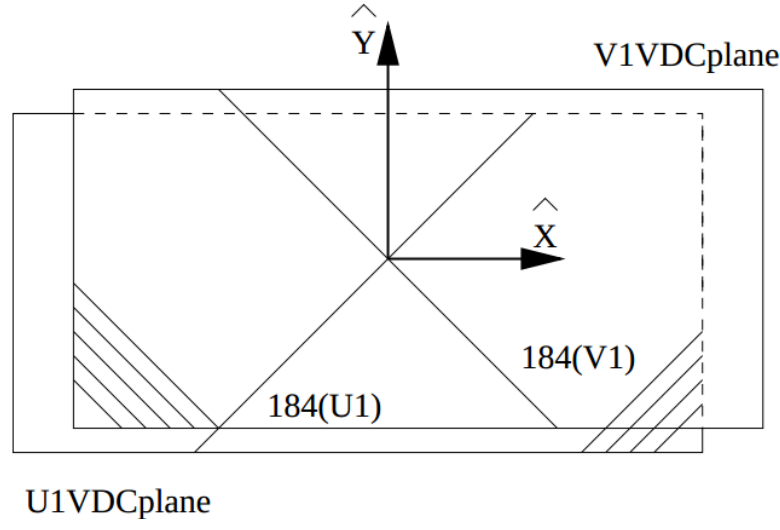


Figure A.2: Target coordinate system (TCS) for left HRS.  $L$  is the distance from Hall center to the sieve plane, while  $D$  is the horizontal displacement of the spectrometer axis from its ideal position. Spectrometer central angle is denoted by  $\Theta_0$ . Note that  $x_{tg}$  and  $x_{sieve}$  are vertically down (into the page)

(V1). The  $z_{det}$  axis is perpendicular to the wire planes and its direction is fixed by demanding that its product with the central spectrometer ray is larger than zero. The  $x_{det}$  axis is defined as the projection on the first wire plane of the vector difference between the spectrometer central ray and a ray for which the momentum has been increased by an infinitesimal amount. Its direction is fixed by requiring an increase in momentum. It would be optimal if the  $x_{det} - z_{det}$  plane would coincide with the spectrometer symmetry plane.

#### A.4 Transport Coordinate System (TRCS)

The TRCS at the focal plane is generated by rotating the DCS clockwise around its  $y_{det}$  by  $45^\circ$ . The  $\hat{z}$  of the TRCS coincides with the central ray of the spectrometer.



U1VDCplane

Figure A.3: Detector coordinate system (DCS)(top view)

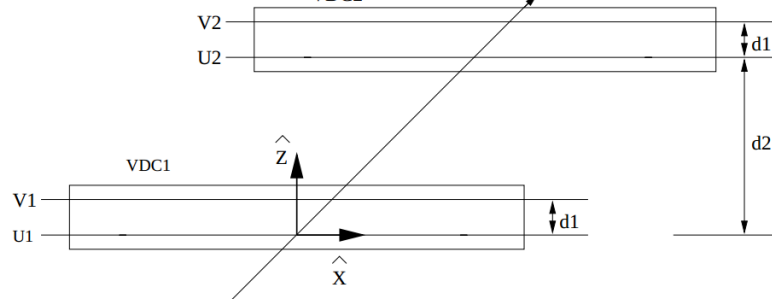


Figure A.4: Detector coordinate system (DCS)(side view)

The TRCS can be expressed in terms of DCS by

$$\theta_{tra} = \frac{\theta_{det} + \tan(\rho_0)}{1 - \theta_{det} \tan(\rho_0)} \quad (A.1)$$

$$\phi_{tra} = \frac{\phi_{det}}{\cos(\rho_0) - \theta_{det} \sin(\rho_0)} \quad (A.2)$$

$$x_{tra} = x_{det} \cos(\rho_0) (1 + \theta_{tra} \tan(\rho_0)) \quad (A.3)$$

$$y_{tra} = y_{det} + \sin(\rho_0) \phi_{tra} x_{det} \quad (A.4)$$

where  $\rho_0$  is the rotation angle,  $-45^\circ$ .

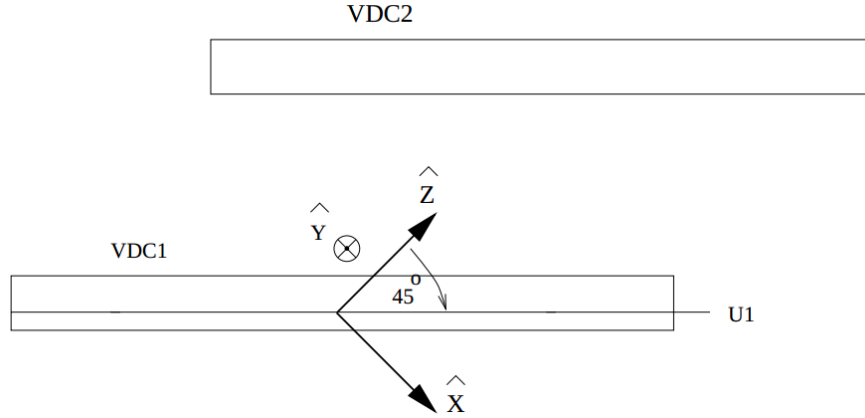


Figure A.5: Transport coordinate system (TRCS)(side view)

## A.5 Focal Plane Coordinate System (FCS)

The FCS is obtained by rotating DCS along its  $y$  axis over an angle  $\rho$ , where  $\rho$  is the angle between the projection of the local central ray ( $\theta_{tg} = \phi_{tg} = 0$  for the corresponding relative momentum  $\frac{\Delta p}{p}$ ). So the new  $z$  axis rotates as a function of the relative particle momentum. The main advantage of the FCS is the fact that the dispersive angle  $\theta$  will be small and thus make the expressions for optics reconstruction converge faster.

The transformation to the FCS includes the offsets due to misalignments in the VDC. The transformation can be expressed as follows:

$$x_{fp} = \cos(\rho_0)(x_{det} - x^{offset}) \quad (\text{A.5})$$

$$y_{fp} = y_{det} - y^{offset} \quad (\text{A.6})$$

$$\theta_{fp} = \frac{\theta_{det} - \tan(\rho)}{1 - \tan(\theta_{det}) \tan(\rho)} \quad (\text{A.7})$$

$$\phi_{fp} = \frac{\phi_{det} - \phi^{offset}}{[\cos(\rho) - \sin(\rho) \tan(\theta_{det})][1 + \phi_{det} \phi^{offset}]} \quad (\text{A.8})$$

where  $\rho_0$  is the rotation angle,  $-45^\circ$ , and  $\rho$  is the angle between the local central ray and the  $z$  axis of DCS.

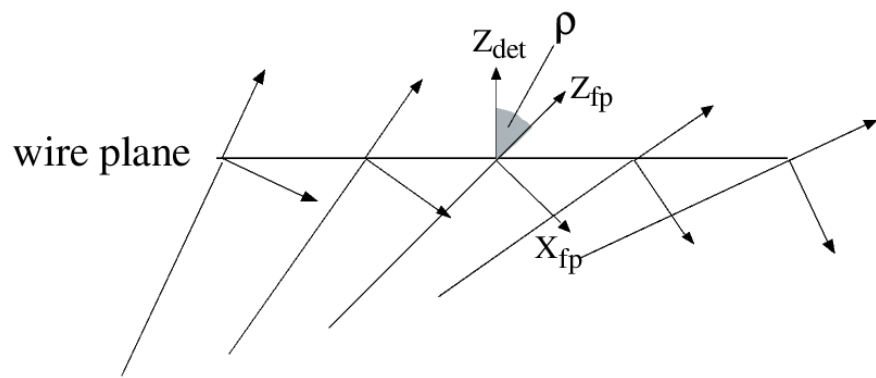


Figure A.6: The focal plane (rotated) coordinate system as a function of the focal plane position(side view)

## Appendix B

# Optics Calibration Procedures

### B.1 Spatial and Angular Calibration

The following are the steps used to perform HRS spatial and angular calibrations for PREX:

1. Take sufficient amount of data using multiple optics targets such as thin carbon, multifoil carbon, tantalum, and watercell target, with the sieve slit inserted. While PREX is only sensitive to the central part (central  $x_{det}$ ), it is better to take data with several spectrometer central momentum settings,  $P_0$ , in order to sweep the scattered electrons across the entire focal plane.
2. Use existing databases to calculate  $\theta_{tg}$ ,  $\phi_{tg}$ , and  $y_{tg}$  for the obtained data. A reasonable database should allow us to distinguish one sieve hole from another in a 2D plot of  $\theta_{tg}$  vs  $\phi_{tg}$ .
3. Plot a 2D histogram of  $\theta_{tg}$  vs  $\phi_{tg}$  and identify each sieve hole in the plot to match the corresponding hole in the sieve slit drawing.
4. For each  $i^{th}$  hole, calculate expected values of  $\theta_{tg,i}$ ,  $\phi_{tg,i}$ , and  $y_{tg,i}$  using its corresponding  $x_{sieve}$ ,  $y_{sieve}$ , and other constants, in Eq. 4.13 - 4.14. These calculated

expected values represent an event passing through an  $i^{th}$  hole in the sieve slit and denote these values as  $\theta_{tg0,i}$ ,  $\phi_{tg0,i}$ , and  $y_{tg0,i}$ .

5. For the  $i^{th}$  hole for each target and each  $P_0$  setting, calculate the square of the differences between the actual values, which obtained from the centroid of the spectrum, and the expected values as the following:

$$\chi_{\theta,i}^2 = (\theta_{tg,i} - \theta_{tg0,i})^2 \quad (\text{B.1})$$

$$\chi_{\phi,i}^2 = (\phi_{tg,i} - \phi_{tg0,i})^2 \quad (\text{B.2})$$

$$\chi_y^2 = (y_{tg,i} - y_{tg0,i})^2 \quad (\text{B.3})$$

where  $\theta_{tg,i}$ ,  $\phi_{tg,i}$ , and  $y_{tg,i}$  are the central values of  $\theta_{tg}$ ,  $\phi_{tg}$ , and  $y_{tg}$  histograms after selecting events passing through only the  $i^{th}$  hole. Note that these values are reconstructed using Eq. 4.2 - 4.4.

6. Sum all values in previous step to get:

$$\chi_{\theta}^2 = \sum_{i=1}^N \chi_{\theta,i}^2 \quad (\text{B.4})$$

$$\chi_{\phi}^2 = \sum_{i=1}^N \chi_{\phi,i}^2 \quad (\text{B.5})$$

$$\chi_y^2 = \sum_{i=1}^N \chi_y^2 \quad (\text{B.6})$$

where  $N$  is the total number of holes obtained from all targets and all  $P_0$  settings.

7. Use TMinuit package in ROOT to optimize tensor elements  $T_{jkl}$ ,  $P_{jkl}$ , and  $Y_{jkl}$  in Eq. 4.6 - 4.8 such that  $\chi_{\theta}^2$ ,  $\chi_{\phi}^2$ , and  $\chi_y^2$  are minimized.
8. Analyze the same data with the new optimized database having the new tensor elements  $T_{jkl}$ ,  $P_{jkl}$ , and  $Y_{jkl}$ .

9. Plot a 2D histogram of  $\theta_{tg}$  vs  $\phi_{tg}$  again to determine if all holes are in the expected locations.
10. Plot a histogram of  $y_{tg}$  to determine if the maximum value of  $y_{tg}$  is in the expected positions.
11. One might try to minimize  $\chi^2_\theta$ ,  $\chi^2_\phi$ , and  $\chi^2_y$  further by adding extra tensor elements  $T_{jkl}$ ,  $P_{jkl}$ , and  $Y_{jkl}$  as becomes apparent in the new reconstruction, or by removing any redundant tensor elements.

## B.2 Momentum Calibration

The following steps are used to perform momentum calibration using sieve data for PREX:

1. Take sufficient amount of data from multiple targets such as thin carbon, multifoil carbon, tantalum, and watercell target, with the sieve slit inserted. It is also better to take data several spectrometer central momentum  $P_0$  settings to sweep the scattered electrons across the entire focal plane.
2. Use the existing database to analyze the data and obtain  $\delta_{tg}$ .
3. Calculate expected values of  $\theta_{tg,i}$  and  $\phi_{tg,i}$  for an  $i^{th}$  hole using Eq. 4.13 and Eq. 4.14. Denote these values as  $\theta_{tg0,i}$  and  $\phi_{tg0,i}$ .
4. Calculate the scattering angle for an event passing through the  $i^{th}$  hole by using the equation

$$\theta_i = \frac{\cos(\theta_0) - \phi_{tg0,i} \sin(\theta_0)}{\sqrt{1 + \theta_{tg0,i}^2 + \phi_{tg0,i}^2}} \quad (\text{B.7})$$

where  $\theta_0$  is the spectrometer central angle.

5. Using the value of  $\theta_i$  from the previous step, calculate the expected final momentum of scattered electrons passing through the  $i^{th}$  hole by using the equation

$$E_{f0,i} = \frac{(E - E_{loss1})}{1 + \frac{2(E - E_{loss1}) \sin^2(\frac{\theta_i}{2})}{M_t}} - E_{loss2} \quad (\text{B.8})$$

where,  $E$ ,  $\theta_i$ ,  $E_{loss1}$  and  $E_{loss2}$  are beam energy, scattering angle, energy loss occurred before the scattering, and energy loss occurred after the scattering respectively.

6. The calculated  $E_{f0,i}$  can be changed to the fractional momentum form by

$$\delta_{f0,i} = \frac{E_{f0,i} - P_0}{E_{f0,i}} \quad (\text{B.9})$$

where  $P_0$  is the spectrometer central momentum setting.

7. For the  $i^{th}$  hole in each target and each  $P_0$  setting, calculate the square of the difference between the actual central value of  $\delta_{tg,i}$  and the expected value of  $\delta_{f0,i}$  as the following:

$$\chi_{\delta,i}^2 = (\delta_{tg,i} - \delta_{f0,i})^2 \quad (\text{B.10})$$

where  $\delta_{tg,i}$  is the central value of  $\delta_{tg}$  histogram after applying a cut on  $i_{th}$  hole. Note that these values are reconstructed using Eq. 4.9.

8. Sum all values in previous steps to get:

$$\chi_{\delta}^2 = \sum_{i=1}^N \chi_{\delta,i}^2 \quad (\text{B.11})$$

where  $N$  is the total number of holes obtained from all target and all  $P_0$  settings.

9. Use TMinuit package in ROOT to optimize tensor elements  $D_{jkl}$  in Eq. 4.9 such

that  $\chi^2_\delta$  is minimized.

10. Analyze the same data using the new optimized database with the new tensor elements  $D_{jkl}$ .
11. Plot a histogram of  $\delta_{tg}$  to determine if the new database produces correct final momentum.
12. One may try to minimize  $\chi^2_\delta$  further by adding or removing tensor elements  $D_{jkl}$  as needed.

## Appendix C

# HRS Optics Tensors Elements for PREX

See section 4.1 for the definition of HRS tensor elements.

## C.1 LHRs Optics Tensors Elements Used for PREX

Element	$C_0$ term	$C_1$ term	$C_2$ term	$C_3$ term
t000	-1.001135e+00	-3.313373e-01	-4.290819e-02	4.470852e-03
y000	-8.060915e-03	1.071977e-03	9.019102e-04	-3.239615e-04
p000	-2.861912e-03	-2.469069e-03	8.427172e-03	2.274635e-03
D000	-1.58403E-03	6.86867E-02	-6.18588E-03	0.00000E+00
D001	3.00285E-02	-4.91856E-02	0.00000E+00	0.00000E+00
D002	-5.42523E-01	0.00000E+00	0.00000E+00	0.00000E+00
D010	-7.14919E-03	7.42244E-03	0.00000E+00	0.00000E+00
D020	4.95037E-01	0.00000E+00	0.00000E+00	0.00000E+00
D100	6.92544E-02	2.56261E-01	0.00000E+00	0.00000E+00
D101	6.14834E+00	0.00000E+00	0.00000E+00	0.00000E+00
D102	-1.20708E+02	0.00000E+00	0.00000E+00	0.00000E+00
D110	-1.94989E+00	0.00000E+00	0.00000E+00	0.00000E+00
D111	3.33984E+02	0.00000E+00	0.00000E+00	0.00000E+00
D200	-1.92746E+00	0.00000E+00	0.00000E+00	0.00000E+00
T000	-1.90620E-02	3.77113E-02	-1.96323E-02	0.00000E+00
T001	2.38406E-01	1.63675E-01	0.00000E+00	0.00000E+00
T002	1.76682E+00	0.00000E+00	0.00000E+00	0.00000E+00
T010	-7.23873E-02	1.25414E-01	0.00000E+00	0.00000E+00
T011	1.01545E+01	0.00000E+00	0.00000E+00	0.00000E+00
T020	-3.31477E-01	0.00000E+00	0.00000E+00	0.00000E+00
T100	-2.81337E+00	5.83337E-01	0.00000E+00	0.00000E+00
T101	2.95086E+01	0.00000E+00	0.00000E+00	0.00000E+00
T110	-1.44390E+01	0.00000E+00	0.00000E+00	0.00000E+00
T111	1.08477E+03	6.56050E+02	0.00000E+00	0.00000E+00

T200	-6.30245E+00	0.00000E+00	0.00000E+00	0.00000E+00
P000	-1.64063E-03	3.23519E-04	3.63165E-03	0.00000E+00
P001	9.63156E-01	-4.57984E-01	0.00000E+00	0.00000E+00
P002	-3.29662E-01	0.00000E+00	0.00000E+00	0.00000E+00
P010	-8.89542E-01	2.27265E-01	0.00000E+00	0.00000E+00
P011	-5.00590E-01	0.00000E+00	0.00000E+00	0.00000E+00
P020	3.38554E+00	0.00000E+00	0.00000E+00	0.00000E+00
P100	-1.49651E-01	1.47151E-01	0.00000E+00	0.00000E+00
P101	1.33493E+00	0.00000E+00	0.00000E+00	0.00000E+00
P111	7.25454E+01	0.00000E+00	0.00000E+00	0.00000E+00
P200	-1.04586E+01	0.00000E+00	0.00000E+00	0.00000E+00
Y000	2.32906E-03	-7.81916E-03	-3.64825E-02	1.91595E-00
Y001	3.64670E-01	5.69594E-01	-2.59403E+00	0.00000E+00
Y002	-4.24172E+00	0.00000E+00	0.00000E+00	0.00000E+00
Y010	1.33195E-01	-1.10855E+00	0.00000E+00	0.00000E+00
Y011	-1.38835E+01	-9.61770E+01	0.00000E+00	0.00000E+00
Y020	-1.37514E+01	-4.22015E+00	0.00000E+00	0.00000E+00
Y110	-2.55549E+01	0.00000E+00	0.00000E+00	0.00000E+00
Y111	-9.50528E+02	0.00000E+00	0.00000E+00	0.00000E+00
Y200	1.53871E+01	0.00000E+00	0.00000E+00	0.00000E+00
Y201	-1.75497E+03	0.00000E+00	0.00000E+00	0.00000E+00
Y210	1.75127E+02	0.00000E+00	0.00000E+00	0.00000E+00
Y101	-1.25722E+01	0.00000E+00	0.00000E+00	0.00000E+00

Table C.1: Tensor elements for LHRS.

## C.2 RHR<sub>S</sub> Optics Tensors Elements Used for PREX

Element	$C_0$ term	$C_1$ term	$C_2$ term	$C_3$ term
t000	-1.007182e+00	-3.355711e-01	-4.038987e-02	-5.355920e-04
y000	-6.641445e-03	1.373258e-03	2.201424e-03	7.172290e-03
p000	-3.388563e-03	-4.328828e-03	-1.200457e-03	1.237351e-03
D000	-2.18755E-05	5.83564E-02	-8.97861E-02	0.00000E+00
D001	-4.77961E-05	-3.04077E-02	0.00000E+00	0.00000E+00
D002	6.17957E-01	0.00000E+00	0.00000E+00	0.00000E+00
D010	1.22309E-02	-3.66978E-02	0.00000E+00	0.00000E+00
D020	1.48990E+00	0.00000E+00	0.00000E+00	0.00000E+00
D100	1.01956E-01	4.35372E-02	0.00000E+00	0.00000E+00
D101	-2.57651E+00	0.00000E+00	0.00000E+00	0.00000E+00
D102	-8.75183E+01	0.00000E+00	0.00000E+00	0.00000E+00
D110	2.45443E+00	0.00000E+00	0.00000E+00	0.00000E+00
D111	3.55107E+02	0.00000E+00	0.00000E+00	0.00000E+00
D120	-2.07021E+02	0.00000E+00	0.00000E+00	0.00000E+00
D200	-2.60914E+00	0.00000E+00	0.00000E+00	0.00000E+00
T000	-9.13470E-03	1.25107E-03	-3.38147E-01	0.00000E+00
T001	1.11609E-02	-1.95523E-01	0.00000E+00	0.00000E+00
T002	3.81762E+00	0.00000E+00	0.00000E+00	0.00000E+00
T010	4.93221E-02	-3.80712E-01	0.00000E+00	0.00000E+00
T011	6.25851E+00	0.00000E+00	0.00000E+00	0.00000E+00
T020	2.25330E+00	0.00000E+00	0.00000E+00	0.00000E+00
T100	-2.73871E+00	-9.61326E-01	0.00000E+00	0.00000E+00
T101	-1.50422E+01	0.00000E+00	0.00000E+00	0.00000E+00
T110	1.39775E+01	0.00000E+00	0.00000E+00	0.00000E+00

T111	1.26014E+03	0.00000E+00	0.00000E+00	0.00000E+00
T200	-1.13484E+01	0.00000E+00	0.00000E+00	0.00000E+00
P000	-3.68017E-03	-7.71753E-04	-3.43996E-02	0.00000E+00
P001	1.00230E+00	-3.43942E-01	0.00000E+00	0.00000E+00
P002	2.99640E-01	0.00000E+00	0.00000E+00	0.00000E+00
P010	-8.76757E-01	1.13293E+00	0.00000E+00	0.00000E+00
P011	5.14713E+00	-1.48055E+01	0.00000E+00	0.00000E+00
P020	-1.25020E+00	0.00000E+00	0.00000E+00	0.00000E+00
P100	4.56809E-02	5.37848E-02	0.00000E+00	0.00000E+00
P101	-1.61988E-01	-2.35163E+00	0.00000E+00	0.00000E+00
P111	4.20689E+02	0.00000E+00	0.00000E+00	0.00000E+00
P200	9.05254E+00	0.00000E+00	0.00000E+00	0.00000E+00
Y000	3.39379E-03	7.15809E-03	-1.19714E-01	-1.20607E+00
Y001	5.61791E-01	2.87989E+00	2.51024E+00	0.00000E+00
Y002	1.97497E+00	0.00000E+00	0.00000E+00	0.00000E+00
Y010	4.02543E-01	-8.41987E-02	0.00000E+00	0.00000E+00
Y011	7.58617E-01	1.92458E+02	0.00000E+00	0.00000E+00
Y020	1.64614E-01	1.86333E+01	0.00000E+00	0.00000E+00
Y110	-1.48500E+01	0.00000E+00	0.00000E+00	0.00000E+00
Y111	2.10641E+02	0.00000E+00	0.00000E+00	0.00000E+00
Y200	-2.00094E+01	-4.08057E+01	3.79764E+02	0.00000E+00
Y201	-1.38529E+03	0.00000E+00	0.00000E+00	0.00000E+00
Y210	2.01782E+03	0.00000E+00	0.00000E+00	0.00000E+00
Y101	2.20540E+01	0.00000E+00	0.00000E+00	0.00000E+00

Table C.2: Tensor elements for RHRs.

# Bibliography

- [1] V.M. Abazov et al. Measurement of the  $w$  boson mass with d0 detector. *Physics Review Letter*, 108(151804), 2012.
- [2] S. Abrahamyan et al. Measurement of the neutron radius of  $^{208}\text{pb}$  through parity-violation in electron scattering. *arXiv*, 2(1201.2568v2), January 2012.
- [3] S. Abrahamyan et al. New measurements of the transverse beam asymmetry for elastic electron scattering from selected nuclei. *Physical Review Letters*, 109(192501), Noverber 2012.
- [4] Z. Ahmed. Prex parity analysis. [http://hallaweb.jlab.org/parity/prex/mtg/col\\_29jan11/PReX\\_01\)29\)2011.pdf](http://hallaweb.jlab.org/parity/prex/mtg/col_29jan11/PReX_01)29)2011.pdf), January 2011.
- [5] Z. Ahmed et al. New precision limit on the strange vector form factors of the proton. *Physical Review Letters*, 108(102001), March 2012.
- [6] J. Alcorn et al. Basic instrumentation for hall a at jefferson lab. *Nuclear Instruments and Methods in Physics Research A*, 522:294–346, 2004.
- [7] M. Beiner, H. Flocard, N. Van Giai, and P. Quentin. Nuclear ground-state properties and self-consistent calculations with the skyrme interaction: (i) spherical description. *Nuclear Physics A*, 238, January 1975.
- [8] J. Beringer et al. Z mass. *Particle Data Group*, D86(010001), 2012.
- [9] SM Bilanky. *Introduction to the Physics of Electroweak*. Pergamon Press, Elmsford, New York, 1982.
- [10] E. Chabanat, P. Bonche, P. Haensel, J. Meyer, and R. Schaeffer. A skyrme parametrization from subnuclear to neutron star densities part ii. nuclei far from stabilities. *Nuclear Physics A*, 635, May 1998.
- [11] K. de Jager, S. Kox, Frank Maas, S. Page, C. Papanicolas, and J. Van de Wiele. From parity violation to hadronic structure and more. In *Proceedings of the 3<sup>rd</sup> International Workshop*, Milos Greece, May 2006.
- [12] Charlotte Elster. Chapter 4: The dirac equation. [http://www.phy.ohiou.edu/~elster/lectures/advqm\\_4.pdf](http://www.phy.ohiou.edu/~elster/lectures/advqm_4.pdf).

- [13] K.G. Fiisum et al. *Vertical Drift Chambers for the Hall A High Resolution spectrometers at Jefferson Lab*, August 2000.
- [14] J.L. Friar and J.W. Negele. The determination of the nuclear charge distribution of  $^{208}\text{pb}$  from elastic electron scattering and muonic x-rays. *Nuclear Physics A*, 212:93–137, June 1973.
- [15] G. Fricke et al. The landolt-bornstein database. <http://www.springermaterials.com/docs/info/b46102.html>.
- [16] M. Friend et al. Upgraded photon calorimeter with integrating readout for hall a compton polarimeter at jefferson lab. Draft before submission, 2011.
- [17] B. Frois et al. High-momentum-transfer electron scattering from  $^{208}\text{pb}$ . *Physical Review Letters*, 38(4), January 1977.
- [18] C. Garcia-Recio, J. Nieves, and E. Oset. Neutron distributions from pionic atoms. *Nuclear Physics A*, 547:473, 1992.
- [19] A.V. Glamazdin et al. Electron beam møller polarimeter at jlab hall a. *arXiv:hep-ex*, 1(9912063), December 1999.
- [20] J. Grames, J. Hansknect, M. Poelker, and R. Suleiman. Jefferson lab injector development for next generation parity violation experiments. *European Journal of Hyperfine Interactions*, 2009.
- [21] K. Grotz and H.V. Klapdor. *The Weak Interaction in Nuclear, Particle, and Astrophysics*. ADAM HILGER, Bristol, Philadelphia, 1990.
- [22] J. Hansknecht and M. Poelker. Synchronous photoinjection using a frequency-doubled gain-switched fiber-coupled seed laser and eryb-doped fiber amplifier. *Physical Review Special Topics*, 9, 2006.
- [23] J. Heisenberg, J. Lichtenstadt, C.N. Papanicolas, and J.S. McCarthy. Excitation of low lying natural parity levels in  $^{208}\text{pb}$  by inelastic electron scattering. *Physical Review C*, 25(5), May 1982.
- [24] C. Horowitz. private communication.
- [25] C.J. Horowitz. Parity violating elastic electron scattering and coulomb distortion. *Physical Review C*, 57(6), June 1998.
- [26] C.J. Horowitz et al. Weak charge form factor and radius of  $^{208}\text{pb}$  through parity violation in electron scattering. *Physical Review C*, 85(032501), March 2012.
- [27] C.J. Horowitz and J. Piekarewicz. Neutron radii of  $^{208}\text{pb}$  and neutron stars. *Physical Review C*, 64(062802), November 2001.
- [28] C.J. Horowitz and J. Piekarewicz. Neutron star structure and the neutron radius of  $^{208}\text{pb}$ . *Physical Review Letters*, 86(25), June 2001.

- [29] C.J. Horowitz, S.J. Pollock, P.A. Souder, and R. Michaels. Parity violating measurement of neutron densities. *Physical Review C*, 63(025501), January 2001.
- [30] C. Hyde-wright, L. Todor, and G. Laveissiere. *Beam Position Studies for E93050*, April 1999.
- [31] Chun-Min Jen. Rescattering background study. <http://ace.phys.virginia.edu/HAPPEX/2620>, April 2011.
- [32] Chun-Min Jen. Review of  $a_t$  analysis for prexi. Report on the analysis, February 2012.
- [33] G. Mark Jones. *A Precision Measurement of the Weak Mixing Angle in Møller Scattering at Low  $Q^2$* . PhD thesis, California Institute of Technology, May 2004.
- [34] Lisa J. Kaufman. *Precision Measurement of the Proton Neutral Weak Form Factors at  $Q^2 \sim 0.1 \text{ GeV}^2$* . PhD thesis, University of Massachusetts Amherst, February 2007.
- [35] H.J. Korner and J.P. Schiffer. Neutron radius of  $^{208}\text{pb}$  from sub-coulomb pickup. *Physical Review Letter*, 27(21), November 1971.
- [36] G.A. Krafft et al. Energy vernier system for cebaf. In *Particle Accelerator Conference*, 1993.
- [37] K.S. Kumar and P.A. Souder. Strange quarks and parity violation. *Progress in Particle and Nuclear Physics*, 45, 2000.
- [38] G. A. Lalazissis, J. Konig, and P. Ring. A new parametrization for the lagrangian density of relativistic mean field theory. *Physical Review C*, 55, July 1996.
- [39] T.D. Lee and C.N. Yang. Question of parity conservation in weak interactions. *Physics Review*, 104(1), October 1956.
- [40] Nilanga Liyanage. *A study of the  $^{16}\text{O}(e,e'p)$  reaction at deep missing energies*. PhD thesis, Massachusetts Institute of Technology, February 1999.
- [41] Nilanga Liyanage. *Optics calibration of the Hall A High Resolution Spectrometers Using the New Optimizer*, July 2002.
- [42] J. Mammei, R. Michaels, K. Paschke, S. Riordan, P.A. Souder, et al. C-rex: Parity-violating measurement of the weak charge distribution of  $^{48}\text{ca}$  to 0.03 fm accuracy. Proposal to Jefferson Lab PAC 39.
- [43] T. Maruyama et al. Systematic study of polarized electron emission from strained gaas/gaasp super lattice photocathodes. *Applied Physics Letters*, 85(13), September 2004.

- [44] R. Michaels, P.A. Souder, G.M. Urciuoli, et al. A clean measurement of the neutron skin of  $^{208}\text{pb}$  through parity violating electron scattering. Proposal to Jefferson Lab PAC 17.
- [45] R. Michaels, P.A. Souder, G.M. Urciuoli, et al. Update of e00003: Neutron skin of  $^{208}\text{pb}$  through parity violating electron scattering. Proposal to Jefferson Lab PAC 23.
- [46] R. Michaels, P.A. Souder, G.M. Urciuoli, K. Paschke, K. Kumar, et al. Prex-ii: Precision parity-violating measurement of the neutron skin of lead. Proposal to Jefferson Lab PAC 38.
- [47] Robert Michaels. foldedacc.dat. <http://hallaweb.jlab.org/parity/prex/accept/foldedacc.dat>.
- [48] Robert Michaels. *Precision Integrating HAPPEX ADCs*, August 2003.
- [49] Robert Michaels. *PREX Collimator Alignment Procedure*, December 2009.
- [50] Robert Michaels and Phil Adderley. *Hall A Target Configuration (PREX)*, March 2010.
- [51] S. Mizutori, J. Dobaczewski, G.A. Lalazissis, W. Nazarewicz, and P.G. Reinhard. Nuclear skins and halos in the mean-field theory. *Physics Review C*, 61(044326), 2000.
- [52] Bryan J. Moffit. *Elastic Scattering of Longitudinally Polarized Electrons from  $^4\text{He}$* . PhD thesis, The College of William and Mary in Virginia, 2007.
- [53] Krishna Myneni. Symmetry destroyed: The failure of parity. <http://ccreweb.org/documents/parity/parity.html>.
- [54] Andre Norman. *Electron Scattering from Lead Nuclei*. PhD thesis, University of Virginia, August 1978.
- [55] Eddy Offerman. *ESPACE User's Guide*, February 1997.
- [56] A. Ong, J.C. Berengut, and V.V. Flambaum. Effect of spin-orbit nuclear charge density corrections due to the anomalous magnetic moment on halonuclei. *Physical Review C*, 82(014320), July 2010.
- [57] D. Parno et al. Preliminary results from integrating compton photon polarimetry in hall a of jefferson lab. *arXiv*, 1(1106.4851), June 2011.
- [58] P. Ring et al. Ground state properties of the  $\beta$  stable nuclei in various mean field theories. *Nuclear Physics A*, 624:349–369, October 1997.
- [59] Seamus Riordan. Multiple scattering effects in prex acceptance. [http://solid.physics.umass.edu/~seamus/prex\\_multscat.pdf](http://solid.physics.umass.edu/~seamus/prex_multscat.pdf).

- [60] K. Saenboonruang. Finite acceptance. [http://ace.phys.virginia.edu/HAPPEX/110425\\_121759/Finite\\_acceptance.pdf](http://ace.phys.virginia.edu/HAPPEX/110425_121759/Finite_acceptance.pdf), April 2011.
- [61] F. Sauli. Gem: A new concept for electron amplification in gas detector. *Nuclear Instruments and Methods in Physics Research A*, 386:531–534, 1997.
- [62] Nikolai Aleksandrovich Savvinov. *Charge Form Factor of The Neutron Through  $\vec{d}(\vec{e}, e'n)$  at  $Q^2=1.0$  ( $GeV/c$ ) $^2$* . PhD thesis, University of Maryland, 2003.
- [63] D.V. Shetty and S.J. Yennello. Nuclear symmetry energy: An experimental overview. *Pramana-Journals of Physics*, 75(2), August 2010.
- [64] Rupesh Silwal. *Probing the Strangeness Content of the Proton and the Neutron Radius of  $^{208}Pb$  using Parity-Violating Electron Scattering*. PhD thesis, University of Virginia, May 2012.
- [65] Karl J. Slifer. *Spin Structure of  $^3He$  and the Neutron at Low  $Q^2$ ; A Measurement of the Extended GDH Integral and the Burkhardt-Cottingham Sum Rule*. PhD thesis, Temple University, August 2004.
- [66] A.W. Steiner, J.M. Lattimer, and E.F. Brown. The equation of state from observed masses and radii of neutron stars. *The Astrophysical Journal*, 722(33), October 2010.
- [67] Riad Suleiman. Parity violation experiments and beam requirements. MCC Ops Training, August 2009.
- [68] B.G. Todd-Rutel and J. Piekarewicz. Neutron-rich nuclei and neutron stars: A new accurately calibrated interaction for the study of neutron-rich matter. *Physical Review Letters*, 95(122501), September 2005.
- [69] Herbert Uberall. *Electron Scattering From Complex Nuclei*. Academic Press, INC, New York, New York, 1971.
- [70] D. Vautherin and D. M. Brink. Hartree-fock calculations with skyrme’s interaction. i. spherical nuclei. *Physical Review C*, 5, March 1972.
- [71] D. Wang. Dithering plots. [http://hallaweb.jlab.org/halog/log/html/1004\\_archive/100429041111.html](http://hallaweb.jlab.org/halog/log/html/1004_archive/100429041111.html), April 2010.
- [72] J. Wexler. Prex results, separated by ihwp/wien state. <http://ace.phys.virginia.edu/HAPPEX/2802>, January 2012.
- [73] C.S. Wu, E. Ambler, R.W. Hayward, D.D. Hoppes, and R.P. Hudson. Experimental test of parity conservation in beta decay. *Physics Review*, 105:1413–1415, February 1957.
- [74] C. Yan, N. Sinkine, and R. Wojcik. Linear beam raster for cryogenic targets. *Nuclear Instruments and Methods in Physics Research A*, 539:1–15, February 2005.

- [75] Eduardo G. Yukihara. Luminescence properties of beo optically stimulated luminescence (osl) detectors. *Radiation Measurements*, 46, 2011.
- [76] Xiaochao Zheng. *Precision Measurement of Neutron Spin Asymmetry  $A_1^n$  at Large  $x_{Bj}$  Using CEBAF at 5.7 GeV*. PhD thesis, Massachusetts Institute of Technology, December 2002.